博士論文

Flow Deformation Characteristics of Sandy Soils under Constant Shear Stress

(一定せん断応力条件下における砂質土の流動変形特性)

リスキ　ファリス　ヒダーヤト

Flow Deformation Characteristics of Sandy Soils under Constant Shear Stress

(一定せん断応力条件下における砂質土の流動変形特性)

By

Risqi Faris Hidayat

(リスキ　ファリス　ヒダーヤト)

A thesis submitted in partial fulfillment
of the requirements for the degree of

Doctor of Philosophy

Department of Civil Engineering
The University of Tokyo
Tokyo, Japan
March, 2020

Abstract

The phenomena and problems associated with liquefaction can vigorous in perspective by considering two different conditions encountered in the field; level ground condition and the sloping ground. In the level of ground condition, the soil liquefaction itself becomes the primary concern. However, for the sloping ground case, the associated phenomenon resulted from the soil liquefaction, such as flow failure or massive lateral movement should become the main attention, in addition to the occurrence of soil liquefaction itself.

The recent 2018 Sulawesi earthquake in Indonesia proves that large-scale flow failure could occur even in the gently sloping ground (1-5%). This very gentle slope, logically, could not trigger massive movement. Thus, the flow failure that occurred in the gently sloping ground could not be explained by the framework of the previous concept of the initiation of the flow liquefaction, which emphasizing the static shear stress as the main factor of the movement.

Several hypotheses have been proposed to explain how this flow failure could travel in a long distance in the gentle slope. The scenario of the water infiltrating to the sandy soil undergoes the earthquake shaking is one of the appropriate concepts, considering its possibility in the field. The water could be coming from the seepage forces from the sub-liquefied layer or the confined aquifer as part of geological features, that infiltrates to the upper-sandy-layer.

This study will utilize the water inflow concept to trigger large movement using static liquefaction test in strain-controlled Triaxial Apparatus as well as hollow cylindrical Torsional Shear Apparatus. As far as the author investigated in the literature study, there exists no previous study on the role of investigating the flow rate characteristics of sandy soils under constant static shear stress. In the previous studies, several researchers had conducted static liquefaction tests on clean sand to understand the development of strains under these circumstances by controlling the density and static shear stress variables.

In the static liquefaction test, after consolidating specimen to a specific condition, in this test was p'_{ini}=100 kPa, the specimen was subjected to initial static shear stress to illustrate the inclination of ground slope. From this point, the mean effective stress (p'_{ini}) will be reduced by increasing the back-pressure, while keeping the static shear stress constant under drained condition. The specimen failed when the effective mean stress reached the failure line. In this state, the shear strain and the volumetric strain were developed continuously and the rate of shear strain development could be measured under the constant static shear stress and constant mean effective stress condition.

With the intention of investigating the flow rate characteristics of sandy soils under constant static shear, a series of static liquefaction test was performed on Toyoura sand (clean sand) using the strain-controlled Triaxial Apparatus by varying densities, static shear stresses, and fine contents of the material. The observation was terminated when the axial strain reached 20% in Triaxial Apparatus. In order to understand the flow behavior and characteristics in the larger strain, series of static liquefaction tests were also performed on Toyoura sand (clean sand) and disturbed samples from flow failure sites on 2018 Sulawesi Earthquake using the hollow cylindrical Torsional Shear Apparatus. This apparatus has been modified to achieve 100% of the shear strain rate in a single amplitude. Furthermore, as this apparatus has the non-coupled stress mode, it could perform the static liquefaction test under the low static shear stress to illustrate the gentle slope condition.

According to the study of flow deformation behavior on the different static shear stress and initial density, the development of shear strain and volumetric strain can be distinguished into three stages: initial stage, limited flow, and continuous flow. The measurement of flow rate was conducted at the continuous flow stage by calculating the differentiation of shear strain increment to the time under constant static shear stress and mean effective stress.

The consequence of conducting the static liquefaction test under drained condition is the specimen showed dilation behavior, showed by volume expansion.

Experiment on Toyoura Sand showed that the specimen would dilate toward the steady-state line, regardless of the initial densities and static shear stress applied to the specimen. This condition corresponded to the void redistribution phenomenon of the sandy specimen during this type of shearing process.

In the strain-controlled Triaxial Apparatus, the static shear stress is notated as the deviatoric stress. It is found that the static shear stress has no major effect on the dilation behavior of the specimen. Nevertheless, the dilation behavior, represented by volume expansion, is more pronounced by the initial density of the sandy soil. The dense materials showed more volume expansion compared to the loose materials. According to the previous research, all the sandy soils will dilate toward their critical state line and dense material will expand more to reach the critical state line, compared to the loose soil.

Nevertheless, it is confirmed that static shear stress has a significant effect on the flow failure rate, represented by the shear strain rate. Under the controlled condition, the higher the static shear stress, the faster the rate of the flow failure. This condition can be explained by imagining that when the angle of friction of specimen is reduced due to the shearing process, by keeping the stress ratio constant, the dilatancy will not recover the soil strength and the progressive failure is continued, shown by the development of strains. In this condition, as the soil loses its strength, the shear strain rate is more driven by the amount of static shear stress acting on the soil.

On the other side, the initial density also showed a significant effect on the shear strain rate. The denser the initial density, the faster the rate of the flow failure will be. By using the same analogy, when the angle of friction is reduced and the soil loses its strength, the state of volume expansion will define the volumetric strain rate and the shear strain rate.

It is noted that from the clean sand, the rate of flow failure is affected by both static shear stress and the initial density of the specimen. However, the effect of static shear stress are more prominent on the dense specimen and decayed as the initial density of the specimen is looser. Thus, it could be concluded that the effect of static shear stress acting on the specimen during the flow failure state will be not significant if the volume of expansion is small.

In order to understand the effect of fine content on the flow rate characteristics, static liquefaction tests were conducted to the mixed sand with various fine content (FC=0-20%), and various initial densities. It is found that the volume of expansion of sand with fines is mostly affected by the amount of fine content. The experiment results on the Triaxial apparatus showed that the higher the amount of fine content, the less the volume expansion will be developed. This mechanism shows that the fine content terminate the development of volumetric strain as well as the void redistribution. Under the examined conditions, sand with fine content showing the different trends as the Toyoura sand. In the Toyoura sand (clean sand), the densest the specimen is, the faster the shear strain rate will be developed. Nevertheless, as the fine content terminate the void redistribution, the densest material is likely to have smaller volume expansion making the shear strain rate will become slower.

Observing the flow deformation and rate characteristics of sandy soils at large deformation, the author conducted a series of static liquefaction tests on hollow cylindrical Torsional Shear Apparatus using Toyoura sand (clean sand) under the small static shear stress. It is found that even at the small static shear stress, the flow failure could be observed on the clean sand specimen. The experiment conducted at Torsional Shear Apparatus with a hollow cylindrical specimen showed a good agreement as at the Triaxial Apparatus in terms of dilation behavior of clean sand, in which the more the volume expansion will be developed for denser initial density. Also, in the shear strain rate characteristic, the relationship between the initial density and the shear strain rate showed the same tendency for both apparatuses.

In the Torsional Shear Apparatus, after the shear strain rate developed rapidly, the sudden stress drop can be observed, particularly on medium dense to dense specimens at the large shear strain. This phenomenon might correspond to the phenomenon of particle soil loss their contact or buckling. After the drop, the stress

was recovered showing that the void redistribution happens to make the soil strength recovered. This phenomenon was not observed in the Triaxial Apparatus.

In order to promote a hypothesis of the mechanism of this long-distance flow failure, series of the undrained cyclic test have been conducted to the disturbed sample of gravelly sand layer taken from the Sibalaya Trench 3 in Triaxial Apparatus. The results indicate that this sample has low liquefaction resistance and probably liquefied during the 2018 Sulawesi Earthquake. In addition, a sandy soil layer above the gravelly layer is assumed as the flow layer.

In order to investigate whether this sample could flow under a mechanism solely by soil liquefaction, an undrained cyclic loading test follow by the undrained monotonic loading test has been conducted. The result shows that even after the liquefied state, the specimen still can mobilize the stress from the monotonic loading, showing no flow behavior. On the other hand, a static liquefaction test also has been conducted to this sand layer, permitting water injected to the specimen during the shearing process. The result shows that flow behavior can be observed vividly after shear strain reaches 5.5%, with the volumetric strain around 1.8%. These test results indicate that the phenomenon of long-distance flow failure in Palu City could not be explained solely by undrained condition and conventional soil liquefaction theory.

. By elaborating on the field observation and the soil element testings conducted in the laboratory, a mechanism of lateral flow with confined aquifer is proposed to explain how this long-distance flow failure is possibly promoted by an external factor, which is a confined aquifer.

Acknowledgment

First and foremost I would like to express my deepest and sincerest gratitude to my supervisor, Associate Professor Takashi Kiyota, Institute of Industrial Science, The University of Tokyo, for his valuable suggestions, constructive criticisms and amazing patience, in making this research a reality. His wide knowledge and his logical way of thinking have been of great value for me. His understanding, encouraging and personal guidance have provided a great basis for the present thesis

Besides, I am deeply grateful to the Ph.D. thesis committee members, Professor Junichi Koseki, Professor Reiko Kuwano (Institute of Industrial Science), Associate Professor Kenji Watanabe and Professor Mitsui Okamura (Ehime University) for their valuable comments, criticisms, suggestions and important support for my research.

My special appreciation goes to Mr. Toshihiko Katagiri, Kiyota Laboratory, for his highly cooperative supports in assembling both the mechanical and electronic components of the employed testing apparatus and advising on troubleshooting. Thanks also for being smiling and offering fun on every occasion.

I am grateful to Mrs. Mina Takahashi, the secretary of Kiyota Laboratory, for her kind support in handling the administrative aspects during my study.

My sincere appreciation is also forwarded to Kiyota Laboratory members. Especially thanks to Dr. Umar Muhammad for teaching me how to perform torsional shear tests. I also fell to be very fortunate to meet Mr. Masataka Shiga and Mrs. Rosiyani, who are truly warm and kind-hearted friends for sharing many exciting experiences, covering research, and non-research activities. Mr. Ryo Teramoto, Mr. Takanobu Kumagai, Mr. Matthew Chua, Mr. Koki Nakao, Mr. Nazish Ullah, Ms. Amani Guizani, Ms. Marina Oya for their kind and cooperative supports during my stay is highly appreciated. I also express my sincere gratitude to all fellow members not listed above. I wish them all the best in their own study and future life.

My special gratitude for Mr. Masakazu Inori, my host-family father while staying in Tokyo. Thank you for introducing me to Japanese culture and traditions and for all the sincere supports for the last minutes of my study. I feel honored to have a family bonding with you.

I would like to thank all my friends in Indonesia, in Japan and all around the world for keeping our friendships alive.

I sincerely acknowledge the Indonesian Endowment Fund for Education as the sponsor of my Ph.D. studies in Japan.

Last but not least, I would like to express my deepest gratitude to my family members, especially to my parents, for their never-ending support and encouragement during my whole course of study. My special gratitude is due to my brothers, Muhammad Zulfikar Ismail and Ahmad Kurnia Ramadani. I wish you can achieve your future dream and happiness.

This thesis and my future achievements are all dedicated to them with genuine appreciation and respect.

Tokyo in Winter season January 2019

Risqi Faris Hidayat

Table of Content

List of Tables

List of Figures

Chapter 1 INTRODUCTION

1.1. Liquefaction-induced-flow deformation

Soil liquefaction becomes one of the significant concerns for constructing infrastructure above the saturated loose sandy ground. This typical disaster and its associated failure could produce substantial economic loss and a large number of casualties. After the catastrophic 1964 Niigata earthquake, which results in enormous soil liquefaction phenomena, research about soil liquefaction become more renowned and essential.

Soil liquefaction can be associated with the event when cohesionless soils such as sands and limited cases of gravels, completely lose their strength under high-frequency cyclic loading (i.e., earthquake shaking) and transform their behavior like a liquid than a solid. This phenomenon had caused dramatic consequences to social infrastructures (bridges, dams, roads, embankments), buildings, as what happened on the area suffered by large-scale earthquake events (Anchorage, Alaska, 1964; Niigata, Japan, 1964; San Fernando, California, 1971; Emperial Valley, California, 1979; Nihonkai-Chubu, Japan, 1983 Superstition Hills, California, 1987; Loma Pietra, California, 1989; Kobe, Japan, 1995; Kocaeli, Turkey, 1999; Niigata, Japan, 2004; Christchurch, New Zealand, 2010; etc…).

According to the soil mechanics theory, coarse-grained soils are arranged by individual grain, that contacts among others. The contact forces arise between the contiguous soil grains, with a normal and a shear component. Since the behavior of soil is mainly promoted by its friction, its strength depends on the extent of the normal forces. In the principle of effective stresses, the strength of a cohesionless saturated soil depends on the normal effective stress components, which are equal to the difference between the total typical stress components and the pore water pressure. If the total stress components remain unchanged, an increase in pore water pressure has the effect of reducing the normal effective stresses and may lead to the collapse of soil.

In a more microscopic approach, under such quick cyclic loading conditions, the soil structure is profoundly modified, with the particles tending to move in a denser configuration. For clean sands, there is not enough time for the water to be expelled out from the soil pores, and thus a build-up of water pressure occurs. When this pressure becomes equal to the total stress acting on the soil, the normal effective stresses are disappeared, and finally, the soil particles become free to move independently from the neighboring ones, or the soil behaves like a liquid. The occurrence of this phenomenon is governed by the seismic event (magnitude, peak ground acceleration) as well as the properties of the soil.

When the ground is subjected to strong shaking during an earthquake, various engineering phenomena can be observed, such as the onset liquefaction event that resulting in the ground settlement or flow failure event that involving the soil masses movement. The phenomena and problems associated with liquefaction can be put in perspective by considering two different conditions encountered in the field; level ground condition and the sloping ground (Ishihara, 1993). In the level ground condition, the soil liquefaction itself becomes the primary concern. Nevertheless, for the sloping ground case, the associated phenomenon resulted from the soil liquefaction, such as flow failure or massive lateral movement should become the main attention, in addition to the occurrence of soil liquefaction itself.

1.2. Flow failure phenomenon in the gently sloping ground due to soil liquefaction

During past earthquakes, several cases related to the flow movement behavior in the field have been recorded after the earthquake. The deformation could reach several centimeters to several hundred meters, even at the gentle ground inclination (0.1% to 6%).

1.2.1. Permanent ground displacement in Kawagishi-cho, Niigata station, and Ohgata area due to 1964 Niigata Earthquake

Hamada et al. (1991) measured the displacement of several areas in Niigata city after the 1964 Niigata earthquake. Figure 1-1 shows the horizontal vectors of the permanent ground displacements in Kawagishi-cho and Niigata Station areas, with the ground failures, such as sand boiling, cracks, subsidences, etc.

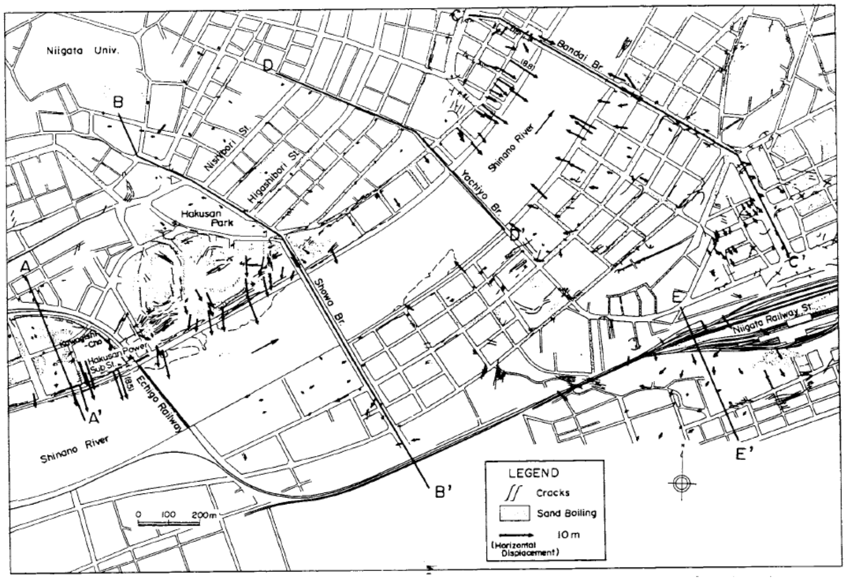

Figure 1-1 Permanent ground displacement in Kawagishi-cho and Niigata station area (Hamada et al., 1991)

The maximum horizontal displacement was 8.5 m in the proximity of the Hakusan power substation and 8.8 m on the left bank near the Bandai Bridge. The directions of the horizontal vectors of the displacements were almost perpendicular to the river. The magnitude of the permanent ground displacement in the area near the Niigata Railway Station was 2 to 3 m, smaller than that along the Shinano River, but, notably, the directions of the displacement was not toward the river but toward the station. Large permanent ground displacements toward the Shinano river occurred on both banks. About 300 m from the river toward Niigata Railway Station, permanent ground displacements of 1 to 2 m occurred in the direction away from the river. The ground surface in this area was almost flat, but the lower boundary face of the liquefied layer was estimated to be sloped with a small gradient of 2-3 % toward Niigata Station. For this reason, the permanent ground displacements in this area might be in the direction away from the river.

Further, Ishihara and Koga (1981) conducted a detailed soil investigation in the Kawagish-cho area by using the Standard Penetration Test and Dutch Cone Penetration Test together with taking undisturbed samples. The results of the site investigation showed that the deposits of clean sands existed down to the depth of 20 m, with the sudden drop of N-value at a depth of 19 m.

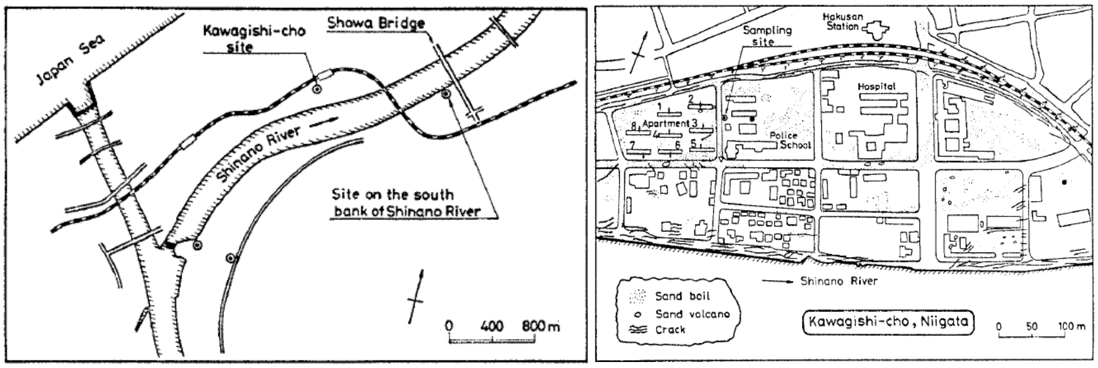

Figure 1-2 Location of the tests site in Niigata city (left) and the location of sampling site in the Kawagishi-cho area (right) (Ishihara & Koga, 1981)

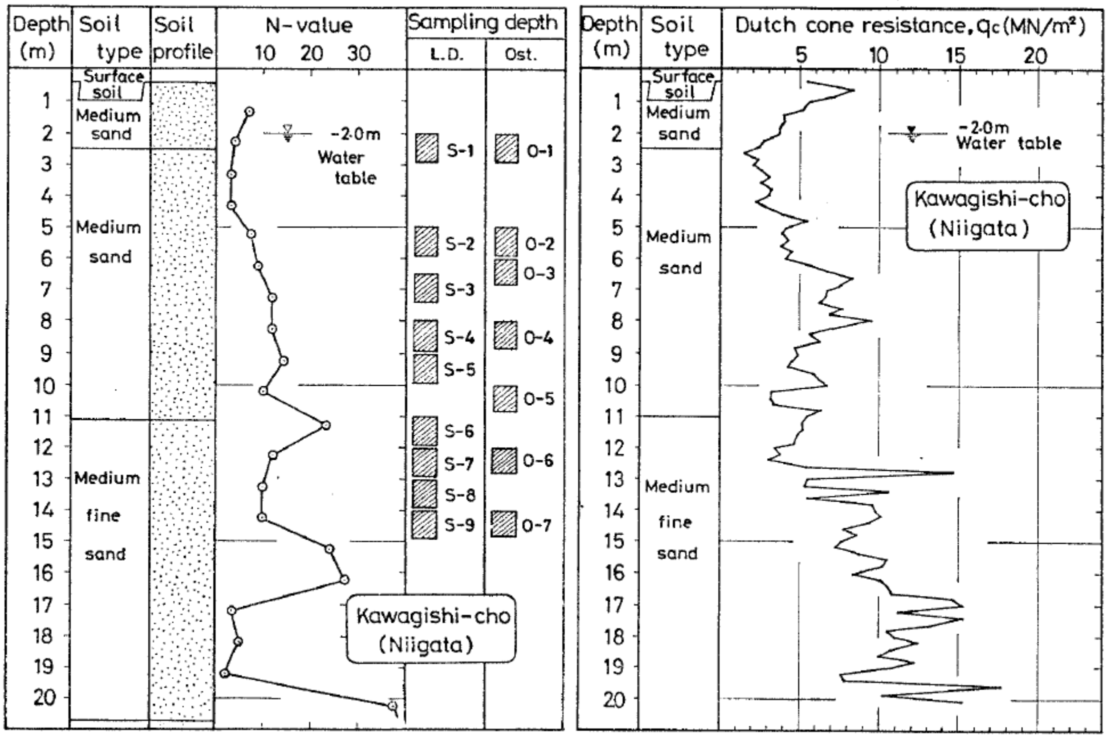

Figure 1-3 Soil profile at Kawagischi-cho site (left) and the penetration resistance using Dutch Cone Penetration Test (right) (Ishihara & Koga, 1981)

The samples were tested in the laboratory using the Cyclic Triaxial Test Apparatus to determine the cyclic strength of in-situ intact sand. The laboratory test showed that the cyclic stress ratio producing initial liquefaction in 20 cycles ranged between 0.15 ad 0.20in which lower than corresponding cyclic shear stress that must have been induced in the deposit of Kawagishi-cho site during the 1964 event.

Figure 1-4 shows the measured permanent ground movement in the Ohgata area. From the schoolyard of Ohgata Elementary School, large permanent ground displacements had occurred in a radial direction, with the maximum displacement reaching approximately 10 m. The ground surface was almost flat, but a very small highland, of 1.5 m in height, was developed at the south side of the Tsusen River. It can be seen that large permanent ground displacements were concentrated at almost the wedge of the highland.

Based on the results of the soil investigations, soil layer profiles along many section lines were estimated. Figure 1-5 shows an estimated profile along the B-B' line in Figure 1-1. In this section, the estimated liquefied layer slopes gently toward the Tsusen River and has a thickness of about 4 m. The ground surface has also slopes gently, the average gradient of the slope being only 0.5 %.

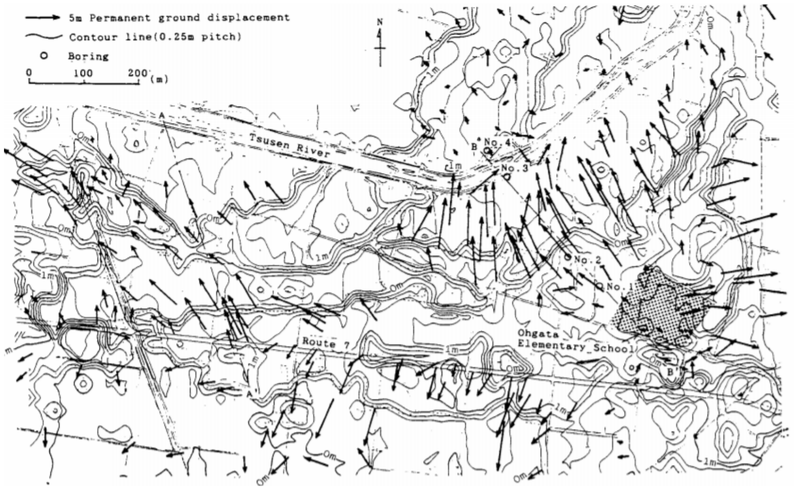

Figure 1-4 Permanent horizontal displacements and contour lines in Ohgata area (Hamada, et al., 1991)

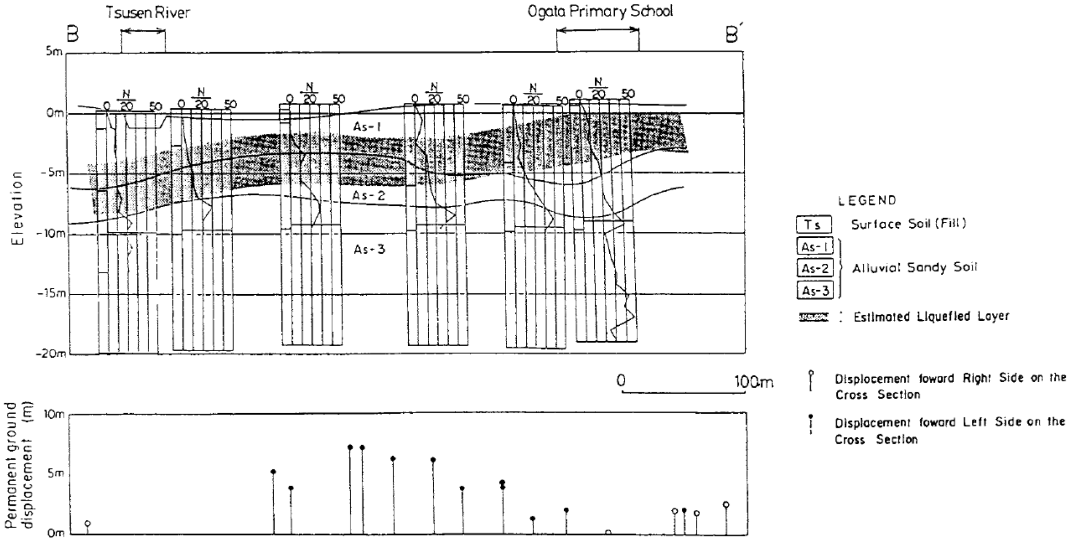

Figure 1-5 Estimated soil profile and liquefied layer along B-B’ Line in Ohgata area (Hamada, et al., 1991)

1.2.2. Long-distance flow slides in Palu City due to 2018 Sulawesi Earthquake, Indonesia

The recent 2018 Sulawesi earthquake in Indonesia also revealed that flow failure could occur in very gentle ground inclination. The United States Geological Survey (2018) informed that the epicenter (0.256 S and 119.846 E) was located 70 km from the northern part of Palu city at the shallow depth of around 20 km. This earthquake was driven by the mechanism of super-shear rupture of the Palu-Koro fault (Bao, et al., 2019; Socquet, et al., 2019). The strike-slip movement created the mainshock, as observed from its epicenter location, hypocentre depth, and the aftershock distribution.

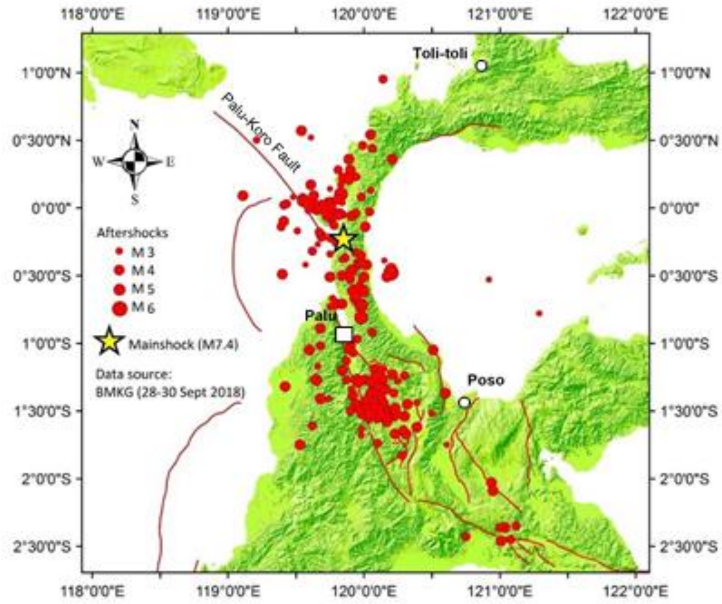

Figure 1-6 Epicenters of the Palu earthquake 2018 and the aftershock distributions (red dots) along Palu-Koro fault in Central Sulawesi edited from Indonesian Society for Geotechnical Engineering, The National Research Centre for Earthquake, Ministry of Public Works (2018)

The National Agency of Disaster Management of Indonesia (2018) reported that this earthquake triggered a tsunami in the coastal areas of Palu, Donggala, and Mamuju and long-distance flow slides in some areas, such as Petobo, Balaroa, and Jono Oge and resulted in 2,101 people died, 4,438 people injured, 1,309 people missing. Kadarusman et al. (2011), Bellier et al. (2001), and Watkinson et al. (2011) mentioned in their paper that Sulawesi Island has a complex tectonic collage that separates the converging Eurasian, Indo-Australian, and Philippines Sea Plate. This condition creates various geological conditions in each area, as well as Palu city. As a result of the collision and interaction of those three plates, Sulawesi Island has several active faults, one of which is a Palu-Koro fault that crossed the Palu city and assumed to have triggered this major earthquake. In addition to the uniqueness of its geological structure, Thein et al. (2014) added that Palu city is composed of alluvial deposits in the valley, Granite fragments on the northwest, Granite and Granodiorite rocks on the west to north part, Schistphyllitic rocks on the south part, and Molasses to the eastern part.

The geomorphology of Palu city has been described as an area consisting of fluvial, denudation, and hills. According to regional geology, the Palu area is composed of Holocene alluvium deposits and beach deposits containing gravel, sand, mud, and limestone. In general, this patterned layer is found in the shallow river, delta, and sea environments. Regarding the age-deposition, this young sediment layer has believed not undergone a complete process of cementation. Zeffitni (2013) also claimed that the uniqueness of geological structure (graben structure) in the Palu area defines its hydro-morphological condition, including the groundwater basin in this area.

The topography gradient of all affected areas was identified as gentle with the gradient of 1 to 3%. Hidayat et al. (2020) revealed that sand ejecta, as the evidence of soil liquefaction, has been found in several places around the affected areas as well as the spring freshwater pond even two weeks after the disaster occurred. The results of Dynamic Cone Penetration Test (DCPT), conducted in four points at the Petobo area, also showed that the soil condition was loose with the converted N-SPT value was less than 5 and the groundwater level was found at the shallow depth. Both factors imply that the liquefaction risk in the affected area is high.

Figure 1-7 Condition before the earthquake (left) and the condition aftermath (right) (Hidayat, et al., 2020)

Figure 1-7 shows the condition before and aftermath in Petobo area. At the top, tensile crack and massive subsidence have been found, identified as the crown of the mass movement. The earthquake motion destroyed and transported all the buildings on the ground resulting in a debris deposition in the bottom part. The ground surface was already dry and walkable, but some cracking part was still very loose. Even though little rainfall occurred after the earthquake, a significant water inundation could still be observed in many parts. In this area, the groundwater level is identified to be shallow. The witnesses informed that the sand ejecta was produced after the shaking of the earthquake.

Figure 1-8 Tensile crack on soil body due to the earthquake motion (Point A), Inundation at the bottom part of the debris zone found at Petobo (Point B), and sand ejecta found in the non-affected area (Point C and D) (Hidayat, et al., 2020).

Figure 1-9 Location of DCPT test at Petobo, highlighted by the red circle. Points 1 and 4 are outside the affected areas while points 2 and 3 are near the crown area (Hidayat, et al., 2020).

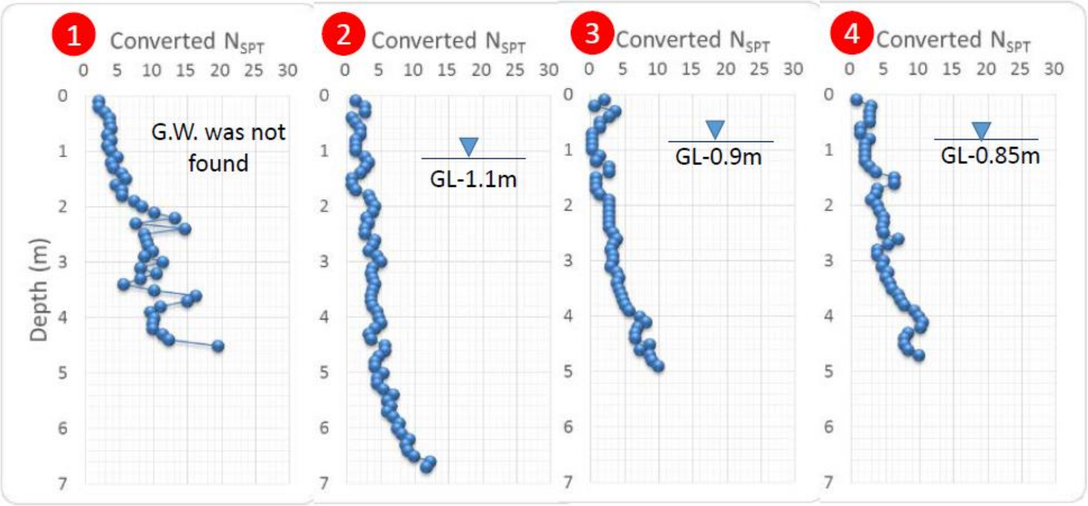

Figure 1-10 Converted N-SPT value from the DCPT test. Groundwater level (GL) at Point 2, 3, and 4 are shallow (Hidayat, et al., 2020).

1.3. The previous study on the flow behavior due to soil liquefaction

The flow failure of alluvial sandy ground has induced catastrophic damage to social infrastructures. The deformation of this slightly to moderately sloped ground tends to occur following the softening of soils due to liquefaction, is controlled by the static gravity force, and is more predominant than cyclic deformation induced by shaking. Flow failure is a phenomenon resulting from steady-state deformation following the unstable behavior of soils with a sudden drop in shear strength. Steady-state is a state of deformation of sol without effective stress increment or decrement with no migration of pore water. If the sands are looser, a point of minimum effective mean stress appears where the dilatancy behavior changes from contractive to dilative, named phase transformation (Ishihara, et al., 1975). If the steady-state follows by the drop of shear stress, this transient steady-state has been called the quasi steady-state (Alarcon-Guzman, et al., 1988). Verdugo (1996) studied the undrained behavior of Toyoura sand in the Triaxial compression apparatus, covering a wide range of density and initial consolidation stress levels, showing in Figure 1-11. At the very large deformation state, as long as the density of the sand is the same, irrespective of the initial condition stress level, a unique steady will be achieved at the final stage of undrained shearing. This phase is called ultimate-steady-state.

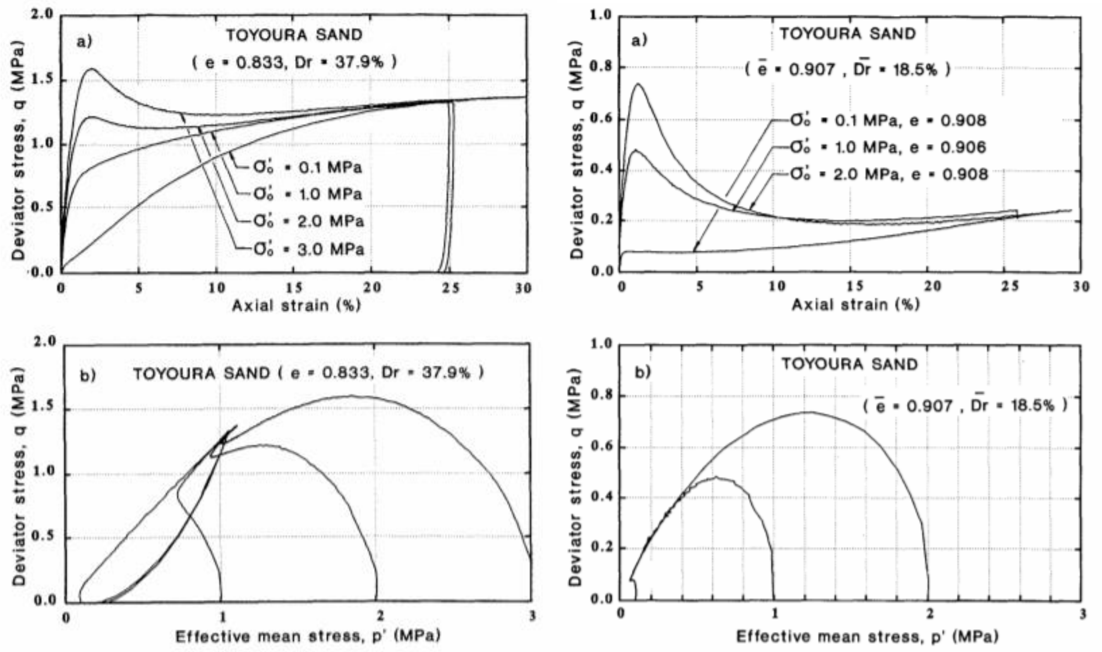

Figure 1-11 Undrained triaxial tests for e =0.833 (left) and e =0.907 (right): a) stress-strain curve; b) effective stress path (Verdugo & Ishihara, 1996).

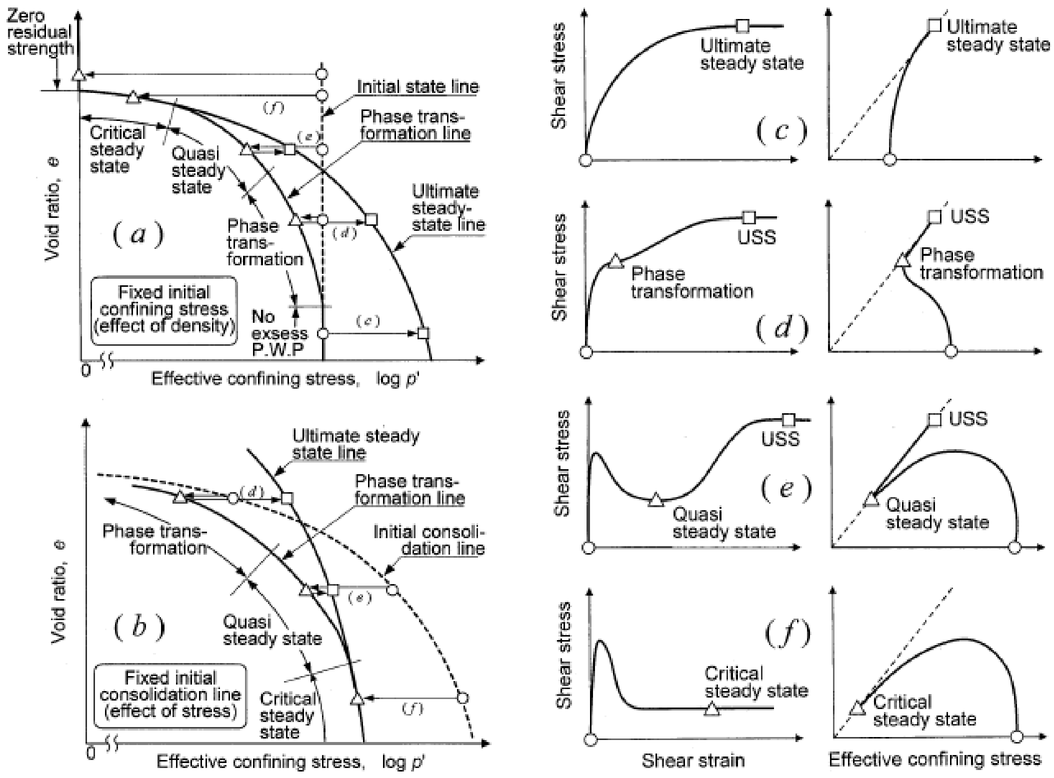

Figure 1-12 General undrained shear behavior of sand under large deformation (Yoshimine and Ishihara, 1998)

Robertson and Wride (1998) distinguished between liquefaction due to cyclic loading and the liquefaction due to strain softening. For the case of liquefaction due to cyclic loading, the effective burden stress can reach zero during the cyclic loading with resulting in loss of soil stiffness. On the other hand, the liquefaction due to strain softening is related to the loss of shear strength that could lead to the loss of stability (flow liquefaction). A further explanation has been drawn by Yoshimine and Ishihara (1998). When the residual shear strength is smaller than the static shear load, generated by the gravity force, the equilibrium will be lost and flow failure will occur. Once the flow failure is triggered by the ground shaking, the deformation can continue without shaking until the static shear load decreases to the same level of residual strength or the strength of soil recovers up to the static shear load. In the case of shear strength is larger than the static shear load, no flow failure but cyclic mobility is expected. The deformation is stable throughout the process and it stops immediately when shaking is terminated.

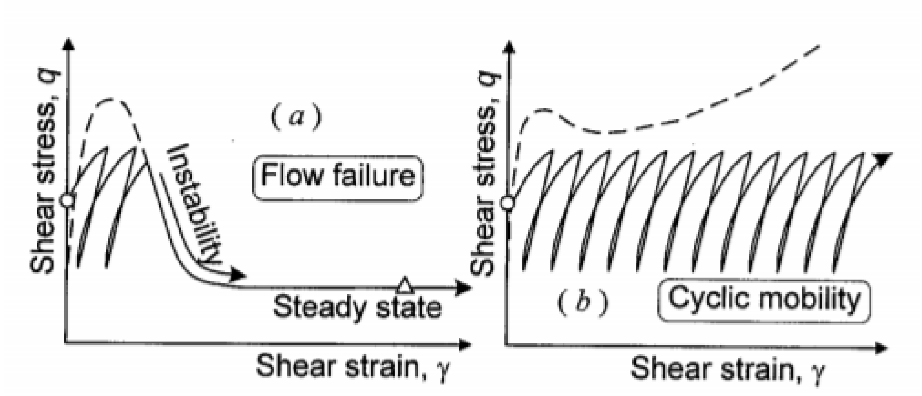

Figure 1-13 Illustration of flow failure (a) and cyclic mobility (b) (Yoshimine & Ishihara, 1998)

National Research Council (1985) of the U.S. National Academy of Science defined flow liquefaction as the condition where a soil mass can deform continuously under the condition where the shear stress less than or equal to the static shear stress applied to it. This statement is also in line with the statement from Kramer (1996), who explained that this flow liquefaction could happen when the shear stress required for static equilibrium of a soil mass is greater than the shear strength of the soil in its liquified state. Both statements emphasize the importance of shear stress acting on the sloping ground to create flow movement behavior. Flow liquefaction is also referred to as static liquefaction (e.g. Jefferies & Been, 2006) even the triggering factor could be by either static or cyclic loading (Ishihara, 1993; Kramer, 1996; Lade, 1992; Vaid & Chern, 1983).

In the current understanding, when a soil layer is liquefied in the field, the excess pore water pressure will dissipate to the upward direction and the void redistribution takes place, followed by the ground settlement. Laboratory scale models, built on conventional shake tables and centrifuges, have been used to study the post-liquefaction behavior under controlled conditions. A series of large shake table tests intended to study the behavior of liquefaction-induced lateral spreads have been reported by Towhata et al. (1989; 1991), Sasaki et al. (1991; 1992), Yasuda et al. (1991; 1992), and Tokida et al. (1993). Even though a shake table model might not realistically simulate the liquefaction event in the field due to several limitations such as the limitation of depth scale (Arulananan and Scott, 1993), different soil response for the conditions where static shear stresses exceed the residual strength of a liquefied soil deposit (Ishihara et al. 1991), and the shorter drainage path in scale model (Rauch, 1997), qualitatively, the behavior of these models matches with the field observations in which some critical features such as the down-slope oriented movement, tension cracks and subsidence at the crown, and small displacements as well as heaving at the toe of the slope can be observed.

Whitman (1985) described situations where the pore water seepage driven by earthquake-induced excess pore water pressure gradients could lead to the localized loosening of the liquefied soil as illustrated in Figure 1-14. Boulanger and Truman (1996) described this phenomenon as the void redistribution on the liquefied sand during the post-liquefaction state.

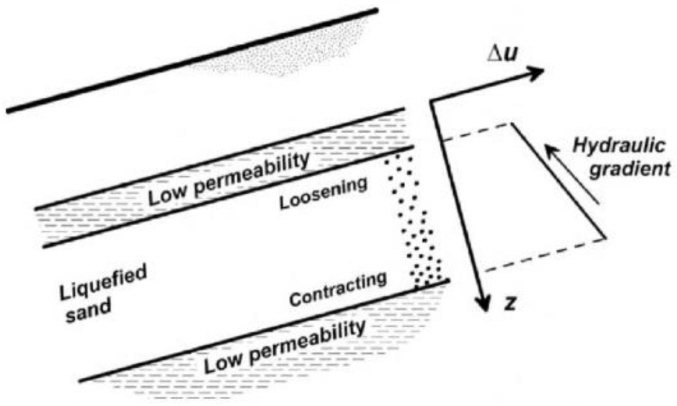

Figure 1-14 Schematic of void redistribution in a confined sand layer due to upward seepage driven by earthquake-induced excess pore water pressure gradients (after Idriss and Boulanger, 2007)

When the upward excess pore water pressure meets less permeable silt of the clayey layer, the water will be accumulated and create a water interlayer with very-low shear resistance in between the liquefied layer and the less permeable layer. Physical and analytical modeling of this water-interlayer phenomenon has been studied by Fiegel and Kutter (1994), Kokusho (2000; 2003), Kulasingam et al. (2004), and Malvick (2006).

Kokusho (1999) also reported based on his experimental results that when the water interlayer is formed below the sloped less permeable layer, a large deformation takes place in the less permeable layer and its upper layers due to the gravity force while maintaining their shape. However, this water interlayer concept could not fully explain the occurrence of long-distance flow slides in Palu City. Okamura et al. (2020) who conducted several trench surveys in the Sibalaya area reported that in order to employ the water interlayer as the only factor to promote this long-distance flow slide, the water interlayer should be smooth and continuous all over the area and this assumption was not always met with the investigation results. Kiyota et al. (2020) reported that the shallow groundwater in the affected areas was under-pressure (based on the interview with the residents) and considered that the possibility of the long-distance flow-slide was because the effective stress and the shear strength of the surface ground significantly reduced by a large amount of groundwater supplied from the confined aquifer. This assumption is supported by the fact that a lot of surface water due to spring water was found at many locations in the flow-slide affected areas despite not having a lot of rainfall, even two weeks after the disaster.

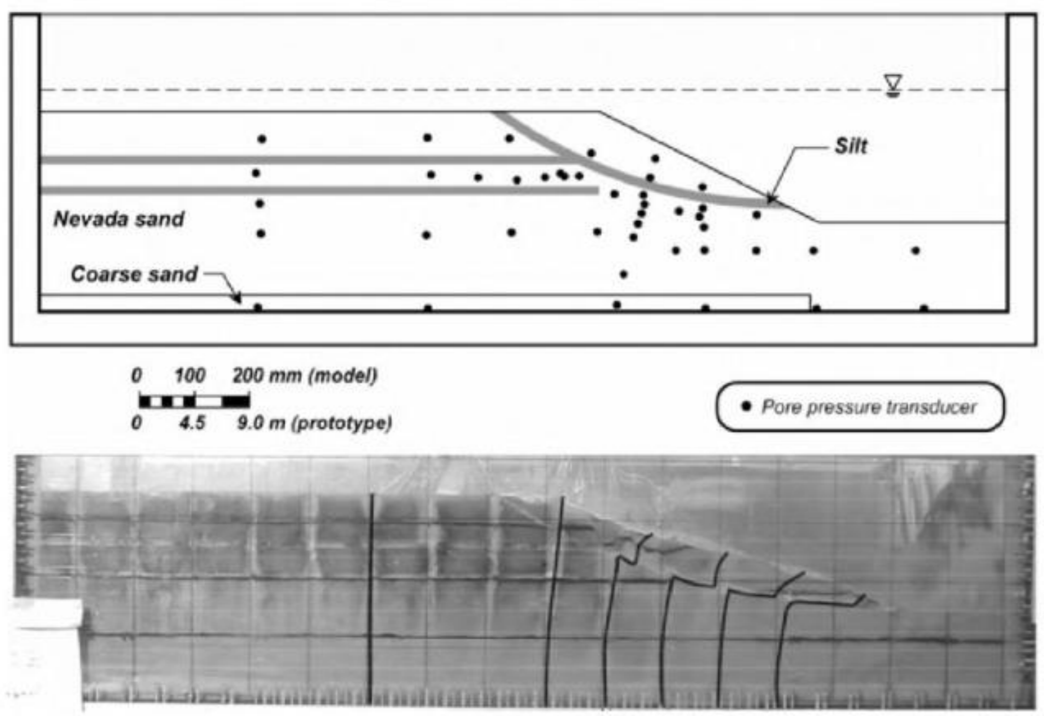

Figure 1-15 Centrifuge model showing localization under a silt layer in a saturated sand slope due to liquefaction-induced void redistribution (Malvick et al. 2004)

In the typical laboratory undrained shear test, positive dilatancy associated with increasing shear strain is restrained, and strength and stiffness are eventually recovered even in very loose sand (Kiyota et al., 2013). This experiment results probably suggest that the long-distance flow-slide is unlikely to occur at the gently sloped ground under the undrained condition. However, considering the inflow of the groundwater from the confined aquifer, the significant positive dilatancy is allowed to occur for surface ground due to the water absorption, so that the shear resistance of the surface ground reduced significantly, resulting in a long-distance flow-slide even in the gently sloped ground.

A series of laboratory experiments related to this issue has been conducted by several researchers, emphasizing on the post-liquefaction behavior of sand. Boulanger and Truman (1996) compared the behavior of medium dense (Dr=55%) Sacramento sand in Post-cyclic Constant Shear Stress (PCV-CST), which allows the injection of water moved into the specimen, and in Isotropically Consolidated with Drained

Triaxial Compression (ICD-TC). The results showed that the PCV-CST tests could evaluate the post-earthquake behavior of the sand layer in an infinite gentle slope and the dilation behavior between both tests was comparable as shown in Figure 1-16.

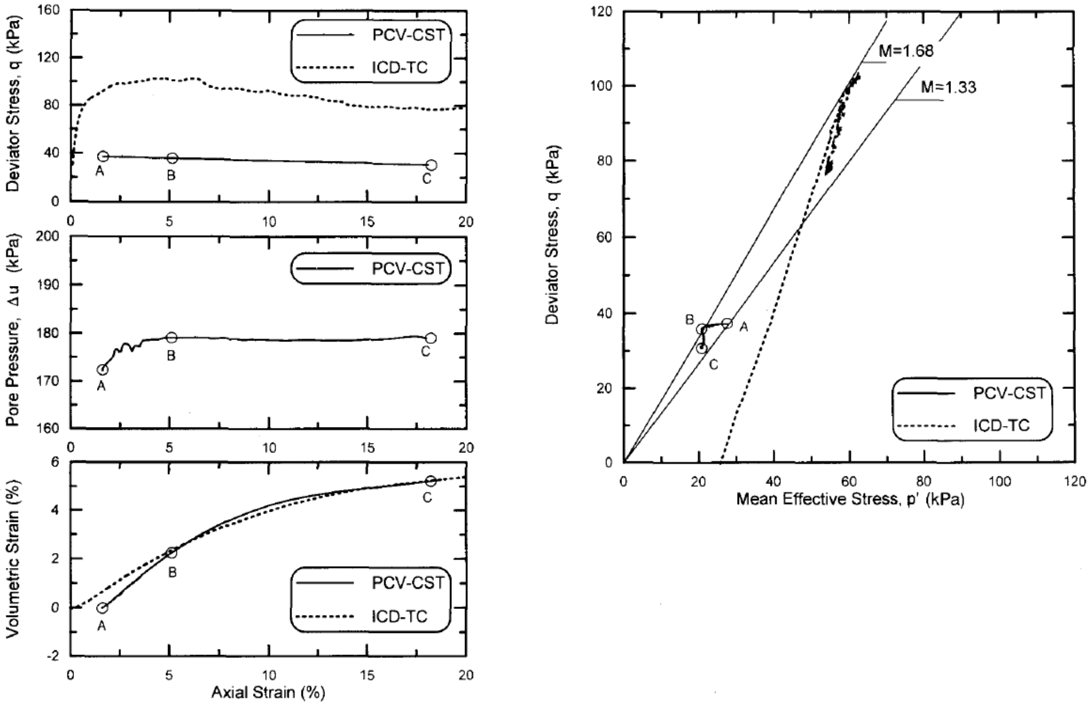

Figure 1-16 Results of PCV-CST and ICD-TC tests on Dr=55% specimens (Boulanger and Truman, 1996)

Sento et al. (2004) conducted pore water injection in Triaxial tests (specimen size was 50-mm in diameter and 100-mm in height) in which initial static shear stress corresponding to the slope angle was maintained until the axial strain reached 5%, following by the drainage. The experiment using Toyoura sand with initial static shear stress 0, 25, 37, and 54 kPa and a relative density of 30%, 60%, and 85% showed that the large shear strains develop after the samples reach the failure line and the denser sand requires much more injected pore water to develop the same level of shear strain compared to the loose sand. This made an initial assumption that the dense sand is more resistant to the flow failure compared to the loose one. However, this initial assumption could be misleading as the strain observed in this experiment is very limited.

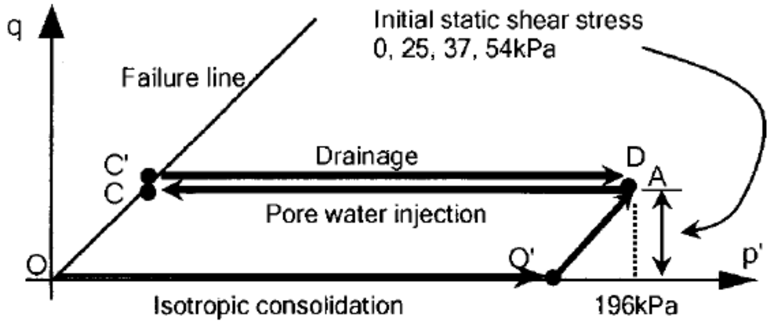

Figure 1-17 Stress path of pore water injection test (Sento, 2004)

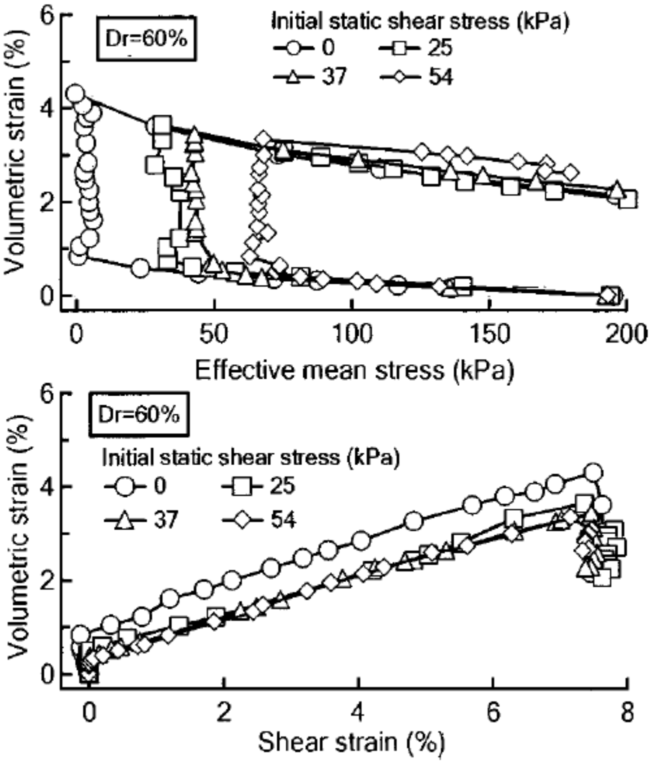

Figure 1-18 Effect of initial shear stress on flow failure deformation characteristics due to pore water inflow (Sento, 2004)

Yoshimine et al. (2006) also conducted the similar pore water injection with keeping deviatoric stress constant as previous researchers, so-called static liquefaction test for various relative densities (Dr=1%-94%) and various stress ratio (q/p'_{ini}) using Toyoura sand at Triaxial apparatus (specimen size was 50-mm in diameter and 100-mm in height) until the axial strain reached 30%. The results showed that the dilatancy behavior of the sand was hardly affected by the shear stress and the initial confining stress levels, but it is the function of the initial density of the sand. The denser the material, the more the volume expansion will be developed.

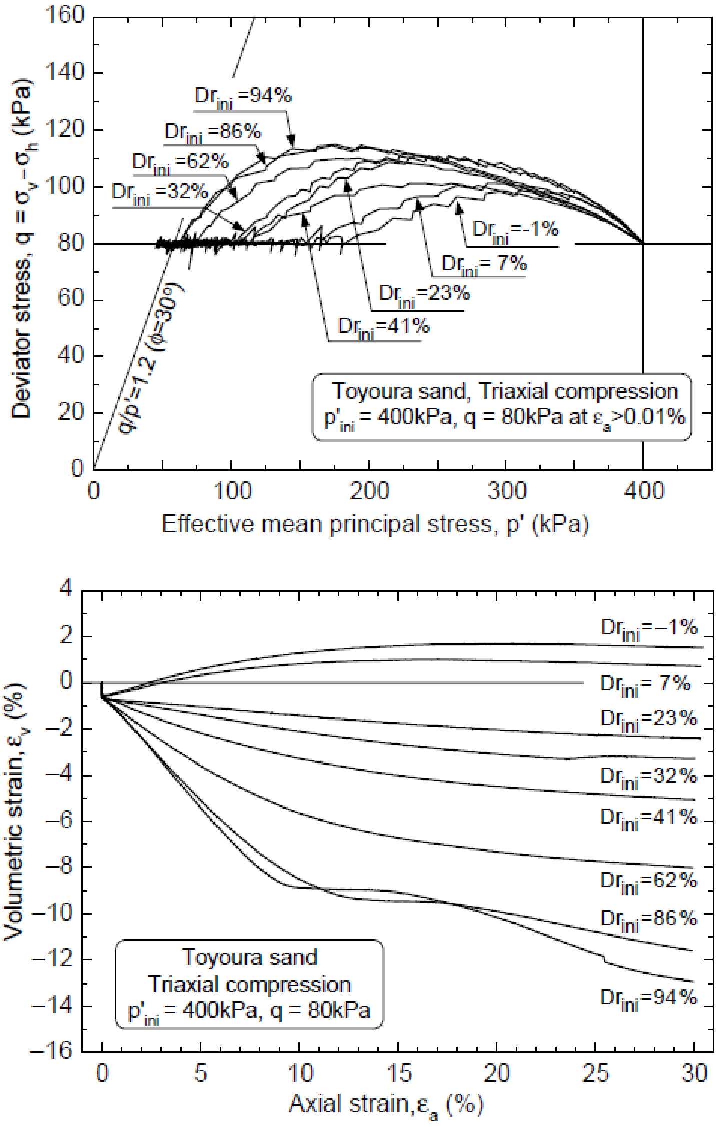

Figure 1-19 Effective stress path and axial strain and volumetric strain relationship of static liquefaction test for various densities (Yoshimine, 2006)

Considering the real disaster phenomenon that occurred in the field, there are two major variables that should be addressed, such as the starting point of the flow failure and the rate of flow failure occur after the earthquake stops. Both variables become essential to describe the flow behavior associated with real behavior in the field. This dissertation will investigate the possibility of this mechanism occurred in a very gently sloping ground using element tests to develop a clear understanding of the key variables, by elaborating the flow phenomenon occurs in the field.

1.4. Objectives of this study

The objectives of this study are summarized as follow:

1. To investigate the flow deformation characteristics by using the water inflow concept in Strain-controlled Triaxial Apparatus.

Sento et al. (2004) and Yoshimine et al. (2006) conducted several static liquefaction tests using element tests to demonstrate the possibility of flow failure generated with water inflow concept in the clean sand. However, both researchers only examined the dilatancy behavior of the soil. This study will examine more in-depth, not only the development of strains during the flow failure state but also how the initiation and the progression of this flow failure could happen in the static liquefaction test. Furthermore, the recent 2018 Sulawesi Earthquake that triggers flow failure in Palu city has demonstrated many challenges to studying such as the possibility of this flow failure happened in the gently sloping ground with the shallow depth, the characteristics of flow failure rate developed, and the fine content effect to the flow behavior.

By using this apparatus, this study will emphasize more on the rate characteristic of flow failure by seeing the effect of initial density and static shear stress, on the clean sand (Toyoura sand) and sand with fine content.

2. To evaluate the flow deformation characteristics in the large strain behavior using a Hollow Cylindrical Torsional Shear Apparatus.

The limitation of Triaxial Apparatus to achieve large strain development as well as the indirect shear behavior become the main concern to conduct the test using a modified hollow cylindrical Torsional Shear Apparatus. In this apparatus, the real behavior of direct shear that represents a more reliable earthquake motion acting on soil specimens could be observed. On the other hand, this study utilizes a modified Torsional Shear Apparatus in the Institute of Industrial Science, The University of Tokyo that could achieve 100% of shear strain in a single amplitude. Kiyota (2008, 2013) studied the maximum possible deformation of liquefied soil in extremely-large strain areas by conducting a series of cyclic undrained torsional shear tests on this apparatus until reaching approximately 100% of shear strain. Chiaro (2011) also studied the effect of initial static shear stress on the undrained cyclic behavior of saturated loose Toyoura sand by this torsional shear loading up to single amplitude of shear strain of about 50 % under various combinations of static and subsequent cyclic shear stresses. The test results show that the presence of initial static shear does not always lead to an increase in the resistance to liquefaction and shear strain accumulation up to 50%; in fact, both can either increase or decrease by increasing the static shear depending on the magnitude of the combined shear stress, the type of loading and the failure behavior in undrained condition.

Considering the possibility of water inflow mechanism occurred in the field, a series of static liquefaction tests will be conducted on clean sand (Toyoura sand) using this torsional shear apparatus to understand the flow behavior under large strain development in drained condition, associated with the gentle inclination and various densities.

1.5.Organization of thesis

Following the background and the objectives, this thesis will be delivered in this arrangement as follow.

Table 1-1 List of the thesis organization

Thesis part	Description
Chapter 1	This chapter introduces the background and motivation of this study. The objectives will be focused on two primary purposes

	that set the milestone of this study. In the last part, the arrangement of this thesis is presented.
Chapter 2	This chapter presents the test materials, apparatus, and testing procedures in strain-controlled Triaxial Apparatus and hollow cylindrical Torsional Shear Apparatus, respectively. The physical properties of Toyoura sand, fine materials including DL Clay (non-plastic fine material) and Kaolin (plastic fine material), as well as natural sand is introduced. The static liquefaction testing procedures is also explained in this part of the thesis.
Chapter 3	This chapter gives the basics of soil mechanics theory, focusing on the stress and strain calculation on both apparatuses; Triaxial apparatus and Torsional Shear apparatus.
Chapter 4	This chapter describes the dilation behavior of sandy soils under the static liquefaction test series conducted in strain-controlled Triaxial apparatus with the following sub-sections: - Flow deformation characteristics during this type of shearing process. - Development of volume expansion of the specimen. - Effect of static shear stress to the dilation behavior. - Effect of initial density to the dilation behavior. - Effect of fine content to the flow failure behavior. - Correlation of initial density and static shear stress to the flow failure rate.
Chapter 5	This chapter describes the dilation behavior of sandy soils under the static liquefaction test series conducted in strain-controlled Triaxial apparatus with the following sub-sections: - Effect of static shear stress on the flow rate characteristics. - Effect of initial density on the flow rate characteristics. - Effect of fine content on the flow rate charateristics.

	- Correlation of initial density and static shear stress to the flow failure rate.
Chapter 6	This chapter delivers the observation of flow deformation and rate characteristics of sandy soils at large strain and very gentle slope on hollow cylindrical Torsional Shear Apparatus with the following sub-sections: - The dilation behavior of sandy soils under small static shear stress on Torsional Shear Apparatus and its comparison to that of the Triaxial Apparatus. - The flow rate characteristics of sandy soils under small static shear stress on Torsional Shear Apparatus and its comparison to that of the Triaxial Apparatus. - Loss of particle interlocking phenomenon at the large strain on Torsional Shear Apparatus.
Chapter 7	This chapter delivers the illustration of the flow behavior phenomenon occurred at very gentle slope using disturbed samples taken from the flow failure site at Palu City during the 2018 Sulawesi Earthquake by associating the element test with field parameters and emphasizing on: - Liquefaction resistance of gravelly layer below the flow layer soils. - Flow deformation and rate characteristics of flow layer soils under very gentle slope.
Chapter 8	This chapter summarizes the conclusions of this study and gives possible recommendations for future research.

1.6. References

Alarcon-Guzman, A., Leonards, G. A. & Chameau, J. L., 1988. Undrained monotonic and cyclic strength of sands. *Journal of Geotechnical Engineering ASCE,* 114(No. 10), pp. 1089-1109.

Ampadu, S., 1991. *Undrained behavior of kaolin in torsional simple shear,* Tokyo: The University of Tokyo.

Ampadu, S. & Tatsuoka, F., 1993. Effect of setting method on the behavior of clays in triaxial compression from saturation to undrained shear. *Soils and Foundations 33 (2),* pp. 14-34.

Arulanandan, K. & Scott, R. F., 1993. Project VELACS-control test results. *Journal of Geotechnical Engineering,* 1199(No. 8), pp. 1276-1292.

Bao, H., Ampuero, J. & Meng, L., 2019. Early and Persistent Supershear Rupture of the 2018 Magnitude 7.5 Palu Earthquake. *Nat. Geosci.*, pp. 200-205.

Bardet, J. P., 1997. *Experimental soil mechanism.* Los Angeles: Prentice Hall.

Bellier, O. et al., 2001. High Slip Rate for a Low Seismicity along the Palu-Koro Active Fault in Central Sulawesi (Indonesia). *Terra Nova*, 13(6), pp. 463-470.

Boulanger, R. W. & Truman, S. P., 1996. Void redistribution in sand under post-earthquake loading. *Canadian Geotechnical Journal*, pp. Vol. 33: 829-834.

Bradley, K., Mallick, R. & Andikagumi, H., 2019. Earthquake-triggered 2018 Palu Valley Landslides Enabled by Wet Rice Cultivation. *Nat. Geosci.*, pp. 932-939.

Casagrande, A. & Rendon, F., 1978. *Gyratory shear apparatus design, testing procedures,* Vicksburg: U.S. Army Corps of Engineers, Waterways Experiment Stations .

Chiaro, G., Sato, T., Kiyota, T. & Koseki, J., 2011. *Effect of intial static shear stress on the undrained cyclic behavior of saturated sand by torsional shear loading.* Santiago, Chile, s.n.

Committee on Earthquake Engineering, Comission on Engineering and Technical Systems, National Research Council, 1985. *Liquefaction of soils during earthquakes.* Washington D.C.: National Academy Press.

Fiegel, G. L. & and Kutter, B. L., 1994. Liquefaction-induced lateral spreading of mildly sloping ground. *Journal of Geotechnical Engineering,* 120(No. 12), pp. 2236-2243.

Fiegel, G. L. & Kutter, B. L., 1994. Liquefaction mechanism for layered souls. *Journal of Geotechnical Engineering,* April, 120(No. 4), pp. 737-755.

Hamada, M., Yasuda, S. & Wakamatsu, K., 1991. *Liquefaction induced permanent ground displacement in Niigata city.* St. Louis, s.n.

Hidayat, R. F. et al., 2020. Reconnaissance on Liquefaction-induced flow failure caused by the 2018 Mw 7.5 Sulawesi Earthquake, Palu, Indonesia. *Journal of Engineering and Technological Sciences,* 52(No. 1).

Hight, D., Gens, A. & Symes, M., 1985. Discussion: The development of a new hollow cylinder apparatus for investigating the effects of principal stress rotation in soils under undrained anisotropy and principal stress rotation in saturated sand. *Geotechnique, 35(1),* pp. 78-85.

Hyodo, M., Murata, H., Yasufuku, N. & Fujii, T., 1991. Undrained cyclic shear strength and residual shear strain of saturated sand by cyclic triaxial tests. *Soils and Foundations 31 (3),* pp. 60-76.

Idriss, I. M. & Boulanger, R. W., 2007. *SPT- and CPT-based relationships for the residual shear strength of liquefied soils.* AA Dordrecht, The Netherlands, Springer, pp. 1-21.

Indonesian Society for Geotechnical Engineering, The National Research Centre for Earthquake, Ministry of Public Works, 2018. *Damages Associated with Geotechnical Problems in 2018 Palu Earthquake Indonesia,* Jakarta: The National Research Centre for Earthquake.

Ishihara, K., 1993. Liquefaction and flow failure during earthquakes. 43(No. 3).

Ishihara, K., 1993. Liquefaction and flow failure during earthquakes. *Geotechnique No.3,* 43(No. 3), pp. 351-415.

Ishihara, K. & Koga, Y., 1981. Case study of Liquefaction in the 1964 Niigata Earthquake. *Soils and Foundations,* 21(No. 3), pp. 35-52.

Ishihara, K. & Li, S. I., 1972. Liquefaction of saturated sand in Triaxial Torsion Shear Test. *Soils and Foundations, 12(2),* pp. 19-39.

Ishihara, K., Tatsuoka, F. & Yasua, S., 1975. Undrained deformation and liquefaction of sand under cyclic stresses. *Soils and Foundations,* 15(No. 1), pp. 29-44.

Ishihara, K., Tatsuoka, F. & Yasua, S., 1975. Undrained deformation and liquefaction of sand under cyclic stresses. *Soils and Foundations,* 15(No. 1), pp. 29-44.

Ishihara, K., Verdugo, R. & Acacio, A. A., 1991. Characterization of cyclic behavior of sand and post-seismic stability analysis. *Proceeding 9th Asian Regional Conference of Soil Mechanics and Foundation Engineering,* Desember, Volume 2, pp. 45-67.

Japanese Geotechnical Society, 1998. *Standard of Japanese Geotechnical Society for laboratory shear test.* Tokyo: Japanese Geotechnical Society.

Japanese Geotechnical Society, 2015. *Japanese Geotechnical Standards, Laboratory Testing Standards of Geomaterials Vol. 1.* Tokyo: Japanese Geotechnical Society.

Japanese Society of Civil Engineers, 1966. *The report of damage investigation in the 1964 Niigata earthquake*, Tokyo: Japanese Society of Civil Engineers.

Jefferies, M. G. & Been, K., 2006. *Soil liquefaction-A critical state approach.* London: Taylor and Francis.

Kadarusman, A., Leeuwen, T. v. & Sopaheluwakan, J., 2011. *Eclogite, Peridotite, Granulite, and Associated High-Grade Rocks from The Palu Region, Central Sulawesi, Indonesia: An Example of Mantle and Crust Interaction in A Young Orogenic Belt.* Makassar, s.n.

Kawakami, M. & Asada, A., 1966. Damage to the ground and earth structures by the Niigata earthquake of June 16, 1964. *Soils and Foundations,* 6(1), pp. 14-30.

Kiyota, T. et al., 2020. Overview of long-distance flow-slide caused by the 2018 Sulawesi earthquake, Indonesia. *Soils and Foundations (submitted).*

Kiyota, T., Koseki, J. & Sato, T., 2013. Relationship between limiting shear strain and reduction of shear moduli due to liquefaction in large strain torsional shear tests. *Soil Dynamics and Earthquake Engineering,* Volume 49, pp. 122-134.

Kiyota, T., Sato, T., Koseki, J. & Abadimarand, M., 2008. Behavior of liqueified sands under extremely large strain levels in cyclic torsional shear tests. *Soils and Foundations*, 48(5), pp. 727-739.

Kokusho, T., 1999. Water film in liquefied sand and its effect on lateral spread. *Journal of Geotechnical and Geoenvironmental Engineering*, 125(10), pp. 817-826.

Kokusho, T., 2000. Mechanism for water film generation and lateral flow in liquefied sand layer. *Soils and Foundatons* , 40(No.5), pp. 99-111.

Kokusho, T., 2003. Current state of research on flow failure considering void redistribution in liquified deposits. *Soil Dynamics and Earthquake Engineering,* pp. Vol. 23 (585-603).

Kramer, S., 1996. *Geotechnical Earthquake Engineering.* Upper Saddle River: Prentice Hall.

Kulasingam, R., J, M. E., Boulanger, R. W. & Kutter, B. L., 2004. Strength loss and localization at silt interlayers in slopes of liqeufied sand. *Journal of Geotechnical and Geoenvironmental Engineering,* 130(11), pp. 1192-1202.

Lade, P., 1992. Static instability and liquefaction of loose fine sandy slopes. *Journal of Geotechnical Engineering,* pp. 118(1):51-71.

Lambe, T. W. & Whitman, R. V., 1969. *Soil Mechanics.* New York: John Willey & Sons.

Malvick, E. J., Kutter, B. L., Boulanger, R. W. & Feigenbaum, H. P., 2004. Post-shaking failure of sand slope in centrifuge test. *11th International Conference on Soil Dynamics and Earthquake Engineering, and 3rd International Conference on Earthquake Geotechnical Engineering* , 2(Doolin D et al. (eds)), pp. 447-455.

Malvick, E. J., Kutter, B. L., Boulanger, R. W. & Kulasingam, R., 2006. Shear localization due to liquefaction-induced void redistribution in a layered infinite slope. *Journal of Geotechnical and Geoenvironmental Engineering,* 132(10), pp. 1293-1303.

Munoz, H., Taheri, A. & Chanda, E., 2016(a). Fracture energy-based brittleness index development and brittleness quantification by pre-peak strength parameters in rock unaxial compression. *Rock Mechanics and Rock Engineering,* 49(12), pp. 4587-4606.

Munoz, H., Taheri, A. & Chanda, E., 2016(b). Pre-peak and post-peak rock strain characteristics during uniaxial compressiion by 3D digital image correlation. *Rock Mechanics and Rock Engineering,* 49(7), pp. 2541-2554.

Munoz, H., Taheri, A. & Chanda, E., 2017(a). Local damage and proggresive localization in porous stone. *Rock Mechanics and Rock Engineering,* 50(1), pp. 3253-3259.

Munoz, H., Taheri, A. & Chanda, E., 2017(b). Specimen aspect ratio and proggresive field strain development of sandstone under uniaxial compression by three-dimensional digital image correlation. *Journal of Rock Mechanics and Geotechnical Engineering,* 9(1), pp. 599-610.

National Research Council , 1985. *Liquefaction of soils during earthquakes,* Washington D.C.: National Academy Press.

National Research Council of United States, 1985. *Liquefaction of soils during earthquakes* , Washington, D.C: National Academy Press.

Okamura, M. et al., 2020. Large-scale flowslide in Sibalaya caused by the 2018 Sulawesi Earthquake. *Soils and Foundations (submitted).*

Poulos, S. J., Castro, G. & France, J. W., 1985. Liquefaction Evaluation Procedure. *Journal of Geotechnical Engineering Vol. 111, Issue 6*, pp. 772-792.

Rauch, A. F., 1997. *EPOLLS: An Empirical Method for Prediciting Surface Displacements Due to Liquefaction-Induced Lateral Spreading in Earthquakes.* Doctoral Dissertation ed. Virginia: Virginia Polytechnic Institute and State University.

Robertson, P. K. & Wride, C. E., 1998. Evaluating cyclic liquefactionpotential using the CPT. *Canadian Geotechnical Journal,* pp. 35 (3) 442-459.

Saada, A. S., 1988. *State-of-the-art paper: Hollow cylindrical torsional devices: their advantages and limitations.* s.l.:ASTM International.

Sasaki, Y., Tokida, K., Matsumoto, H. & Saya, S., 1991. Shake table tests on lateral ground flow induced by soil liquefaction. *Proceeding 3rd Japan-U.S. Workshop on Earthquake Resistant Design of Lifeline Facilities and Countermeasures for Soil Liquefaction,* Tech. Rep. NCEER-91-0001(O'Rourke and M. Hamada (eds)), pp. 371-385.

Sasaki, Y. et al., 1992. Mechanism of permanent displacement of ground casued by seismic liquefaction. *Soils and Foundations*, 32(No. 3), pp. 79-96.

Seed, H. B., 1987. Design problems in soil liquefaction. *Journal of Geotechnical Engineering, 113(8),* pp. 827-845.

Sento, N. et al., 2004. Possibility of postliquefaction flow failure due to seepage. *Journal of Geotechnical and Geoenvironmental Engineering*, pp. Vol. 130, No. 7, 707-716.

Skempton, A. W., 1954. The pore pressure coefficients A and B. *Geotechnique, 4(4)*, pp. 143-147.

Socquet, A., Hollingsworth, J. & Pathier, E., 2019. Evidence of Supershear during the 2018 Magnitude 7.5 Palu Earthquake from Space Geodesy. *Nat. Geosci.*, pp. 192-199.

Sutton, M. A., Orteu, J. J. & Schereier, H., 2009. *Image Correlation for Shape, Motion, and Deformation Measurements.* s.l.:Springer US.

Takase, M. & Sasada, M., 2013. The Application of Portable Dynamic Cone Penetration Test to the Geo-Disaster Reconnaissance (in Japanese). *Japan Geotechnical Consultants Association Technical Forum 2013 in Nagano*, pp. 64-65.

Tatsuoka, F., Muramatsu, M. & Sasaki, T., 1982. Cyclic undrained stress-strain behavior of dense sand by torsional simple shear test. *Soils and Foundations, 22 (2)*, pp. 55-69.

Tatsuoka, F., Ochi, K., Fujii, S. & Okamoto, M., 1986. Cyclic undrained triaxial and torsional shear strength of sands for different sample preparation methods. *Soils and Foundations, 26 (3)*, pp. 23-41.

Tatsuoka, F. et al., 1986. Failure and deformation of sand in torsional shear test. *Soils and Foundations, Vol. 26, No. 4,* pp. 79-97.

The National Agency of Disaster Management, Indonesia, 2018. *Geoportal.* [Online]
Available at: https://bnpb.go.id/geoportal.html
[Accessed 10 10 2018].

The National Agency of Disaster Management, 2018. *Gempa Bumi Sulteng.* [Online]
Available at: https://bnpb.go.id/geoportal.html
[Accessed 13 11 2018].

The United States Geological Survey, Earthquake Hazards Program, The United States Geological Survey, 2018. *https://earthquake.usgs.gov/earthquakes/eventpage/us1000h3p4/executive.* [Online]
Available at:
https://earthquake.usgs.gov/earthquakes/eventpage/us1000h3p4/executive

The United States Geological Survey, Earthquake Hazards Program, The United States Geological Survey, n.d. [Online].

The United States Geological Survey, 2019. *Earthquake Hazard Program.* [Online]
Available at:
https://earthquake.usgs.gov/earthquakes/eventpage/us1000h3p4/executive

Thein, P. S. et al., 2014. Estimation of Seismic Ground Motion and Shaking Parameters Based on Microtremor Measurements at Palu City, Central Sulawesi Province, Indonesia. *World Academy of Science, Engineering and Technology, International Journal of Geological and Environmental Engineering, Vol. 8, No.5,* pp. 308-319.

Timoshenko, S. & Goodier, J., 1970. *Theory of elasticity.* New York: McGraw Hill.

Tokida, K., Matsumoto, H., Azuma, T. & Towhata, I., 1993. Simplified procedure to estimate lateral ground flow by soil liquefaction. *Soil Dynamics and Earthquake Engineering VI,* Issue A. S. Cakmak and C. A. Brebbia (eds.), pp. 381-396.

Tokimatsu, K., Taya, Y. & Zhang, J. M., 2001. *Effects of pore water redistribution on post-liquefaction deformation of sands.* Rotterdam , Balkema, pp. 289-292.

Towhata, I. et al., 1991. Prediction of permanent lateral displacement of liquefied ground by means of variational principle. *Proceeding 3rd Japan-U.S. Workshop on Earthquake Resistant Design of Lifeline Facilities and Countermeasures for Soil Liquefaction,* Tech. Rep. NCEER-91-0001(O'Rourke and M. Hamada (eds)), pp. 237-251.

Towhata, I., Yamada, K., Kubo, H. & Kikuta, M., 1989. Analytical solution of permanent displacement of ground caused by liquefaction. *Proceeding 2nd U.S.-Japan Workshop on Liquefaction, Large Ground Deformation, and Their Effects on Lifelines ,* Tech. Rep. NCEER-89-0032(O'Rourke and M. Hamada (eds.)), pp. 131-144.

Uchida, K. & and Vaid, Y. P., 1994. *Sand behavior under strain path control.* Rotterdam, Proceeding 8th International Conference on Soil Mechanics and Geotehnical Engineering Balkema.

Vaid, Y. & Chern, J., 1983. Effect of static shear on resistance to soil liquefaction. *Soil Foundations,* pp. 23(1):47-60.

Vaid, Y. & Eliadorani, A., 1998. Instability and liquefaction of granular soils under undrained and partially drained states. *Canadian Geotechnical Journal ,* Volume 35, pp. 1053-1062.

Vaid, Y. P. a. C. J., 1983. Effects of static shear on resistance to liquefaction. *Soils and Foundations, 23 (1),* pp. 47-60.

Vaid, Y. P. a. F. W., 1979 . Static shear and liquefaction potential. *Journal of Geotechnical Engineering Division ASCE,* pp. 1233-1246.

Verdugo, R. & Ishihara, K., 1996. The steady state of sandy soils. *Soils and Foundations Vol. 36, No. 2,* pp. 81-91.

Watkinson, I. M., 2011. Ductile Flow in the Metamorphic Rocks of Central Sulawesi. *The SE Asian Gateway: History and Tectonics of the Australia-Asia Collision,* Volume 355, pp. 157-176.

Whitman, R. V., 1985. *On liquefaction.* San Fransisco, A.A. Balkema, pp. 1923-1926.

Yasuda, S. et al., 1992. The mechanism and simplified procedure for the analysis of permanent ground displacement dur to liquefaction. *Soils and Foundations*, 32(1), pp. 149-160.

Yasuda, S., Nagase, H., Kiku, H. & Uchida, Y., 1991. A simplified procedure for the analysis of the permanent ground displacement. *Proceeding 3rd Japan-U.S. Workshop on Earthquake Resistant Design of Lifeline Facilities and Countermeasures for Soil Liquefaction,* Tech. Rep. NCEER-91-0001(O'Rourke and M. Hamada (eds)), pp. 225-236.

Yasuda, S., Nagase, H., Kiku, H. & Uchida, Y., 1991. *Countermeasures against the permanent ground displacement due to liquefaction.* Karlsruhe, Germany, Soil Dynamics and Earthquake Engineering V, Proceeding Fifth International Conference.

Yasuda, S. et al., 1992. Shaking table tests on countermeasures againts large ground displacement due to liquefaction. *Proceeding 4th Japan-U.S. Workshop on Earthquake Resistant Design of Lifeline Facilities and Countermeasures for Soil Liquefaction,* Tech. Rep. NCEER-92-0019(M. Hamada and O'Rourke (eds.)), pp. 367-380.

Yasuda, S., Nagase, H., Kiku, H. & Uchida, Y., 1992. The mechanism and a simplified procedure for the analysis of permanent ground displacement due to liquefaction. *Soils and Foundations* , 32(No. 1), pp. 149-160.

Yoshimine, M. & Ishihara, K., 1998. Flow potential of sand during liquefaction. *Soils and Foundations Vol. 38, No. 3,* pp. 189-198.

Yoshimine, M., Nishizaki, H., Amano, K. & Hosono, Y., 2006. Flow deformation of liquefied soil under constant shear load and its application to analysis of flow slide of infinite slope. *Soil Dynamics and Earthquake Engineering*, pp. Vol. 26, Issues 2-4, 253-264.

Youd, T. L., 1973. *Liquefaction, Flow, and Associated Ground Failure,* Virginia: U.S. Geological Survey.

Zeffitni, 2013. Groundwater Potency in Palu Groundwater Basin Based on Hidromorfology and Hidrogeology Approachment (in Bahasa Indonesia). *Jurnal Geografi*, 11(22), pp. 97-106.

Chapter 2 MATERIAL, APPARATUS, AND TESTING PROCEDURES

2.1. Introduction

This chapter introduces the testing materials, apparatus, and test procedures of this study. In this study, two types of apparatuses, strain-controlled-triaxial apparatus and hollow cylindrical torsional shear apparatus, are employed to evaluate the flow failure behavior of soil specimens under the static liquefaction test method. By using the strain-controlled-triaxial apparatus, the flow behavior of sand, emphasized on the strain rate, is observed until the axial strain reaches 20%. On the other side, as this hollow cylindrical torsional shear apparatus can achieve 100% of shear strain, this apparatus gives a description of the flow behavior of sand specimen under the large deformation during static liquefaction test. Clean sand, sand with fines content (FC=10%-20%), and natural sand were tested to understand their flow behavior in this study.

2.2. Testing Material

2.2.1. Toyoura Sand

This study uses Toyoura sand as the clean sand material, which has been used widely as standard sand for laboratory experiments considering its uniformity and the negligible amount of fines content. The grain size distribution of Toyoura sand is shown in Figure 2-1 with a mean particle size of 0.22 mm, a uniformity coefficient of 1.353, a curvature coefficient of 1.128, and a specific gravity of 2.648. Its maximum and minimum void ratio are 0.948 and 0.619, respectively.

2.2.2. Sand with fine content

This study also investigates the flow failure behavior of sand with fine content, which corresponds to the mixture of clean sand (Toyoura sand) and fine materials with a certain proportion in weight percentages. This test uses silty soil with the commercial name “DL clay” as the non-plastic fine material and Kaolin as the plastic fine as the mixture of sand with fine content. The samples used in this study is mentioned in Table 2-1. For the sample having IP=11, the Liquid Limit and Plastic Limit tests have been conducted by following the JGS 0141 (Japanese Geotechnical Society, 2015). The graph showing the determination of Liquid Limit is shown in Figure 2-2.

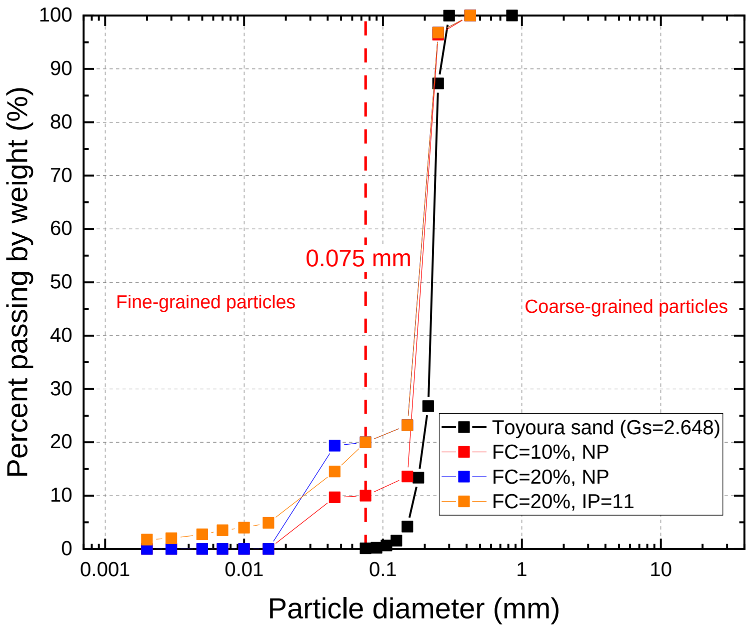

Figure 2-1 Particle size distribution of Toyoura sand and sand with fines content

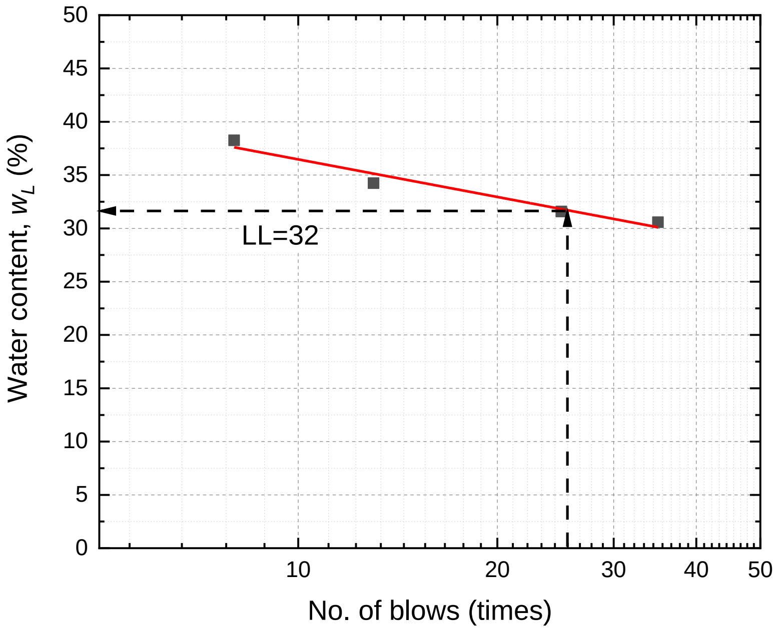

Figure 2-2 Liquid Limit curve for mixed sand FC=20%, IP=11

Table 2-1 The properties of sand with fines

Material	Toyoura sand (%)*	DL Clay (%)*	Kaolin (%)*	Liquid Limit (%)	Plastic Limit (%)	IP	Specific Gravity, G_s
FC=10%, NP	90	10	-	*Not tested*		NP	2.639
FC=20%, NP	80	20	-	*Not tested*		NP	2.630
FC=20%, IP=11	80	15	5	32	21	11	2.620

*Percent by weight

2.2.3. Field sample from Sibalaya Trench No. 3

To examine the possibility of flow failure occurs due to the water inflow concept at several sites in Palu city, the disturbed sample has been extracted from Trench No 3, Sibalaya during the site investigation.

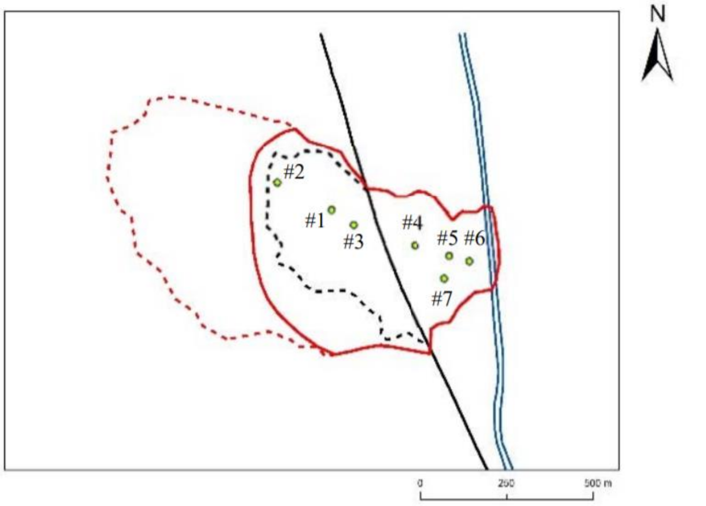

Figure 2-3 Location of the excavated trenches in Sibalaya area (Okamura, 2020)

The grain size distribution of the disturbed samples, which are the gravelly sand samples and the sand samples is shown in Figure 2-4. It is found that the sand samples has a fine content as much as 10% with the field density is 1.6-1.665 g/cm^3, while the gravelly layer has fine content less than 5% with the field density is 1.522-1.66 g/cm^3.

Table 2-2 The properties of field sample (Sibalaya Trench No. 3)

Field sample	Field dry density, γ_d (g/cm^3)	Specific gravity, G_s	Maximum void ratio, e_{max}	Minimum void ratio, e_{min}	Fines content, FC (%)
Sand (Depth - 3.50 m)	1.6	2.642	1.207	0.645	10 (Non-plastic)
Gravelly sand (Depth - 6.00 m)	1.522	2.639	0.948	0.519	5 (Non-plastic)

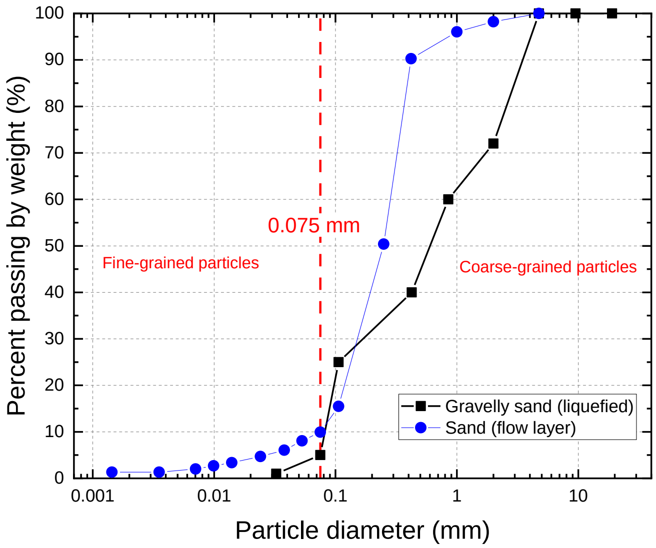

Figure 2-4 Particle size distribution of disturbed samples taken from Trench No. 3 Sibalaya area

2.3. Triaxial Apparatus

Triaxial is a widely performed in the geotechnical laboratory to determine shear strength, soil stiffness, or even cyclic resistance of the soil. In this study, two types of Triaxial Apparatus have been utilized, which are stress-controlled and strain-controlled.

The main difference of both apparatus are the loading system. In the strain-contolled type, the vertical loading system is employed to control the loading while in the stress-controlled system, the BF amplifier is used to impose loading using the pressure.

Triaxial apparatus mainly consists of a vertical loading system, a cell pressure transducer, a set of measurement devices, and a computer. The schematic diagram of the triaxial apparatus in this study is shown in Figure 2-5.

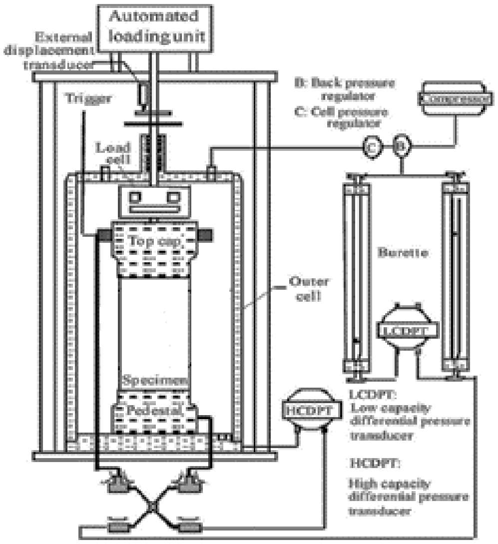

Figure 2-5 Schematic diagram of Triaxial Apparatus

2.3.1. Vertical loading system

In this study, for the stress-controlled apparatus, the BF amplifier is utilized to control the loading by using the difference of pressure. The loading system calibration of the stress-controlled apparatus is shown in Figure 2-6.

The axial loading system in Triaxial apparatus strain-controlled includes an AC servo motor, three sets of gear, electromagnetic clutches, and brakes. This system allows the users to define strain as the control variables. As this study mainly focuses on strain rate behavior during the flow failure phenomenon, the performance of the AC servo motor becomes essential.

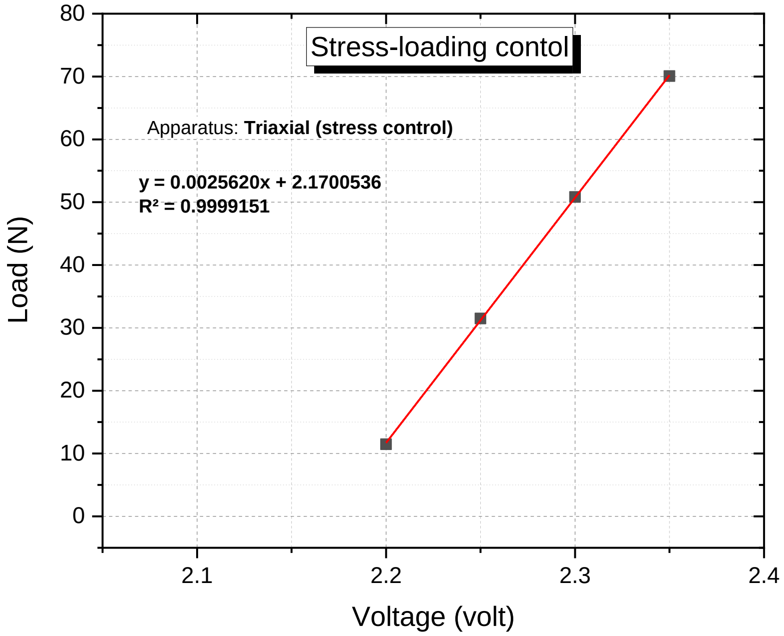

Figure 2-6 The calibration factor of loading control in stress-controlled Triaxial Apparatus (Oya, 2020)

2.3.2. Cell pressure transducer

A stable air pressure pump with a maximum capacity of 700 kPa supplies all the pressure in each experiment test in this study. To control the amount of pressure goes into the cell, two types of regulator; a positive pressure regulator and a negative pressure regulator for vacuum state are utilized.

The positive pressure in the cell can be directly read by the computer program, connected through an amplifier. However, for the vacuum state, the air pressure is connected through a negative pressure regulator. An additional vacuum pump is utilized to the source of negative pressure.

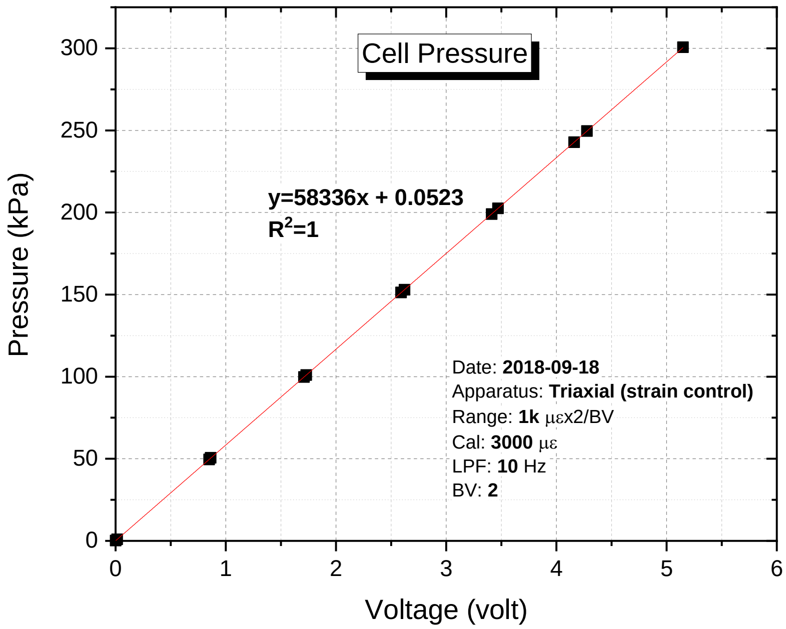

Figure 2-7 The calibration factor of Cell Pressure Transducer

2.3.3. Measurement devices

In order to obtain accurate measurements and results, several transducers are employed to measure the vital parameters in each experiment. These measurement devices are integrated into the software, named “Digital Show Basic”, on the PC through a 16-bit A/D (Analog-Data) and a 16-bit D/A (Data-Analog) board converter system, for giving and receiving a command. Each transducer measures a variable during the test, transferring the information in electric pressure in milivoltage unit. This voltage information will be emphasized by an amplifier, ranging from -10 volt to 10 volts. The emphasized voltage information is then transferred to the A/D board, changing the input data from analog measurement (voltage information) to the data information by a calibration factor. This data information will be read through the Digital Show Basic, and extract it to the output variables by equations.

For the purpose of giving a command, the desired command can be inputted through the Digital Show Basic. This software then will transfer the information back to the transducers through D/A board, converting the information from data to analog information in voltage unit. As a result of measurements, three types of files will be created; voltage file (.vlt), data file (.dat), and output file (.out) automatically.

2.3.3.1. Load cell

A load cell with a capacity of 5 kN is utilized in this apparatus, placed at the bottom of the loading shaft. This load cell read the number of axial forces applied to the specimen. The calibration data of this load cell is shown in Figure 2-8 for strain-controlled and Figure 2-9 for the stress-controlled type.

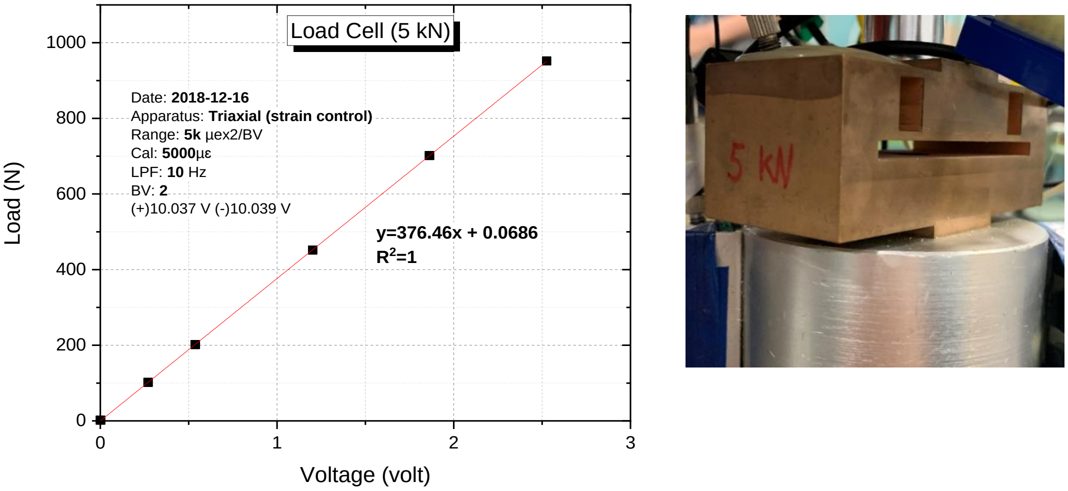

Figure 2-8 The calibration factor of the load cell (left) and the apparatus (right)

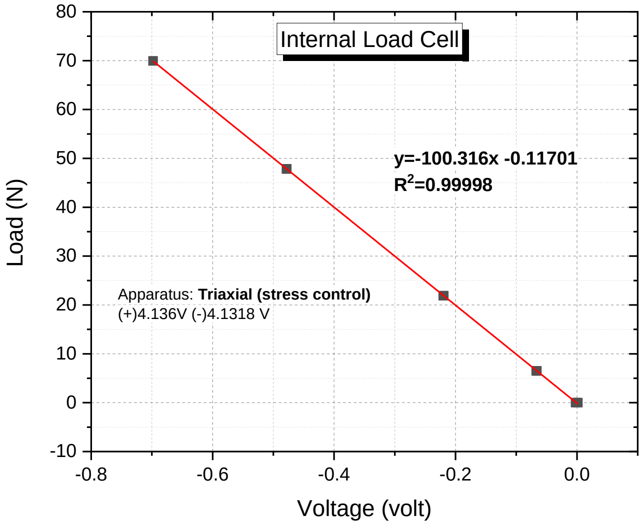

Figure 2-9 The calibration of the load cell in stress-controlled apparatus (Oya, 2020)

2.3.3.2. External linear vertical displacement transducer (LVDT)

External LVDT measures the vertical displacement of the top cap during the experiment. The capacity of LVDT used for both apparatuses in this study is 100 mm. The calibration data of this LVDT is shown in Figure 2-10.

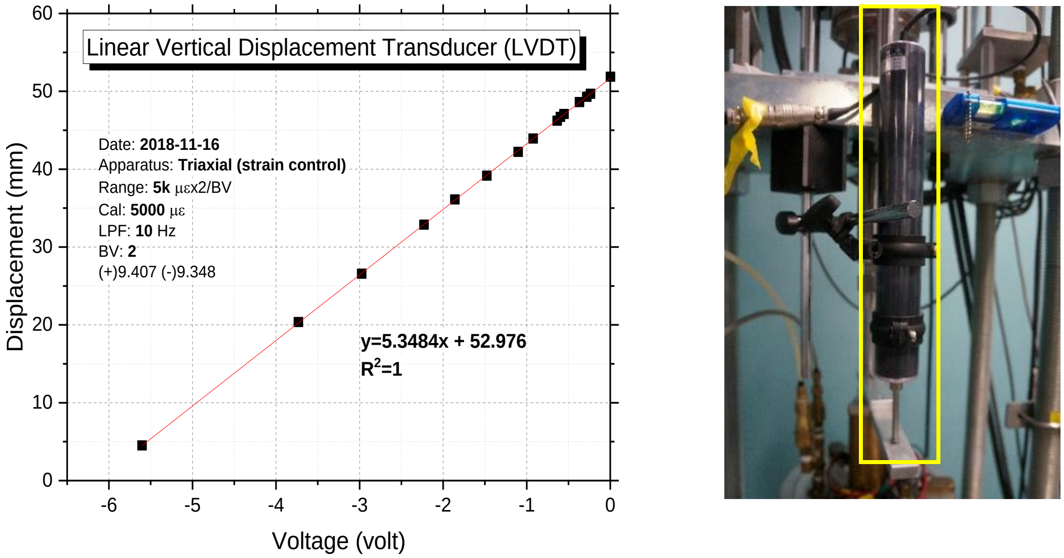

Figure 2-10 The calibration factor of LVDT (left) and the apparatus (right)

2.3.3.3. High capacity differential pressure transducer (HCDPT)

High capacity differential pressure transducer measures the difference of pore water pressure between the cell pressure and the specimen, representing the confining pressure. The calibration data of this HCDPT is shown in Figure 2-11 for strain-controlled type and Figure 2-12 for stress-controlled one.

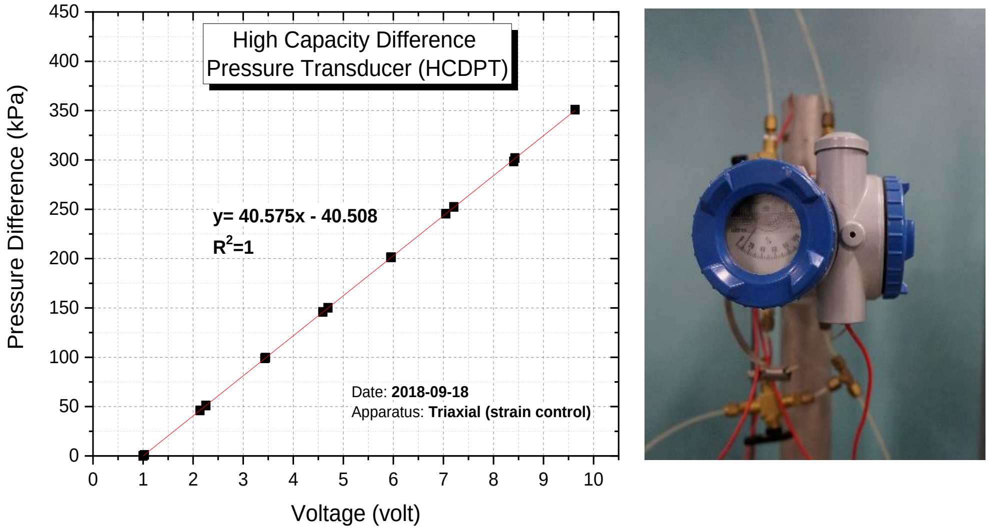

Figure 2-11 The calibration factor of HCDPT (left) and the apparatus (right)

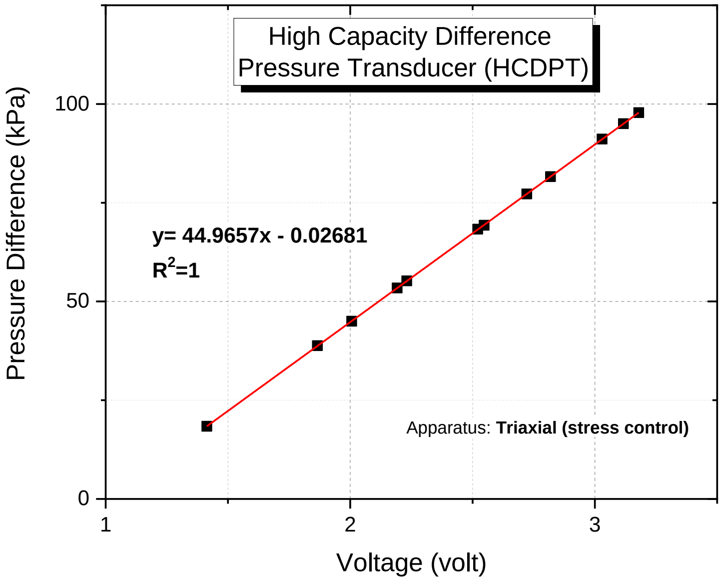

Figure 2-12 The calibration factor of HCDPT in stress-controlled apparatus (Oya, 2020)

2.3.3.4. Low capacity differential pressure transducer (LCDPT)

Low capacity differential pressure transducer measures the volume change of specimen during the test. In this apparatus, one tube LCDPT is utilized that connected to the specimen. This transducer set the initial position of water level in the biuret as the reference. During the test, the water can go in and out from the specimen, making the water level in the biuret fluctuated. The fluctuating behavior of the water in the biuret will be read as the volume change. The calibration data of this LCDPT is shown in Figure 2-13 for strain-controlled apparatus and Figure 2-14 for stress-controlled type.

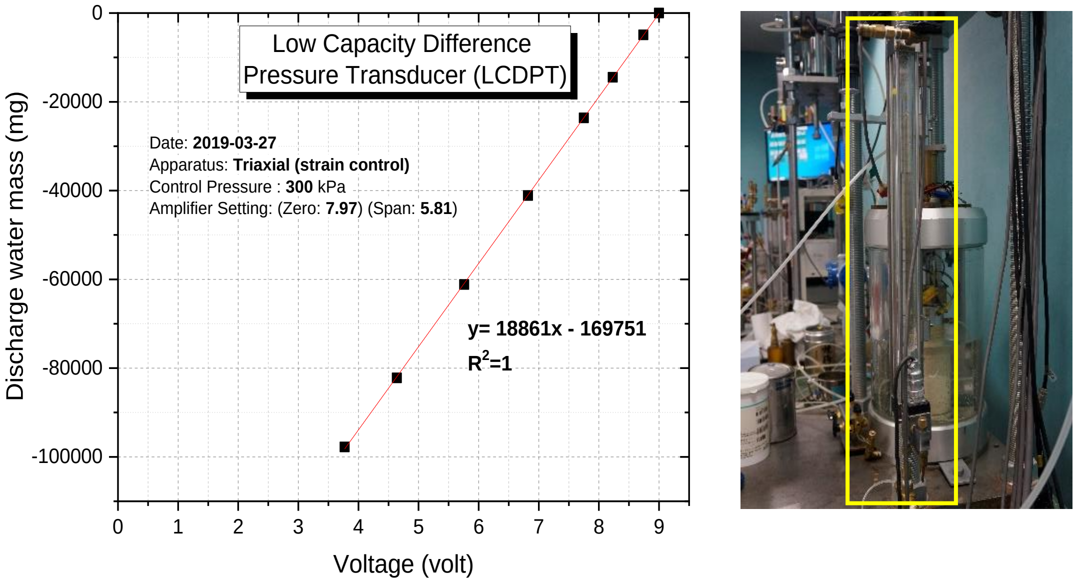

Figure 2-13 The calibration factor of LCDPT (left) and the apparatus (right)

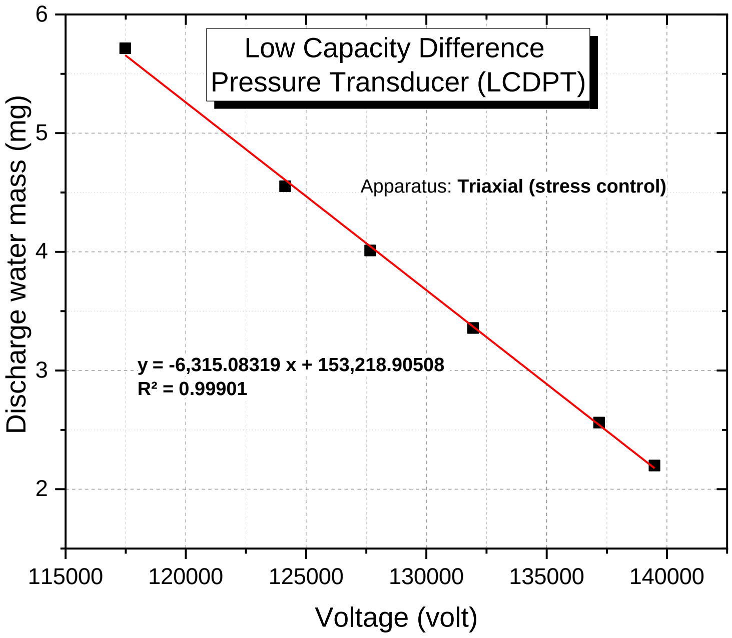

Figure 2-14 The calibration factor of LCDPT in stress-controlled apparatus (Oya, 2020)

2.3.4. Static Liquefaction Test Procedure in Triaxial Apparatus

2.3.4.1. Specimen preparation

There are several items that should be prepared before the specimen preparation, such as rubber membrane with a thickness of 0.3 mm, two pairs of rubber glands with a thickness of 0.3 mm each, one black O-ring, a pair of filter paper, a casting mold, green grease for vacuum, and transparent grease for water-repellent. In this triaxial, the specimen size is 75-mm-diameter and 150-mm-height. There are two kinds of specimen preparation for disturbed samples in this test; those are Air Pluviation (AP) method (Tatsuoka, et al., 1986) for Toyoura sand and dry tamping for sand with fines.

After setting up all the items and putting the filter paper on the bottom pedestal, the mold, consisting of two symmetrical bronze metals, is fixed and tighten together. The mold should be connected to the vacuum regulator, to suck the membrane with the pressure around -30 kPa.

The first preparation method is Air Pluviation (AP). A funnel with an appropriate opening is used to pluviate the naturally dry Toyoura sand. In the AP method, the falling height of sand from the opening part of the funnel to the top surface of the specimen is kept constant during the pluviating process. The target of relative density can be adjusted based on the falling height of the sand. Before approaching to the next steps, the calibration factor of all instruments should be inputted to the Digital Show Basic, and set to 0 value.

After finishing the pluaviation, the top surface is leveled and closed by a filter paper. The amount of all the sand in the mold should be calculated to determine the relative density of the specimen. After checking the relative density, the top cap can be adjusted on the surface of the specimen by controlling it with the counterbalance load to keep the axial stress from the top cap to the specimen nearly 0 N (less than 5 N). The mold can be released after this step, and the size of the specimen can be measured, including the diameter and the height. Three times size measurement in the three different places has been done to measure the specimen’s size accurately.

After completing all the preparation, the green grease should be smeared to the triaxial black O-rings, located at the top and bottom. The cell should be cleaned and assembled to the triaxial body. When the set up is ready, the cell should be locked, the counterbalance should be removed, and the air inside the cell should be released to make the cell pressure equal to 0 kPa.

2.3.4.2. Pre-consolidation

The next step is pre-consolidation. The purpose of this step is to keep the specimen under isotropic stress condition with the deviatoric stress is equal to 0 kPa (±1 kPa range) controlled by AC servo motor. The apparatus is connected and locked to the loading shaft from the vertical loading system. On the Digital Show Basic software, the pre-consolidation mode is set. The locking part connecting the loading system and the specimen should be released so the control of pre-consolidation is fully operated by the software. The triaxial cell can be filled with water until the lower part of top cap in the 0 kPa environment.

The second method in this test is dry tamping for sand with fine content. As this material contains the fine particle, the AP method will not be favorable because the sand particles and the fine particles might be segregated during the pluaviating process, or the funnel might get clogged. In order to make the specimen uniform in terms of the distribution of sand particles and fine particles, the dry pluviation method is employed.

In this test, the specimen is prepared in 5 layers, after mixing the materials in certain proportion. In order to obtain the target relative density and relatively uniform specimen, the weight of sand on each layer and the number of blows are controlled and kept the same each other. The next steps will be the same as the specimen preparation with Air Pluviation (AP).

2.3.4.3. Double vacuum method

The double vacuum procedure (Ampadu & Tatsuoka, 1993) was applied to this study. The purpose of this step is to remove air inside the sand specimen by vacuuming process so that the saturation will be optimum. Before starting the vacuum process, two bottles of de-aired water are connected to the negative regulator for saturation preparation. After setting up the system, by using the negative regulator, the pressure on the cell and inside the specimen are reduced to -68 kPa and -98 kPa, respectively, while keeping the confining pressure as much as 30 kPa during the increment. This vacuuming is kept for 12 hours in this test.

2.3.4.4. Saturation process

In this test, the saturation process is conducted under the vacuum state. One of the bottle tanks is elevated to a higher position than the specimen and one bottle tank is put below the specimen to allow the water to flow slowly under gravitation. The water should flow from the bottom pedestal to the upper pedestal to assure good saturation. The water will occupy the soil’s void and remove the air trapped. The saturation process will be stopped as the amount of water infiltrated to the specimen from the upper tank is equal to two times the size specimen. After making sure that no air bubbles coming from the specimen, both pressures will be increased back to the state of +30 kPa (cell pressure) and 0 kPa (inside the specimen) by keeping the 30 kPa effective stress during the increment.

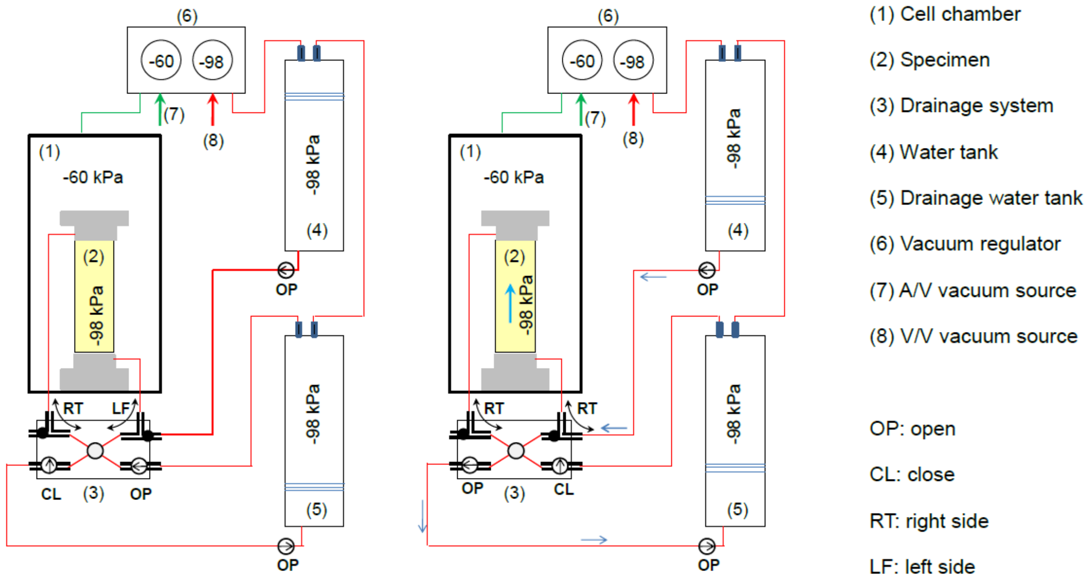

(a) (b)

Figure 2-15 Double vacuum method as used in this study: (a) before saturation to remove air into the specimen; and (b) while saturating the specimen by using de-aired distilled water (Chiaro, 2010)

2.3.4.5. Backpressure and B value measurement

After reaching +30 kPa and 0 kPa for cell pressure and specimen pressure, respectively, all the drainage valves should be closed, and both tanks should be disconnected from the system. The next step will be flushing the air trapped on HCDPT and LCDPT using de-aired water, before using it. After flushing, the HCDPT and LCDPT physical value should be set to zero (on the calibration factor), to start the measurement. All the valves should be switched to measurement mode.

For all the tests, the backpressure value is +200 kPa. The backpressure inside the specimen should be increased from 0 kPa to +200 kPa by maintaining the effective pressure as much as 30 kPa, thus the final cell pressure will be +230 kPa.

Under the state of cell pressure is +230 kPa and the backpressure, which representing the excess pore water pressure, is +200 kPa, the measurement of saturation degree will be conducted. This saturation degree will be evaluated by using the Skempton B value. To start this stage, the valve connecting the LCDPT should be closed to make the condition become an undrained condition. Other valves are kept open. The cell pressure is increased from +230 kPa to +250 kPa while recording the change of pore water pressure increment. All the process of measuring B value is conducted under the isotropic stress condition.

In general, laboratory tests are performed on water-saturated samples because unsaturated sand is significantly less liquefiable than saturated sand (Fig. 3.14). The extent of water saturation of tested specimens can be evaluated by using Skempton's *B* value because B value is a more sensitive index than the degree of saturation when a specimen is near complete saturation. Skempton (1954) described the increment of pore water pressure in soil undergoing undrained stress increments by:

$$\Delta u = B\{\Delta\sigma_3 + A(\Delta\sigma_1 - \Delta\sigma_3)\} \tag{2.1}$$

where:

Δu = increment of pore water pressure;

$\Delta\sigma_1$= increment of major total principal stress;

$\Delta\sigma_3$ = increment of minor total principal stress.

In particular, in Eq. (3.1), the first term ($\Delta\sigma_3$) stands for the contribution as a result of the isotropic stress increment, while the latter ($\Delta\sigma_1 - \Delta\sigma_3$) corresponds to the component produced by shear-induced dilatancy. Under the undrained isotropic loading, equal stress increments ($\Delta\sigma_1 = \Delta\sigma_3$) are applied to the specimen, therefore Skempton's *A* value becomes zero (*A=0*). Hence, the extent of saturation can be evaluated by comparing the measured pore water pressure increment with the theoretical value of fully saturated sand (i.e., for ideally and fully saturated specimen *B =1.0* and Δu = $\Delta\sigma_3$). The calculation of B value is following equation (2.2).

$$B = \frac{\Delta u}{\Delta\sigma_3} \tag{2.2}$$

Where,

Δu is the increment of pore water pressure.

$\Delta\sigma_3$ is the increment of minor total principal stress (isotropic stress consolidation).

The specimen is categorized as fully saturated if the B value is larger than 0.96. 0.95 becomes the low boundary of a fully saturated specimen considering the Japanese Geotechnical Society Standards (Japanese Geotechnical Society, 2015).

2.3.4.6. Consolidation

Since the diameter and height specimens at the preparation step in which the effective stress is 30 kPa under isotropic effective stress, it is assumed that no volume change occurred until the stress reaches +230 kPa and +200 kPa as the condition is kept in isotropic effective stress 30 kPa.

The consolidation stage is conducted under drained conditions that allow the volume change of specimen occurred. The cell pressure is increased from the current effective pressure 30 kPa to a certain effective pressure. In this research, most of the test is conducted at effective stress equal to 100 kPa. All the data during the consolidation stage is saved to the computer.

2.3.4.7. Test Procedure in Triaxial Apparatus

The test condition of this research is to keep static shear stress and total pressure constant while reducing the mean effective stress in the drained condition. The lateral confining stress, $\sigma_3 = \sigma_h$ (cell pressure) and the deviatoric stress, $q = \sigma_1 - \sigma_3$ are kept constant during axial compression process by adjusting pore water pressure manually (increasing back pressure). The procedures is explained as follow:

(1) Drained Consolidation Test

The specimen was consolidated from effective stress (σ') 30 kPa to 100 kPa, with the interval of 20 kPa/5 minute. In between the consolidation increment, at the σ'=50 kPa and σ'=70 kPa creep was conducted for 3 minutes, respectively before continuing to increase the effective pressure. The consolidation step was stopped at σ'=100 kPa.

(2) Drained Monotonic Loading Test

After consolidating the saturated specimen to σ'=100 kPa, monotonic drained was conducted by increasing the devatoric stress (q) to induce initial static shear stress with the rate of 0.2%/min, while keeping the back pressure at 200 kPa. This static shear stress is representing the inclination of the ground slope.

(3) Constant Deviatoric Stress Test

After applying deviatoric stress (q), the effective mean stress was reduced while the lateral confining pressure (cell pressure) and the devatoric stress were adjusted to be constant. The rate of reducing the mean effective stress (p') in this study was 5 kPa/minute with 3 minutes creep in between the reduction to assure that the strains were stopped. This reduction was continuously conducted until the stress path reaches failure line.

During the process of reducing the mean effective stress, the deviatoric stress tended to be unstable thus the rate of the axial loading should be adjusted to keep the deviatoric stress constant. When the effective mean stress reaching the failure line, the positive dilatancy will occur rapidly and continuously. In this phase, all the stresses, including deviatoric stress and the mean effective stress are kept constant by adjusting the loading rate of the axial stress. The volume change of the specimen is recorded by the LCDPT. The test was terminated when the axial strain reaches 20%.

2.4. Modified Hollow Cylindrical Torsional Shear Apparatus

In this study, a high capacity of Hollow Cylindrical Torsional Shear Apparatus which developed at the Institute of Industrial Science, The University of Tokyo was employed. The schematic diagram of the torsional apparatus in this study is shown in Figure 2-22.

The measurement range of shear strain measurement has been modified to achieve more than 100% of single amplitude. The specimen size used in this study is 60 mm inner diameter, 100 mm outer diameter, and 200 mm height. In order to avoid the repetitive description, similar features with Triaxial Apparatus is omitted.

2.4.1. Vertical and Torsional Loading Systems

The vertical loading system in Torsional Apparatus is similar to the axial loading system in Triaxial Apparatus, which consists of AC servo-motor, a reduction gear system, electric magnetic clutches, brakes, and a ball screw with a pre-pressured nut. The motor is capable of working in reversed directions, upward and downward, controlled by separated gears. This independent controller enables the motor to work smoothly without any backlash by the electric clutches.

The torsional loading system also has the same system as the vertical loading. The torque command is transmitted to the load shaft by controlling two metal bands on clockwise and anti-clockwise directions, respectively.

2.4.2. Cell Pressure Transducer

The system of cell pressure in Torsional Apparatus is the same as that of Triaxial Apparatus.

2.4.3. Measurement Devices

The employed system has 24 channels to measure stresses, strains and volume changes. Seven channels were used in this study: two channels for the two-component load cell (axial and torque loads), one channel for the External Displacement Transducer (ETD), two channels for inner and external potentiometers, and one channel each for High Capacity Differential Pressure Transducer (HCDPT) and Low Capacity Differential Pressure Transducer (LCDPT). The remaining channels were used in previous studies for proximity transducers (Gap Sensors) as well as Local Deformation Transducers (LDTs).

2.4.3.1. Load cell

The load cell used in this study is a dual-type load cell which capable of measuring the deviatoric load and the torque without coupling effect between each other. The capacities of the load cell are 8 kN for the axial load and 0.15 kN-m for the torque.

(a) Load cell instrument in Torsional Shear Apparatus

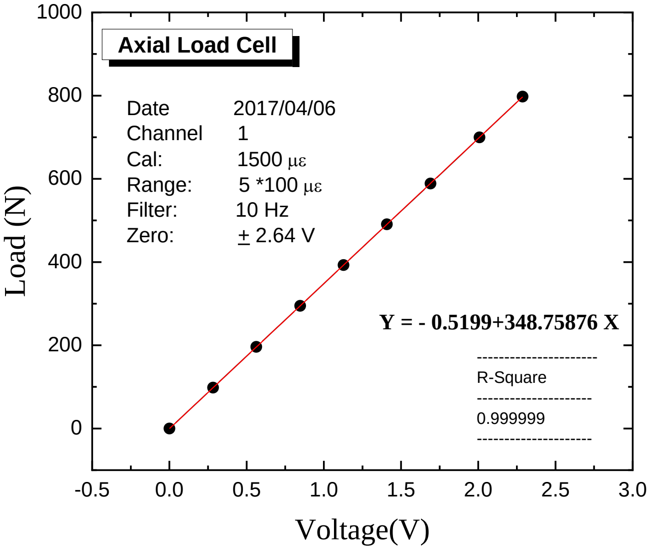

(b) Calibration factor of Axial load

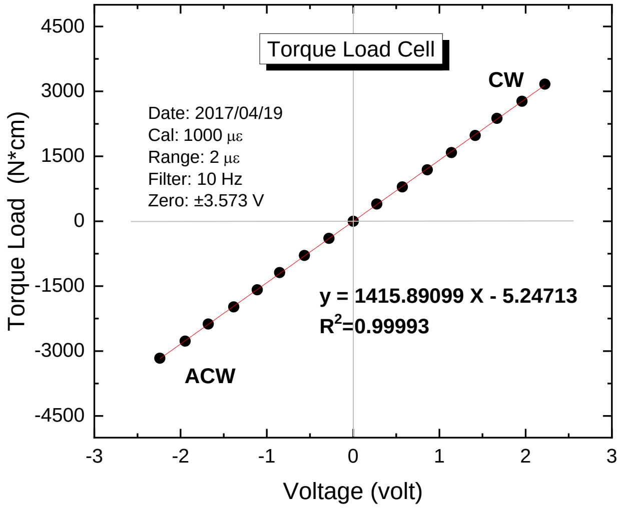

(c) Calibration factor of Torque

Figure 2-16 The load cell and its calibration factors (Umar, 2019)

2.4.3.2. Inner potentiometer

An inner potentiometer with a pulley having a diameter of 50 mm is attached to the top cap for measuring its rotational angle. It can detect shear strain levels up to 6%.

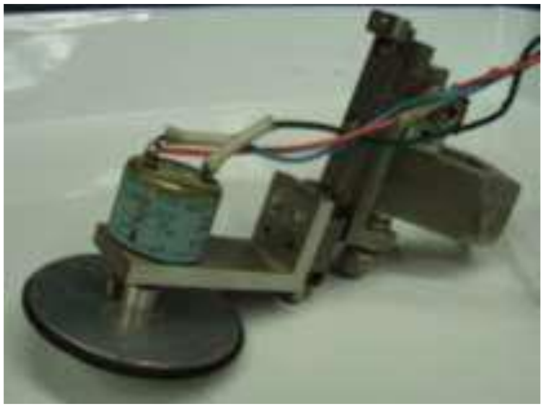

(a) Inner potentiometer instrument in Torsional Shear Apparatus

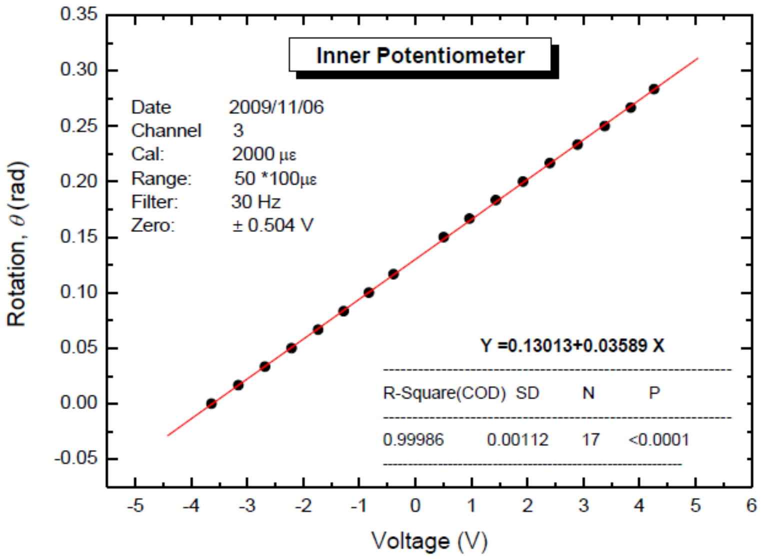

(b) Calibration factor of inner potentiometer

Figure 2-17 The inner potentiometer and its calibration factor (Chiaro, 2010)

2.4.3.3. External potentiometer

An external potentiometer is employed to measure extremely large shear strain levels exceeding 100% in terms of double amplitude.

(a) External potentiometer instrument in Torsional Shear Apparatus

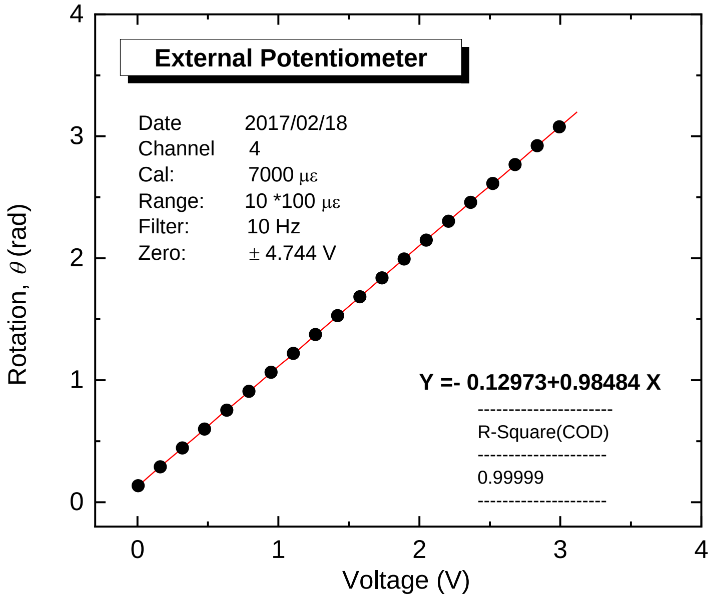

(b) Calibration factor of external potentiometer

Figure 2-18 The external potentiometer and its calibration factor (Umar, 2019)

2.4.3.4. High Capacity Differential Pressure Transducer (HCDPT)

The HCDPT measures the confining stress by the difference in pressures between the cell pressure and the pore water pressure. The positive terminal of the HCDPT is connected with the cell chamber to measure the cell pressure, while the negative one is connected to both the top and bottom drainage tubes of the specimen in order to measure the pore water pressure. The employed HCDPT has a maximum capacity over 600kPa.

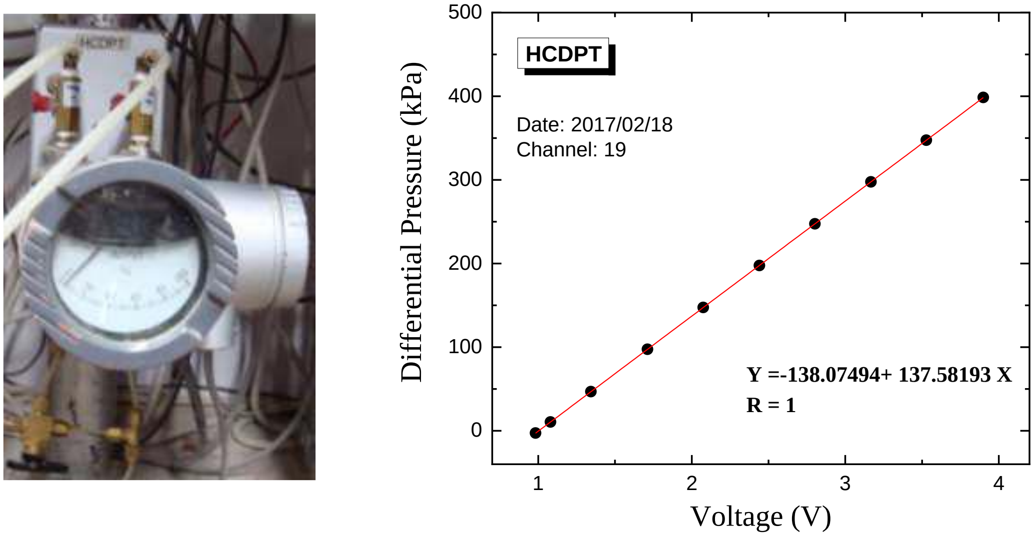

Figure 2-19 HCDPT and its calibration factor (Umar, 2019)

2.4.3.5. Low Capacity Differential Pressure Transducer (LCDPT)

The LCDPT measures the volume change by the difference in water heads between two burettes, one that collects drained water from the specimen and the other used as a reference.

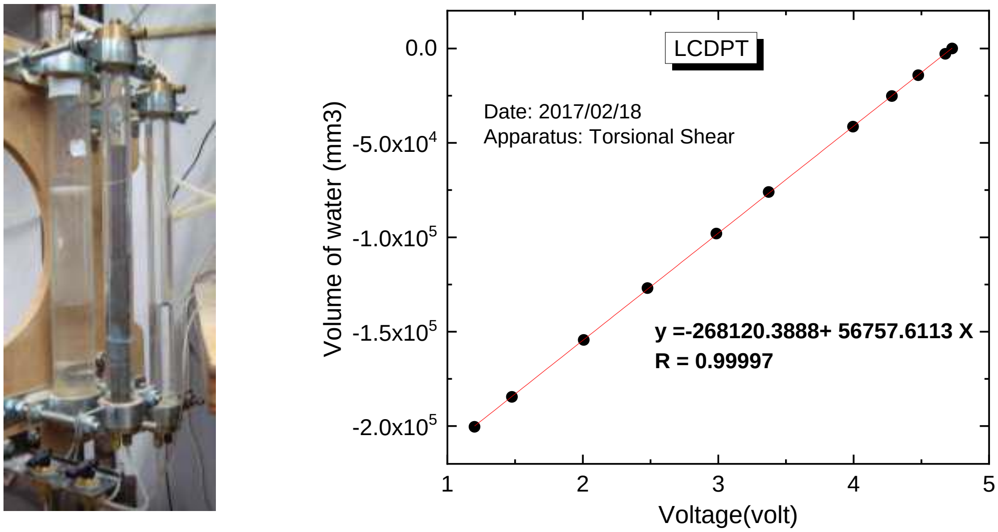

Figure 2-20 LCDPT and its calibration factor (Umar, 2019)

2.4.3.6. External Displacement Transducer

An EDT measures axial deformations outside the cell with a maximum range of 30 mm located along the loading shaft.

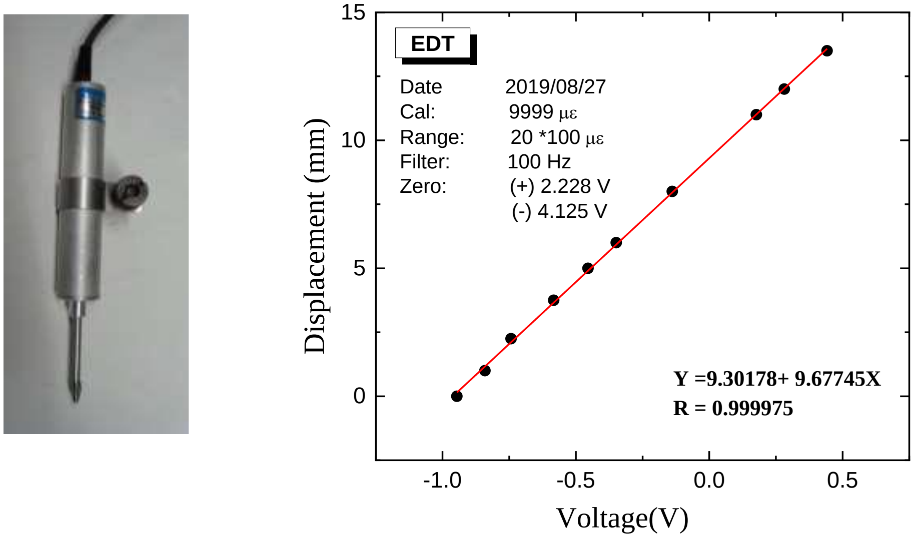

Figure 2-21 EDT and its calibration factor

2.4.4. Static Liquefaction Test Procedure in Hollow Cylindrical Torsional Shear Apparatus

2.4.4.1. Specimen Preparation in Torsional Shear Apparatus

Firstly, the outer latex membrane of 0.3 mm thick was placed over the pedestal which contains a porous stone with blades in order to apply the necessary friction during the torsional shear loading. Then the gap between the outer membrane and the pedestal was sealed by using a rubber band and a rubber O-ring.

The inner latex membrane of 0.3 mm thickness was placed over a metal ring, which has a rubber O-ring at the top. Following this the metal ring together with the membrane was placed into the pedestal hole while taking the inner membrane out from the hole of the pedestal. Extreme care was taken not to damage the membranes at all times. The pedestal was then screwed into the apparatus base firmly.

The inner mold was then set. The inner mold consists of four metal parts, which makes a perfect cylinder, a steel ring that is used to keep the four parts together and a steel rod screwed at the end to keep the inner mold fixed in a vertical position. All four parts of the inner mould were placed inside the inner membrane, which comes out from the pedestal, and the mould was firmly fixed using the ring and rod.

Subsequently, the outer mould was then fixed. This outer mould consists of two symmetrical metal parts with two clamps to tighten them together. A small amount of lubricant (grease) was applied along the edges of the outer mould before fixing it. After fixing the outer mould, the extra part of the outer membrane was put over the outer mould, and it was ensured that the gap between outer membrane and the outer mould was perfectly sealed. A partial vacuum of 30 kPa was then applied to the space between outer membrane and outer mould.

The specimens were prepared by employing the air pluviation method proposed by Hong Nam (2004), which is a slight modification of the one described in the relevant standard procedure (JGS, 1998). This method was introduced in order to reduce the degree of inherent anisotropy in the radial direction of the hollow cylindrical sand specimens (Hong Nam, 2004; and De Silva et al., 2006). Following this method, the specimens were prepared by pouring the sand into a mold while moving radially (R) the nozzle of the pluviator and at the same time circumferentially in alternative directions, i.e. first in clockwise (CW) and then anti-clockwise (ACW) directions, as shown in Fig. 3.11. To obtain specimens with initial relative density (D_r) (i.e., measured after achieving isotropic consolidation of 100 kPa) of about 45%, the falling height was selected to be 25.5 cm.

The falling height was kept constant during the pluviation process to get a specimen with highly uniform density. After pluviating the material to the full height of the specimen, the top surface of the specimen was leveled horizontally by using a metal strip, and the waste material was collected and weighed.

The next step was to place the top cap over the specimen. First, the top cap guider was fixed to one of the four steel poles that come from the base of the apparatus. Then a steel cable with three bolts connected to one end and with a deadweight attached to the other end was attached to the top cap using the three bolts. After that, the cable attached to the top cap was put over the pulleys of the guider and balanced using counterbalances. The horizontality of the top cap surface was maintained by adjusting the three bolts before it was placed on the top of the specimen. Finally, the top cap was placed very carefully over the specimen until it touched the top surface. Two clamps were then fixed symmetrically to two steel poles and the top cap was held in position by attaching it to the clamps using the bolts. After clamping, the extra part of the inner membrane was pulled gently over the top cap inner ring, and the extra part of the outer membrane was placed over the top cap outer ring. The specimen was perfectly sealed by using rubber bands, covering the inner and outer rings of the top cap.

The counterbalance was then applied again, and the clamps were removed. After a partial vacuum of 30 kPa was applied to the specimen, the outer mold was removed. The top cap was clamped again, and the inner mold was removed. The top cap was connected firmly to the load cell which was previously set on zero voltage reading. The other transducers such as inner and external potentiometers, HCDPT and LCDPT were set after before the specimen was covered with the cell.

The cell was filled with water and finally, the cell pressure was increased gradually up to 30 kPa, while reducing the partial vacuum applied to the specimen down to the atmospheric pressure, in order to maintain the same effective stress state acting on the specimen. When changing the vacuum into cell pressure, the dead weight above the specimen was counter-balanced every step of the way.

2.4.4.2. Saturation of the specimen

The saturation of specimen on Torsional Shear Apparatus, in principle, is the same as the saturation process on the Triaxial Apparatus.

2.4.4.3. Test Procedures in Torsional Shear Apparatus

The test condition on this Torsional Shear Apparatus is similar to the Triaxial Apparatus. The difference is explained as follow:

(1) Drained Consolidation Test

The specimen was consolidated from effective stress (σ') 30 kPa to 100 kPa, with the rate of 10 kPa/minute. In between the consolidation increment, creep was conducted for 1 minutes before continuing to increase the effective pressure. The consolidation step was stopped at σ'=100 kPa.

(2) Drained Monotonic Loading Test

After consolidating the saturated specimen to σ'=100 kPa, monotonic drained was conducted by increasing the shear stress (τ_{static}) to induce initial static shear stress with the strain rate of 0.2%/min while keeping the back pressure on 200 kPa. This static shear stress is representing the inclination of the ground slope.

(3) Static Liquefaction Test with constant deviatoric stress

After applying shear stress (τ), the effective mean stress was reduced while the lateral confining pressure (cell pressure) and the devatoric stress were adjusted to be constant. The rate of reducing the mean effective stress (p') was 5 kPa/minute with 3 minutes creep in between the reduction to assure that the strains were stopped. This reduction was continuously conducted until the stress path reaches failure line. The test was terminated when the shear strain, γ_{zq} reached 100%.

2.5.Experiment Lists

The experiment lists in this study are mentioned in Table 2-3 until Table 2-9.

Table 2-3 List of Undrained Monotonic Tests in Triaxial Apparatus

Code Test	Relative density, *Dr* (%)	Mean effective stress, p' (kPa)	B value	Material
TX1 (UML)	31.7	100	0.97	Toyoura sand

TX2 (UML)	31.2	100	0.97	Toyoura sand
TX3 (UML)	49.5	100	0.97	Toyoura sand
TX4 (UML)	45.6	100	0.97	Toyoura sand

Table 2-4 List of Static Liquefaction Tests in Triaxial Apparatus

Code Test	Relative density, *Dr* (%)	Static shear stress, *q* (kPa)	Mean effective stress, *p'* (kPa)	B value	Material
TX5 (SL-5)	35.5	5	100	0.96	Toyoura sand
TX6 (SL-5)	70.2	5	100	0.96	Toyoura sand
TX7 (SL-10)	37.9	10	100	0.97	Toyoura sand
TX8 (SL-10)	72.8	10	100	0.97	Toyoura sand
TX9 (SL-15)	26.9	15	100	0.97	Toyoura sand
TX10 (SL-15)	28. 4	15	100	0.98	Toyoura sand
TX11 (SL-15)	43	15	100	0.98	Toyoura sand
TX12 (SL-15)	50.1	15	100	0.97	Toyoura sand
TX13 (SL-15)	63	15	100	0.96	Toyoura sand
TX14 (SL-40)	24.6	40	100	0.96	Toyoura sand
TX15 (SL-80)	33.6	80	100	0.98	Toyoura sand
TX16 (SL-80)	38.8	80	100	0.97	Toyoura sand
TX17 (SL-80)	44	80	100	0.96	Toyoura sand

Table 2-5 List of Static Liquefaction Tests in Triaxial Apparatus for Sand with fines

Code Test	Global void ratio, *e*	Static shear stress, *q* (kPa)	Mean effective stress, *p'* (kPa)	B value	FC (PI)
TX18 (SL-15)	0.720	15	100	0.95	10 (NP)
TX19 (SL-15)	0.683	15	100	0.95	10 (NP)
TX20 (SL-15)	0.641	15	100	0.96	20 (NP)
TX21 (SL-15)	0.563	15	100	0.96	20 (NP)
TX22 (SL-15)	0.659	15	100	0.95	20 (IP=11)
TX23 (SL-15)	0.548	15	100	0.95	20 (IP=11)

Table 2-6 List of Drained Monotonic Tests in Triaxial Apparatus

Code Test	Global void ratio, *e*	Mean effective stress, *p'* (kPa)	B value	FC (PI)
TX24 (DML)	0.700	100	0.98	0 (NP)
TX25 (DML)	0.729	100	0.96	20 (NP)
TX26 (DML)	0.635	100	0.95	20 (11)

Table 2-7 List of Static Liquefaction Tests in Torsional Shear Apparatus

Code Test	Relative density, *Dr* (%)	Static Shear Stress, τ (kPa)	Mean effective stress, *p'* (kPa)	B value	Material
TS 1 (23-7.5)	23.4	7.5	100	0.96	Toyoura sand
TS 2 (44-7.5)	44	7.5	100	0.96	Toyoura sand
TS 3 (50-7.5)	50	7.5	100	0.96	Toyoura sand
TS 4 (58-7.5)	58	7.5	100	0.97	Toyoura sand
TS 5 (73-7.5)	73	7.5	100	0.96	Toyoura sand
TS 6 (84-7.5)	84	7.5	100	0.96	Toyoura sand

Table 2-8 List of Static Liquefaction Tests in Torsional Shear Apparatus with Half-Drained Mode

Test name	Dr(%)	p'_{ini} (kPa)	τ (kPa)	B value	Material
TS-7	68.4	30	2.25	0.96	Toyoura sand
TS-8	64.1	50	4	0.97	Toyoura sand
TS-9	70.7	100	7.5	0.97	Toyoura sand

Table 2-9 List of Tests using Natural Sands

Code Test	Test	Apparatus	B value	Sample
NS1	Static Liq.	Torsional	0.94	Flow layer

NS2	Undrained Cyclic Test + Monotonic Loading	Torsional	0.94	Flow layer
NS3	Undrained Cyclic Test (CSR=0.3)	Triaxial	0.99	Gravel layer
NS4	Undrained Cyclic Test (CSR=0.2)	Triaxial	0.99	Gravel layer
NS5	Undrained Cyclic Test (CSR=0.17)	Triaxial	0.99	Gravel layer
NS6	Undrained Cyclic Test (CSR=0.1)	Triaxial	0.98	Gravel layer

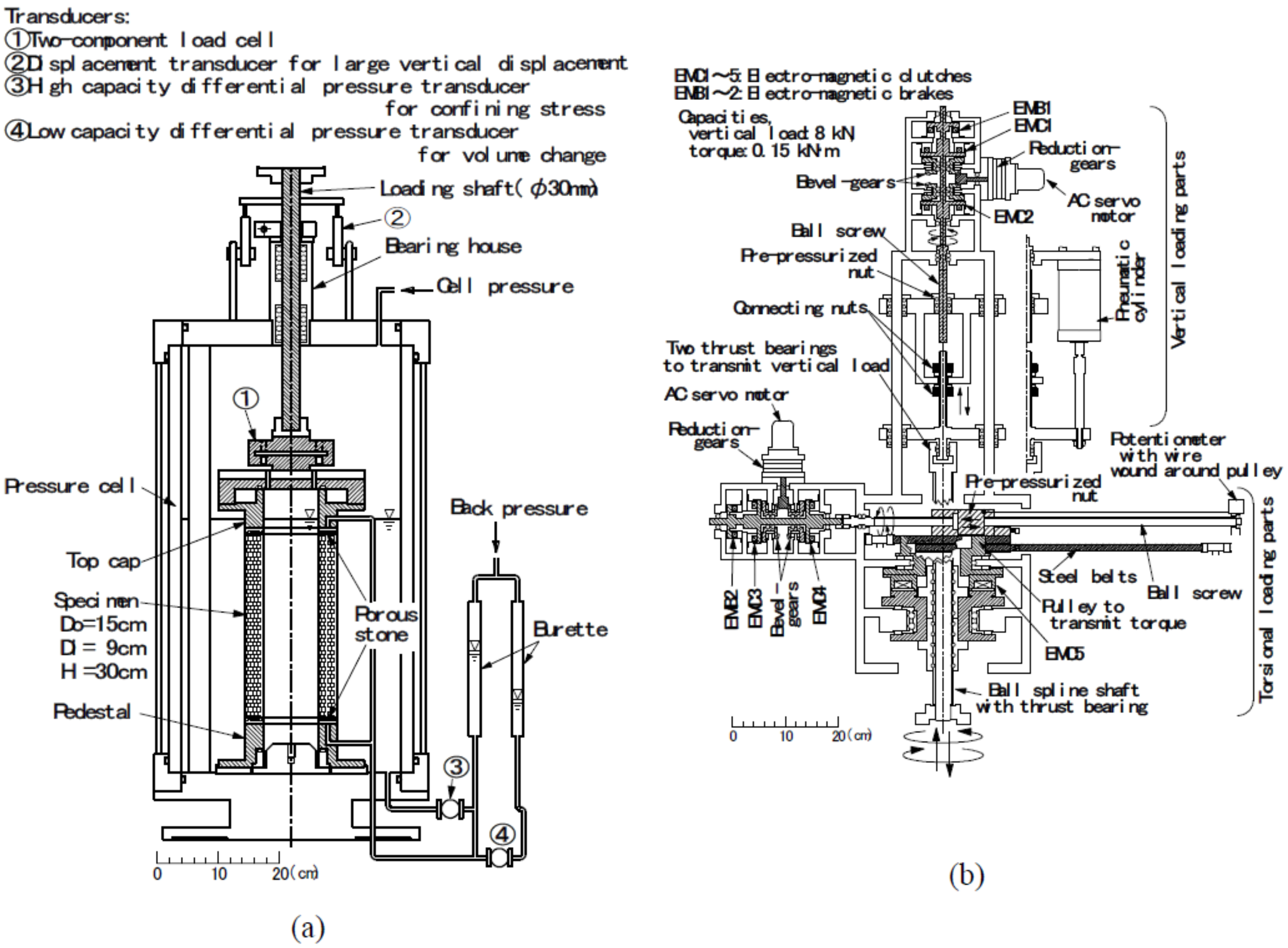

(a)

(b)

Figure 2-22 (a) Torsional shear test apparatus on hollow cylindrical specimen and (b) loading device (Chiaro, 2010)

2.6.References

Ampadu, S. & Tatsuoka, F., 1993. Effect of setting method on the behavior of clays in triaxial compression from saturation to undrained shear. *Soils and Foundations 33 (2)*, pp. 14-34.

Chiaro, G., 2010. *Deformation properties of sand with initial static shear in undrained cyclic torsional shear tests and their modeling.* Tokyo: Ph.D. Thesis, The University of Tokyo.

De Silva, L. I. N., 2008. *Deformation characteristics of sand subjected to cyclic drained and undrained torsional loadings and their modeling.* Tokyo: Ph.D. Thesis, The University of Tokyo.

Hong Nam, N. & Koseki, J., 2005. Quasi-elastic deformation properties of Toyoura sand in cyclic triaxial and torsional loadings and their modeling. *Soils and Foundations 45(5)*, pp. 19-38.

Japanese Geotechnical Society, 1998. *Standards of Japanese geotechnical society for laboratory shear tests.* Tokyo: Japanese Geotechnical Society .

Japanese Geotechnical Society, 2015. *Japanese Geotechnical Standards, Laboratory Testing Standards of Geomaterials Vol. 1.* Tokyo: Japanese Geotechnical Society.

Kiyota, T., Sato, T., Koseki, J. & Abadimarand, M., 2008. Behavior of liqueified sands under extremely large strain levels in cyclic torsional shear tests. *Soils and Foundations,* 48(5), pp. 727-739.

Okamura, M. et al., 2020. Large-scale flowslide in Sibalaya caused by the 2018 Sulawesi Earthquake. *Soils and Foundations (submitted).*

Oya, M., 2020. *Experimental evaluation of the influence of soil fabric and cementation on liquefaction resistance (in Japanese).* Tokyo: Bachelor Thesis, The University of Tokyo.

Skempton, A. W., 1954. The pore pressure coefficient A and B. *Geotechnique Vol. 4, No. 4,* pp. 143-147.

Tatsuoka, F., Ochi, K., Fujii, S. & Okamoto, M., 1986. Cyclic undrained triaxial and torsional shear strength of sands for different sample preparation methods. *Soils and Foundations, 26 (3),* pp. 23-41.

Umar, M., 2019. *Degradation of stress-strain properties of sand in undrained torsional shear tests.* Tokyo: Ph.D. Thesis, The University of Tokyo.

Chapter 3 FORMULATION OF STRESSES AND STRAINS IN ELEMENT TEST APPARATUS

3.1. Introduction

In general, it could be stated that there are two main challenges faced by the soil engineers and researchers when predicting the soil liquefaction: (1) Determining the stress conditions required to trigger the liquefaction, and (2) Determining the consequences of this phenomenon, including the potential sliding and deformation (Seed, 1987). From this statement, it is clear that stress and strain are, basically, the two most important parameters to evaluate the liquefaction properties of soils.

Triaxial apparatus is widely used for laboratory tests due to the rounded cylindrical specimen shape that allows the user to obtain such a good quality in-situ specimen. As introduced in Chapter 2, this cylindrical specimen will be covered by a rubber membrane that is pressurized by an isotropic condition while subjected to an additional vertical load. However, in terms of simulating the stress condition in the field during the earthquake, this condition provided by the Triaxial Apparatus is not the best method to evaluate the mechanical properties of the sand specimens (Ishihara & Li, 1972). One of the drawbacks of the Triaxial apparatus is that the directions of the principal stresses are re-oriented intermittently by 90^o. The intermediate principal stress is also intermittently changed during cyclic loading.

In the torsional apparatus, the stress applied is more realistic considering the field condition during the earthquake. Moreover, the direction of the principal stress is re-oriented continuously and the intermediate principle is almost constant during the shearing. The hollow cylindrical specimen is observed as infinite long on the circumferential direction which eliminates the effect of boundaries. However, the shear stress along the cross-section is not uniform. It is always assumed that the distribution of stress along the radial direction is linear when the shear strain is small, and the sand will act as a rigid plastic material after exceeding a large shear strain. In most cases, the sand stays in the status between elastic and rigid plastic.

In this study, the triaxial apparatus and torsional shear apparatus were employed to investigate the flow behavior of sandy soils under static shear loading. Since the modes of applying stress on the soil element between triaxial and torsional shear apparatuses are different, their stress and strain mode will be introduced, respectively.

3.2.Soil Index Properties

Soils are made of solid particles with voids in-between. For most of the case, the voids are filled with air and water. Therefore, soils are three-phase materials with solid, liquid and air constituents. Fig. 2.1 shows a soil sample of weight W and total volume V.

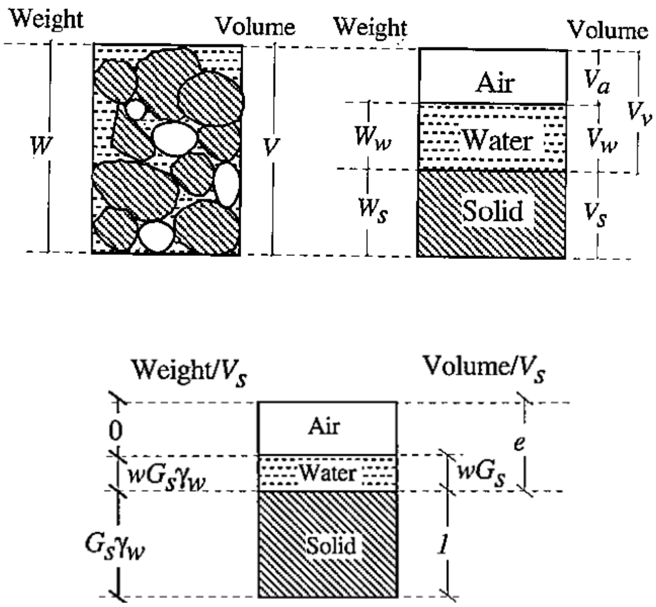

Figure 3-1 Phase diagram of soils (Bardet, 1997)

In soil mechanics, the proportions of the solid, liquid and air constituents are characterized by five dimensionless quantities: e, n, w, S_r and D_r. The void ratio (e) is the ratio of the volume of voids (V_v) to the solid volume (V_s):

$$e = \frac{V_v}{V_s} = \frac{V - V_s}{V_s} \tag{3.1}$$

The porosity (n) is the ratio of the volume of voids (V_v) to the total volume (V):

$$n = \frac{V_v}{V} \tag{3.2}$$

The water content (w) is the ratio of the weight of water (W_w) to the dry weight of the sample (W_s):

$$w = \frac{W_w}{W_s} \tag{3.3}$$

The degree of saturation (S_r) is the ratio of the volume of the water (V_w) to the volume of the void (V_v):

$$S_r = \frac{V_w}{V_v} \times 100 \tag{3.4}$$

S_r ranges from 100% when $V_w = V_v$ (i.e., fully saturated conditions) to 0 when $V_w = 0$ (i.e., perfectly dry conditions).

In case of coarse-grained soils, the relative density (D_r) is defined to characterize the degree of compaction:

$$D_r = \frac{(e_{\max} - e)}{(e_{\max} - e_{\min})} \tag{3.5}$$

where

$e_{\max}$ = maximum void ratio;
$e_{\min}$ = minimum void ratio;
e = current void ratio.

D_r varies from 0 when $e = e_{\max}$ to 100 % when $e = e_{\min}$. In reality, $e_{\max}$ and $e_{\min}$ are not the absolute maximum and minimum void ratios of soil, respectively. They are just index void ratios obtained by standard procedures. In laboratory tests, the current void ratio (e) is evaluated as:

$$e = \frac{G_s \gamma_w}{\gamma_d} - 1 \tag{3.6}$$

where

G_s = specific gravity defined as the ratio of solid and water unit weight, γ_s / γ_w;

γ_d= dry unit weight of soil, W_s / V.

3.3.Triaxial tests

3.3.1. Definition and computation of stress

The following equations are used to calculate the stresses and strains in triaxial tests. The deviatoric stress, q, could be measured directly from the load cell during compression and extension tests. The maximum principal stress changes its direction during cyclic loading. The axial stress under compression condition is calculated by the following equations:

$$\sigma_v = \sigma_1 = \sigma_3 + q = \sigma_r + q \tag{3.7}$$

$$\sigma'_v = \sigma'_1 = \sigma'_3 + q = \sigma'_r + q \tag{3.8}$$

In which σ_v and σ'_v are the total and effective axial stresses. σ_1 and σ_3 are the maximum and the minimum principal stresses, with the corresponding effective stresses of σ'_1 and σ'_3. σ'_r is the effective confining pressure measured by the HCDPT and σ_r is the total confining pressure which includes the back pressure of pore water supplied by the positive regulator.

As for the stresses in extension stage, the calculation method is similar to those in the compression stage, it will not be repeated herein. Mean effective stress (p') is notated as:

$$p' = \frac{\sigma'_v + 2\sigma'_r}{3} \tag{3.9}$$

3.3.2. Definition and Computation of Strain

Strain as a normalized deformation parameter has been widely used to represent the deformation behavior of soils. In the Triaxial Apparatus, the height of the specimen without deformation is measured and set as a reference height. During the cyclic loading, the displacement of the specimen is measured by LVDT and recorded by the computer program. Then, the axial strain is calculated by the following equation:

$$\varepsilon_a = \frac{\Delta H}{H} \tag{3.10}$$

In which, ε_a is the axial strain, ΔH is the displacement of the specimen, and H is the initial height of the specimen.

In the Triaxial testing, the shear stress is applied indirectly to the specimen. The calculation of the maximum shear strain ($\gamma_{\max}$) can be defined as follow:

$$\gamma_{max} = \frac{3}{2}\varepsilon_a - \frac{1}{2}\varepsilon_{vol} \tag{3.11}$$

Where ε_a is the axial strain and ε_{vol} is the volumetric strain.

3.4.Hollow Cylindrical Torsional Shear Tests

In the hollow cylinder torsional shear apparatus, four stress components on the specimen, namely radial stress (σ_r), circumferential stress (σ_θ), axial stress (σ_z) and shear stress ($\tau_{z\theta}$), can be defined by controlling the outer cell pressure (p_0), the inner cell pressure (p_i) the vertical axial load (F_z) and the torque (T), as shown in Figure 3-2. For this reason, hollow cylindrical specimens have four degrees of freedom from the point of view of the loads.

In this study, the averaged stress components acting on hollow cylindrical components were calculated with reference to Ampadu (1991). Similar formulations were employed by Hight et al. (1983), Saada (1988), and among others.

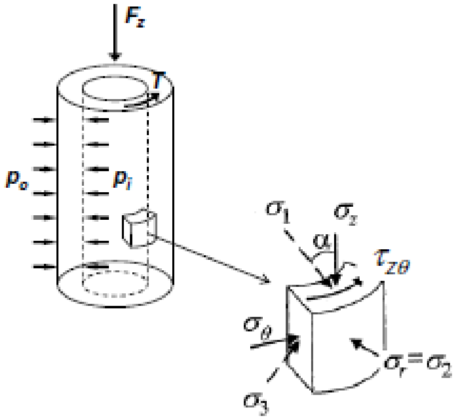

Figure 3-2 External forces and stress components acting on the hollow cylindrical specimen (after Chiaro, 2010)

It should be noted that the actual distribution of stresses in the specimen is very complicated due to the end restraint effect and bedding error. Timoshenko and Goodier (1970) gave a solution to the problem of a right hollow cylinder subjected to uniform inner pressure p_i and outer pressure p_o. Stress distribution is assumed to be symmetrical with respect to the axis z of the hollow cylinder and the stress components do not depend on the radial angle θ and are a function of the radius r only. As a result, shear stress is equal to zero ($\tau_{r\theta} = 0$).

3.4.1. Radial and Circumferential Stresses

The equilibrium equation in the radial direction yields:

$$\frac{\partial\sigma_r}{\partial r} + \frac{\sigma_r - \sigma_\theta}{r} + \omega = 0 \tag{3.12}$$

where ω is the body force. When ω = 0, Eq. (2.9) is satisfied by:

$$\sigma_r = \frac{A}{r^2} + 2C \tag{3.13}$$

$$\sigma_\theta = -\frac{A}{r^2} + 2C \tag{3.14}$$

where A and C are constants obtained by assuming the following boundary conditions:

$$\sigma_r|_{r=r_i} = p_i \tag{3.15}$$

$$\sigma_r|_{r=r_0} = p_0 \tag{3.16}$$

in which r_o and r_i denote the current outer and inner radii of the specimen, respectively.

Due to conditions in Eq. (3.15) and Eq. (3.16), the Eq. (3.13) and Eq. (3.14) becomes:

$$\sigma_r = \frac{p_0{r_0}^2 - p_i{r_i}^2}{{r_0}^2 - {r_i}^2} - \frac{{r_0}^2{r_i}^2(p_0 - p_i)}{{r_0}^2 - {r_i}^2}\frac{1}{r^2} \tag{3.17}$$

$$\sigma_\theta = \frac{p_0{r_0}^2 - p_i{r_i}^2}{{r_0}^2 - {r_i}^2} + \frac{{r_0}^2{r_i}^2(p_0 - p_i)}{{r_0}^2 - {r_i}^2}\frac{1}{r^2} \tag{3.18}$$

Finally, the average stress components are computed as follows:

$$\bar{\sigma}_r = \frac{\int_{r_i}^{r_0} \sigma_r \, dr}{\int_{r_i}^{r_0} dr} \tag{3.19}$$

$$\bar{\sigma}_\theta = \frac{\int_{r_i}^{r_0} \sigma_\theta \, dr}{\int_{r_i}^{r_0} dr} \tag{3.20}$$

and by substituting Eq. (3.17) into Eq. (3.19) and Eq. (3.18) into Eq. (3.20) the following equations are obtained:

$$\bar{\sigma}_r = \frac{p_0 r_0 + p_i r_i}{r_0 + r_i} \tag{3.21}$$

$$\bar{\sigma}_\theta = \frac{p_0 r_0 - p_i r_i}{r_0 - r_i} \tag{3.22}$$

In this study, the outer and inner cell pressures are kept equal to each other ($p_0 = p_i$), therefore, Eq. (3.21) and Eq. (3.22) yield:

$$\bar{\sigma}_r = \bar{\sigma}_\theta \tag{3.23}$$

3.4.2. Vertical stress

Average vertical stress at mid-height of the specimen can be computed as follows:

$$\bar{\sigma}_z = \frac{L_C}{A_S} + \sigma_h + \sigma_g + \sigma_m \tag{3.24}$$

where

L_C = axial load detected by the inner load cell;

$A_S = \pi(r_0{}^2 - r_i{}^2)$ cross-sectional area of the specimen;

σ_h = horizontal stress (= σ_r = σ_θ);

$\sigma_g = \gamma' H/2$, overburden stress of the specimen due to its self-weight at its mid height;

$\gamma' = (G_s - 1)/(1+e)\gamma_w$, unit weight of soil in water;

H = height of the specimen;

σ_m = correction for membrane stress (Tatsuoka, et al., 1986)). In particular results:

$$\sigma_m = 0 \qquad \text{(if } \varepsilon_z > 0\text{, compression)} \tag{3.25}$$

$$\sigma_m = -\frac{3}{8}\varepsilon_z\frac{t_m E_m}{(r_0 - r_i)} \qquad \text{(if } \varepsilon_z < 0\text{, extension)} \tag{3.26}$$

Where

ε_z = axial strain;

t_m = thickness of membrane;

E_m = Young's modulus of the membrane.

3.4.3. Shear Stress

Shear stress $\tau_{z\theta}$ acting on a soil element with area $dA = r\,d\theta\,dr$ can be linked with the torque T that is applied to the specimen as follows:

$$T = \int_{r_i}^{r_0}\int_{0}^{2\pi}\tau_{z\theta}r^2 d\theta dr = 2\pi\int_{r_i}^{r_0}\tau_{z\theta}r^2 dr \tag{3.27}$$

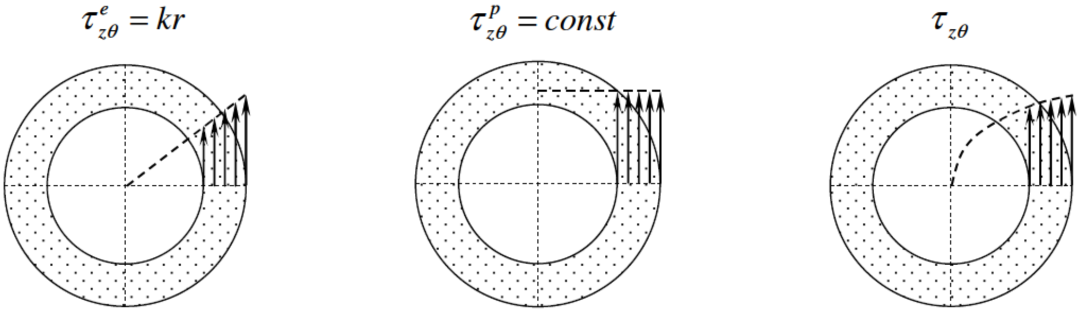

(a) (b) (c)

Figure 3-3 Shear stress distributions in a hollow cylindrical specimen: (a) linear elastic; (b) perfectly plastic; and (c) actual case

For a shear strain that is small enough for the specimen to be well within the elastic range, the shear stress increases in direct proportion with the distance to the center (Figure 3-3a). In this case, the shear stress at any distance along the radial direction can be computed by the following equation:

$$\tau_{z\theta}^{e} = kr \tag{3.28}$$

Therefore Eq. (3.27) can be rewritten as

$$T = 2\pi \int_{r_i}^{r_0} k\, r^3 dr = \frac{\pi}{2}({r_0}^4 - {r_i}^4)k \tag{3.29}$$

and the elastic component of shear stress can be evaluated as:

$$\tau_{z\theta}^{e} = k\frac{r_0 + r_i}{2} = \frac{T}{\pi({r_0}^2 + {r_i}^2)(r_0 - r_i)} \tag{3.30}$$

$$k = \frac{2T}{\pi({r_0}^4 - {r_i}^4)} \tag{3.31}$$

On the contrary, when a large strain is imposed so that the stress reaches its ultimate value at all the points within the cross section, the shear stress is distributed uniformly (Figure 3-3b); therefore, the shear stress at any distance along the radial direction can be computed by the following equations:

$$\tau_{z\theta} = \tau_{z\theta}^{p} = \text{constant} \tag{3.32}$$

$$T = 2\pi\tau_{z\theta}^{p} \int_{r_i}^{r_0} r^2 dr = \frac{2}{3}\pi\tau_{z\theta}^{p}({r_0}^3 - {r_i}^3) \tag{3.33}$$

$$\tau_{z\theta}^{p} = \frac{3T}{2\pi({r_0}^3 - {r_i}^3)} \tag{3.34}$$

A specimen of saturated sand being tested may behave almost elastically at the early stage of cyclic loading, and it will become more and more like a plastic material as it proceeds in the loading stage. Eventually, when liquefaction sets in, the sand will exhibit the behavior as if it were a rigid-plastic material. Therefore it may be reasonable to assume that the real behavior of the sand (Figure 3-3c) is somewhere in-between these two extreme cases for which the difference in the average shear stress is small. For this reason, in this study, the shear stress is averaged from Eq. (3.30) and Eq. (3.34) as shown below:

$$\bar{\tau}_{z\theta} = \frac{\tau_{z\theta}^{e} + \tau_{z\theta}^{p}}{2} = \frac{1}{2}\left[\frac{T}{\pi({r_0}^2 + {r_i}^2)(r_0 - r_i)} + \frac{3T}{2\pi({r_0}^3 - {r_i}^3)}\right] \tag{3.35}$$

In Eq. (3.35), T is the torque acting on the soil which can be evaluated as:

$$T = T_{CL} - T_m \tag{3.36}$$

where

T_{CL} = torque detected by the load cell;

T_m = membrane force (due to inner and outer membranes).

In a hollow cylindrical specimen the membrane force due to inner and outer membranes can be evaluated as:

$$T_m = 2\pi t_m ({r_0}^2 \tau_{z\theta,mo} + {r_i}^2 \tau_{z\theta,mi}) \tag{3.37}$$

The rubber membrane is a linear elastic material with Poisson's ratio $\upsilon = 0.5$; its shear modulus G_m and shear stress τ_m can be calculated as:

$$G_m = \frac{E_m}{2(1+\upsilon)} = \frac{E_m}{3} \tag{3.38}$$

$$\tau_{z\theta,m} = G_m\, \gamma_{z\theta,m} = \frac{E_m}{3} \gamma_{z\theta,m} \tag{3.39}$$

By using the definition in Eq. (3.39), Eq. (3.37) becomes:

$$T_m = \frac{2}{3}\pi t_m E_m ({r_0}^2 \gamma_{z\theta,mo} + {r_i}^2 \gamma_{z\theta,mi}) \tag{3.40}$$

where

$\gamma_{z\theta,mo}$= shear strain on the outer membrane;

$\gamma_{z\theta,mi}$= shear strain on the inner membrane.

$$\gamma_{z\theta,mo} = \frac{r_0}{H}\theta \tag{3.41}$$

$$\gamma_{z\theta,mi} = \frac{r_i}{H}\theta \tag{3.42}$$

Therefore, the membrane force T_m in Eq. (2.33) can be evaluated as:

$$T_m = \frac{2}{3}\pi t_m E_m ({r_0}^3 + {r_i}^3)\frac{\theta}{H} \tag{3.43}$$

where

r_0 = outer radius of the specimen;

r_i= inner radius of the specimen;

t_m = thickness of membrane;

E_m = Young’s modulus of membrane;

E_m = height of specimen;

θ□= rotation angle at top cap detected by potentiometer.

3.4.4. Principal Stresses

The principal stresses can be computed by the four stress components:

$$\begin{Bmatrix}\sigma_1 \\ \sigma_3\end{Bmatrix} = \frac{\sigma_z + \sigma_\theta}{2} \pm \sqrt{\frac{(\sigma_z - \sigma_\theta)^2}{2} + \tau_{z\theta}^2} \tag{3.44}$$

$$\sigma_2 = \sigma_r \tag{3.45}$$

The angle between the directions of the major principal stress □*1* with the vertical direction is:

$$2\alpha = \arctan\left(\frac{2\tau_{z\theta}}{\sigma_z - \sigma_\theta}\right) \tag{3.46}$$

In addition the intermediate principal stress is defined as:

$$b = \frac{\sigma_2 - \sigma_3}{\sigma_1 - \sigma_3} = \frac{1}{2}\left[\frac{\sigma_r - \dfrac{\sigma_z + \sigma_\theta}{2}}{\left(\dfrac{\sigma_z - \sigma_\theta}{2}\right)^2 + \tau_{z\theta}^2} + 1\right] \tag{3.47}$$

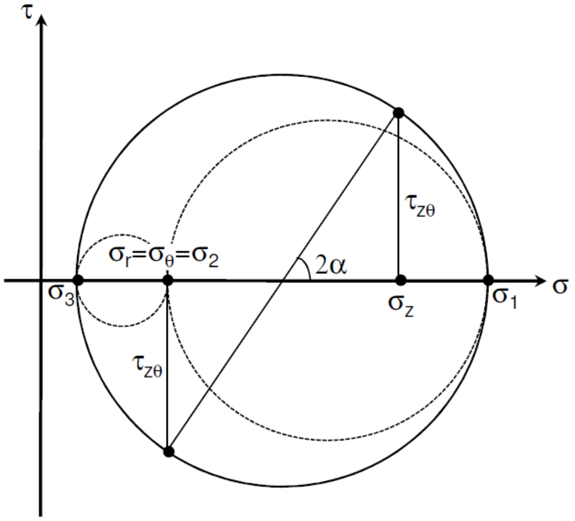

Figure 3-4 Mohr’s circle of stress

3.5.Formulation of Strains

In this study, the averaged strains components acting on hollow cylindrical components were calculated with reference to Ampadu (1991). Axial strain ε_z, radial strain ε_r, circumferential strain ε_θ and shear strain γ_{zq} are the four-strain components of the soil element to be determined.

As shown in Figure 3-4, ε_r and ε_θ of a soil element can be evaluated as:

$$\varepsilon_r = -\frac{\left[u + \left(\frac{\delta u}{\delta r}\right) dr\right] - u}{dr} = -\frac{du}{dr} \tag{3.48}$$

$$\varepsilon_\theta = -\frac{(u + r)d\theta - rd\theta}{rd\theta} = -\frac{u}{r} \tag{3.49}$$

Where,

u = deformation of a soil element in radial direction;

r= distance to the centre of the soil element from the centre of the specimen.

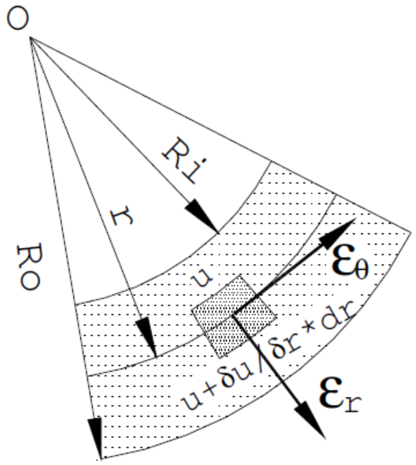

Figure 3-5 Definition of radial and circumferential strains of a soil element

Combining Eq. (3.48) and Eq. (3.49) yields:

$$\frac{d\varepsilon_\theta}{dr} + \frac{1}{r}(\varepsilon_\theta - \varepsilon_r) = 0 \tag{3.50}$$

If it is assumed that distribution of *u* is linear in the radial direction:

$$u = \frac{u_0 - u_i}{r_0 - r_i} r + \frac{u_i r_0 - u_0 r_i}{r_0 - r_i} \tag{3.51}$$

Then the average radial strain $\bar{\varepsilon}_r$ results:

$$\bar{\varepsilon}_r = \frac{\int_{r_i}^{r_0} \varepsilon_r \, r \, dr}{\int_{r_i}^{r_0} r \, dr} = -\frac{u_0 - u_i}{r_0 - r_i} \tag{3.52}$$

Whereas, the average circumferential strain□□□□can be calculated as:

$$\bar{\varepsilon}_\theta = \frac{\int_{r_i}^{r_0} \varepsilon_\theta \, r \, dr}{\int_{r_i}^{r_0} r \, dr} = -\frac{u_0 + u_i}{r_0 - r_i} \tag{3.53}$$

On the other hand, the average axial strain $\bar{\varepsilon}_z$ and the average shear strain $\bar{\gamma}_{z\theta}$ can be calculated by:

$$\bar{\varepsilon}_z = -\frac{dw}{dz} = -\frac{\Delta H}{H} \qquad \text{(positive in compression)} \tag{3.54}$$

$$\bar{\gamma}_{z\theta} = \frac{\int_{r_i}^{r_0} \gamma_{z\theta}\, r\, dr}{\int_{r_i}^{r_0} r\, dr} = \frac{2\theta({r_0}^3 - {r_i}^3)}{3H({r_0}^2 - {r_i}^2)} \tag{3.55}$$

where

H = height of the specimen;

θ= rotation angle at top cap detected by the potentiometer.

Evaluation of volumetric strain in a hollow cylindrical specimen is generally not easy, due to technical difficulties on the measurement of the change of the inner and outer diameters.

To overcome these troubles, it is possible to employ a method to evaluate the change of both inner and outer diameters during the consolidation process, which is made based on the assumption of the same ratio of change in the inner and outer radius of the specimen by using the following formulae (Japanese Geotechnical Society, 1998)

$$d_i = d_{i0}\sqrt{\frac{1 - \varepsilon_{\mathrm{vol}}}{1 - \varepsilon_z}} \tag{3.56}$$

$$d_o = d_{o0}\sqrt{\frac{1 - \varepsilon_{\mathrm{vol}}}{1 - \varepsilon_z}} \tag{3.57}$$

Where,

$\varepsilon_{\mathrm{vol}}$ = volumetric strain of the specimen;

ε_z = axial strain of the specimen;

d_{i0} = initial inner diameter of the specimen;

d_{o0} = initial outer diameter of the specimen.

3.6.Membrane Force Correction

As Koseki et al. (2007) among others pointed out, in torsional shear tests on hollow cylindrical specimen, due to the presence of inner and outer membranes, the effect of membrane force cannot be neglected. Furthermore, it becomes significantly important when shear strain reaches extremely high level as Kiyota et al. (2008) indicated. Usually, the membrane force has been corrected based on the linear elasticity theory, which uses the Young's modulus of the membrane. The theoretical apparent shear stress (τ_m) induced by the inner and the outer membranes can be evaluated as:

$$\tau_m = \frac{t_m E_m (r_o^3 + r_i^3)\theta}{(r_o^3 - r_i^3)H} \tag{3.58}$$

Where

r_o = outer radius of the specimen;

r_i= inner radius of the specimen;

t_m= thickness of membrane;

E_m = Young's modulus of membrane;

H = height of specimen;

θ = rotation angle detected by potentiometer.

In the previous study by Kiyota (2008), Chiaro (2010), and Umar (2019), using this modified torsional shear apparatus, in order to confirm the validity of (3.58) in correcting the effect of membrane force, a special test was performed by filling with water the area between the inner and outer membranes and shearing it cyclically under undrained condition up to double amplitude shear strain (γ_{DA}) of 100%. Chiaro (2010) evaluated the membrane force for the medium size hollow specimen size with the outer diameter was 150 mm, inner diameter was 90 mm, and the height of 300 mm. The result of the membrane correction is shown in Figure 3-6.

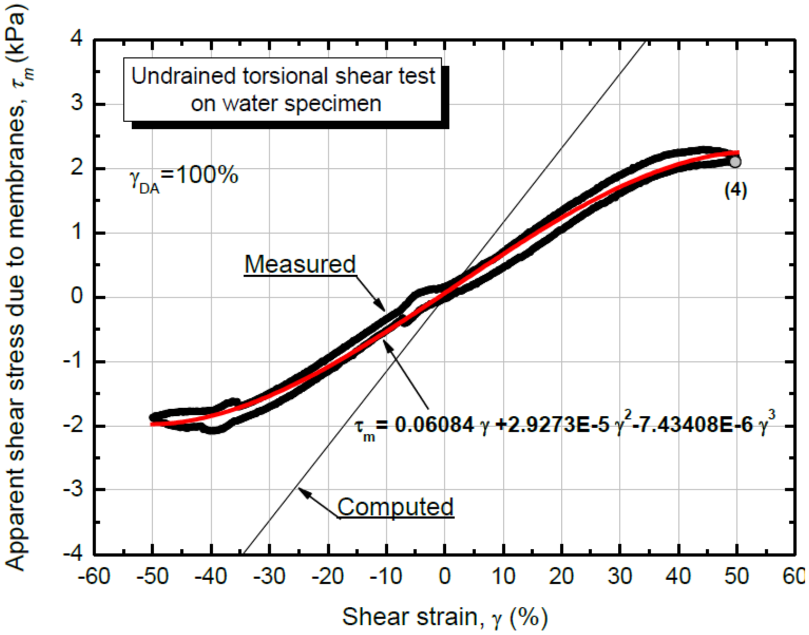

Figure 3-6 Relationships between γ - τm on the range of γDA= 100% (Chiaro, 2010)

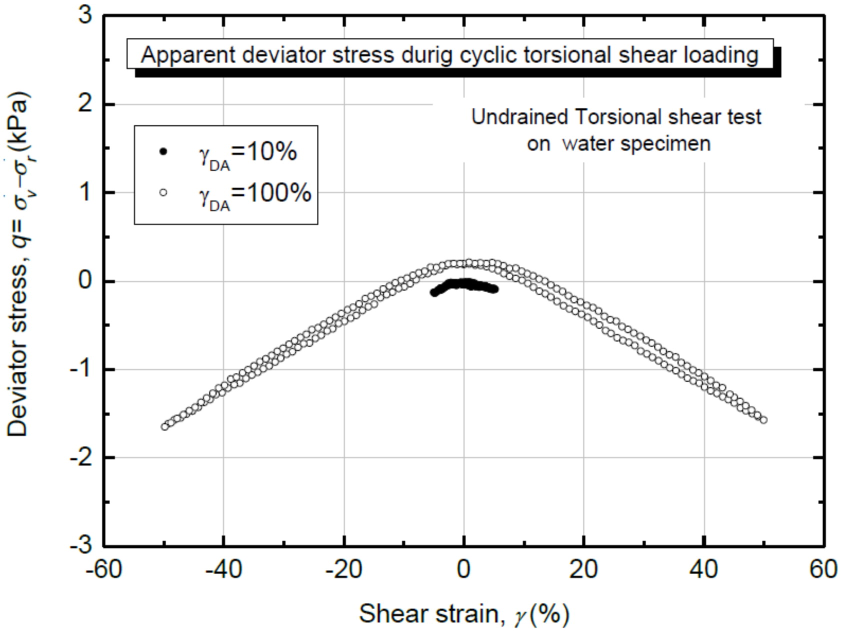

Figure 3-7 Apparent deviator stress during undrained cyclic torsional shear loading on water specimen (Chiaro, 2010)

Further, Umar (2019) conducted the same test on the smaller specimen with the outer diameter was 100 mm, inner diameter was 60 mm, and the height was 200 mm. It is confirmed that the test result was identical to the one provided by Chiaro (2010). Thus, in this study, the membrane correction provided by Chiaro (2010) will be employed to the calculation results for hollow cylindrical torsional shear test.

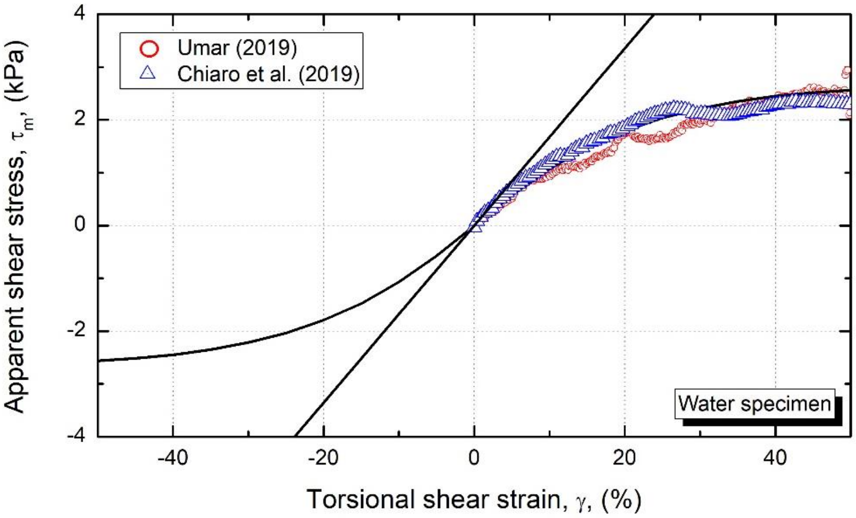

Figure 3-8 Comparison of relationships between between γ - τ_m on the range of γ_{DA}= 100% for different specimen size (Umar, 2019)

3.7. References

Ampadu, S. I. K., 2008. *Undrained behavior of Kaolin in torsional simple shear.* Tokyo: Ph.D. Thesis, The University of Tokyo.

Bardet, J. P., 1997. *Experimental soil mechanism.* Los Angeles: Prentice Hall.

Chiaro, G., Sato, T., Kiyota, T. & Koseki, J., 2011. *Effect of intial static shear stress on the undrained cyclic behavior of saturated sand by torsional shear loading.* Santiago, Chile, s.n.

Hight, D. W., Gens, A. & Symes, M. J., 1983. The development of a new hollow cylinder apparatus for investigating the effects of principal stress rotation in soils. *Geotechnique,* 33(No. 4), pp. 355-383.

Ishihara, K. & Li, S. I., 1972. Liquefaction of saturated sand in Triaxial Torsion Shear Test. *Soils and Foundations*, 12(No. 2), pp. 19-39.

Japanese Geotechnical Society, 1998. *Standard of Japanese Geotechnical Society for laboratory shear test.* Tokyo: Japanese Geotechnical Society.

Kiyota, T., Sato, T., Koseki, J. & Abadimarand, M., 2008. Behavior of liqueified sands under extremely large strain levels in cyclic torsional shear tests. *Soils and Foundations,* 48(5), pp. 727-739.

Saada, A. S., 1988. Hollow cylindrical torsional devices: their advantages and limitations. In: R. T. Donaghe, R. C. CHaney & M. L. Silver, eds. *Advanced Triaxial Testing of Soil and Rock.* Philadelphia: ASTM STP 977, pp. 766-795.

Seed, H. B., 1987. Design problems in soil liquefaction. *Journal of Geotechnical Engineering, 113(8),* pp. 827-845.

Tatsuoka, F. et al., 1986. Failure and deformation of sand in torsional shear test. *Soils and Foundations, Vol. 26, No. 4,* pp. 79-97.

Timoshenko, S. P. & Goodier, J. N., 65-71. *Theory of elasticity.* 3rd ed. New York: McGraw-Hill Book Company.

Umar, M., 2019. *Degradation of stress-strain properties of sand in undrained torsional shear tests.* Tokyo: Ph.D. Thesis, The University of Tokyo.

Chapter 4 DILATION BEHAVIOR OF SANDY SOILS UNDER CONSTANT STATIC SHEAR

4.1. Introduction

Soil elements within the sloped ground are subjected to initial static shear stress on the horizontal plane or an assumed failure plane. During earthquake shaking, these elements are subjected to additional cyclic shear stress due to shear waves propagating vertically upward from the bedrock. The superimposition of static and cyclic shear stresses can have major effects on the response of soil, leading to liquefaction-induced failure of natural and artificial slopes of sandy deposits and the consequent development of extremely large ground deformation.

Soil liquefaction also can lead to massive displacements in a flow slide, which involves the undrained shear of saturated, contractive soils that flow in a steady-state condition (Poulos, et al., 1985). This flow failure type can occur if the shear resistance of the soil in the steady-state line is lower than the static driving shear stress. Although it is a common understanding that this instability only occurs for loose granular material under undrained conditions, it is vital to understand the possibility of flow slides occurs in drained conditions.

The study of investigating the flow behavior using swelling-induced-large deformation due to water inflow has been conducted by several researchers by implementing static liquefaction tests on soil elements in drained conditions. Uchida and Vaid (1994) examined triaxial tests on the dense specimen in which the increment in strain ratio was controlled. They suggested that softening behavior occurs before reaching the failure line when the increment of this strain ratio is smaller than -0.5. Vaid and Eliadorani (1998) examined the partially drained triaxial tests on sand subjected to the initial static shear stress and concluded that partially drained conditions render sand unstable even if the sand is stable in completely undrained conditions.

Sento et al. (2004) conducted several experiments in Triaxial Apparatus using Toyoura sand with mean effective stress (p') is 200 kPa with the static shear stress (q) are 0 kPa, 25 kPa, 37 kPa, and 54 kPa for various densities. Yoshimine et al. (2006) also conducted the same test using Toyoura sand with the mean effective stress (p') of

100 kPa, 200 kPa, and 400 kPa to the various relative densities, ranging from 1%-94%. The deviatoric stress is ranging from 20 kPa to 240 kPa for each stress condition.

However, as of now, the number of studies about this topic is very limited. Thus, the flow behavior of sand under this condition is still not well understood. In this chapter, the investigation will be emphasized the dilation behavior of sandy soils in the low deviatoric stress (q) condition, which corresponds to the very gently sloping ground using various initial densities. Besides, this study also will investigate the effect of fines on the dilation behavior of mixed sand under this circumstance using Triaxial Apparatus.

4.2. Stress Condition on a Soil Element at Sloping Ground

The soil elements within the sloping ground are, in principle, subject to additional static shear stress due to the gravity. In the element test, in order to evaluate this static stress ratio, simplified assumptions are commonly used to describe the condition of an infinite slope. It is assumed that:

- Soil is cohesionless and homogenous;
- Failure is the result of shallow translational sliding and occurs in a single layer;
- The failure plane and the water table are parallel to the ground surface;
- The failure plane is of infinite length.

It is assumed that there is a sloped ground surface, a soil column of unit width and length, and the water table is located in-between the ground surface and the examined failure surface. The ground has an inclination of β. The soil layer located at the upper groundwater level has a unit weight of γ_t, while the soil layer immersed in the groundwater has a unit weight of γ_{sat}. The depth of the soil layer above the failure surface is notated as z, while the height of groundwater is represented by z_w. This condition is illustrated in Figure 4-1.

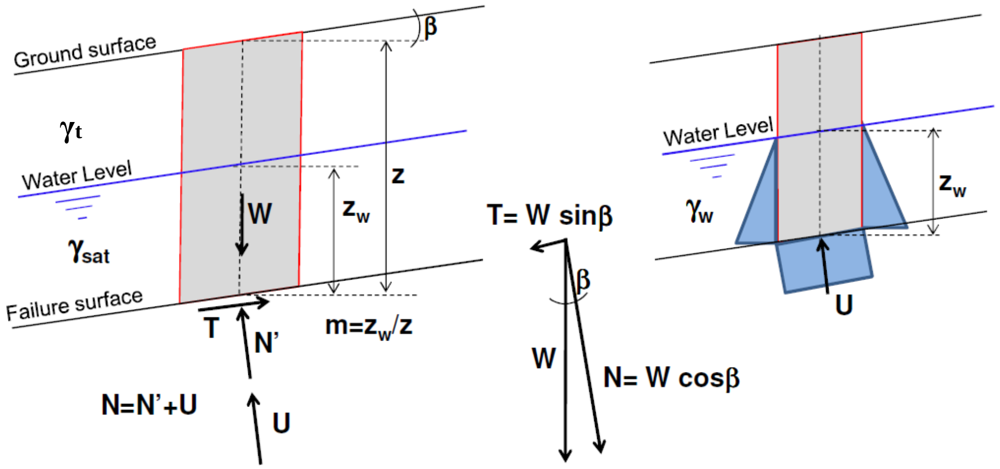

Figure 4-1 Infinite slope conditions assumed for the derivation of the static stress due to the gravity

By referring to the equilibrium of forces on a plane parallel to the slope at the bottom of the soil column, the resistance force (T) and the normal force (N) can be evaluated as follow.

$$T = W \sin\beta = [(1-m)\gamma_t + m\gamma_{\mathrm{sat}}]z \sin\beta \tag{4.1}$$

$$N = W \cos\beta = [(1-m)\gamma_t + m\gamma_{\mathrm{sat}}]z \cos\beta \tag{4.2}$$

In which, W is the total weight of the saturated soil, T is the slope parallel component of gravity, N is the total normal component of gravity, β is the gradient of the slope, $m = z_w/z$ as defined in Figure 4-1, γ_{sat} is the unit weight of the saturated soil, and γ_t is the unit weight of dry soil.

The pore water pressure (U) at the bottom of the soil column can be evaluated as follows.

$$U = \gamma_w z_w = m\gamma_w z \cos\beta \tag{4.3}$$

Subsequently, in accordance with the principle of effective stress/force, the effective normal force N' can be defined as follow.

$$\begin{aligned} N' = N - U &= [(1-m)\gamma_t + m\gamma_{sat} - m\gamma_w]z \cos\beta \\ &= [(1-m)\gamma_t + m\gamma']z \cos\beta \end{aligned} \tag{4.4}$$

Where γ' is the unit weight of the saturated soil immersed in the water.

Considering that gravity component forces act on a surface having an area $A = 1/\cos\beta$, the associated stress components results as:

$$\begin{aligned}\tau_{static} &= \frac{T}{A} = \frac{[(1-m)\gamma_t + m\gamma_{\mathrm{sat}}]z\sin\beta}{1/\cos\beta} \\ &= [(1-m)\gamma_t + m\gamma_{\mathrm{sat}}]z\sin\beta\cos\beta\end{aligned} \tag{4.5}$$

$$\begin{aligned}\sigma' &= \frac{N'}{A} = \frac{[(1-m)\gamma_t + m\gamma']z\cos\beta}{1/\cos\beta} \\ &= [(1-m)\gamma_t + m\gamma']z\cos^2\beta\end{aligned} \tag{4.6}$$

Where, τ_{static} is the resistance force of initial driving static shear stress, and σ' is the effective normal stress at the bottom of soil column.

In the performing element test, the effective mean principal stress (p') acting on a soil element can be evaluated as follows.

$$\begin{aligned}p' &= \frac{\sigma'_v + 2\sigma'_h}{3} = \frac{\sigma'_v + 2K_0\sigma'_v}{3} = \left(\frac{1+2K_0}{3}\right)\gamma' z \\ &= \left(\frac{1+2K_0}{3}\right)\sigma'\end{aligned} \tag{4.7}$$

Where σ'_v and σ'_h is the vertical and the horizontal effective stresses, respectively, K_0 is the coefficient of earth pressure at rest, and γ' is the unit weight of the saturated soil immersed in the water of buoyant unit weight.

Thus, the effective mean principal stress (p') acting on a soil element of sloped ground can be evaluated as follows:

$$p' = \left(\frac{1+2K_0}{3}\right)\sigma' = \left(\frac{1+2K_0}{3}\right)[(1-m)\gamma_t + m\gamma']z\cos^2\beta \tag{4.8}$$

In this study, based on the above-simplified assumptions on which generally infinite slope method relies, and considering the element test conditions, the stress condition in the specific location of soil layer can be estimated in the element test as follow.

$$\frac{\tau_{static}}{p'} = \left(\frac{3}{1+2K_0}\right)\frac{[(1-m)\gamma_t + m\gamma_{\text{sat}}]}{[(1-m)\gamma_t + m\gamma']}\tan\beta \tag{4.9}$$

This stress ratio is also known as the static stress ratio (SSR). By assuming that the suction effects happened on the soil layer, the dry or partially dry saturated soil above the water table might completely wet, so it can be assumed that$\gamma_t = \gamma_{sat}$. Under this assumption, Equation (4.9) can be simplified as follow:

$$\begin{aligned}\frac{\tau_{static}}{p'} &= \left(\frac{3}{1+2K_0}\right)\frac{\gamma_{\text{sat}}}{[\gamma_{\text{sat}} - m\gamma_{\text{sat}} + m\gamma']}\tan\beta \\ &= \left(\frac{3}{1+2K_0}\right)\frac{\tan\beta}{\left(1-m+m\dfrac{\gamma'}{\gamma_{\text{sat}}}\right)}\end{aligned} \tag{4.10}$$

Finally, by simplifying the condition that dry soils is half weight of saturated soil or $\frac{\gamma'}{\gamma_{\text{sat}}} \approx 0.5$, the following expression for stress ratio on the site can be drawn as follow:

$$\frac{\tau_{static}}{p'} = \frac{3\tan\beta}{(1+2K_0)(1-0.5m)} \tag{4.11}$$

The represented condition of the slope inclination with the above assumption at the element test have been idealized by Chiaro (2010) and can be written as:

$$\beta = \tan^{-1}\left(\frac{\tau_{static}(1+2K_0)(1-0.5m)}{3p'}\right) \tag{4.12}$$

In which, in Triaxial apparatus, as it is classified as the indirect shear condition, the shear stress is simplified as $\tau_{static} = \frac{q}{2}$, in which q is the deviatoric stess.

In this study, in order to evaluate the dilation behavior of saturated sand in the static liquefaction test with constant deviatoric stress, various combinations of initial static shear stress and initial density were considered. The lists of the experimental test conducted at the strain-controlled Triaxial Apparatus using Toyoura sand are listed as follow:

Table 4-1 The list of experiments conducted at strain-controlled Triaxial Apparatus and its estimated sloping ground condition

Code Test	Relative density, *Dr* (%) at *p'*=100 kPa	Void ratio, *e*	Deviatoric stress, *q* (kPa)	Mean effective stress, *p'* (kPa)	Estimated ground inclination, *β* (%)*	Volumetric strain development at axial strain=20% (%)
TX5 (SL-5)	35.5	0.836	5	100	0.833	-1.5**
TX6 (SL-5)	70.2	0.710	5	100	0.833	-6.82***
TX7 (SL-10)	37.9	0.827	10	100	1.667	-2.5***
TX8 (SL-10)	72.8	0.698	10	100	1.667	-7.21
TX9 (SL-15)	26.9	0.867	15	100	2.5	-1.44
TX10 (SL-15)	28.4	0.862	15	100	2.5	-2.15
TX11 (SL-15)	43	0.800	15	100	2.5	-4.18
TX12 (SL-15)	50.1	0.782	15	100	2.5	-4.63
TX13 (SL-15)	63	0.735	15	100	2.5	-9.25
TX14 (SL-40)	24.6	0.875	40	100	6.667	-1.24
TX15 (SL-80)	33.6	0.843	80	100	13.333	-2.73
TX16 (SL-80)	38.8	0.826	80	100	13.333	-1.78**
TX17 (SL-80)	44	0.804	80	100	13.333	-2.67
TX27 (SL-15)	*81.2*	*0.690*	*15*	*100*	*2.5*	*-6.95****

*The estimated ground inclination follows the equation (4.12) and assuming that K_0=0.5 and m=1. TX27 was conducted at Stress-controlled apparatus.
**The final state of TX5 was 7.3% of axial strain and TX16 was 10.15%.
***The final state of TX6, TX7, and TX27 were 16% of axial strain.

4.3. Characteristics Line of Sand in Undrained Monotonic Loading and Drained Monotonic Loading

The critical state and steady-state theories are widely accepted for simulating the soil behavior and providing a basis for liquefaction evaluation and constitutive modeling. However, there was conflicting evidence regarding the critical state and steady-state of sands in the last decades. In some cases, the critical state and steady-state are taken to be identical and in others, they differ significantly.

The critical void ratio (CVR) of sands has been a subject of much discussion since the pioneering work of Casagrande (1936). A major step forward was the development of critical state soil mechanics by Roscoe et al. (1958), where an elastic-plastic constitutive model was developed and implemented into the framework of the critical state. In this theory, it is assumed that specimens yield at the “critical state” that remain as constant volume, and the plastic yielding can continuously occur without changing in deviatoric stress or a void ratio (Kang, et al., 2019).

On the other side, Castro and Poulos (1977) first defined the concept of steady-state of deformation: “a soil can flow at the constant void ratio, constant effective minor principal stress and constant shear stress.” This definition seems quite similar to the concept of “CVR state” proposed by Roscoe et al. (1958). To eliminate the confusion between these two technical terms, following Poulos (1981), this study will utilize the term “steady-state” to describe the behavior of continuous deformation in the constant volume on sand.

According to Yoshimine and Ishihara (1998), steady-state is a state of deformation of soil without effective stress increment or decrement and with no migration of pore water. If the density of sand is loose, a point of minimum effective stress appears and the dilatancy behavior is changed from dilative to contractive, is mentioned as Phase Transformation Point (Ishihara, et al., 1975). By connecting the Phase Transformation Point of each initial consolidation stress level, the Phase Transformation Line can be drawn in the stress-path plane.

The steady-state condition is classified in several states as in Figure 4-2. At the very large deformation state, one unique steady-state will be achieved irrespective of the initial consolidation state when the density is the same. This state is named as Ultimate Steady State (USS). However, if the steady-state is appeared after the phase transformation and following by the drop of the shear stress, this transient steady-state is mentioned as the Quasi Steady-State. In the case of the phase transformation or quasi-steady-state coincides with the ultimate steady-state and no hardening will be observed after the minimum stat, this condition is mentioned as a Critical Steady State.

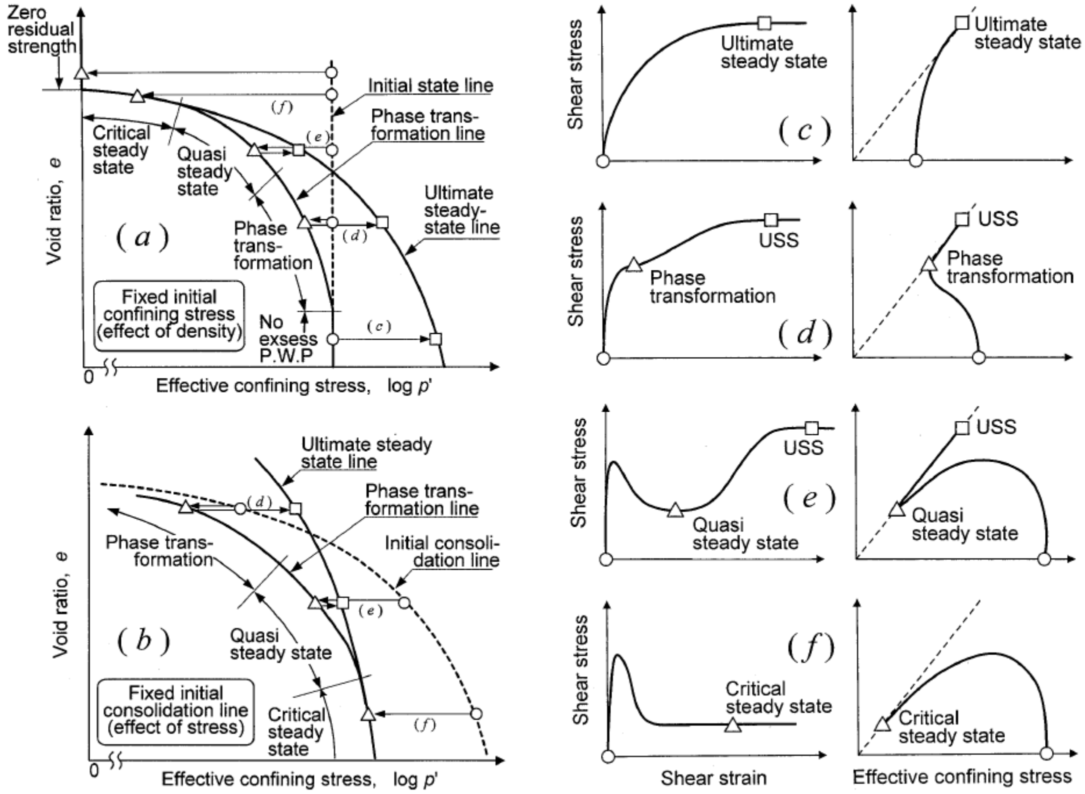

Figure 4-2 General undrained behavior of sand under large deformation (Yoshimine and Ishihara, 1998)

In this study, the undrained monotonic loading test with the loading rate of 0.2%/min has been conducted to draw the characteristics line of sand in undrained behavior. These tests were mostly terminated when the deviatoric stress reached 800 kPa, considering the maximum capacity of the load cell in this machine. All the specimen were prepared with the Air Pluviation method with the B value was more than 0.95. The specimen was consolidated to p'=100 kPa, isotropically, before the shearing process. The list of undrained monotonic loading tests in this Triaxial Compression is presented in Table 4-2.

Table 4-2 The list of Undrained Monotonic Loading Test in Triaxial Apparatus

Code Test	Relative density, *Dr* at *p'*=100 kPa (%)	Void ratio, *e*	Mean effective stress, *p'* (kPa)
TX1 (UML)	31.7	0.849	100
TX2 (UML)	31.2	0.852	100
TX3 (UML)	49.5	0.784	100
TX4 (UML)	45.6	0.799	100

The strain-stress relationships of the Undrained Triaxial Test (TX1-TX4) are presented in Figure 4-3 and Figure 4-4. In Figure 4-3, the steady-state of specimen TX1 and TX2 at the large deformation can be observed at the axial strain (ε_a) of 16%. Starting from this point, TX1 and TX2 tend to deform under constant increment of deviatoric stress within the constant volume (undrained condition). As the previous illustration by Yoshimine and Ishihara (1998), this state is mentioned as Ultimate Steady State (USS). However, for the specimen TX3 and TX4, the ultimate steady-state cannot be identified clearly, due to the limitation of measurement. Both TX3 and TX4 do not show the constant behavior as shown in Figure 4-2 even if the deviatoric stress reached 800 kPa. The Ultimate Steady State Line can be drawn in the stress-path by identifying the USS points at $q - \varepsilon_a$ plane and connecting those points with a line to the 0 point in stress-path curve.

The Phase Transformation Point for TX1, TX2, TX3, and TX4 could be identified at $q - \varepsilon_a$ plane during the shearing process as shown in Figure 4-4, following the illustration by Yoshimine and Ishihara (1998). Further, by connecting the Phase Transformation Point of each test (TX1-TX4) with a line toward the 0 point in the $q - p'$ plane, the Phase Transformation Line (PTL) can be drawn in the stress path as shown in Figure 4-5.

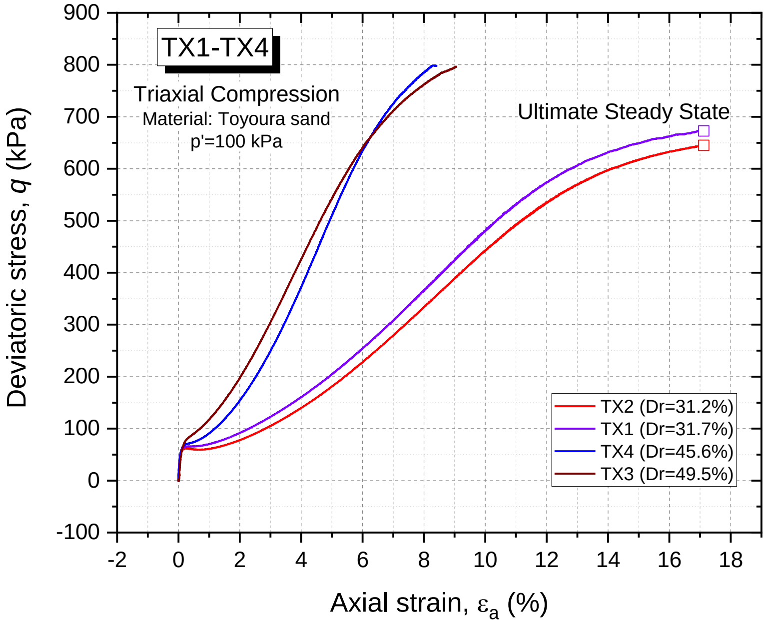

Figure 4-3 Relationships of axial strain and deviatoric stress of the undrained monotonic test

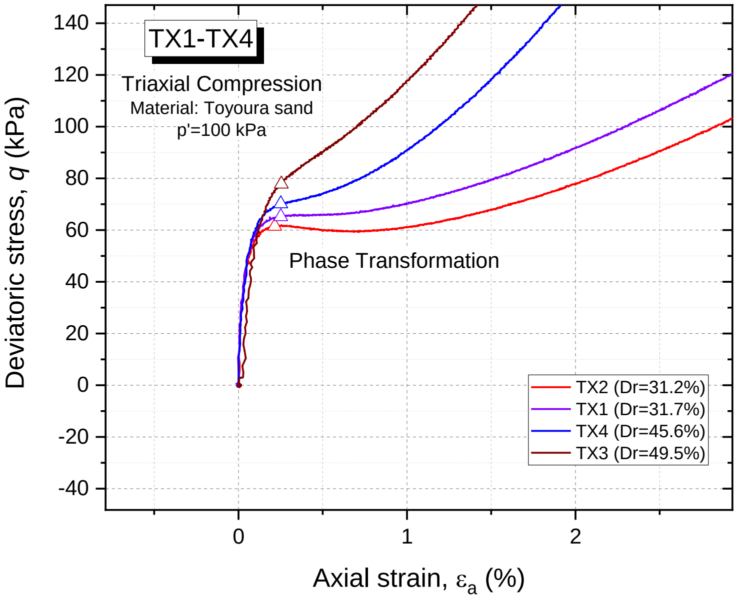

Figure 4-4 Phase transformation point at the undrained monotonic test in the lower stress-strain level

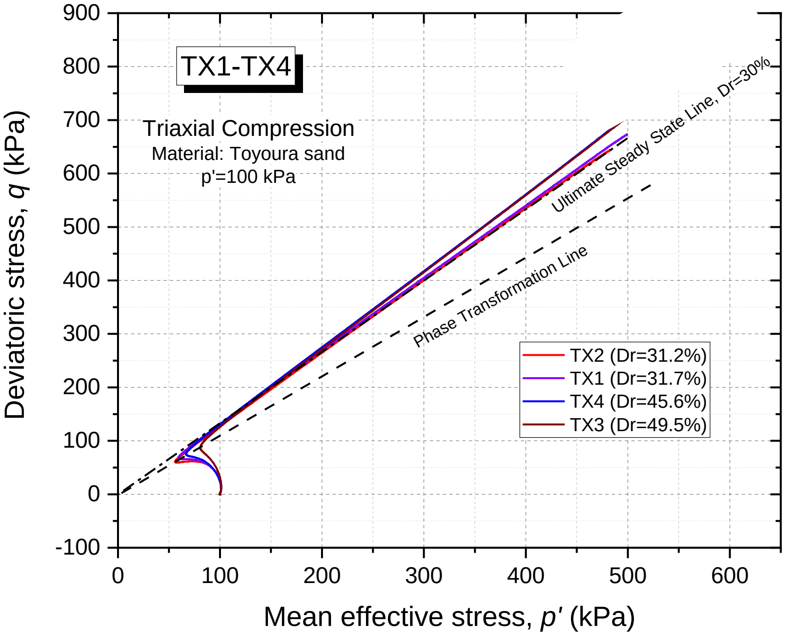

Figure 4-5 Stress-path of undrained monotonic test on Triaxial Apparatus

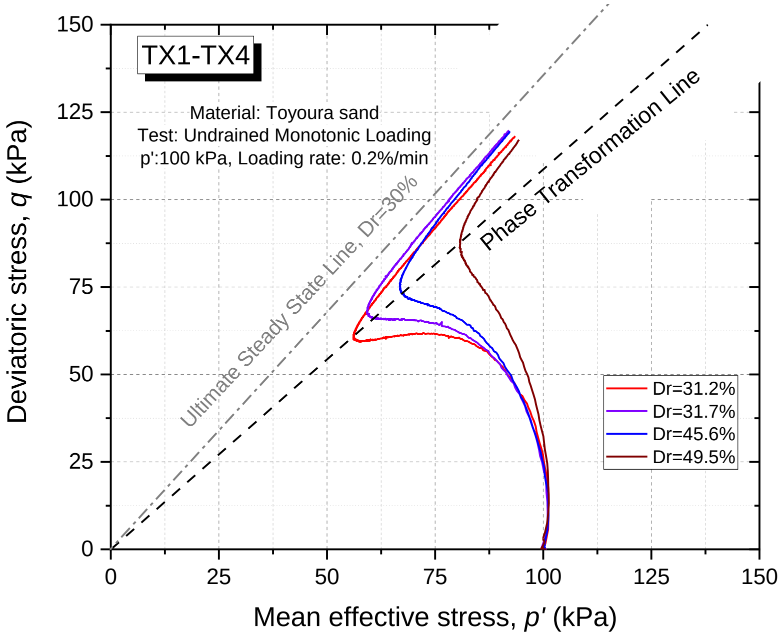

Figure 4-6 Ultimate Steady State Line and Phase Transformation Line at the lower-stress level in $q - p'$ plane

To clarify whether TX1-TX4 reaches the ultimate steady-state at the final state during the shearing process, these results were plotted with the previous studies by

Verdugo (1992; after Yoshimine, 1998) on *e*-*p*’ plane (Figure 4-7). From the starting point of the initial consolidated state at *p*’=100 kPa, under the undrained shearing condition, the effective stress condition moved toward the Phase Transformation Line. After reaching the phase transformation point, the behavior was changed in which the effective stress moved toward the Ultimate Steady-state Line.

The final states of TX1-TX2 are almost reaching the Ultimate Steady State Line (USSL) of Toyoura sand, inferring that the final state of TX1-TX2 might be classified as ultimate steady state. However, the final states of TX3-TX4 are still quite far from the USSL provided by this previous studies implying that the previous hypotheses is reasonable that the final state of TX3-TX4 was not representing the ultimate steady-state condition.

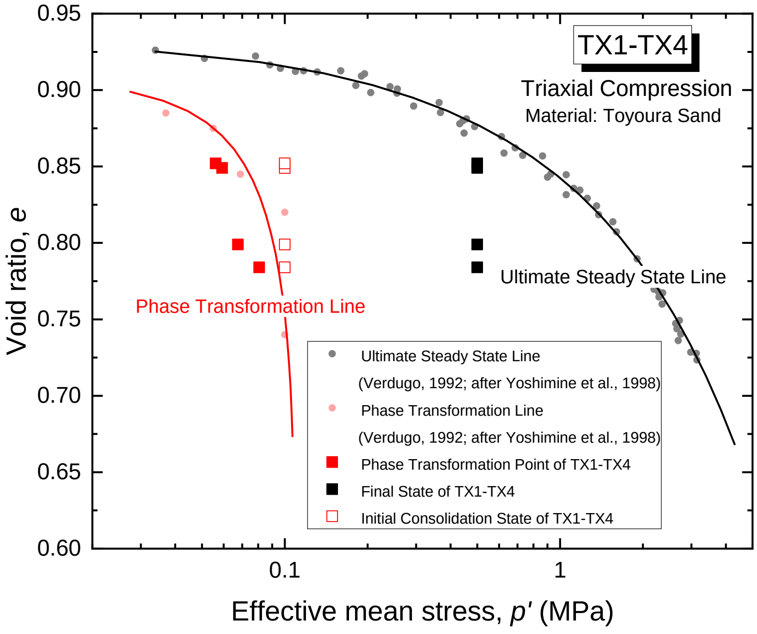

Figure 4-7 The *e*-*p*’ plane of TX1-TX4

In comparison, to identify the behavior of sand in drained shearing conditions, a drained monotonic loading test using Toyoura Sand has been conducted in Triaxial Apparatus. The rate of loading was set as much as 0.2%/min. The detail of the test is shown in Table 4-2.

Table 4-3 The list of Drained Monotonic Loading Test in Triaxial Apparatus using Toyoura sand

Code Test	Relative density, *Dr* at *p'*=100 kPa (%)	Void ratio, *e*	Mean effective stress, *p'* (kPa)
TX24 (DML)	70.2	0.699	100

Figure 4-35 shows the stress path of TX24 (DML) and the TX1-TX4 for the comparison. It is identified that the stress path of the Drained Monotonic Loading Test (TX24) happened at the path of 1:3 and could reach the maximum deviatoric stress, mentioned as peak strength, at q=345 kPa. After reaching the peak strength, the stress path is reverted back to the same stress-path with the reduction of q, signaling the failure occurs.

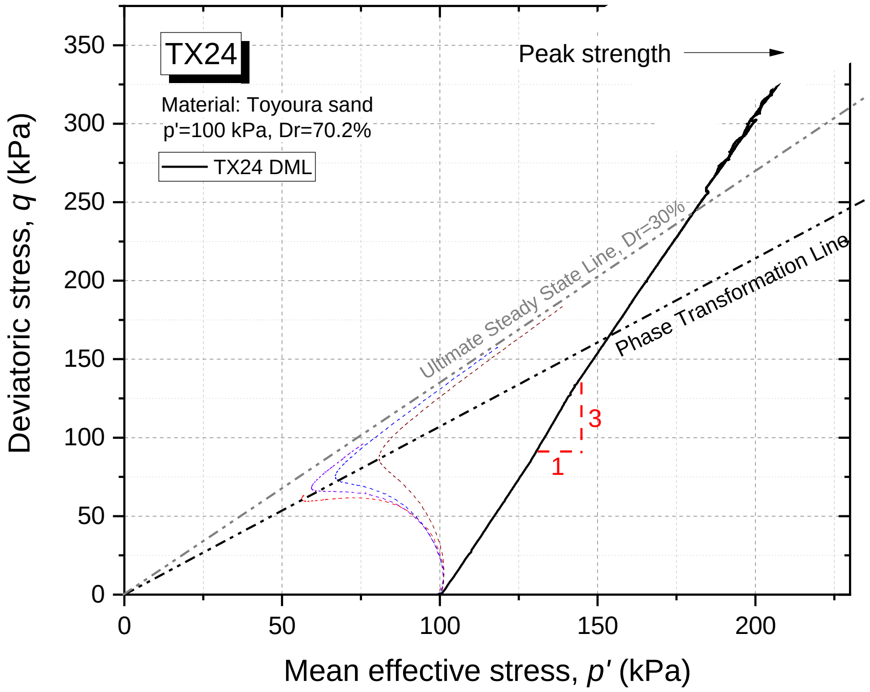

Figure 4-8 The stress path of TX24 in drained monotonic loading test

The stress-strain relationship of TX24 is shown in Figure 4-9 and Figure 4-10, for axial strain and maximum shear strain, respectively. The peak strength of this material happened at the axial strain of 7.5% and shear strain of 12%. The specimen dilated as much as 3% of volumetric strain at the peak strength. The reduction of q can be observed after the peak strength with the progression of deformation. However, the state in which the deformation happened at the constant volume is not observed in this study, even the axial strain reached 17%.

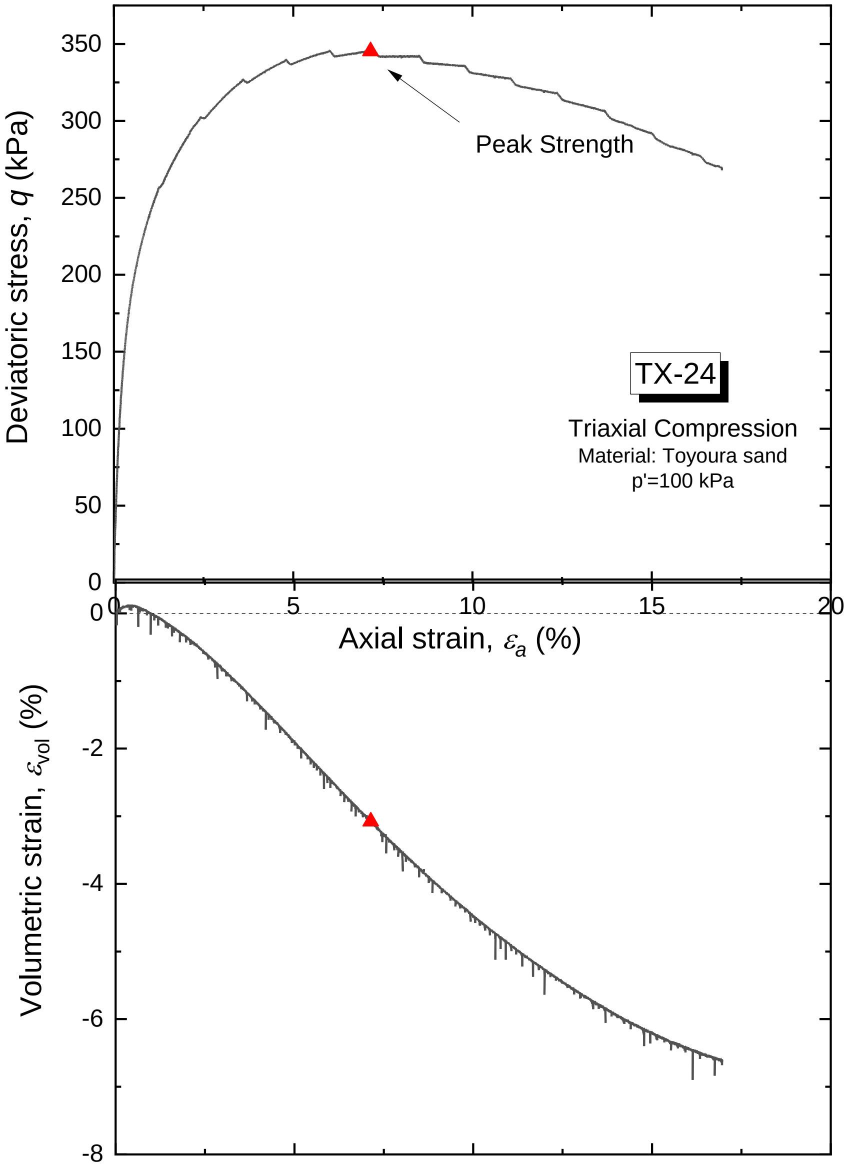

Figure 4-9 The relationship between deviatoric stress-volumetric strain and axial strain of TX24

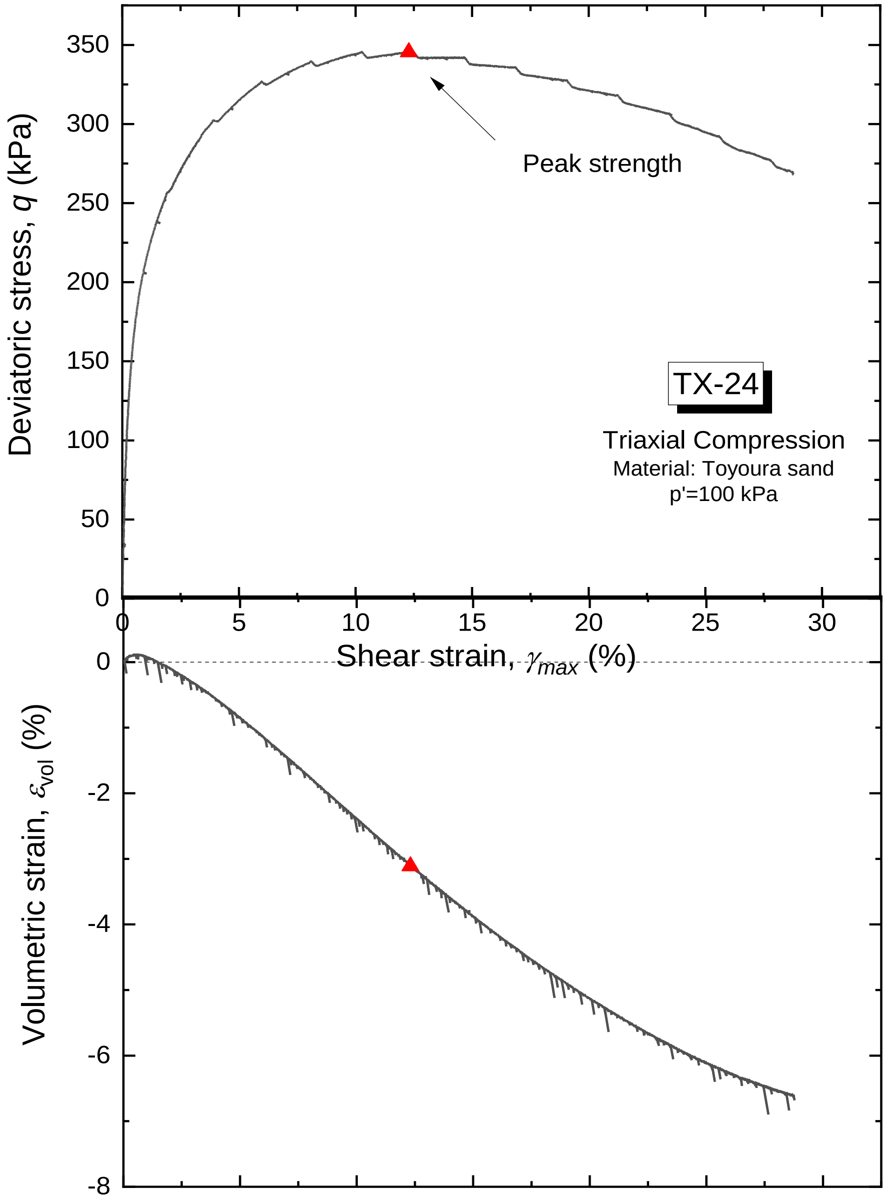

Figure 4-10 The relationship between deviatoric stress-volumetric strain and maximum shear strain of TX24

4.4. Failure characteristics of Sandy Soil under Constant Shear Stress Test

In this study, in order to produce the flow behavior on the sand specimen in the drained condition, a series of static liquefaction test with constant deviatoric stress was employed. The procedure of the test has been explained at the prior sub-chapter for Triaxial Apparatus. The typical stress path of static liquefaction test with constant deviatoric stress and its strain development is shown in Figure 4-11 until Figure 4-19, for loose specimen (TX-10), medium dense specimen (TX-17) and dense specimen (TX-6).

As shown in stress path curve for each tests, after the specimen was isotropically consolidated to the *p'*=100 kPa, the specimen was subjected to the monotonic drained loading to a certain static shear condition (deviatoric stress). This static shear condition represents the shear stress acting on the soil due to the inclination of the ground. After reaching certain deviatoric stress, the mean effective stress was reduced while maintaining the deviatoric stress constant until reaching the point in which the deformation of the specimen is developed largely and continuously without the reduction of mean effective stress or stress condition is constant. This point is defined as the “starting point of flow failure” in this study.

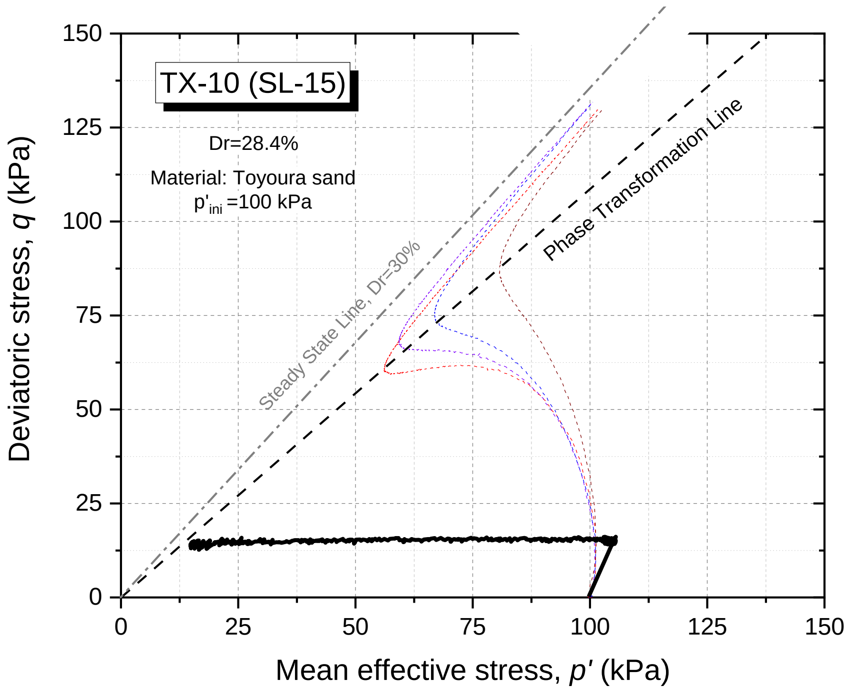

Figure 4-11 Stress path of static liquefaction test with constant deviatoric stress on loose sand (Dr=28.4%, *q*=15 kPa)

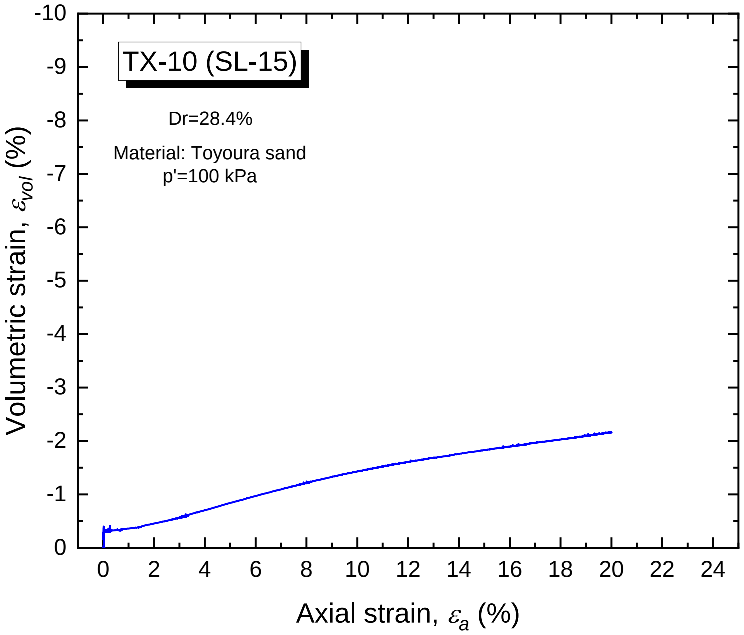

Figure 4-12 The relationship between volumetric strain and axial strain of static liquefaction test on loose sand (Dr=28.4%, *q*=15 kPa)

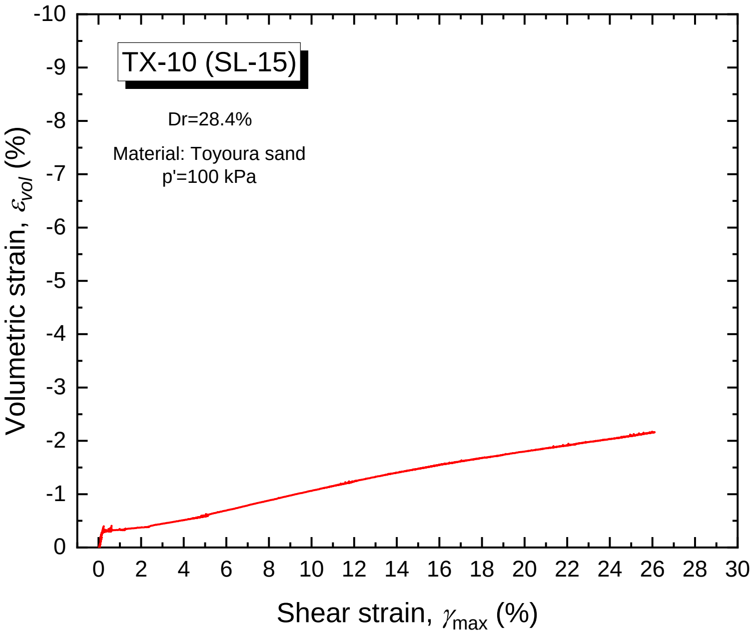

Figure 4-13 The relationship between volumetric strain and maximum shear strain of static liquefaction test on loose sand (Dr=28.4%, *q*=15 kPa)

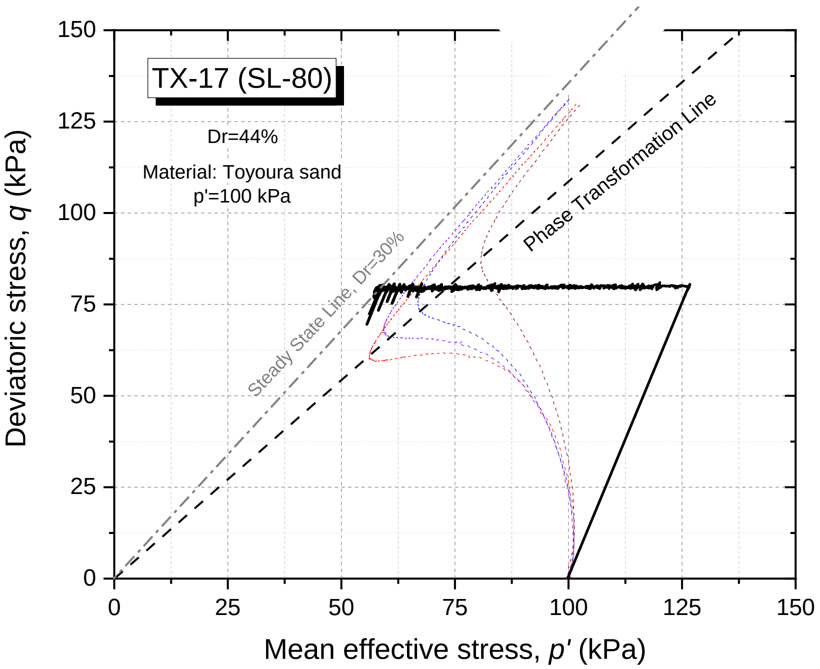

Figure 4-14 Stress path of static liquefaction test with constant deviatoric stress on medium dense sand (Dr=44%, *q*=80 kPa)

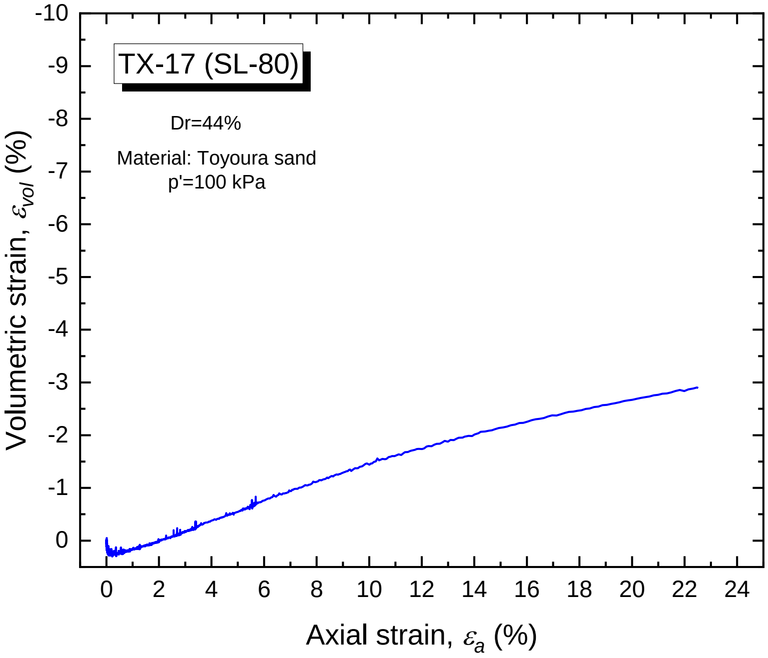

Figure 4-15 The relationship between volumetric strain and axial strain of static liquefaction test on medium dense sand (Dr=44%, *q*=80 kPa)

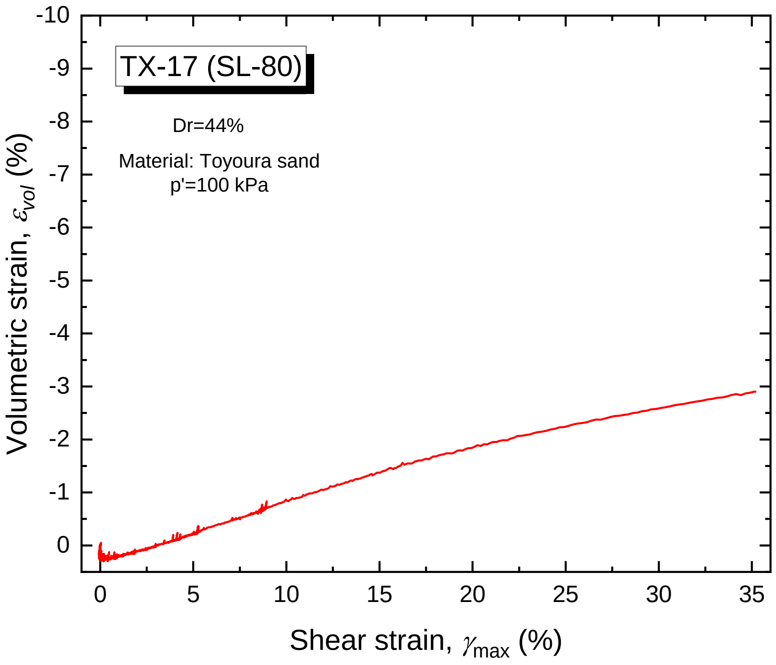

Figure 4-16 The relationship between volumetric strain and shear strain of static liquefaction test on medium dense sand (Dr=44%, q=80 kPa)

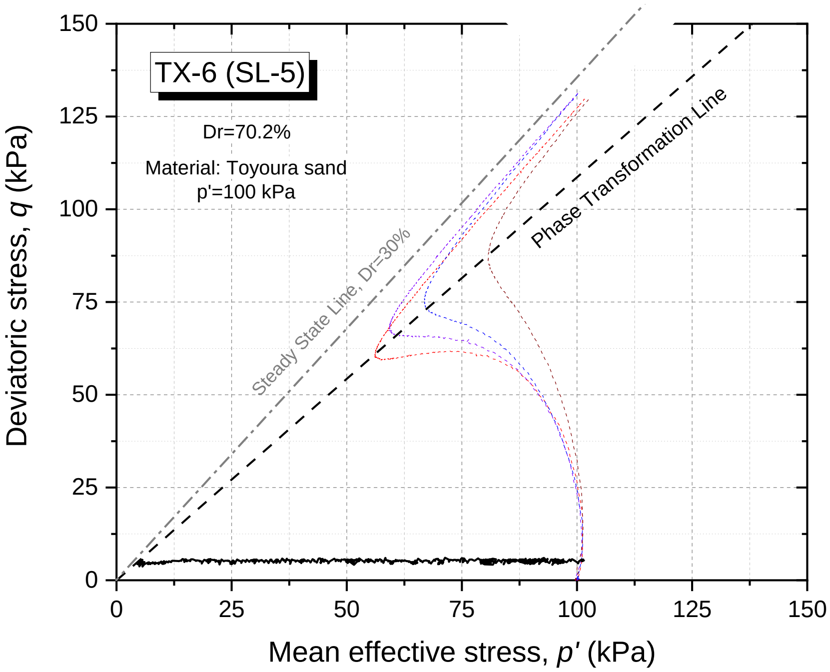

Figure 4-17 Stress path of static liquefaction test with constant deviatoric stress on dense sand (Dr=70.2%, q=5 kPa)

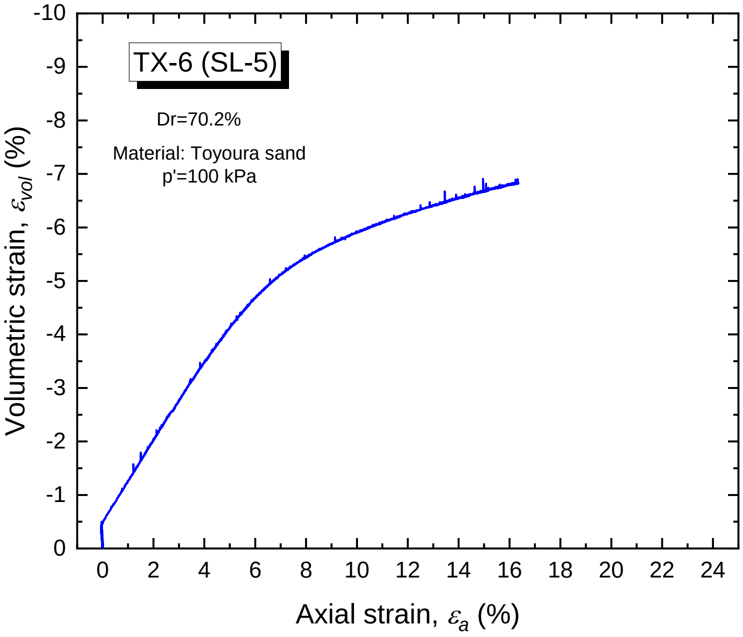

Figure 4-18 The relationship between volumetric strain and axial strain of static liquefaction test on loose sand (Dr=70.2%, *q*=5 kPa)

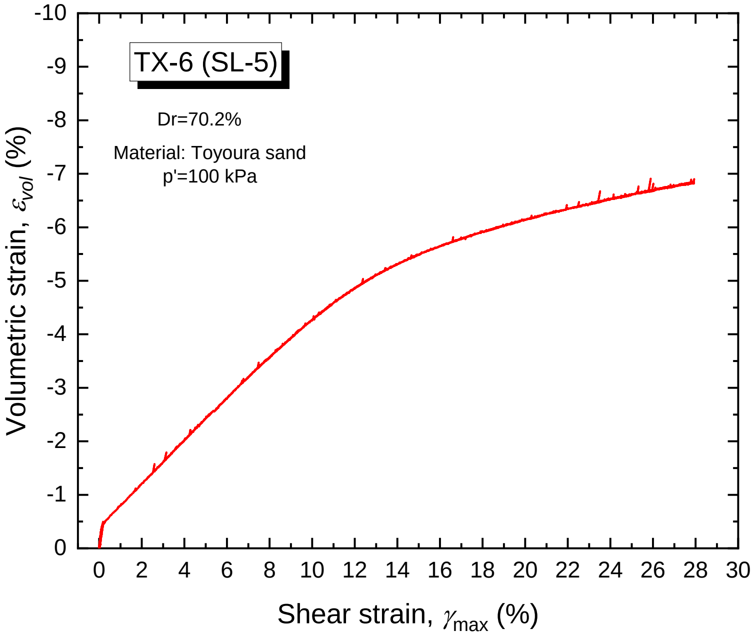

Figure 4-19 The relationship between volumetric strain and maximum shear strain of static liquefaction test on loose sand (Dr=70.2%, *q*=5 kPa)

For all the tests conducted, the behavior of flow could be observed at the point when the effective mean stress (*p'*) is reaching the phase transformation line (TX10 and TX6) for the low deviatoric stress level or ultimate steady state line (TX17) for the high deviatoric stress level. This reduction of mean effective stress (*p'*) while keeping the deviatoric stress (q) constant is, in principle, associated with the shearing process in this typical test. The starting point of flow behavior is defined as the point in which all the stresses, both mean effective stress (*p'*) and deviatoric stress (*q*), are constant (creep) but the strains (axial strain and volumetric strain) develop continuously. Irrespective of the initial density of the material, the strain development, representing the dilative behavior of specimen, can be classified into three areas: initial stage, limited flow, and continuous flow as in Figure 4-20 until Figure 4-22.

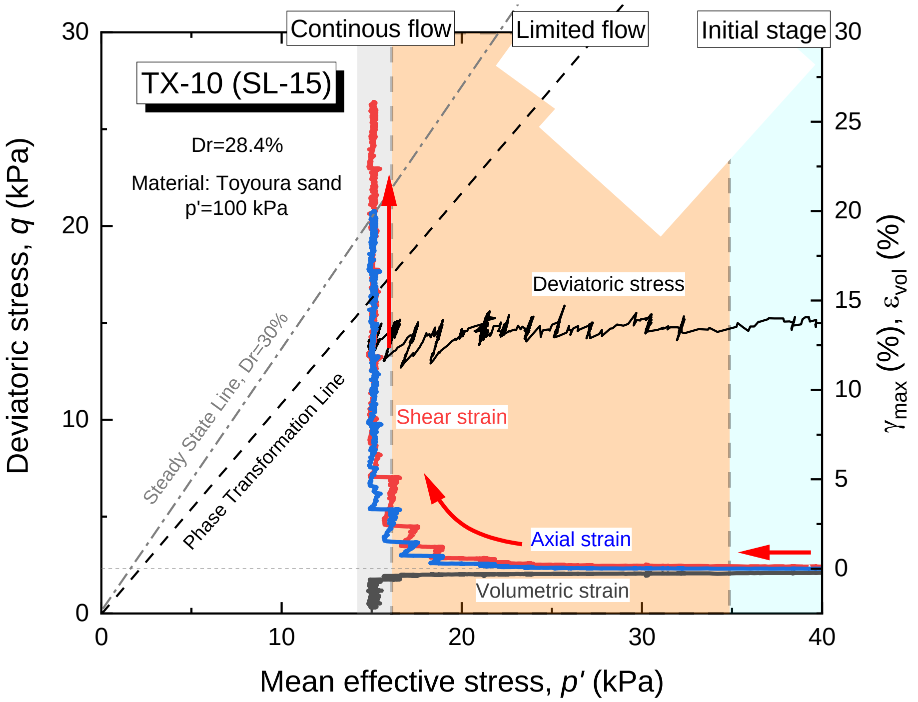

Figure 4-20 The enlargement part of stress path and classification strain development stages in p'-q plane on loose sand (Dr=28.4%, *q*=15 kPa)

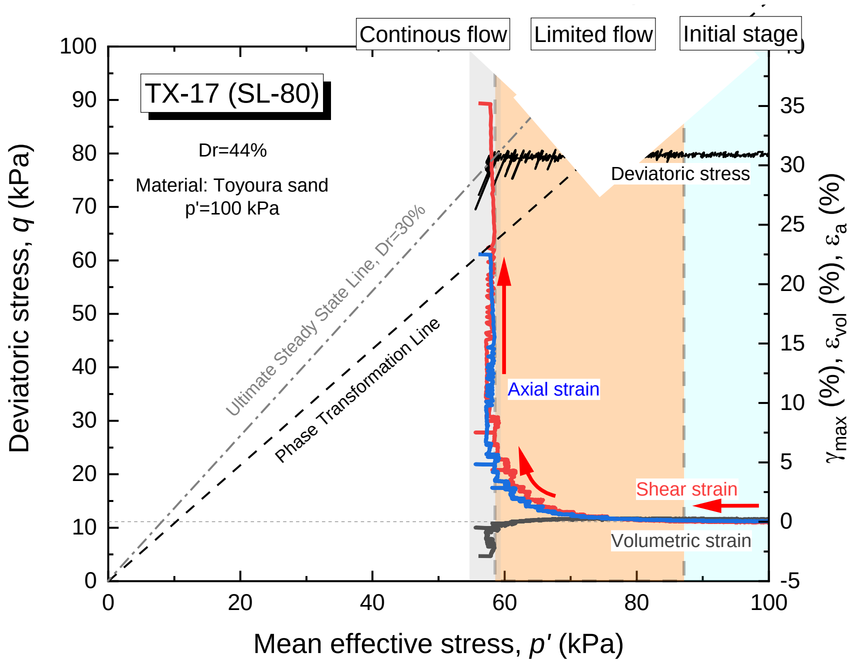

Figure 4-21 The enlargement part of stress path and classification strain development stages in p’-q plane on medium dense sand (Dr=44%, *q*=80 kPa)

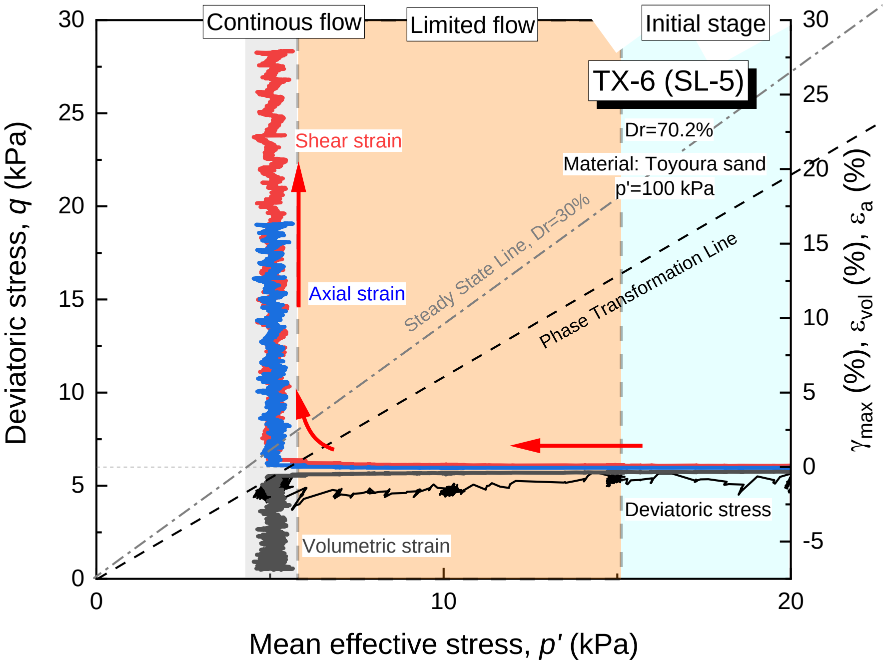

Figure 4-22 The enlargement part of stress path and classification strain development stages in p’-q plane on loose sand (Dr=70.2%, *q*=80 kPa)

4.4.1. The initial stage of strain development

The initial stage represents the condition when the axial strain is not developed yet during the preliminary reduction of mean effective stress (*p'*), which represents the shearing process on the specimen. In this stage, the reduction of mean effective stress induces the pore water pressure build-up. This build-up of pore water pressure will generate the development of volumetric strain in a recoverable state (less than 0.5%) which can be associated with the dilatancy of soil particles. The volumetric strain development of TX10 (q=15 kPa) and TX6 (q=5 kPa) at this stage is found to be dilative (negative volumetric strain). However, TX17 with the higher static shear stress (q=80 kPa), the volumetric strain development at this stage is preceded with the contractive behavior (positive volumetric strain). The initial static shear stress might affect the development of volumetric strain at the initial stage.

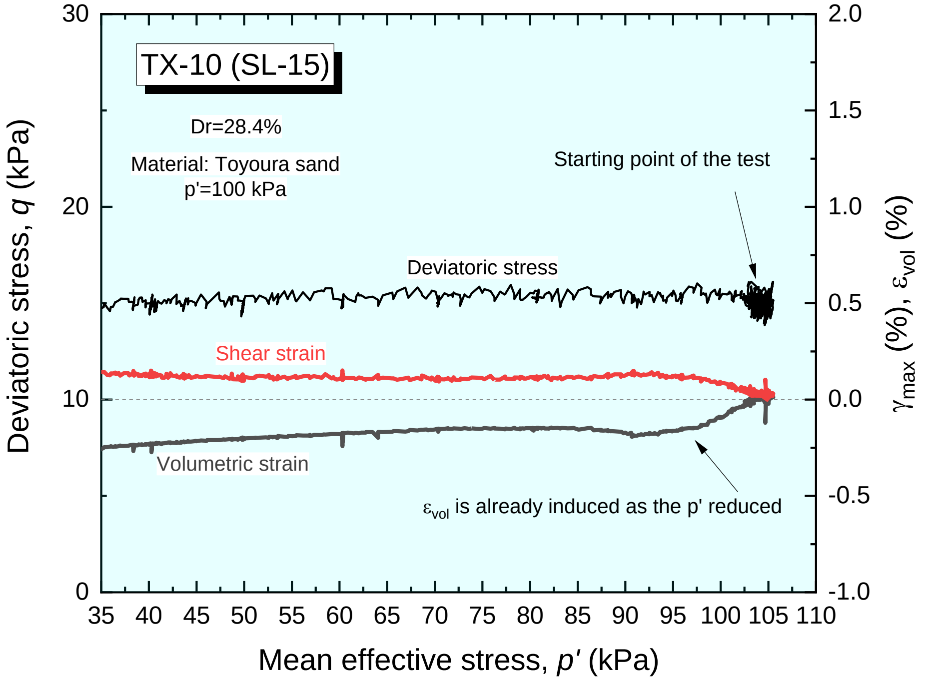

Figure 4-23 Strain development in the initial stage of loose specimen (Dr=28.4%, *q*=15 kPa)

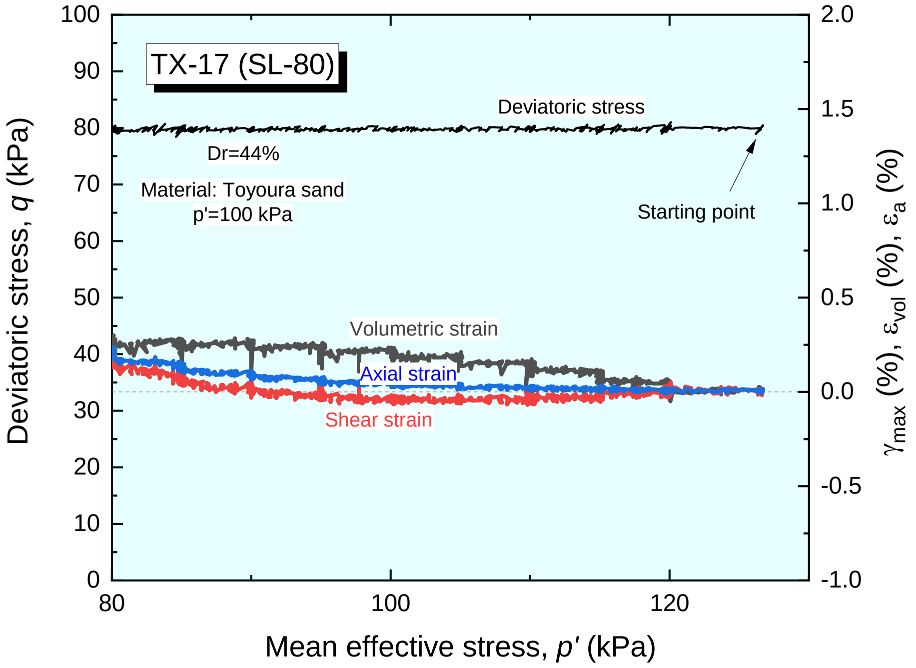

Figure 4-24 Strain development in the initial stage of the medium dense specimen (Dr=44%, *q*=80 kPa)

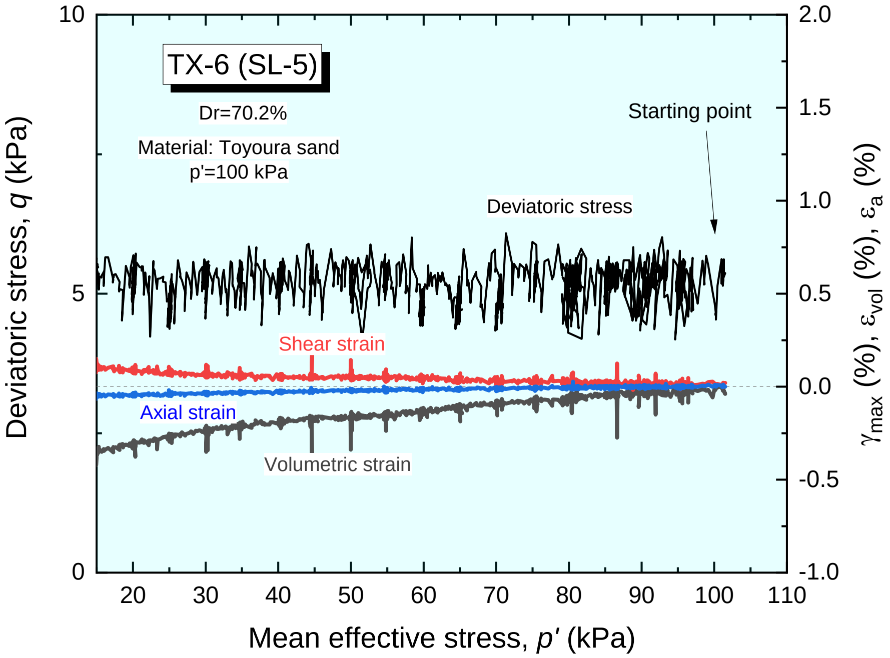

Figure 4-25 Strain development in the initial stage of the dense specimen (Dr=70.2%, *q*=5 kPa)

4.4.2. The limited flow stage

As the effective mean stress (p’) is kept reduced with a rate of 5 kPa/minute and creep about 3 minutes in between the reduction, the pore water pressure build-up will induce the generation of volumetric strain to the non-recoverable state. As a result, as the volumetric strain is developed, the axial strain is also generated. In this stage, the reduction of mean effective stress (*p’*) will induce both developments of volumetric strain and axial strain. Nevertheless, the development of both strains will be terminated as no shear applied to the specimen (creep time between the reduction of the mean effective stress). This explains that the development of strains in this stage is promoted by the shearing process and occurs in a limited way. It is interesting that the TX17 showed a turn-point from contractive to the dilative in this stage, while TX10 and TX5 keep showed dilative behavior since the beginning of the test.

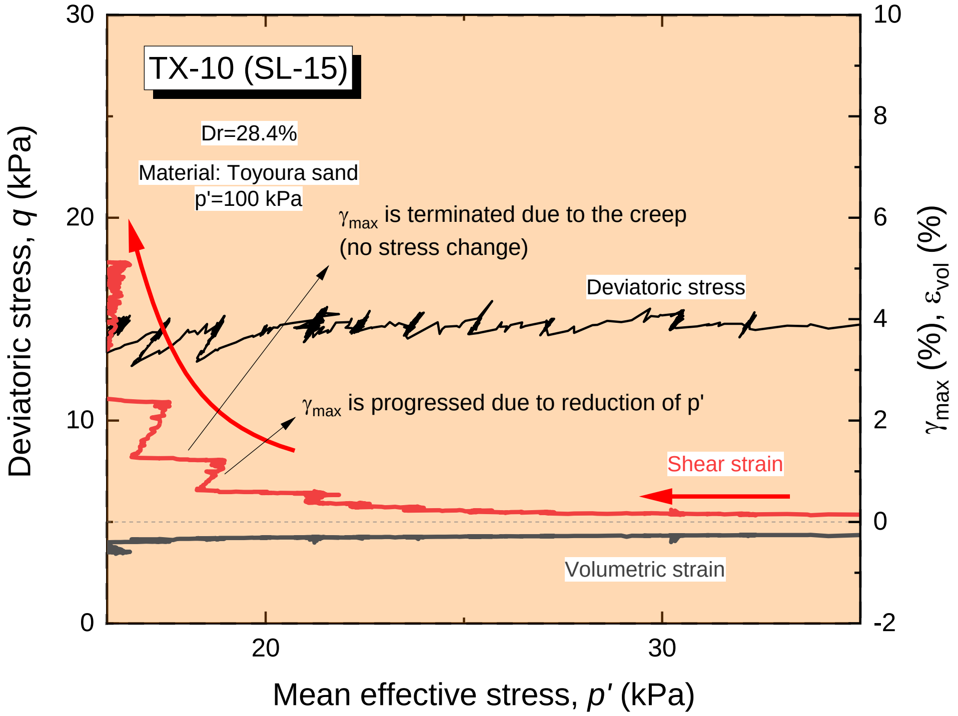

Figure 4-26 Strain development in the limited flow stage of the loose specimen (Dr=28.4%, *q*=15 kPa)

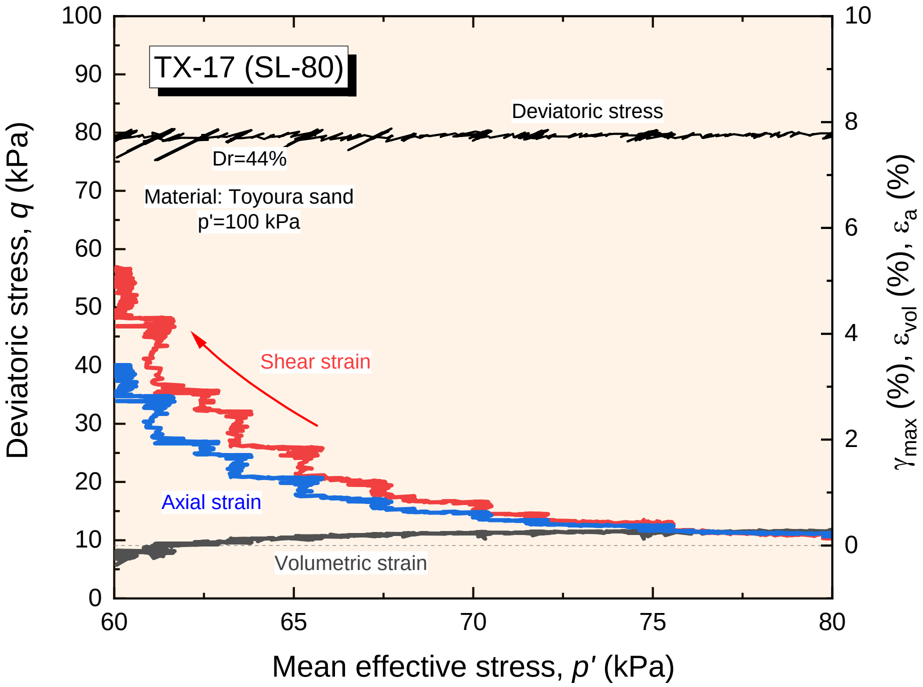

Figure 4-27 Strain development in the limited flow stage of the medium dense specimen (Dr=44%, *q*=80 kPa)

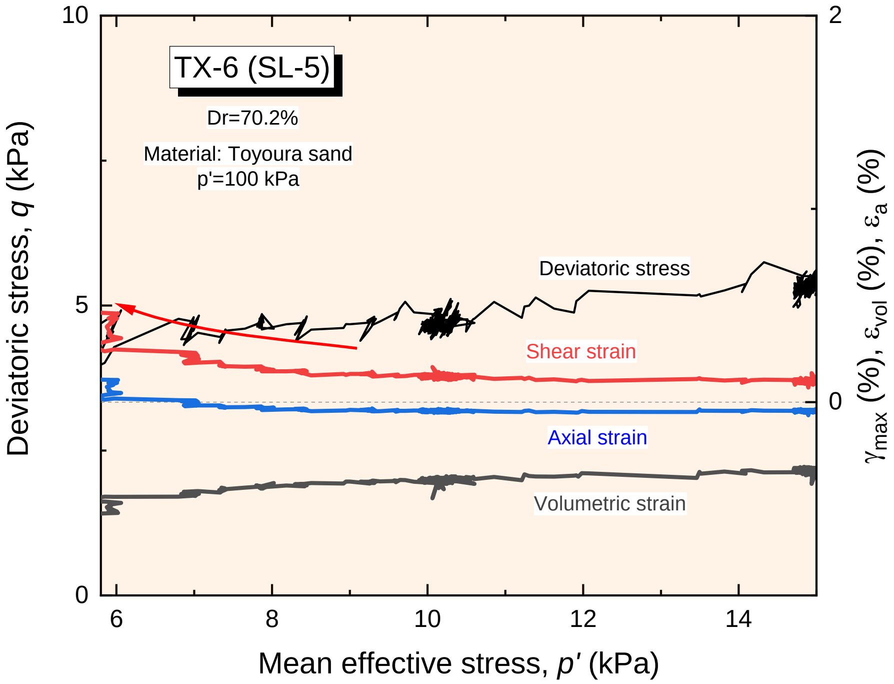

Figure 4-28 Strain development in the limited flow stage of the dense specimen (Dr=70.2%, *q*=5 kPa)

4.4.3. The continuous flow stage

When the effective mean stress (*p'*) approach the failure line, the development of strains become larger, showing the softening behavior in the specimen that leads to the flow behavior. At this stage, the reduction mean effective stress (*p'*) is terminated and all components of stresses are kept constant, including the deviatoric stress (*q*), mean effective stress (*p'*), and total mean stress (*p*). At this point, the development of the axial strain and volumetric strain can be observed during the creep of the stress (no stress change).

The point in which the strains keep developed while the stresses are controlled constantly identified as the starting point of flow failure. From this point, the dilation behavior, including the rate of the development of shear strain can be quantified.

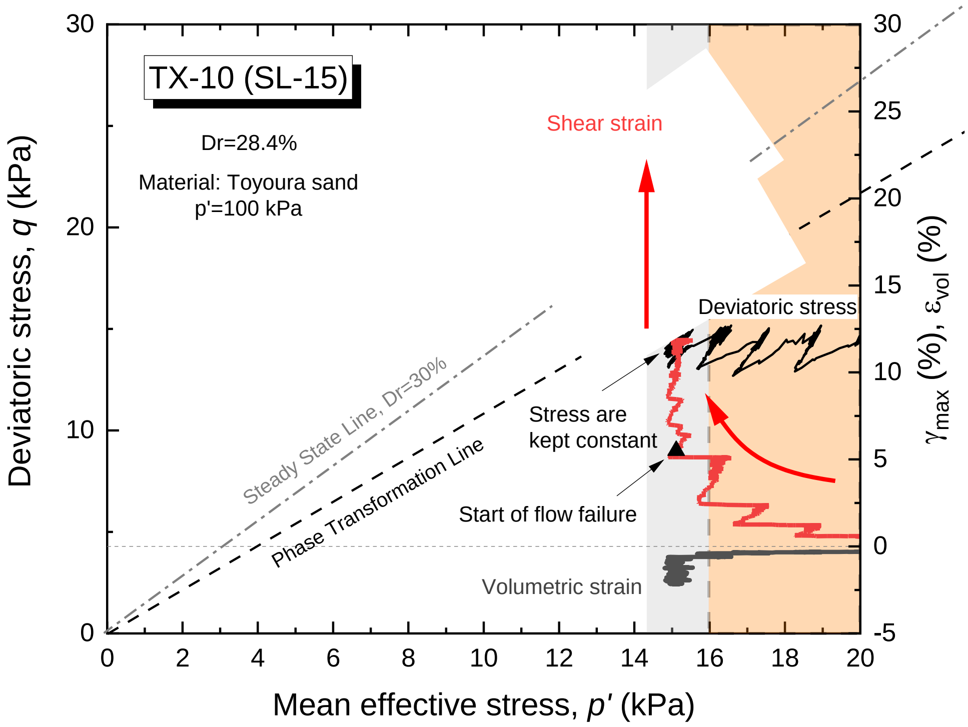

Figure 4-29 Continous flow stage of static liquefaction test on loose sand (Dr=28.4%, *q*=15 kPa)

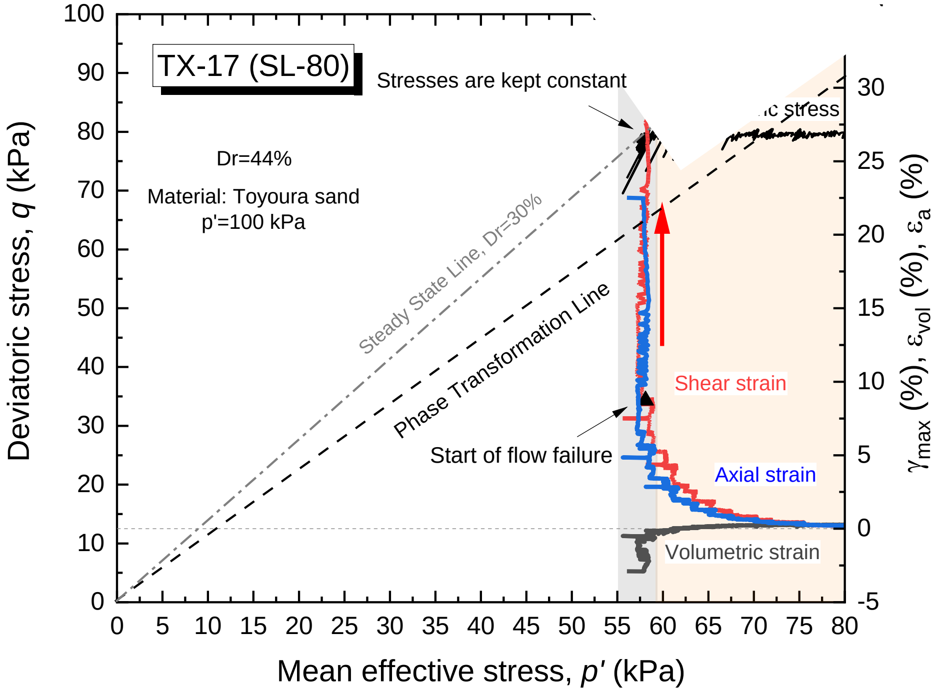

Figure 4-30 Continous flow stage of static liquefaction test on medium dense sand (Dr=44%, q=80 kPa)

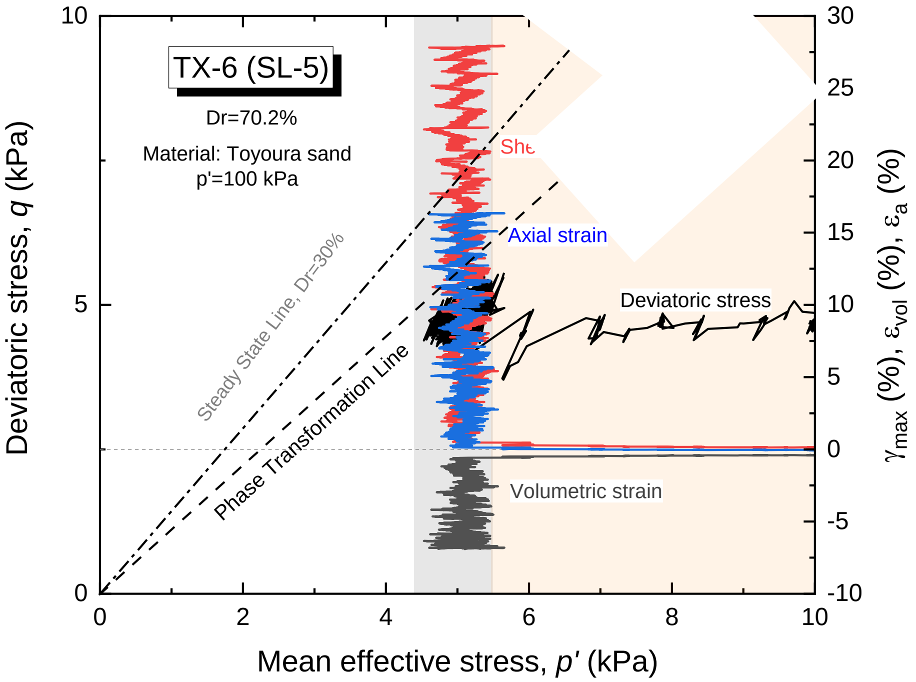

Figure 4-31 Continuous flow stage of static liquefaction test on dense sand (Dr=70.2%, q=5 kPa)

On the other side, Figure 4-32 shows the progression of both shear strain and volumetric strain in time elapsed. The measurement of shear strain rate is conducted when the strains develop large and continuous during the constant stress ratio by differentiating shear strain increment to the time. This shear strain rate value represents the condition of the preliminary move of the flow failure in which, at that condition, the inclination of the sloping ground does not change and the shear strain of the ground does not develop very large (shear strain less than 20%).

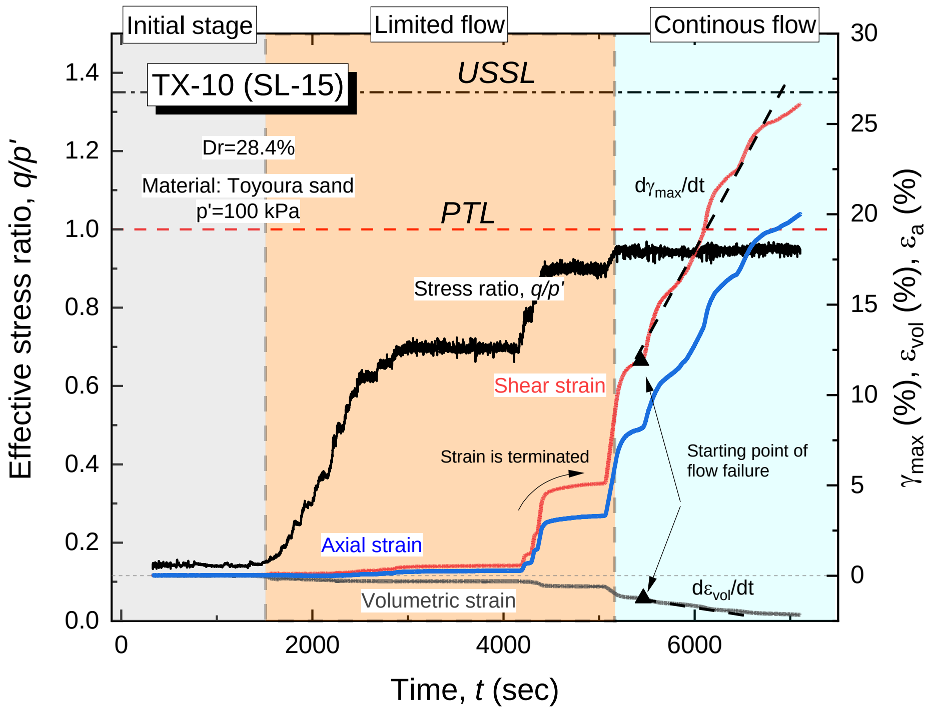

Figure 4-32 The strain development of loose sand (Dr=28.4%, *q*=15 kPa) in q/p'-time plane

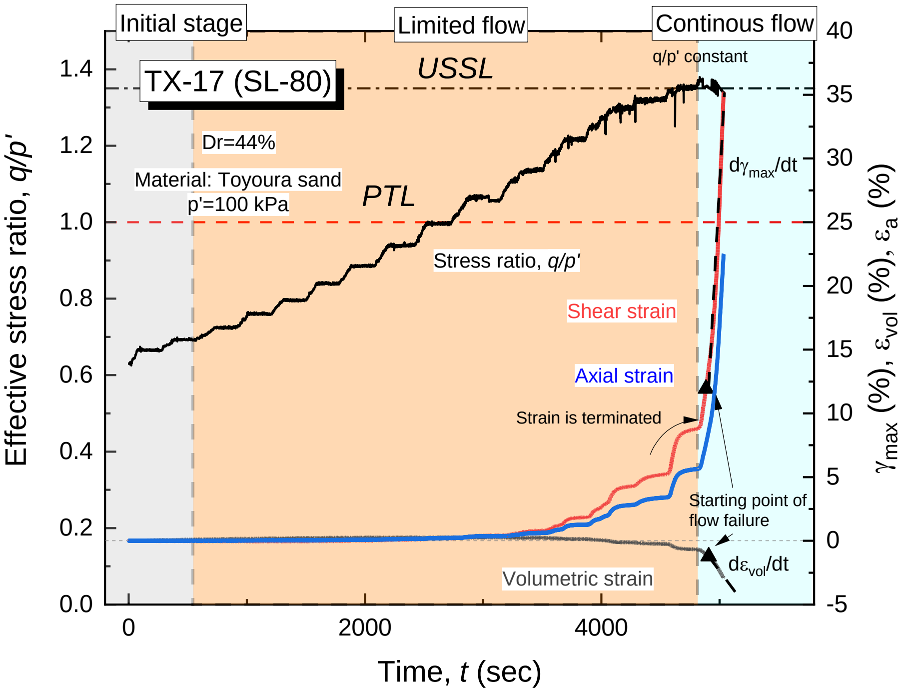

Figure 4-33 The strain development of dense sand (Dr=44%, *q*=80 kPa) in q/p'-time plane

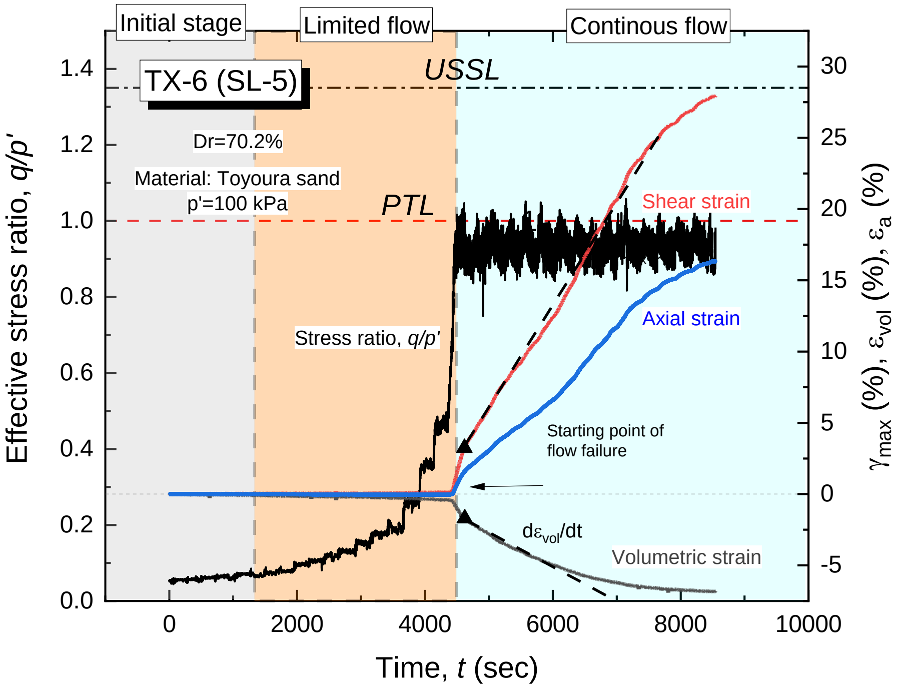

Figure 4-34 The strain development of dense sand (Dr=70.2%, *q*=5 kPa) in q/p'-time plane

4.4.4. Comparison between Static Liquefaction Test with Drained Monotonic Loading Test

A comparison between the results of the static liquefaction test and the drained monotonic test is presented in this study by using Triaxial Apparatus. Both testings are having the same condition; drained tests. Three specimens having the same relative densities (Dr=70%-72%) and the same p'_{ini}=100 kPa are subjected to different loading conditions. TX6 (SL-5) is subjected to a static liquefaction test with q=5 kPa, TX8 (SL=10) is also undergo a static liquefaction test with q=10 kPa, and TX24 is subjected to drained monotonic loading test with the loading rate of 0.2%/min. The stress path loading of these tests is shown in Figure 4-35.

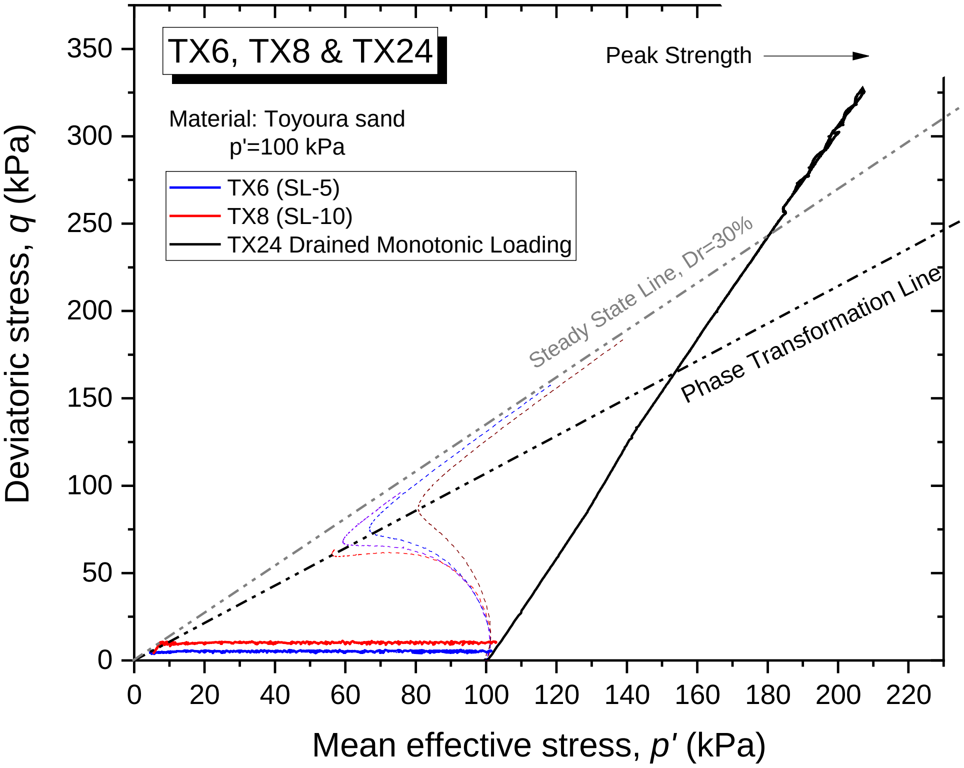

Figure 4-35 The stress path loading of static liquefaction test and drained monotonic loading test

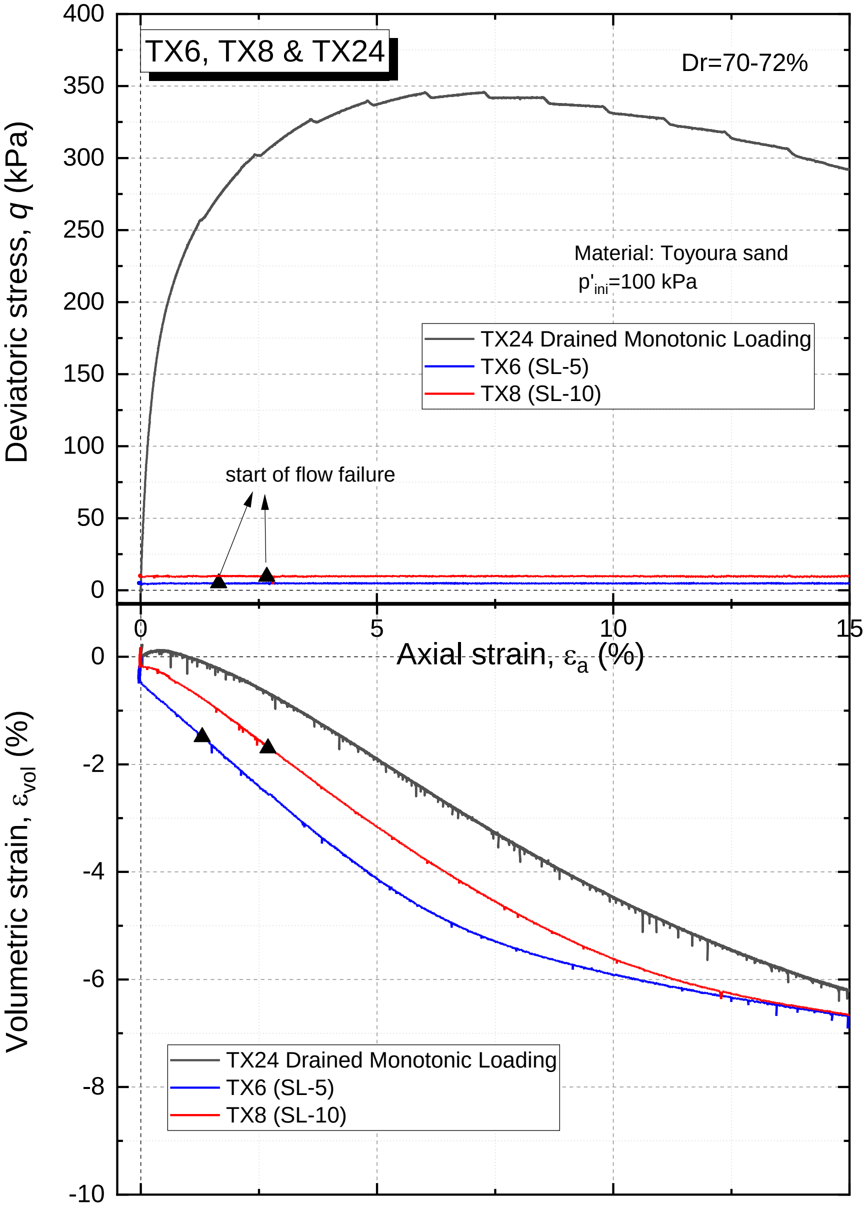

Figure 4-36 The deviatoric stress- axial strain relationship of testing TX6, TX8, and TX24

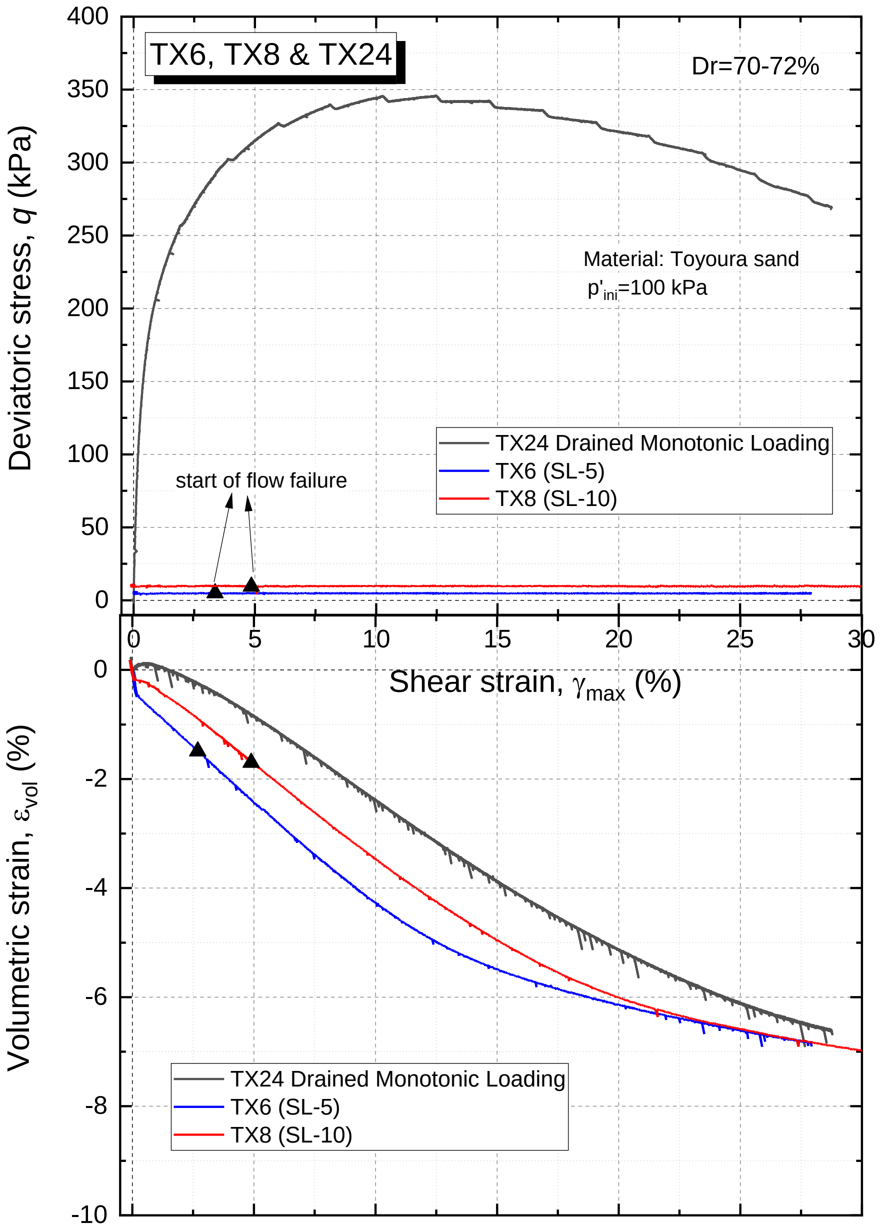

Figure 4-37 The deviatoric stress – shear strain relationship of testing TX6, TX8, and TX24

The comparison of the stress-strain relationship of the three tests is presented in Figure 4-36 and Figure 4-37. TX6 and TX8 are loaded with constant deviatoric stresses, 5 kPa, and 10 kPa, respectively until the end of the test. The start of flow failure points from both tests occurs at the axial strain around 2-3% of axial strain. On the other hand, TX24 is subjected to monotonic drained loading, with the maximum q is 320 kPa, at the axial strain is 5%.The dilatancy characteristics of both tests; static liquefaction test and drained monotonic loading test are represented in Figure 4-38. It shows that the dilatancy characteristics resulted from the static liquefaction test (TX6 and TX8) are different from the drained monotonic test (TX24).

At the beginning of the test, TX6 and TX8 show dilative behavior. As the mean effective stress is reduced, both TX6 and TX8 move toward the contractive behavior, even though there is a turning point that the specimen shows a sudden change from contractive to dilative behavior afterward. The dilative behavior continues until the specimen reaches the flow failure state. On the other side, TX24 shows a different trend. The contractive behavior is already started since the beginning of the test until it reaches the peak at the dilation part. The effective stress ratio will show a turning point after reaching the peak at the dilation part.

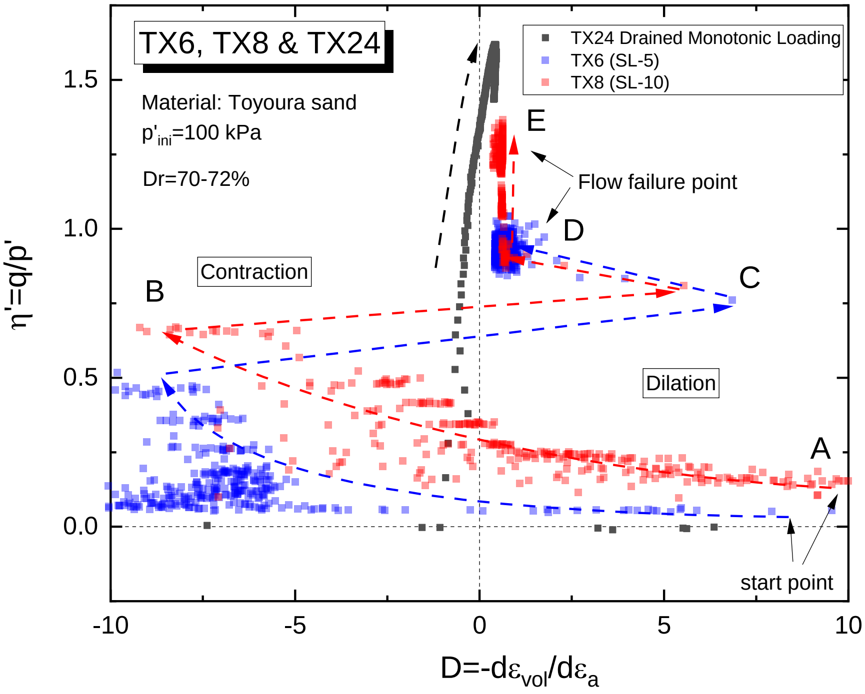

Figure 4-38 The dilatancy characteristics of static liquefaction test and drained monotonic test

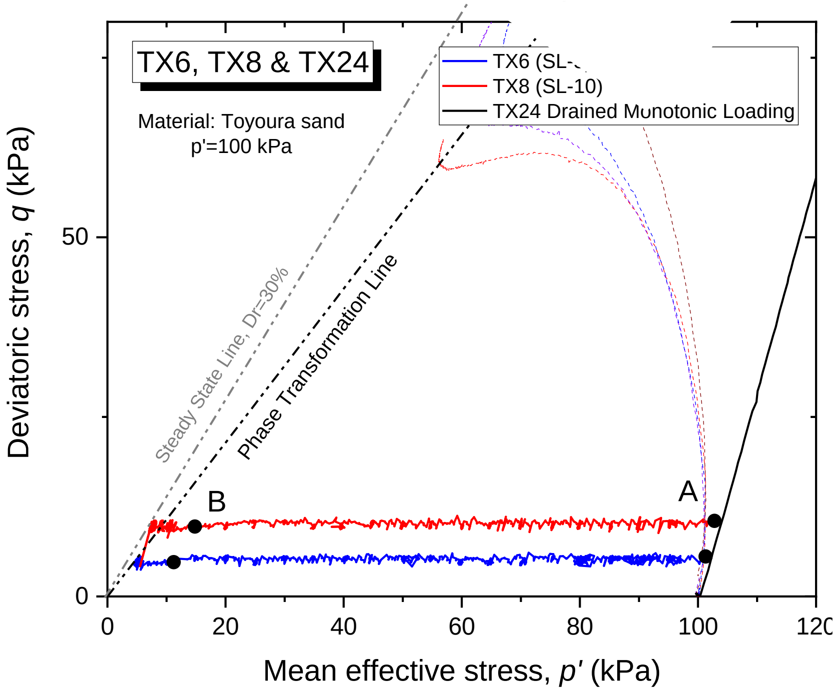

Figure 4-39 The location of Points A and B in stress-path

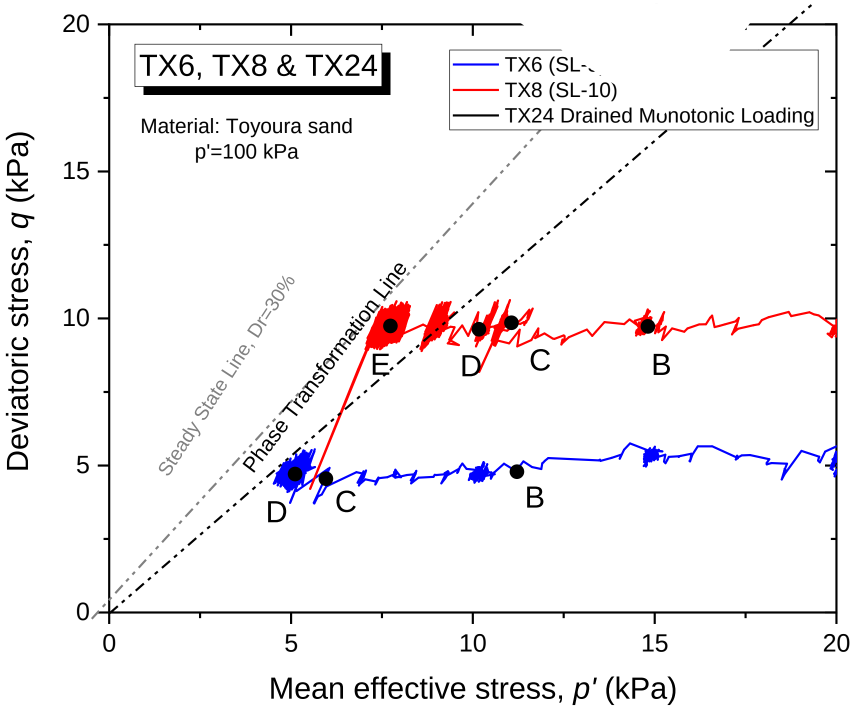

Figure 4-40 The location of Point C, D, and E in the stress-path

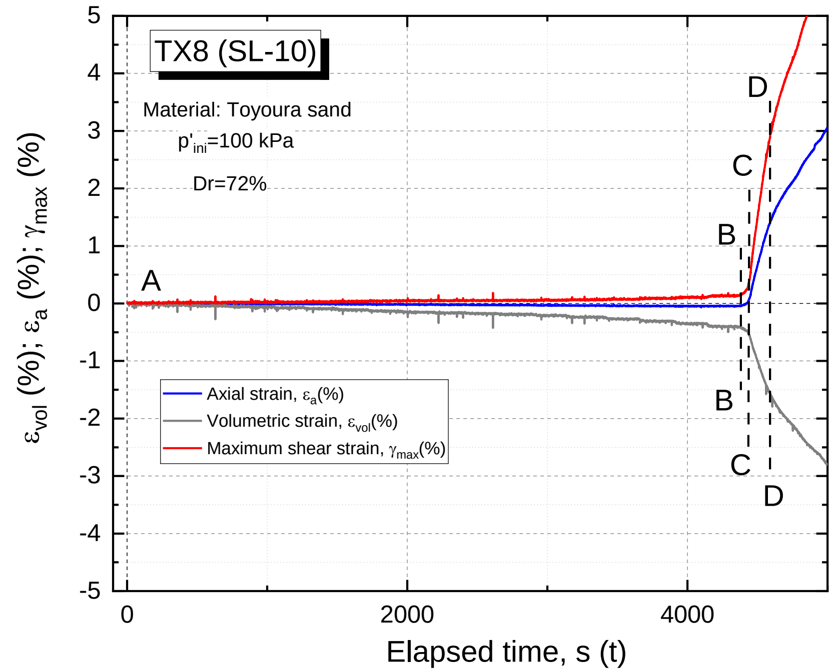

Figure 4-41 The location of Points A, B, C, and D in the strain-time plane of TX8

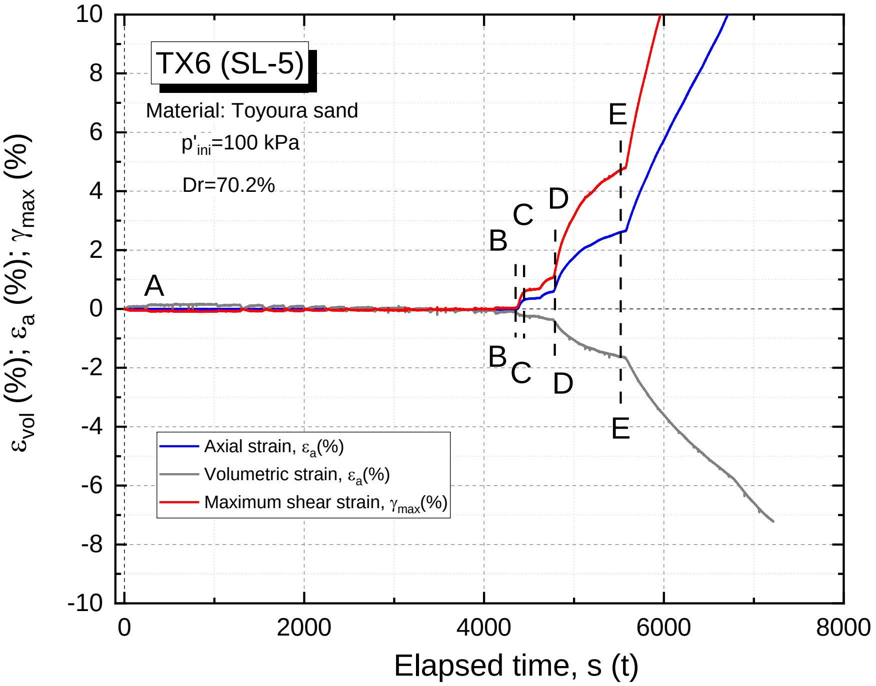

Figure 4-42 The location of Points A, B, C, and D in the strain-time plane of TX6

The different trend is shown in Figure 4-43 compared to the Figure 4-38. By drawing the dilatancy behavior using shear strain, instead of using axial strain, the clear turning point behavior of dilative (A point), contractive (B point), dilative (C point) behavior that previously appeared in the Figure 4-38 could not be observed in Figure 4-43. It is assumed that the previous dilatancy behavior are the part of scattered behavior at the low dilatancy rates. Instead, it can be observed that TX6 and TX8 are showing clear dilative behavior and continue until reaching failure while TX24 showing the conversely manner, from contractive to dilative. However, at the end, all the specimens showed dilative behavior. Figure 4-44 enlarged the characteristics of dilatancy at the failure part.

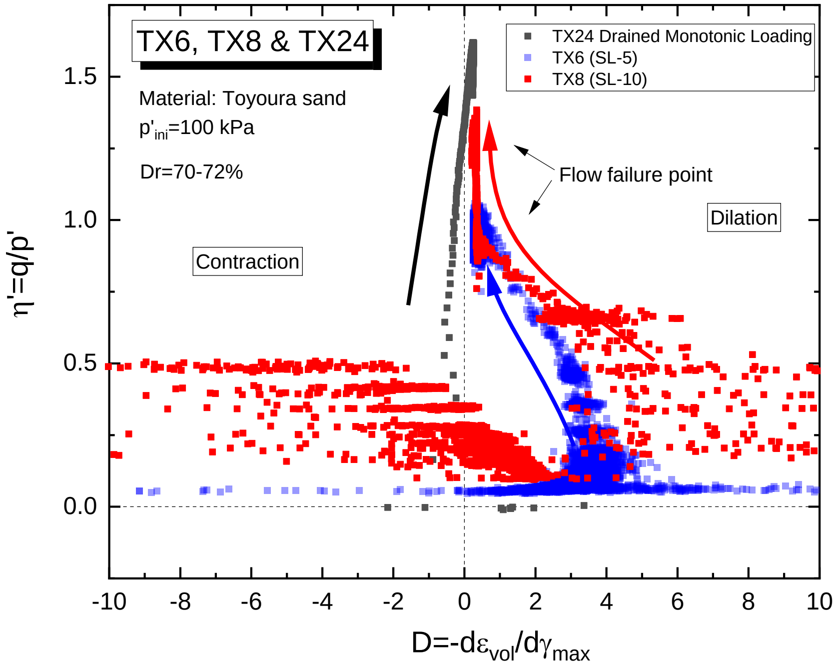

Figure 4-43 The dilatancy characteristics of static liquefaction test and drained monotonic test

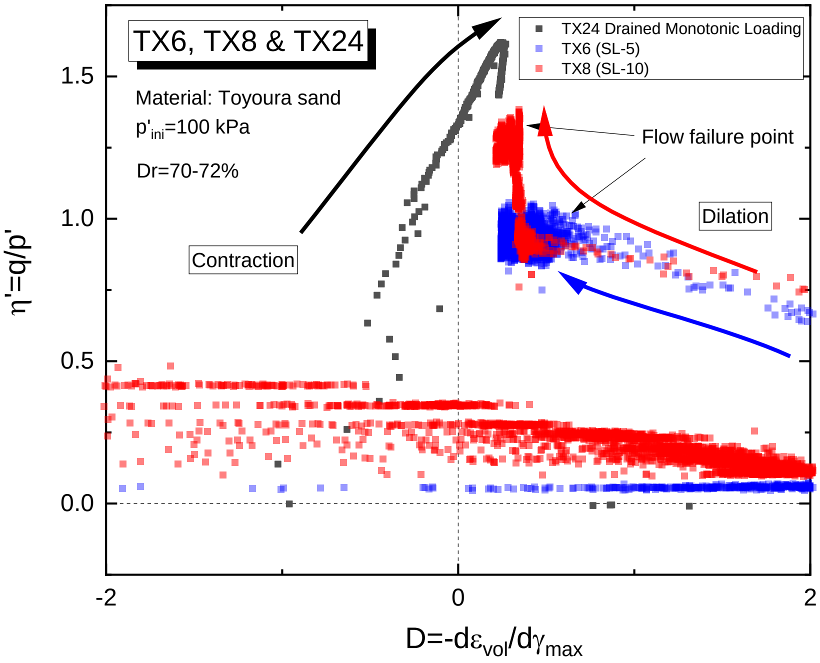

Figure 4-44 The dilatancy characteristics of static liquefaction test and drained monotonic test

It can be inferred that the tendencies of volumetric strain development during the tests are same. The TX24 shows clear contractive behavior as theoretically validated for the dense materials while TX6 and TX8 do not show the contractive behavior clearly, instead they show the dilative behavior due to the injection of pore water pressure since the beginning of the tests.

4.5. Dilation Behavior of Sand in Static Liquefaction with Constant Deviatoric Stress

As seen in the sub-chapter 0, the flow failure, representing the dilative behavior of sand, is promoted by the development of volumetric strain. To understand the dilative behavior of sand in this typical test, comprehensively, series of tests have been conducted in various initial static shear stress and initial density to examine the effect of both variables.

4.5.1. Effect of initial static shear stress to the dilation behavior of sand

As mentioned before, the soil element in the sloping ground is subjected to initial static shear stress. In this study, the effect of initial static shear stress on the flow behavior under constant static shear is examined. Verdugo and Ishihara (1996) drew a good correlation between the specimen void ratios and the effective mean stress at the large deformation, which corresponds to the steady-state points in the undrained monotonic test using Toyoura sand.

The stress-path of static liquefaction test for initial relative density around 30% with various shear static stress is shown in Figure 4-45. From the beginning of the test, the deviatoric stress is controlled constant during the reduction of mean effective stress. TX14 and TX15 show the instability of deviatoric stress value when reaching the failure line. This condition represents the state where the shear strain and volumetric strain is developed.

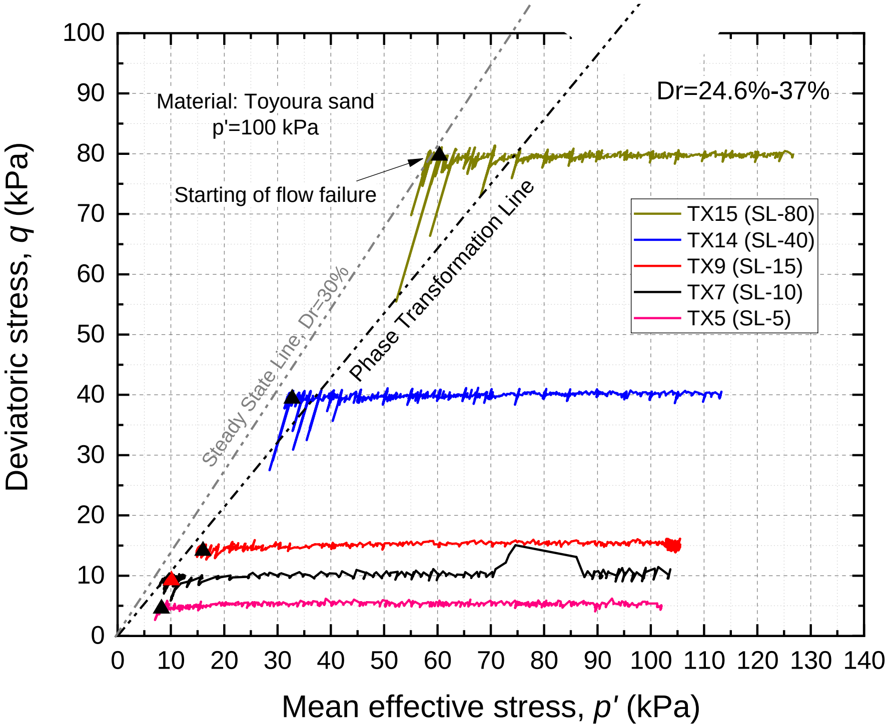

Figure 4-45 Stress path of static liquefaction test with constant deviatoric stress with various static stress

In this study, using Toyoura sand, all the specimens dilate toward the steady-state line regardless of the initial static shear stress acting on the specimen, as mentioned in Figure 4-46.

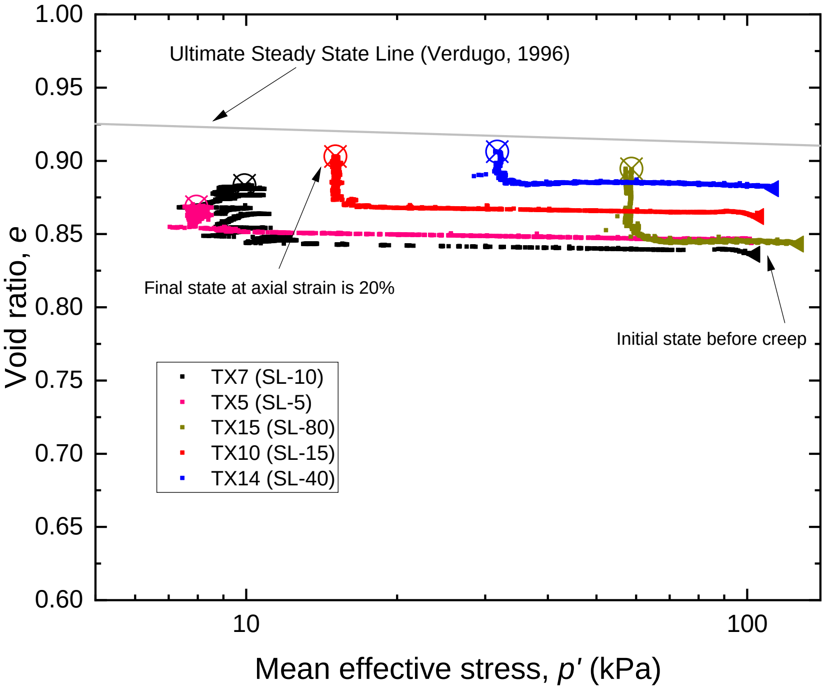

Figure 4-46 Dilation behavior with different static shear stress in log p'-e plane

To understand the effect of static shear stress to the volumetric strain development of sandy specimen, Figure 4-47 shows the comparison between the results of TX10 and TX15. When the axial strain is equal to 20%, TX-10 (SL-15) having the q=15 kPa and Dr_{ini}=28.4% can dilate up to ε_{vol}=-2.17% while TX-15 (SL-80) undergoes q=80 kPa and Dr_{ini}=33.8% dilate up to ε_{vol}=-2.75%. The difference between both specimens is varied to $\Delta\varepsilon_{vol}$=-0.58% which is quite small. Thus, it can be inferred that the effect of different static shear stress on the dilate behavior, represented by the volumetric strain development, is not significant.

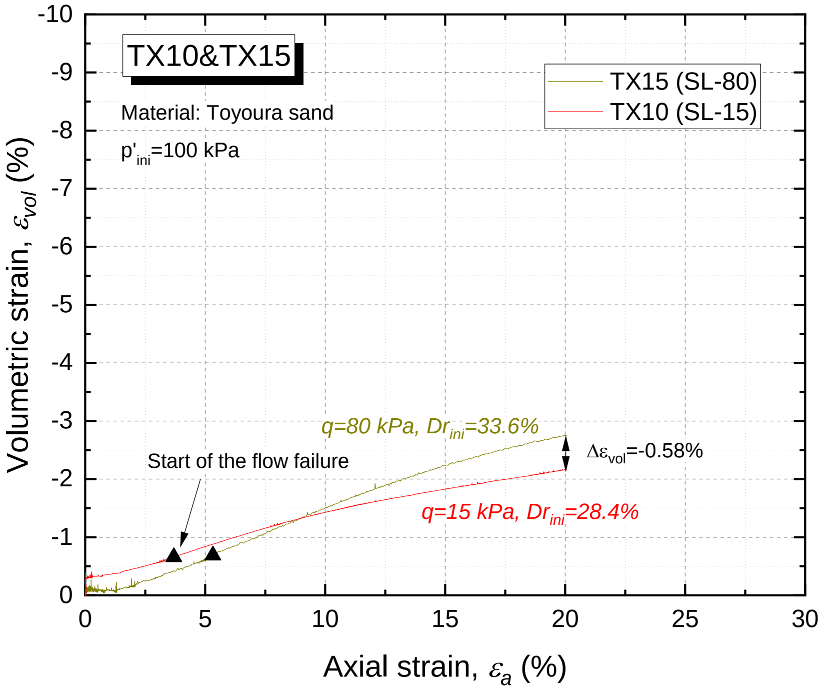

Figure 4-47 Relationship of volumetric strain and axial strain of TX10 and TX15

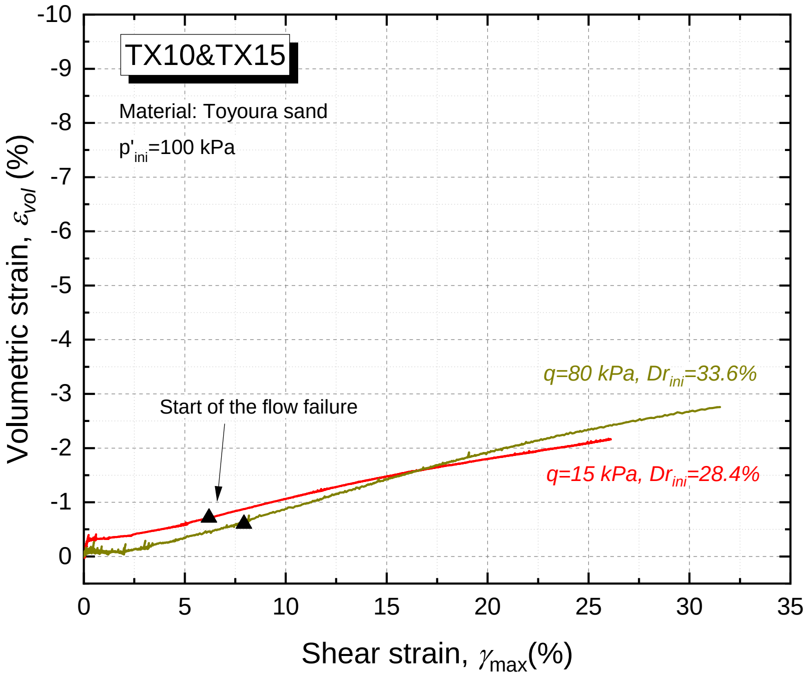

Figure 4-48 Relationship of volumetric strain and shear strain of TX10 and TX15

4.5.2. Effect of initial density to the dilation behavior

Experiment using Toyoura sand also proved that even the specimen prepared in the different initial density, all the materials will dilate toward the steady-state line. In general, at the low confinement stress, dense granular soils exhibit a dilative response when subjected to shear loading conditions (Lambe & Whitman, 1969). The dense materials will travel longer to the steady-state line than the loose materials in the log p'-e plane. This inferred that the dense material will be more dilative as the volumetric strain will be developed more. In this saturated condition, the dilation-induced increase in volume is accommodated due to the migration of fluid into the created additional pore-space.

Following the results from Figure 4-50, TX13 (SL-15) with q=15 kPa and Dr_{ini}=63.1% dilate up to ε_{vol} =-9.22% at the ε_a =20% while the TX10 (SL-15) with q=15 kPa and Dr_{ini}=28.4% dilate up to ε_{vol}=-2.17% at the same axial strain level. This volumetric strain difference is comparatively large compared to the previous comparison, considering the effect of static shear stress. The strain development of each experiment conducted in the Triaxial apparatus is presented in Figure 4-52.

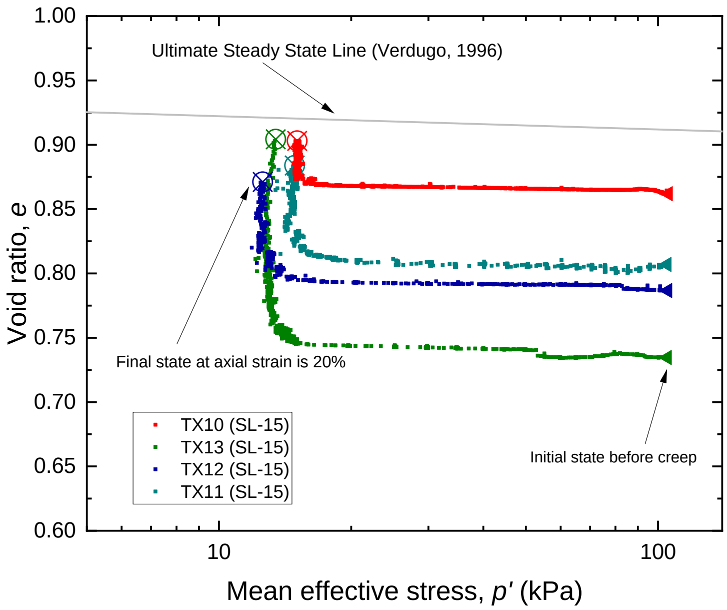

Figure 4-49 Dilation behavior with different initial density in log p'-e plane

In addition, Figure 4-50 also shows the different states of volumetric strain between TX10 and TX13 at the start of the flow failure point. It is clear that TX13 absorbs more water to produce flow failure compared to the TX10. From this point, it can be concluded that dense specimens require more volume of water to flow, compared to the loose specimen.

Figure 4-52 clearly shows that even the specimen is subjected to the different deviatoric stresses (5 kPa to 80 kPa), the development of volumetric strain behavior among the specimens with the same initial densities (Dr_{ini}=24.6%-37%) only ranging from 1-1,5%. Conversely, the initial density of the material mainly promotes the development of dilation behavior. The same results are also proved by Yoshimine (2006).

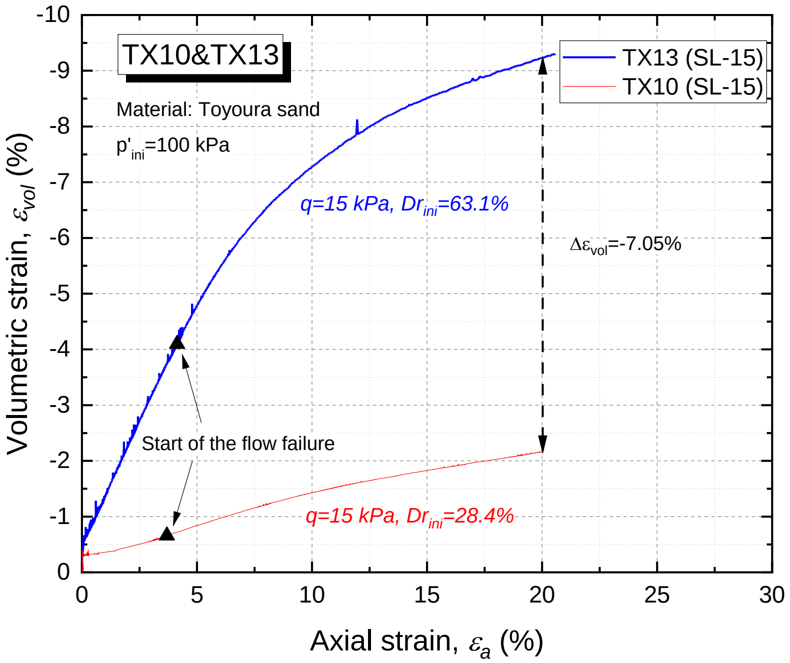

Figure 4-50 Relationship of volumetric strain and axial strain of TX10 and TX13

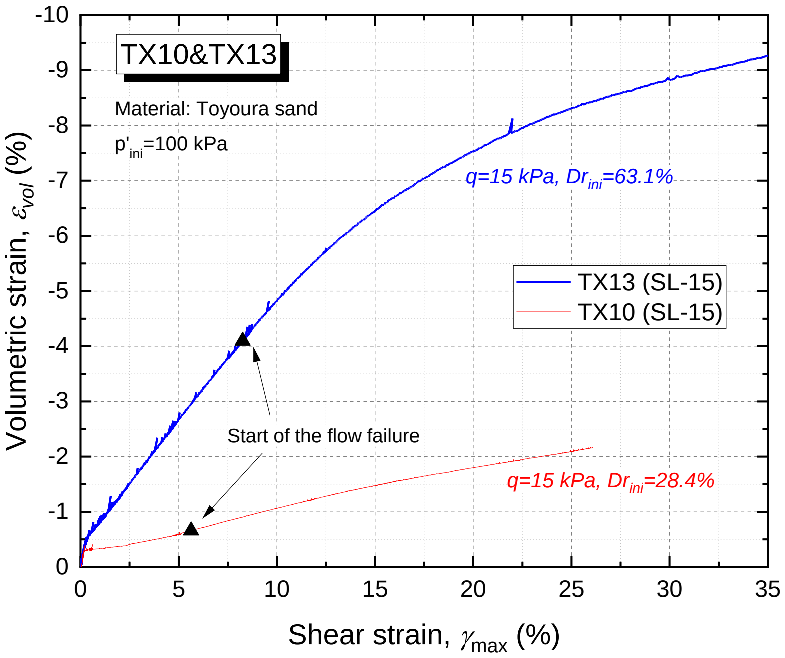

Figure 4-51 Relationship of volumetric strain and shear strain of TX10 and TX13

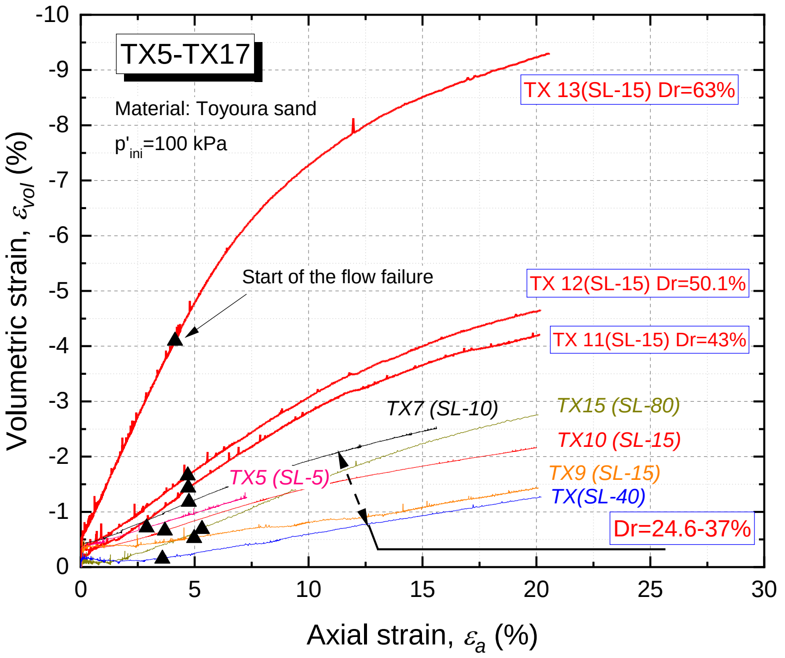

Figure 4-52 The dilation behavior (volumetric strain and axial strain) of specimens (Toyoura sand) with different static shear stress and initial density

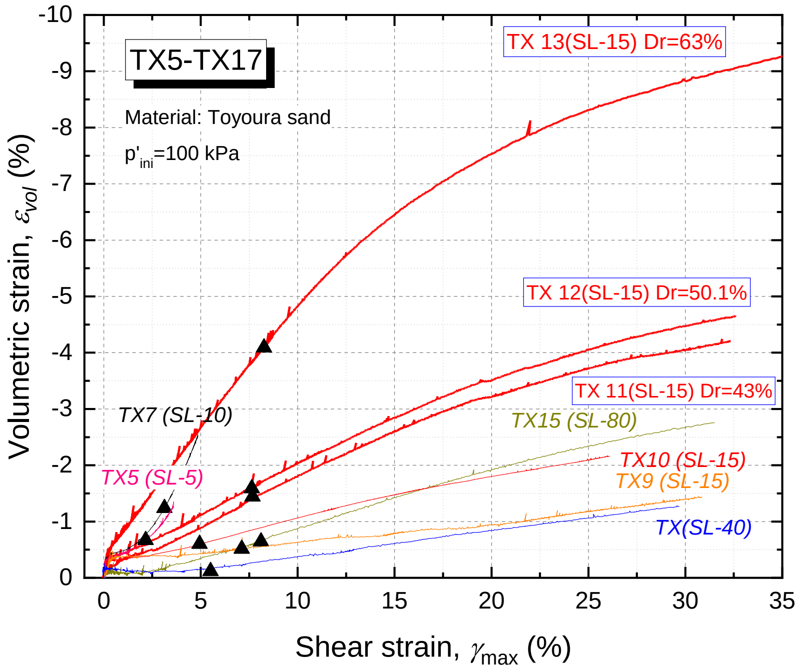

Figure 4-53 The dilation behavior (volumetric strain and shear strain) of specimens (Toyoura sand) with different static shear stress and initial density

It is investigated that the initial density of the specimen plays a vital role in the dilation behavior of the specimen. This evidence can be associated with the void redistribution phenomenon in the sand that occurred after the earthquake loading. The same mechanism also is in line with the explanation from Boulanger and Truman (1996).

4.5.3. Effect of fine content to the dilation behavior

In order to investigate the effect of fine content on the dilation behavior, two types of artificial fine content (FC) are used, which are DL Clay as the non-plastic fines (NP) and Kaolin as the plastic fines. These fines are mixed with clean sand (Toyoura sand) in several mass proportions; FC=0% with non-plasticity (NP), FC=10% NP, FC=20% NP, and FC=20% with index of plasticity (IP) is 11. The list of the specimen is shown in Table 4-4. To examine the index of plasticity (IP), Atterberg's test has been conducted to measure the Liquid Limit (LL) and the Plastic Limit of the mixed sand following the procedure of JGS 0141 (Japanese Geotechnical Society, 2015).

Table 4-4 The list of experiments on the sand with fines conducted at strain-controlled Triaxial Apparatus

Code Test	Global void ratio, *e*	Static shear stress, *q* (kPa)	Mean effective stress, *p'* (kPa)	FC (PI)	Volumetric strain at axial strain is 15% (%)
TX18 (SL-15)	0.720	15	100	10 (NP)	
TX19 (SL-15)	0.683	15	100	10 (NP)	-4.11
TX20 (SL-15)	0.641	15	100	20 (NP)	-0.81
TX21 (SL-15)	0.563	15	100	20 (NP)	
TX22 (SL-15)	0.659	15	100	20 (IP=11)	+0.10
TX23 (SL-15)	0.548	15	100	20 (IP=11)	

It is clear that the fine content did not affect the start of flow failure point at the stress path. The stress path of TX20 having FC=20% with Non-plasticity and TX22 having FC=20% and IP=11 shows that flow failure start when the stress path reached Phase Transformation Line as the previous results using Toyoura Sand with FC=0%. The strain development also can be identified as initial stage, limited flow, and continuous flow.

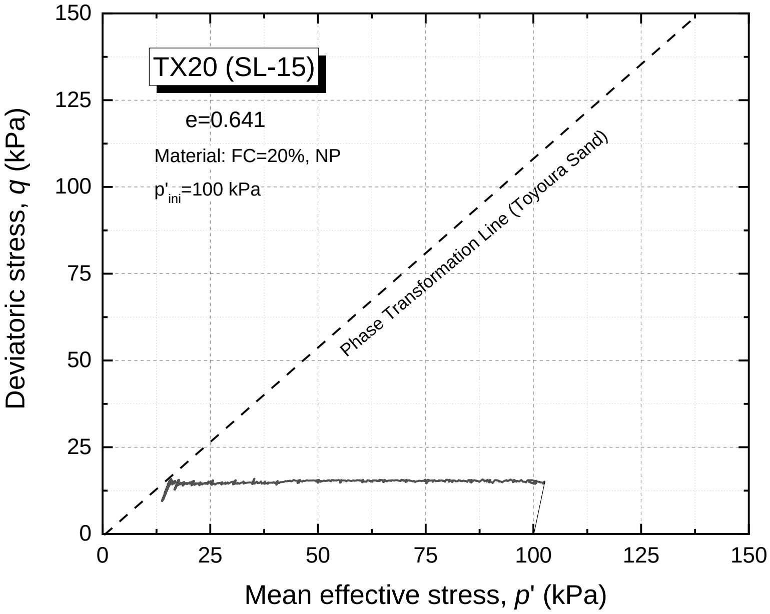

Figure 4-54 Stress path of TX20 in static liquefaction test

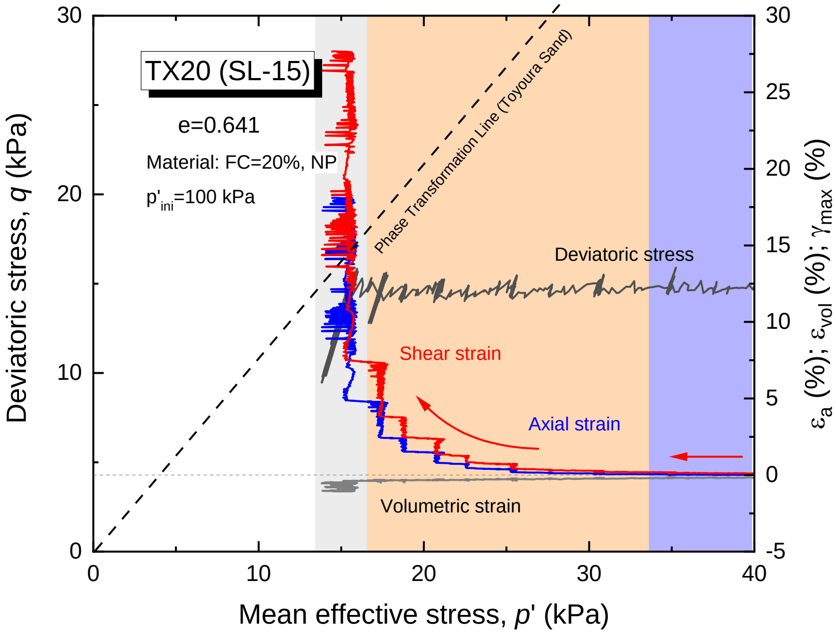

Figure 4-55 Enlargement part of stress path of TX20 at low stress

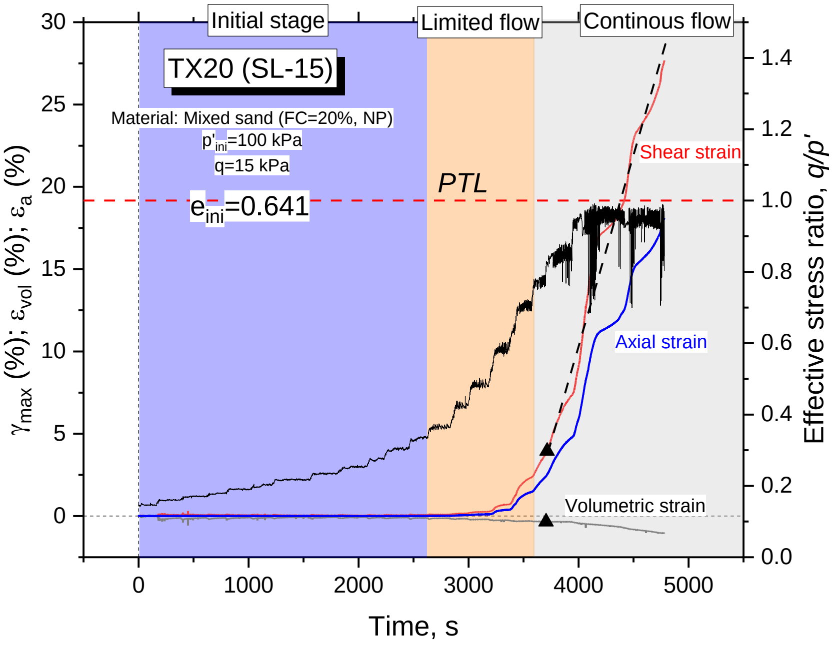

Figure 4-56 The strain development of TX20 in q/p'-time plane

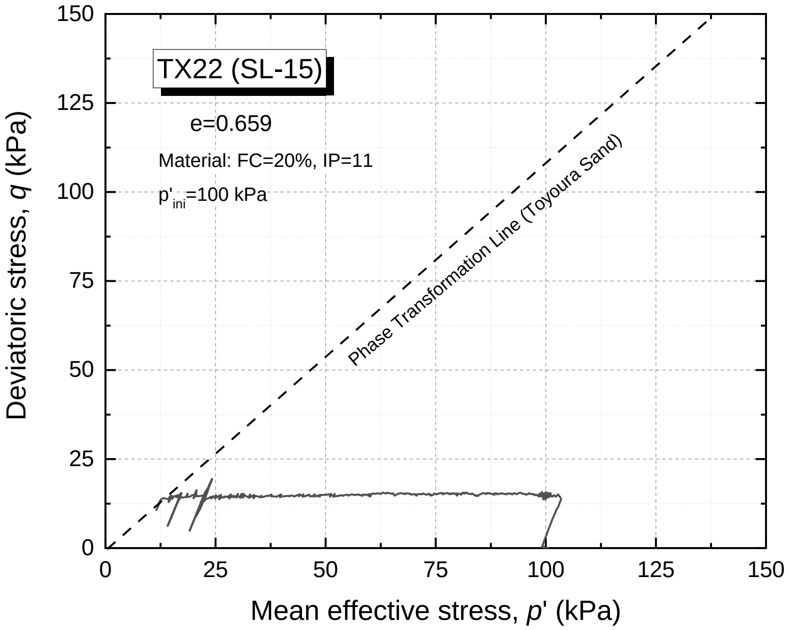

Figure 4-57 Stress path of TX22 in static liquefaction test

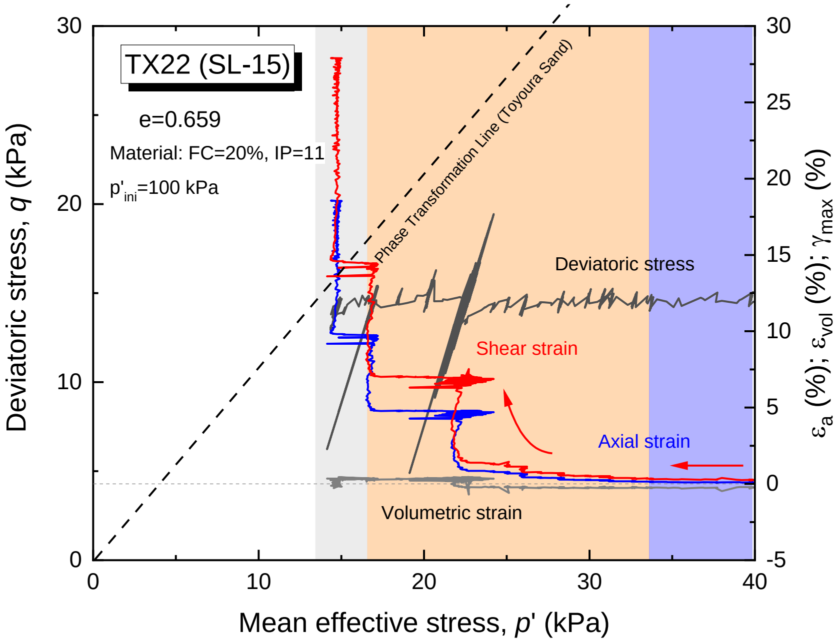

Figure 4-58 Enlargement part of stress path of TX22 at low stress

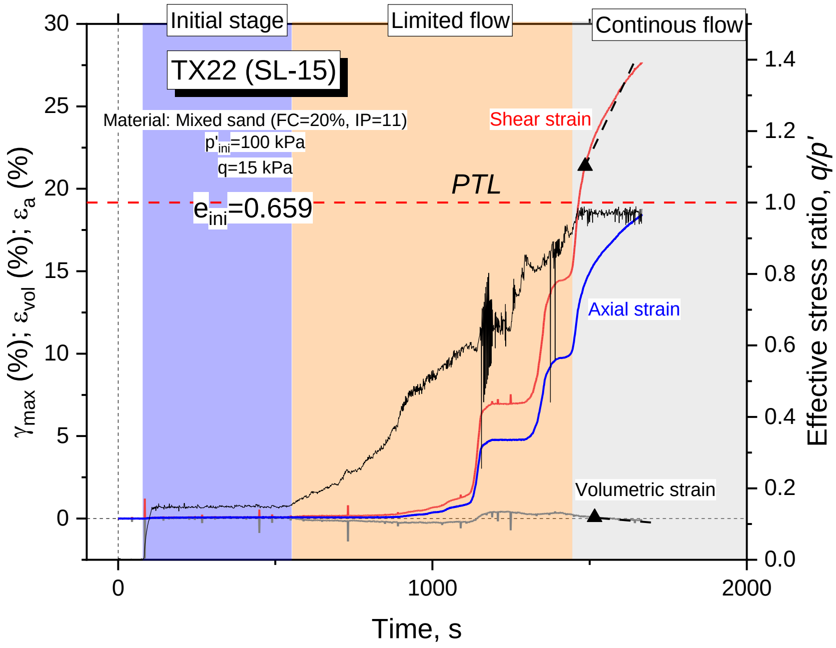

Figure 4-59 The strain development of TX22 in q/p'-time plane

The experiments using the same global void ratio with different fines content show that the fines content affect the dilation behavior of the specimens. At the final state of axial strain reach 15%, TX27 whose having FC=0%, dilate up to ε_{vol}=-6.87% while TX22 whose FC=20% and IP=11, show contractive behavior with ε_{vol}=0.1%. These results (Figure 4-60) reflect that the higher the number of fines content on the soil, the less dilative the material will behave under this test condition. It is also obvious that the plastic fines reduces the volumetric strain development for specimen TX22 whose index of plasticity is 11.

It is also shown that the higher the amount of the fines, the less the water it needs to flow. For example, The TX27 specimen absorbs approximately -1.7% of ε_{vol} for producing the flow behavior while the TX20 whose having FC=20% with non-plasticity needs -0.3% of ε_{vol} to flow. From both results, it is clear that fine content affects the void redistribution of the mixed materials. As this void redistribution mechanism is driven by the migration of fluid to the soil body, the fines content hinders this migration which resulting in less development of volume expansion.

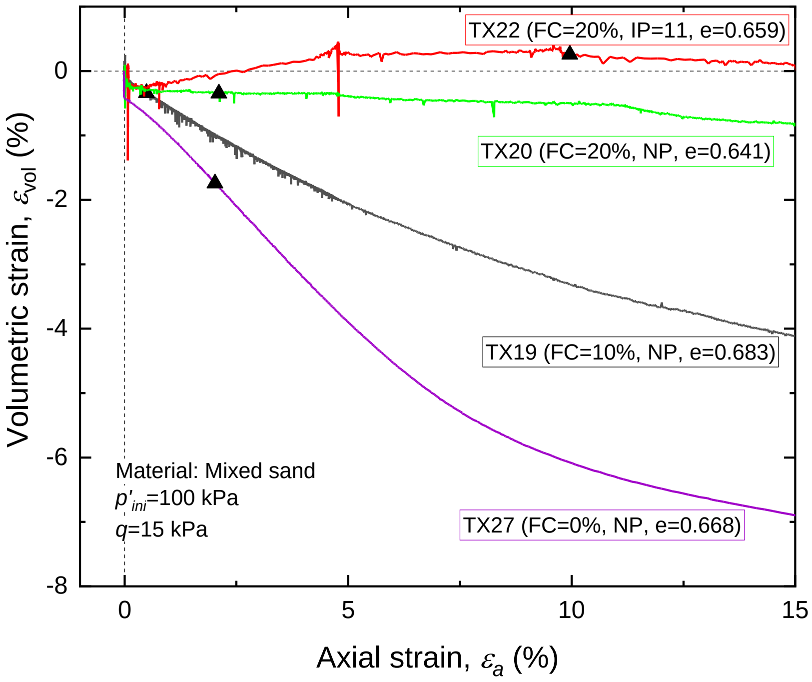

Figure 4-60 Strain development of sand with fines under static liquefaction test

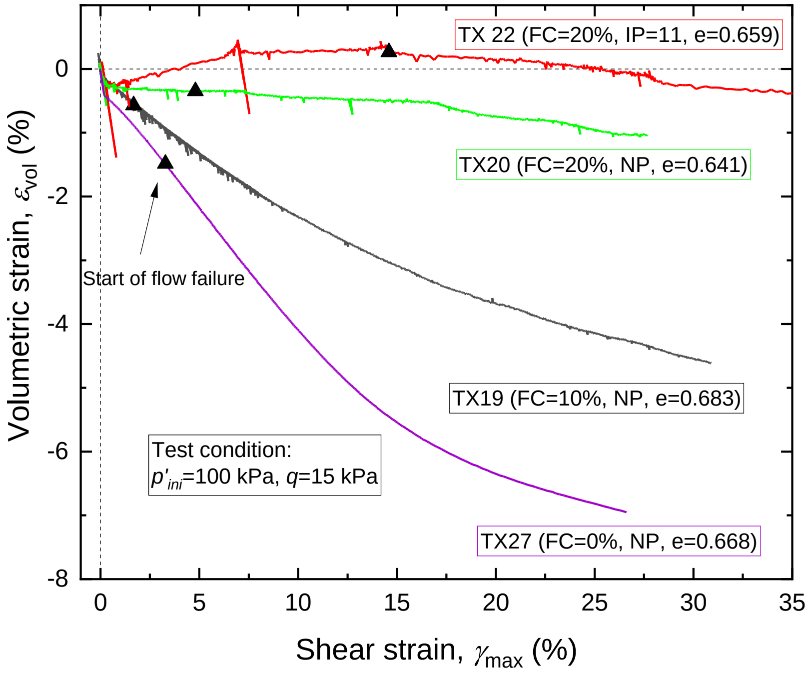

Figure 4-61 Strain development of sand with fines under static liquefaction test

Monotonic Drained Loading test has been conducted to validate the hypothesis of how the fines content affects the volumetric strain behavior of mixed sand. The list of the tests is shown in Table 4-5.

Table 4-5 The lists of specimen for Drained Monotonic Loading Test

Code Test	Global void ratio, *e*	Mean effective stress, *p'* (kPa)	FC (PI)	Peak strength (kPa)	Volumetric strain at peak (%)
TX24 (DML)	0.700	100	0 (NP)	345	-2.50
TX25 (DML)	0.729	100	20 (NP)	230	+0.50
TX26 (DML)	0.635	100	20 (11)	225	+2.20

The stress-strain relationship of the Drained Monotonic Test is shown in Figure 4-62. The peak strength of TX24 having non fines is higher compared to the TX25 (FC=20%, NP) and TX26 (FC=20%, IP=11). This shows that the fines content reduces the peak strength of specimen. It is also showed that TX24 reached the peak strength at smaller axial strain compared to other specimens. After reached the peak at axial strain equal to 7%, TX24 showed reduction of deviatoric stress lead to failure condition as the deformation keep increased. TX25 showed the peak strength at axial strain of 14.5% and slighty reduction of deviatoric stress until reaching the axial strain of 20%. Meanwhile, TX26 did not show clear peak strength, even the axial strain already reached 20% in this study.

Furthermore, the TX24 show more dilative behavior compared to other specimens. At the axial strain equal to 15%, the TX 24 dilated up to ε_{vol}=-6.1% while the other specimens having fines content show different behavior. Until the axial strain reaches 15%, both TX25 and TX26 show contractive behavior with TX26, whose having IP=11 showing more contractive behavior than another. These results support the previous evidence that sand with fines will tend to behave as a contractive material than dilative material. This reason also proves that fine content exhibit as an inhibitor to the development of dilation behavior on the sand.

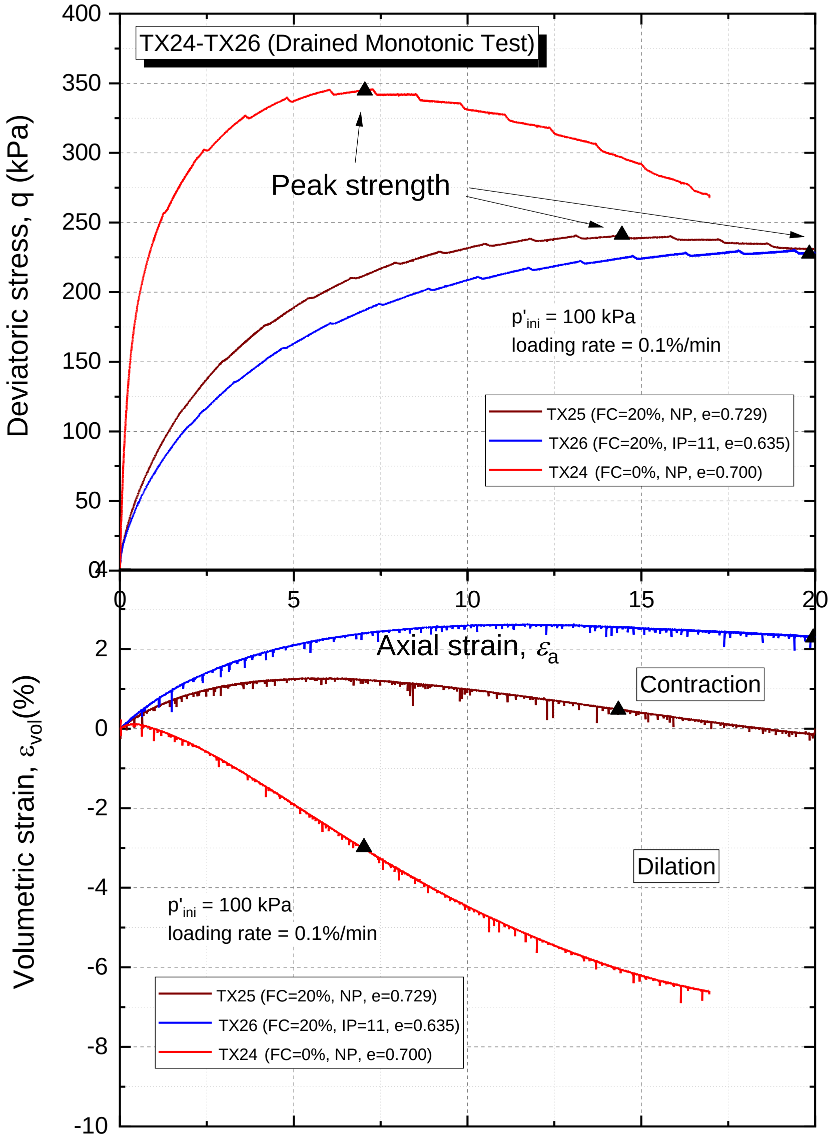

Figure 4-62 Stress-strain relationship of specimens under Drained Monotonic Loading Test

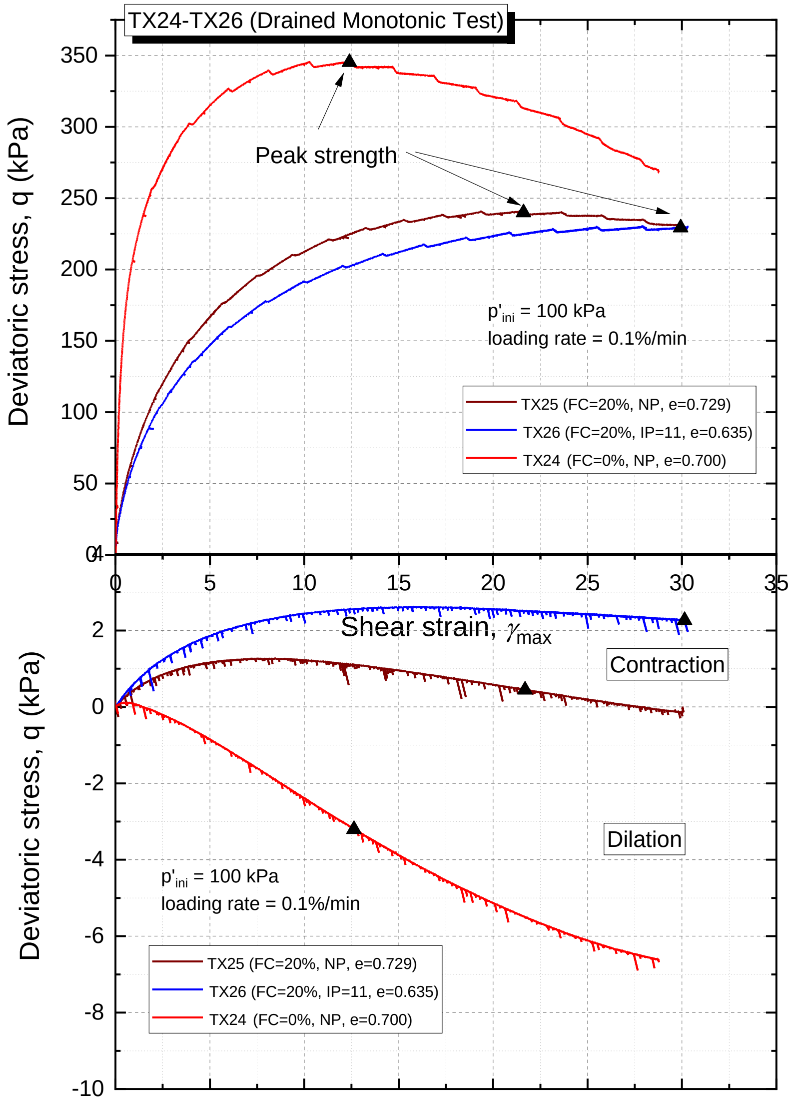

Figure 4-63 Strain relationship in Drained Monotonic Test

4.6.Summary

In order to investigate the dilation behavior sandy soils under constant static shear stress, series of static liquefaction tests have been conducted on Toyoura sand with different static shear stresses, initial densities, and fine content to a single amplitude of axial strain of 20%. The following conclusion can be drawn from this study:

1. From all the results of the experiment under static liquefaction test, the development of axial and volumetric strain, which corresponds to the dilative

behavior of soils, are classified into three areas, which are initial state, limited flow, and rapid flow. The phenomenon of unlimited flow failure can be observed at the rapid flow area, in which even the stress is kept constant, the specimen is kept dilating.

2. All the specimens are dilated toward the steady-state line, regardless of having different static shear stress and initial density. This dilation behavior could be observed in the log p’-e plane.
3. The effect of the static shear stress to the dilation behavior of the specimen having the same initial density is not significant. Specimen undergo the small static shear stress (q=5 kPa) and the specimen with large static shear stress (q=80 kPa) show only 1% of volumetric strain difference. In addition, the dilative behavior is more pronounced by another factor, which is initial density.
4. The effect of the initial density of the specimen to the dilative behavior is significant. The initial density of the material will define the volume expansion of the specimen. The densest the material, the more volumetric expansion will be developed, implying the more dilative the material.
5. Fine content affects the volumetric expansion of the material. The more fine content on the sand, the less dilative the specimen will be. As the fine content having smaller particle size compared to the granular material, the fine material will fill the void of the granular material resulting in the change of the void redistribution and the permeability will be reduced. This reduction of and void redistribution change will reduce the development of volume expansion.

4.7. References

Boulanger, R. W. & Truman, S. P., 1996. Void redistribution in sand under post-earthquake loading. *Canadian Geotechnical Journal,* pp. Vol. 33: 829-834.

Casagrande, A., 1936. Characteristics of Cohessionless Soils Affecting the Stability of Slopes and Earth Fills. *Journal of the Boston Society of Civil Engineers, Reprinted in Contributions to Soil Mechanics, Boston Society of Civil Engineers 1940,* p. 257–276.

Castro, G. & Poulos, S. J., 1977. Factors affecting liquefaction and cyclic mobility. *Journal of Geotechnical Engineering Division, ASCE,* 103(GT6), pp. 501-516.

Hamada, M., Yasuda, S. & Wakamatsu, K., 1991. *Liquefaction induced permanent ground displacement in Niigata city.* St. Louis, s.n.

Ishihara, K., Tatsuoka, F. & Yasua, S., 1975. Undrained deformation and liquefaction of sand under cyclic stresses. *Soils and Foundations,* 15(No. 1), pp. 29-44.

Japanese Geotechnical Society, 2015. *Japanese Geotechnical Standards, Laboratory Testing Standards of Geomaterials Vol. 1.* Tokyo: Japanese Geotechnical Society.

Japanese Society of Civil Engineers, 1966. *The report of damage investigation in the 1964 Niigata earthquake*, Tokyo: Japanese Society of Civil Engineers.

Kang, X. et al., 2019. The critical state and steady state of sand: A literature review. *Marine Georesources and Geotechnology,* 37(No. 9), pp. 1105-1118.

Kawakami, M. & Asada, A., 1966. Damage to the ground and earth structures by the Niigata earthquake of June 16, 1964. *Soils and Foundations,* 6(1), pp. 14-30.

Lambe, T. W. & Whitman, R. V., 1969. *Soil Mechanics.* New York: John Willey & Sons.

Poulos, S. J., 1981. The steady state of deformation. *Journal of Geotechnical Engineering Division, ASCE,* 107(GT5), pp. 553-562.

Poulos, S. J., Castro, G. & France, J. W., 1985. Liquefaction Evaluation Procedure. *Journal of Geotechnical Engineering Vol. 111, Issue 6*, pp. 772-792.

Roscoe, K. H., Schofield, M. A. & Wroth, C. P., 1997. Factors Affecting Apparent Position of Steady State Line. *Journal of Geotechnical and Geoenvironmental Engineering ASCE,* 123(No. 3), pp. 281-288.

Sento, N. et al., 2004. Possibility of postliquefaction flow failure due to seepage. *Journal of Geotechnical and Geoenvironmental Engineering,* pp. Vol. 130, No. 7, 707-716.

Uchida, K. & and Vaid, Y. P., 1994. *Sand behavior under strain path control.* Rotterdam, Proceeding 8th International Conference on Soil Mechanics and Geotehnical Engineering Balkema.

Vaid, Y. & Eliadorani, A., 1998. Instability and liquefaction of granular soils under undrained and partially drained states. *Canadian Geotechnical Journal* , Volume 35, pp. 1053-1062.

Verdugo, R. & Ishihara, K., 1996. The steady state of sandy soils. *Soils and Foundations Vol. 36, No. 2*, pp. 81-91.

Yoshimine, M., Nishizaki, H., Amano, K. & Hosono, Y., 2006. Flow deformation of liquefied soil under constant shear load and its application to analysis of flow slide of infinite slope. *Soil Dynamics and Earthquake Engineering*, pp. Vol. 26, Issues 2-4, 253-264.

Chapter 5 FLOW RATE CHARACTERISTICS OF SANDY SOILS UNDER CONSTANT STATIC SHEAR

5.1. Introduction

Residual deformation over several meters due to liquefaction has been observed in the 1964 Niigata earthquake (Kawakami & Asada, 1966; Hamada, et al., 1991). An apartment house in Kawagishi-Cho, Niigata city, continued to move for few minutes aftaer the earthquake before it stopped at the final tilted position (Kawakami & Asada, 1966) and a girder of Showa bridge that toppled a few minutes after the earthquake stopped (Japanese Society of Civil Engineers, 1966) are some examples of how the large movement could have happened after the earthquake.

Flow failure phenomenon occurred due to 2018 Sulawesi Earthquake in Palu City, Indonesia had been an extraordinary case in liquefaction-induce-phenomena as this catastrophic disaster killed thousands of lives and many people reported missing. Many people could not escape from the flow failure as the ground moved at a certain rate covering the large areas. From this phenomenon, it is essential to investigate the flow failure rate behavior of soil under these circumstances.

Tokimatsu et al. (2001) studied the shear deformation behavior under arbitrary water drainage conditions using hollow torsional cylindrical shear tests and found that mobilized shear stress tends to decrease due to pore water migration from the lower liquefied layer. In addition, Boulanger and Truman (1996) studied the response of sand to post-earthquake loading on an infinite slope by triaxial apparatus and suggested a mechanism of void redistribution within a confined layer of sand in an infinite gentle slope. The void redistribution phenomenon was first observed to occur within laboratory sand specimens (Casagrande & Rendon, 1978). The dilation behavior of sand is governed by the void distribution of a material, which is corresponded to the initial density. Void redistribution due to earthquake loading may have an important influence on the residual shear strength, or steady-state strength, of saturated sand (National Research Council of United States, 1985).

In the element test, the dilation behavior can be represented by the volumetric strain development. The development of volumetric strain will induce the shear strain. It is also important to understand how the volumetric strain development affects the shear strain rate development, which related to the flow failure rate behavior of the sand. In the Triaxial Apparatus, the shear stress is applied indirectly to the specimen. The maximum shear strain rate can be calculated by derivating the maximum shear strain to the time or can be expressed as follow.

$$\dot{\gamma}_{max} = \frac{d\gamma_{max}}{dt} \tag{5.1}$$

In this test, the calculation of the shear strain rate is conducted under constant stress ratio when the stress path approaches the rapid flow area. This assumes that the flow failure rate occurs in the constant ground inclination.

5.2.Shear Strain Rate Development of Toyoura Sand

In the element test, in particular, Triaxial Apparatus, the dilative behavior of a specimen can be observed through the volumetric strain development. The volumetric strain development will define the shear strain development and its rate.

In the previous chapter, the development of strains can be distinguished into three areas, which are initial state, limited flow, and continuous flow. In the initial state, as the development of shear strain is negligible, the shear strain rate can also be negligible. At the limited flow, the volume expansion already induces the shear strain. Nevertheless, the shear strain is progressed in the limited step, which is mostly promoted by the reduction of the mean effective stress.

In this study, if the effective mean stress reaches the failure line in the stress path plane (p’-q plane), the flow behavior will be transited from limited flow to continuous flow. This behavior is promoted by the termination of dilatancy to recover the stiffness of the soil. The softening behavior will continue as the dilatancy is terminated and the flow behavior could be observed at a certain rate, even the stress condition does not change. The point in which the flow behavior changed from limited flow to continuous flow is mentioned as the starting point of flow failure in this research.

5.3.Shear Strain Rate Characteristics of Clean Sand

The importance of understanding the shear strain rate has arisen to predict whether the flow failure will move at a slow pace or fast rate. In this study, the shear strain rate characteristics will be investigated by considering two major factors; the effect of static shear stress and the effect of the initial density of the specimen. The results of the shear strain rate measurements are listed in Table 5-1.

Table 5-1 The test results of shear strain rate measurement conducted on Triaxial Apparatus for Toyoura sand

Code Test	Relative density, *Dr* (%) at *p'*=100 kPa	Void ratio, *e*	Deviatoric stress, *q* (kPa)	Mean effective stress, *p'* (kPa)	Volumetric strain at flow failure point (%)	Shear strain rate, $\dot{\gamma}$ (%/min)
TX5 (SL-5)	35.5	0.836	5	100	-0.67	0.07
TX6 (SL-5)	70.2	0.710	5	100	-1.79	0.42
TX7 (SL-10)	37.9	0.827	10	100	-1.00	0.49
TX8 (SL-10)	72.8	0.698	10	100	-2.30	2.10
TX9 (SL-15)	26.9	0.867	15	100	-0.60	0.65
TX10 (SL-15)	28.4	0.862	15	100	-1.21	0.67
TX11 (SL-15)	43	0.800	15	100	-1.75	0.95
TX12 (SL-15)	50.1	0.782	15	100	-1.69	1.98
TX13 (SL-15)	63	0.735	15	100	-3.78	3.45
TX14 (SL-40)	24.6	0.875	40	100	-0.23	2.68
TX15 (SL-80)	33.6	0.843	80	100	-0.98	6
TX16 (SL-80)	38.8	0.826	80	100	-1.29	2.62
TX17 (SL-80)	44	0.804	80	100	-1.17	11.20
TX27 (SL-15)	*81.2*	*0.690*	*15*	*100*	*-1.77*	*5.86*

5.3.1. Effect of static shear stress on shear strain rate characteristics of sandy soils

In the previous chapter, it is mentioned that the effect of static shear stress is not significant to the development of volumetric strain, which corresponds to the dilation behavior of sandy specimens. The time-series behavior of the specimen TX15 during the static liquefaction test is presented in Figure 5-1. This result shows the illustration of how continuous flow occurs in the constant mean effective stress and constant deviatoric stress. The shear strain rate observation is conducted at the continuous flow stage. The detail of measurement is presented in Figure 5-2.

It is clear that even the reduction of mean effective stress (p’) as much as around 1 kPa, the shear strain rate will be developed largely. This condition supports the assumption of the flow failure start at this point. At the beginning of the flow failure, the rate of the shear strain is dominantly affected by the indirect shearing from the reduction of mean effective stress (p’). After the p’ is stable, the shear strain tends to develop at a constant rate, and become faster as the shear strain becomes larger. This phenomenon could be associated with the softening behavior of soil in the plastic region due to water infiltration to the soil body.

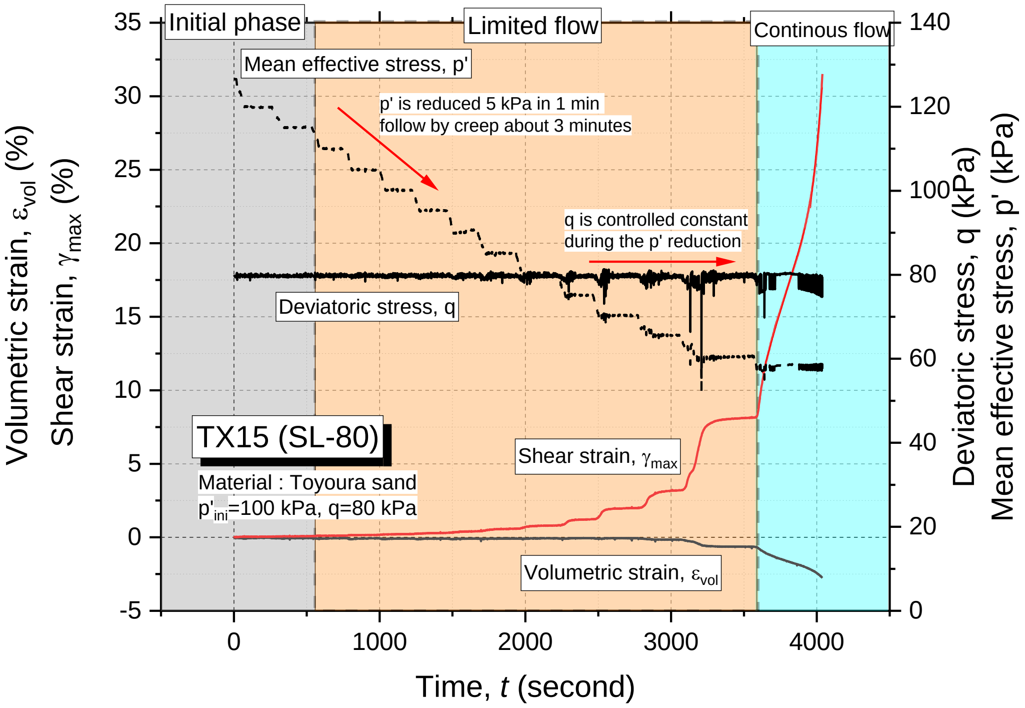

Figure 5-1 The experimental result of TX15 (SL-80) in time series

In Figure 5-2, the TX15 (SL-80) shows that the shear strain rate increase from $\dot{\gamma}_{max-1}$=2.02%/min to be $\dot{\gamma}_{max-2}$=6.08%/min after the shear strain reaches 23%. In comparison, the shear strain measurement of TX5 (SL-15) has been drawn in Figure 5-3. It is also can be seen that in TX5, the rate of shear strain is, at first, influenced by the reduction of mean effective stress. TX5 shows a lower shear strain rate compared to the TX15 whose having q=80 kPa. It is estimated that the $\dot{\gamma}_{max}$=0.68%/min for TX5 with the starting point of flow failure occurred at γ_{max}=11%. Therefore, it can be concluded that the static shear stress has a significant effect on the shear strain rate.

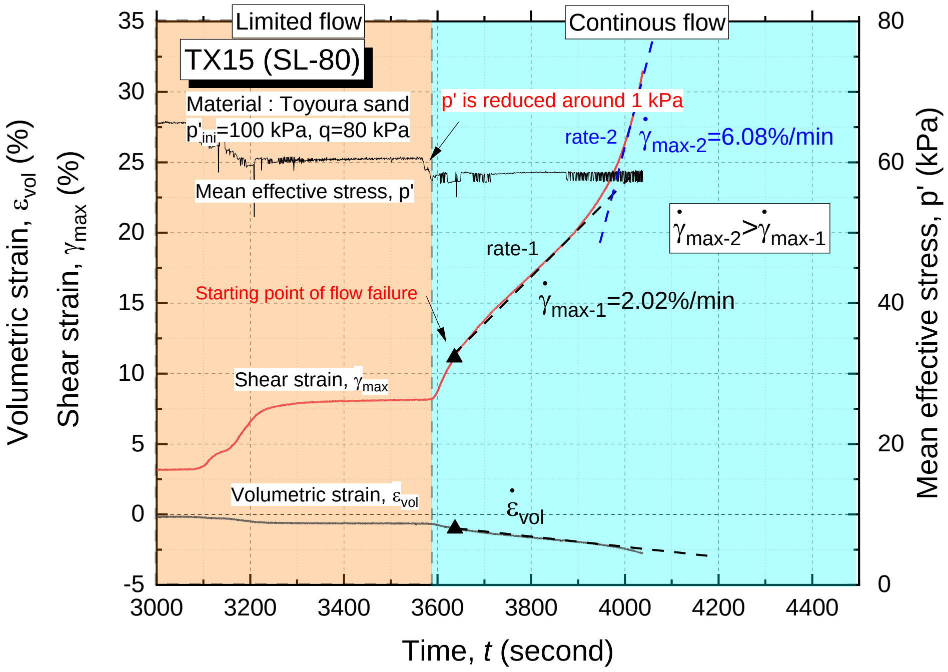

Figure 5-2 The shear strain rate measurement for TX15 (SL-80)

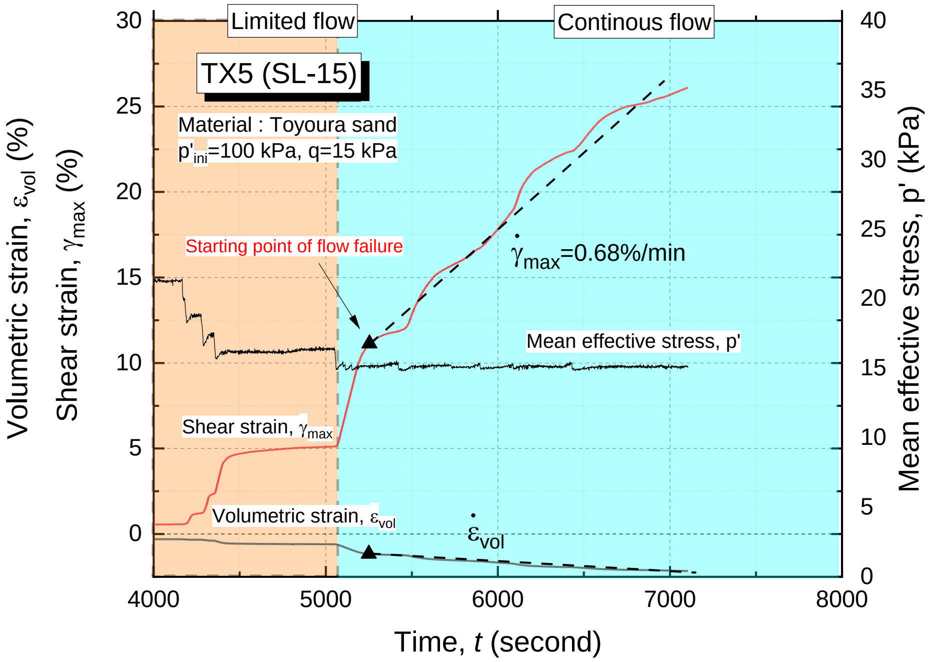

Figure 5-3 The shear strain rate measurement for TX5 (SL-5)

The stress-path, the strain development, and the shear strain measurement on Toyoura Sand conducted in Triaxial Apparatus are shown as follows.

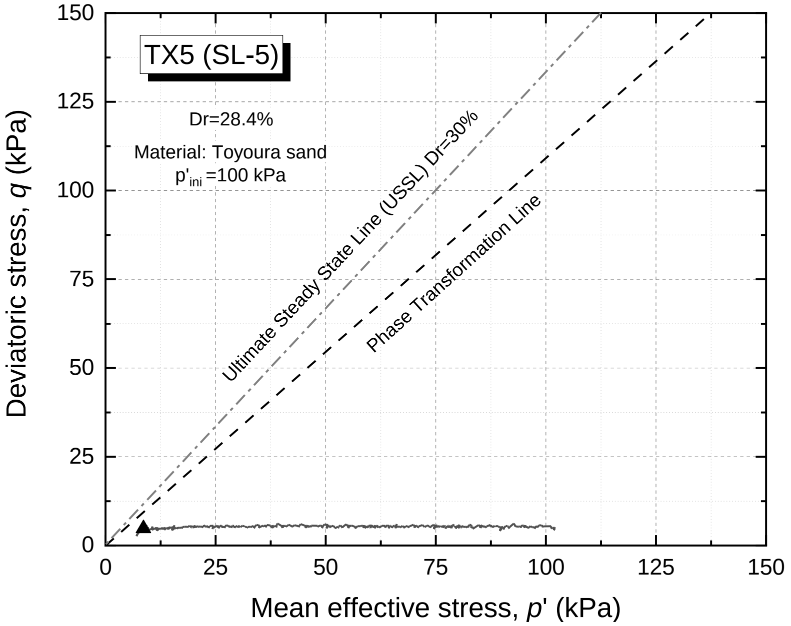

Figure 5-4 The stress path of TX5 (SL-5)

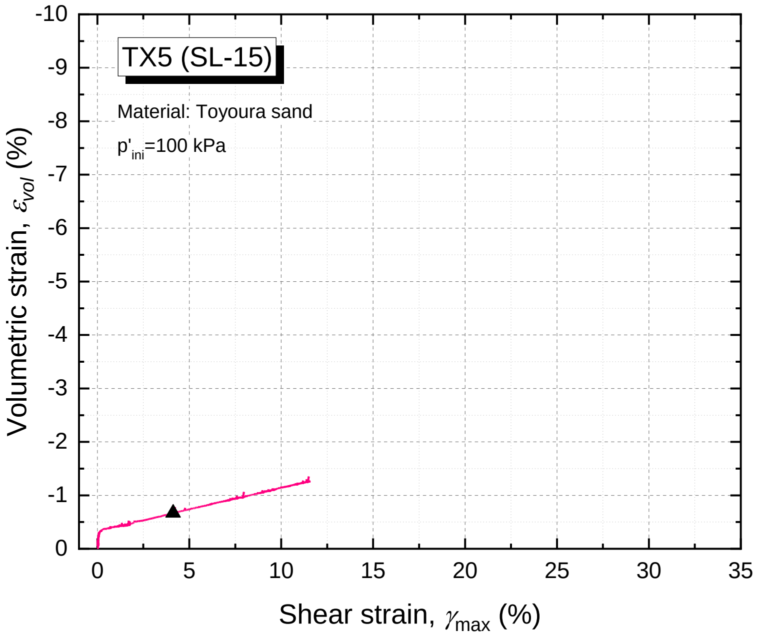

Figure 5-5 Relationship of volumetric strain and shear strain of TX5

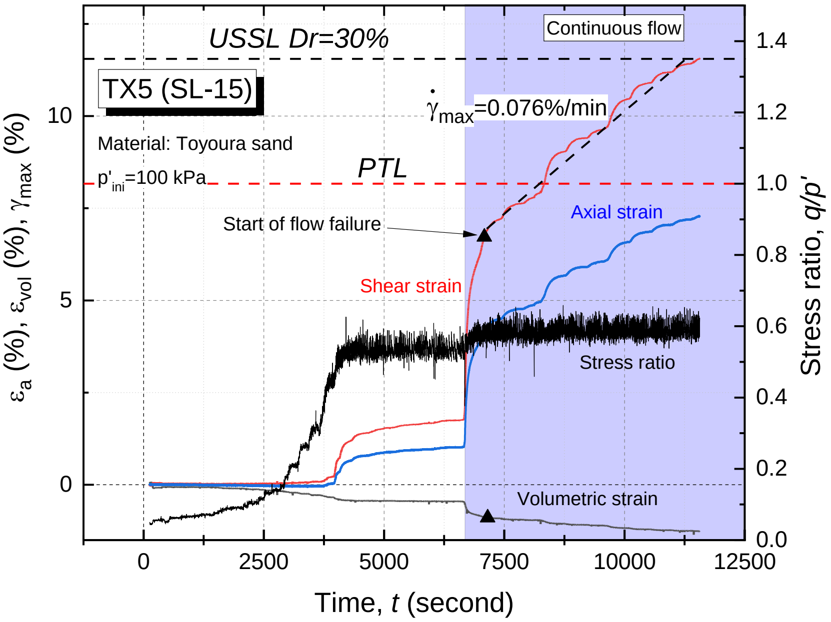

Figure 5-6 Strains development in time series of TX5

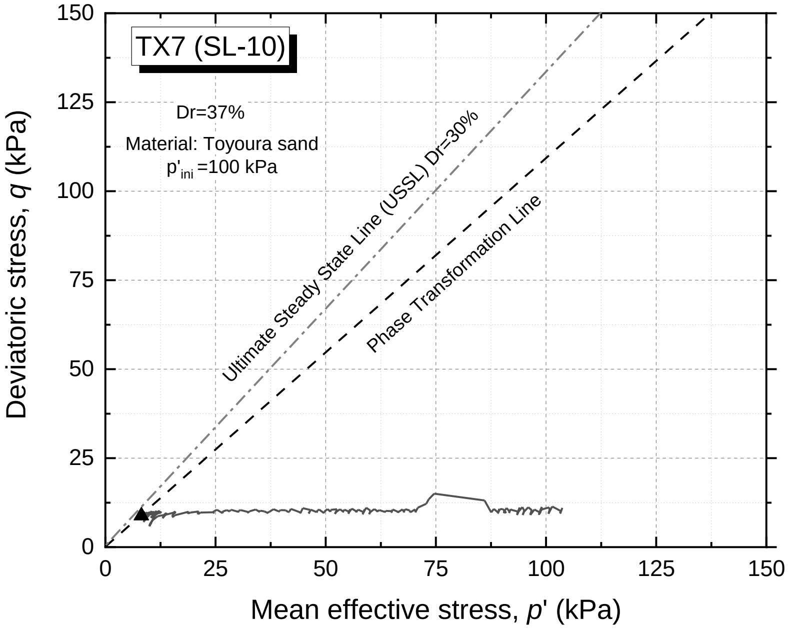

Figure 5-7 The stress path of TX7 (SL-10)

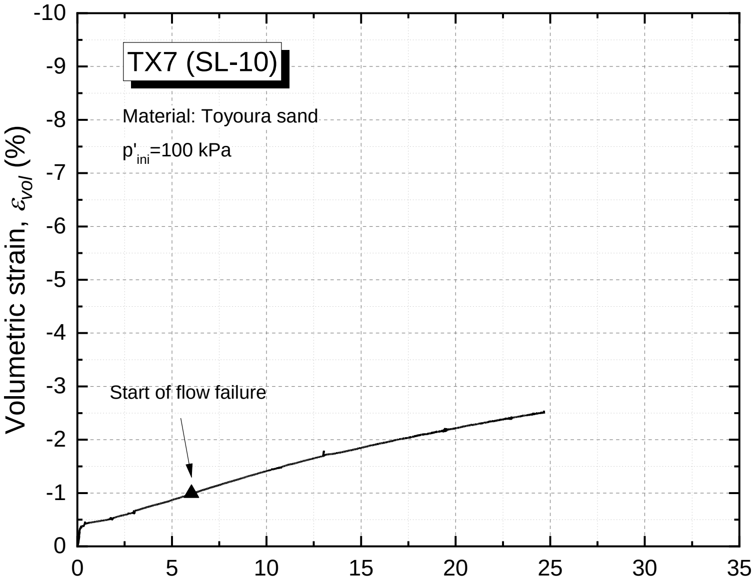

Figure 5-8 Relationship of volumetric strain and shear strain of TX7

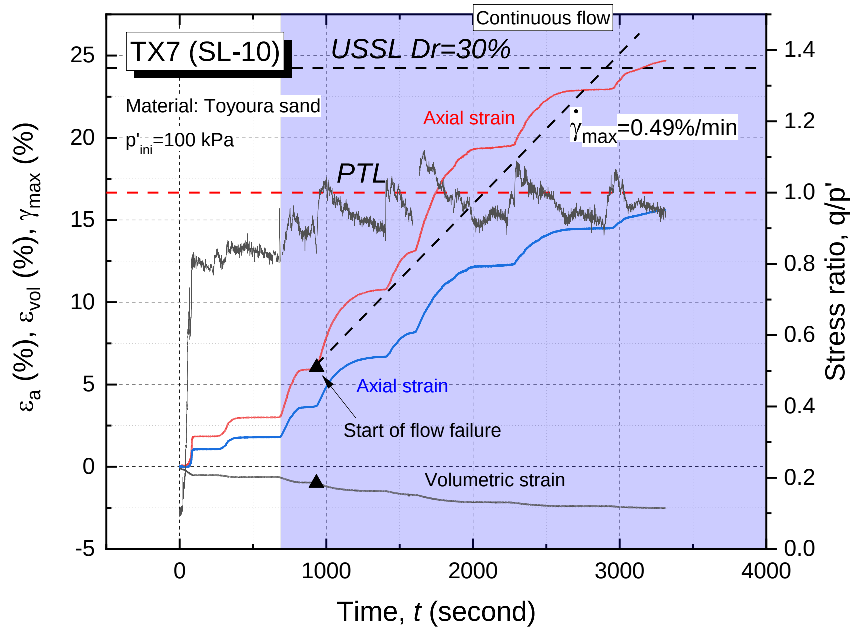

Figure 5-9 Strains development in time series of TX7

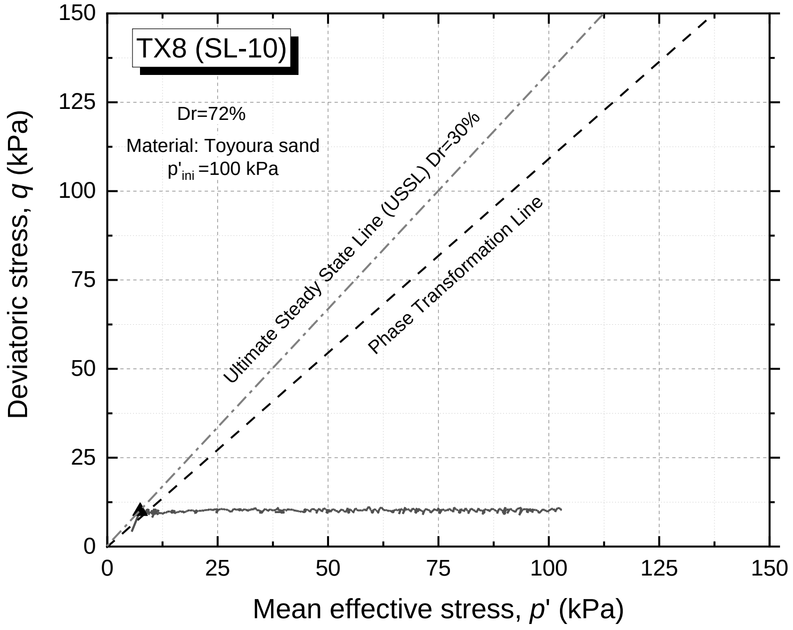

Figure 5-10 The stress path of TX8 (SL-10)

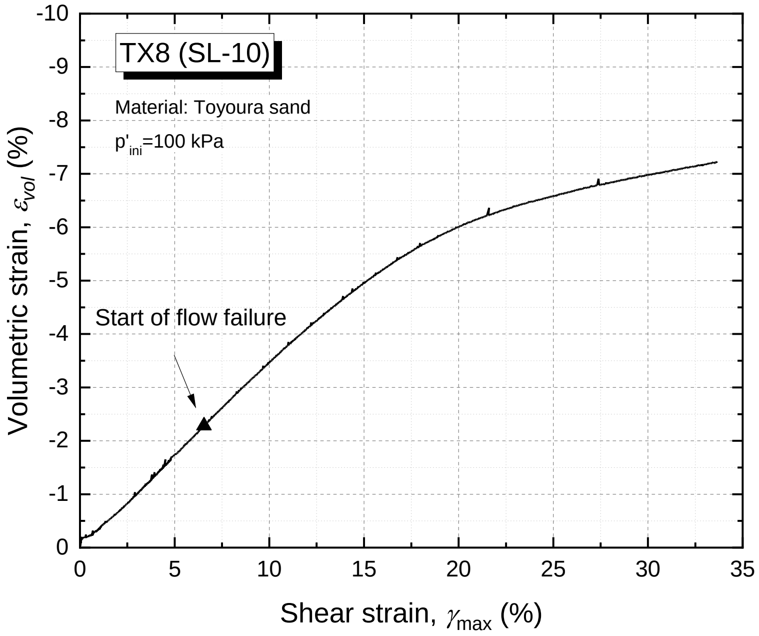

Figure 5-11 Relationship of volumetric strain and shear strain of TX8

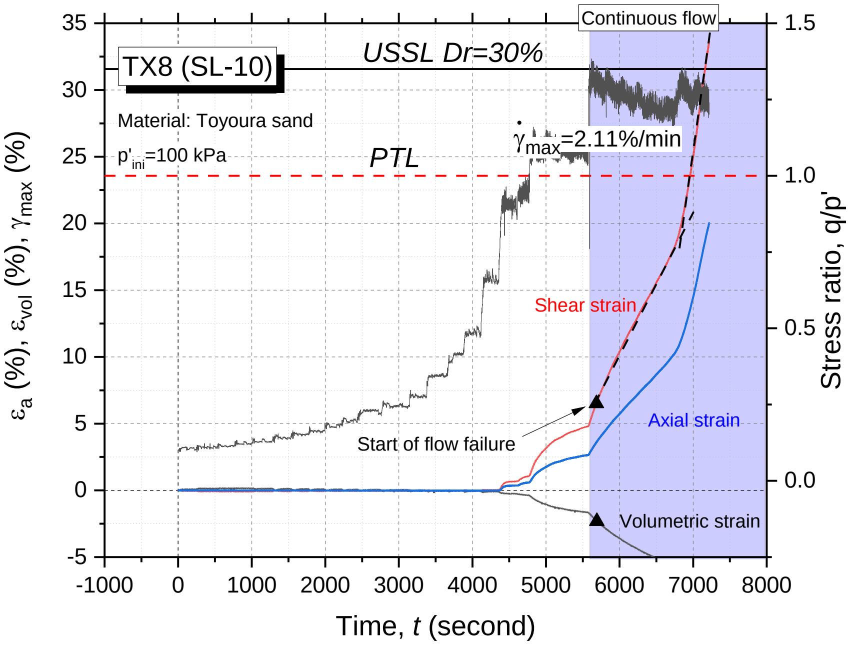

Figure 5-12 Strains development in time series of TX8

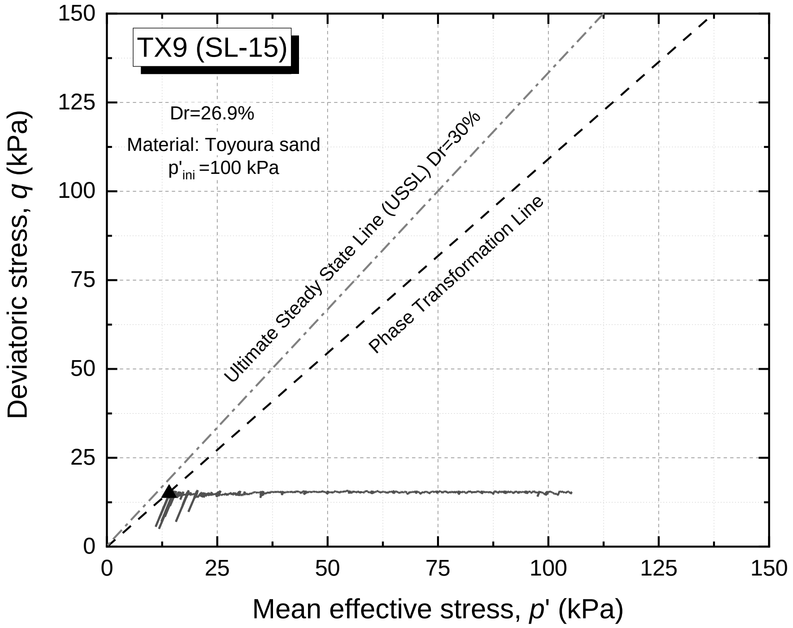

Figure 5-13 The stress path of TX9 (SL-15)

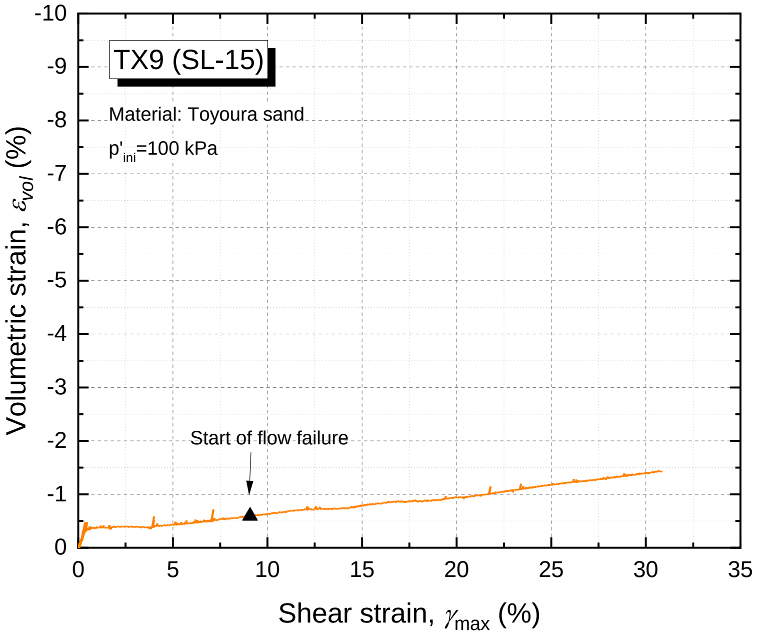

Figure 5-14 Relationship of volumetric strain and shear strain of TX9

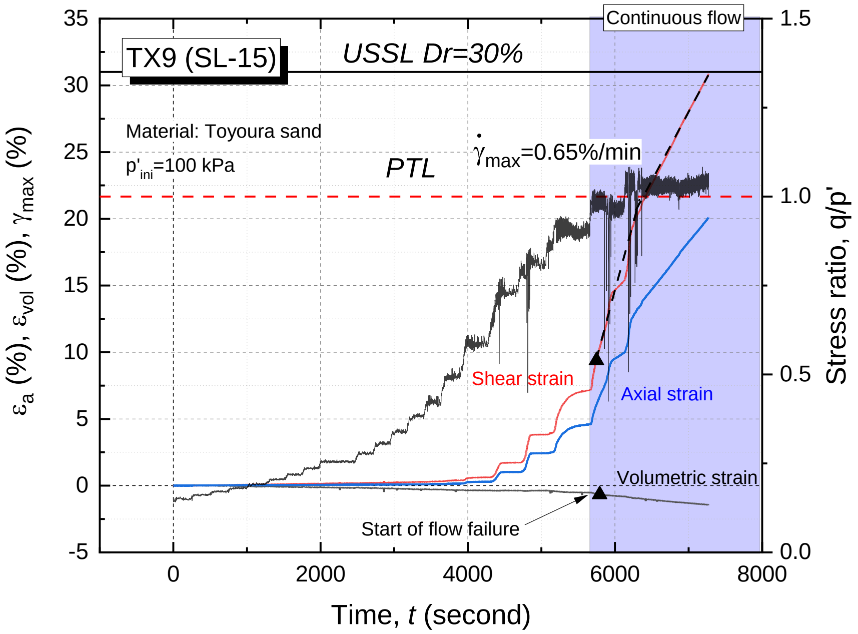

Figure 5-15 Strains development in time series of TX9

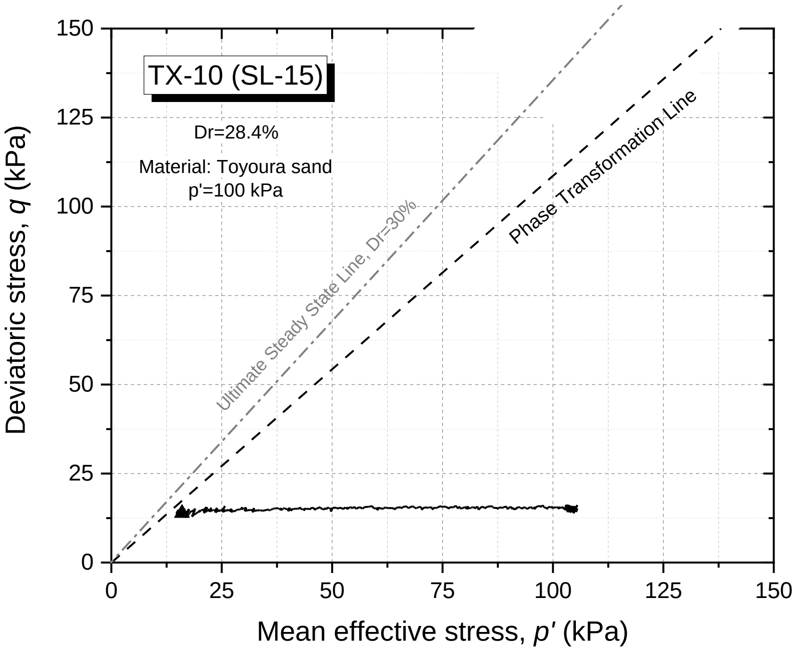

Figure 5-16 The stress path of TX10 (SL-15)

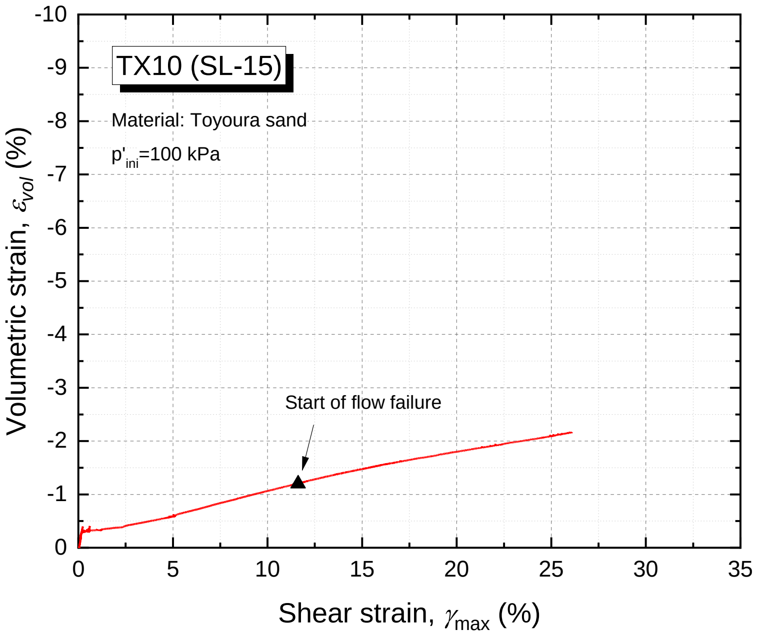

Figure 5-17 Relationship of volumetric strain and shear strain of TX10

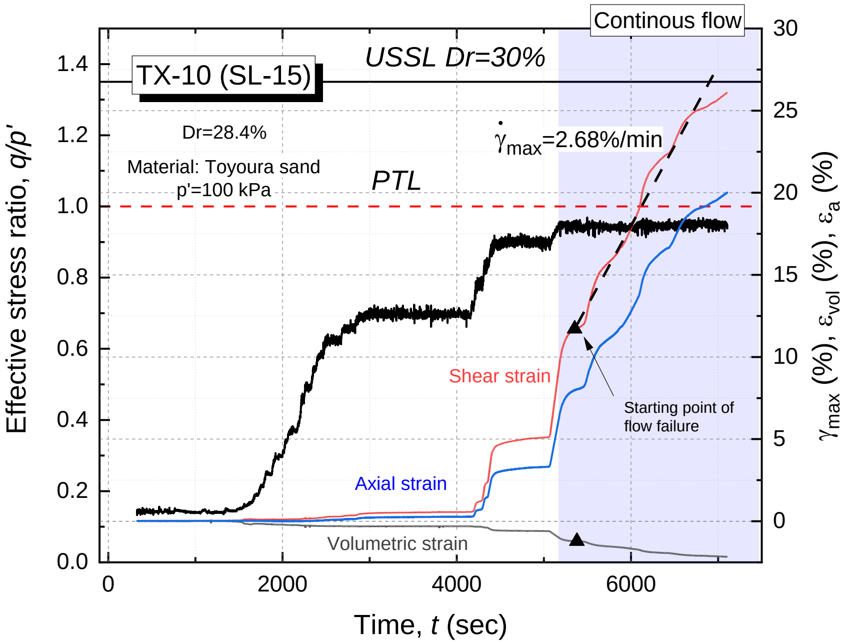

Figure 5-18 Strains development in time series of TX10

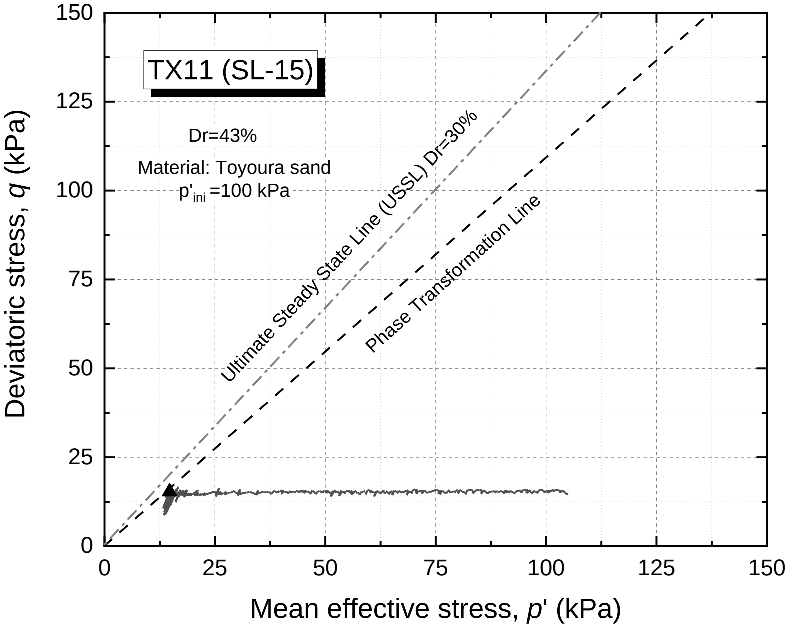

Figure 5-19 The stress path of TX11 (SL-15)

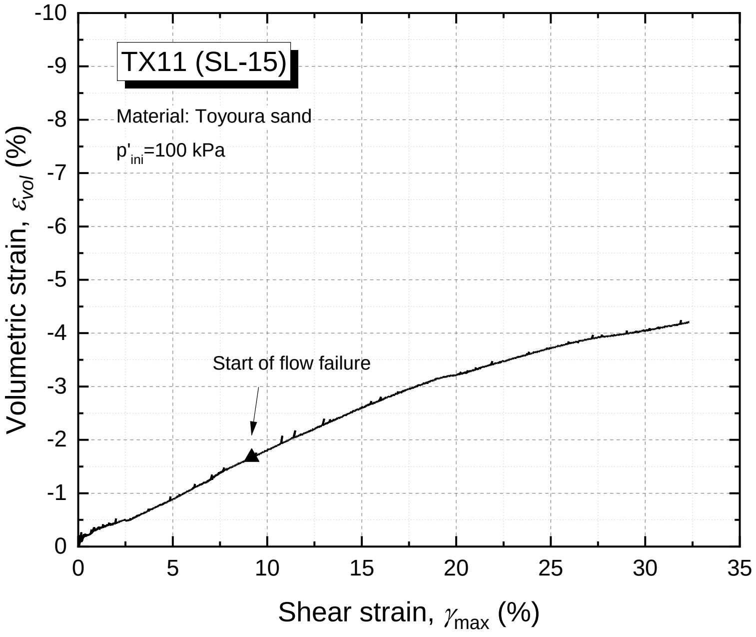

Figure 5-20 Relationship of volumetric strain and shear strain of TX11

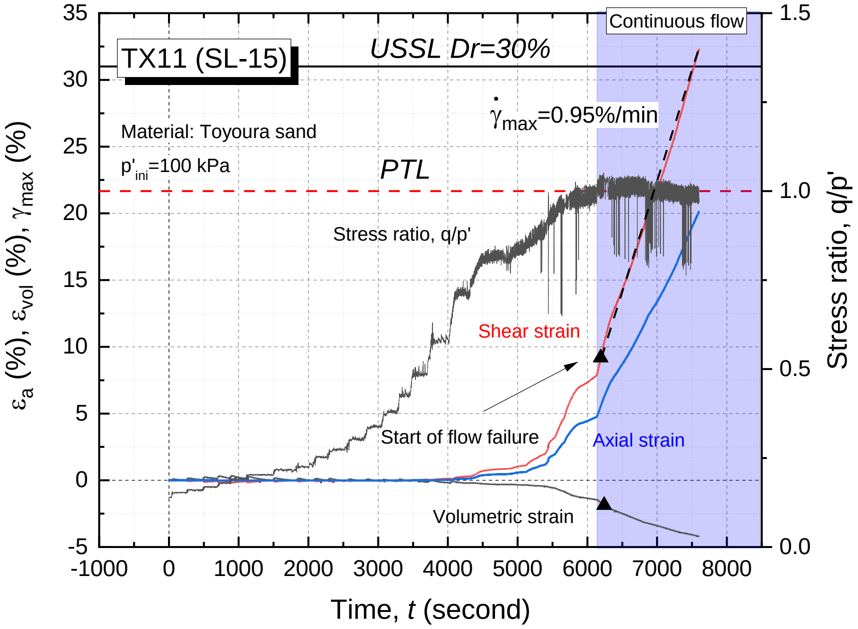

Figure 5-21 Strains development in time series of TX11

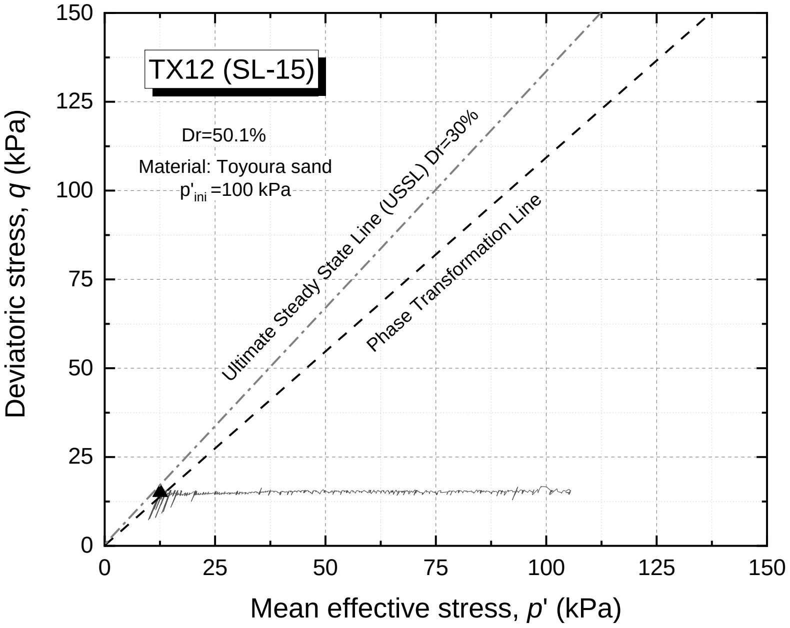

Figure 5-22 The stress path of TX12 (SL-15)

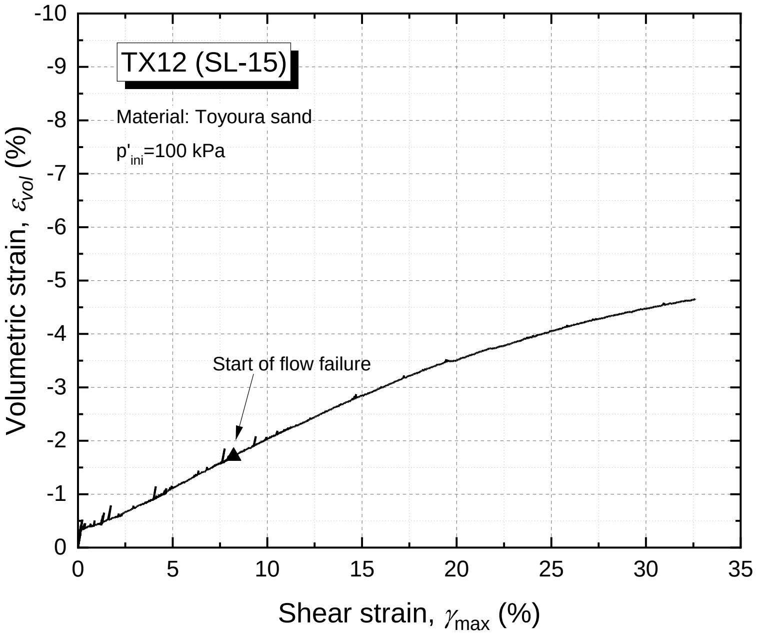

Figure 5-23 Relationship of volumetric strain and shear strain of TX12

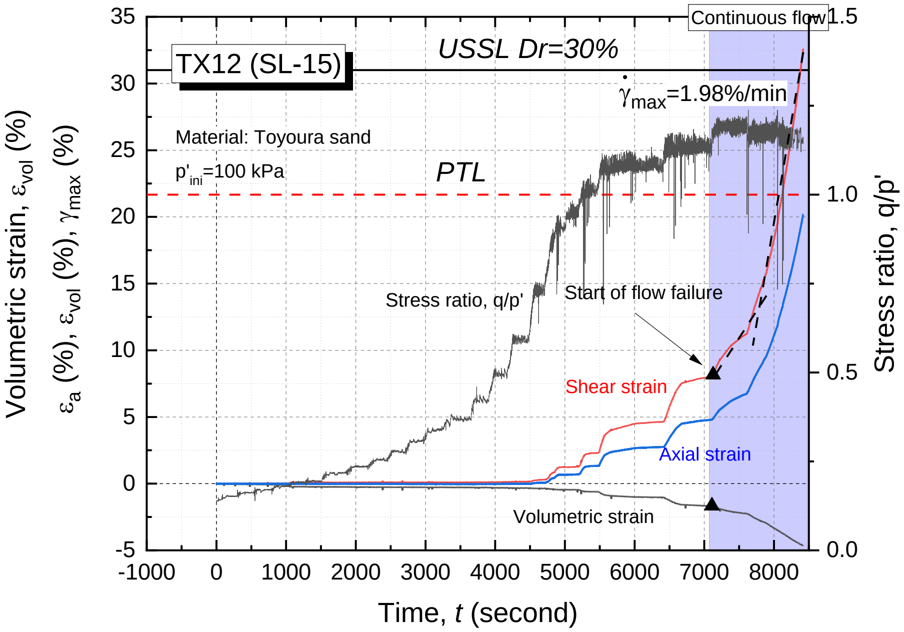

Figure 5-24 Strains development in time series of TX12

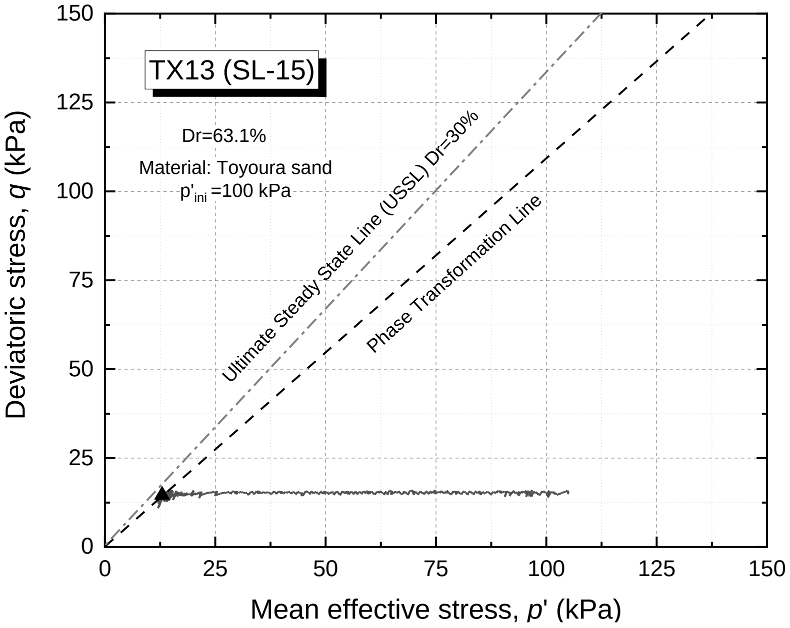

Figure 5-25 The stress path of TX13 (SL-15)

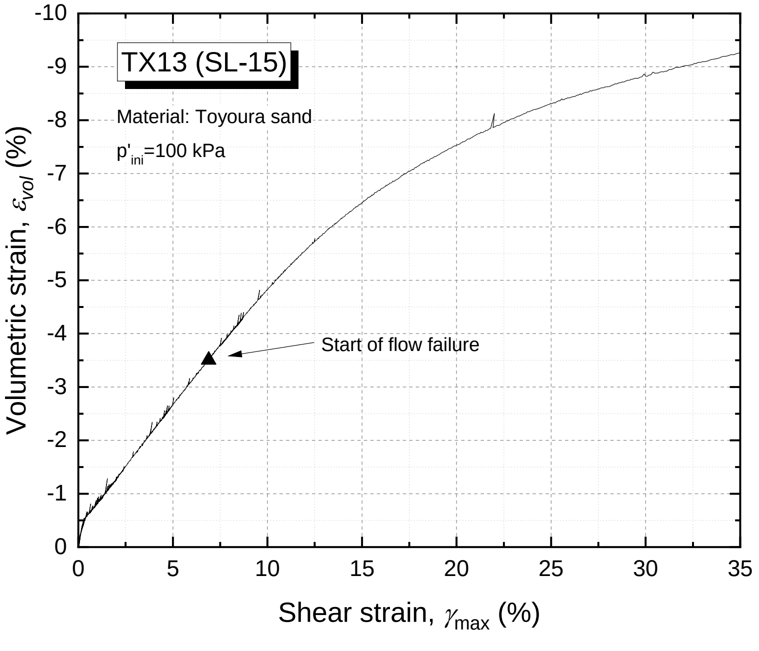

Figure 5-26 Relationship of volumetric strain and shear strain of TX13

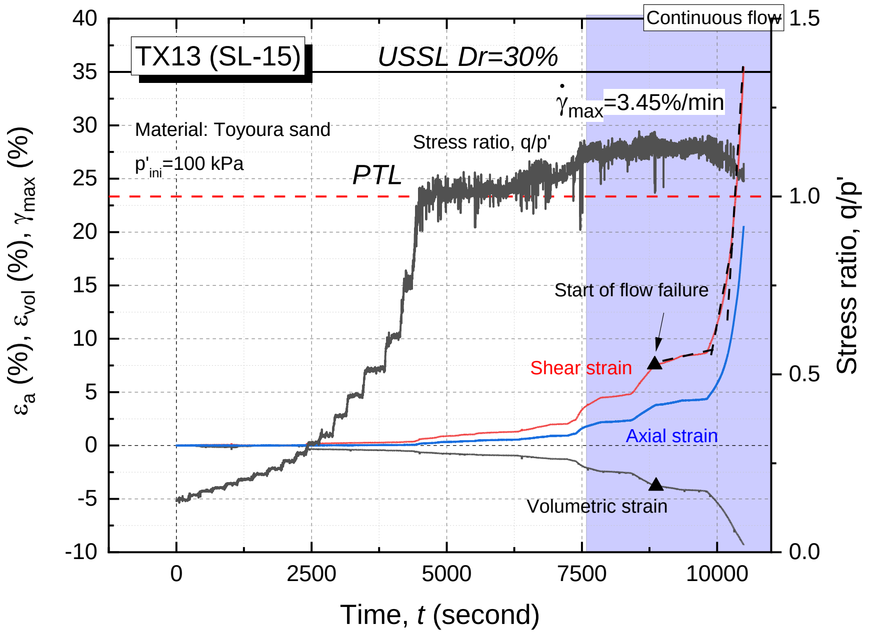

Figure 5-27 Strains development in time series of TX13

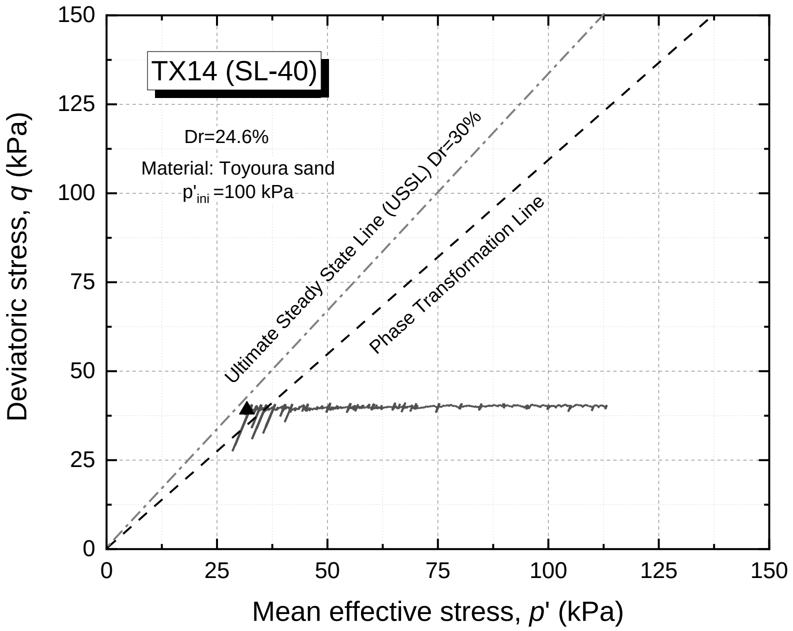

Figure 5-28 The stress path of TX14 (SL-15)

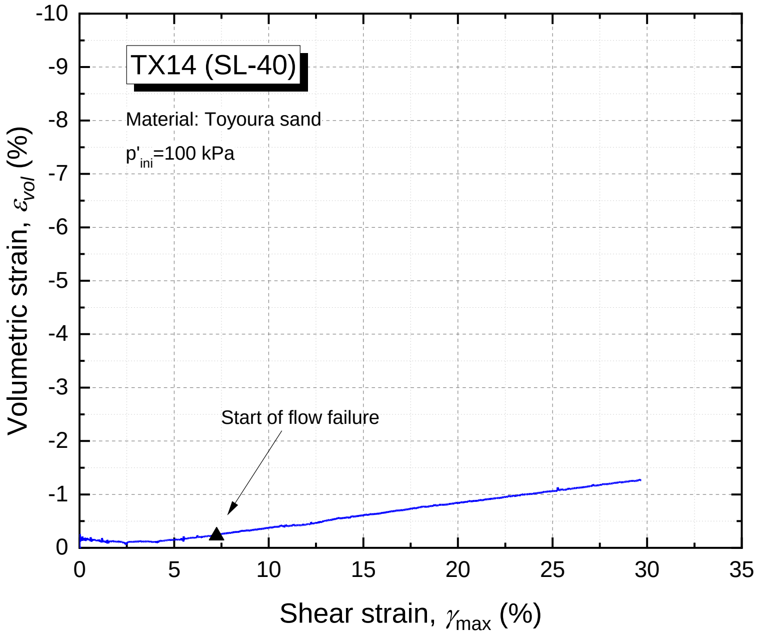

Figure 5-29 Relationship of volumetric strain and shear strain of TX14

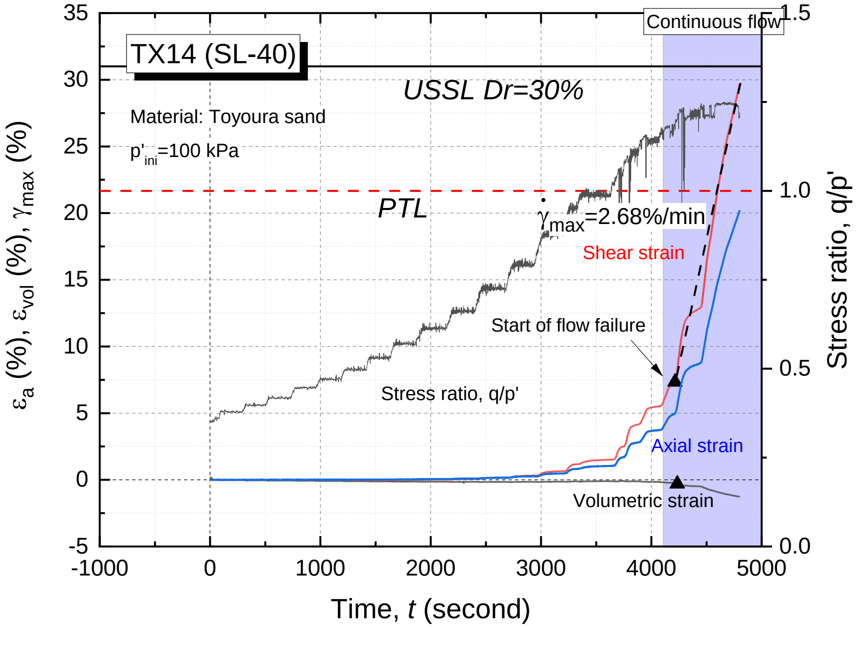

Figure 5-30 Strains development in time series of TX14

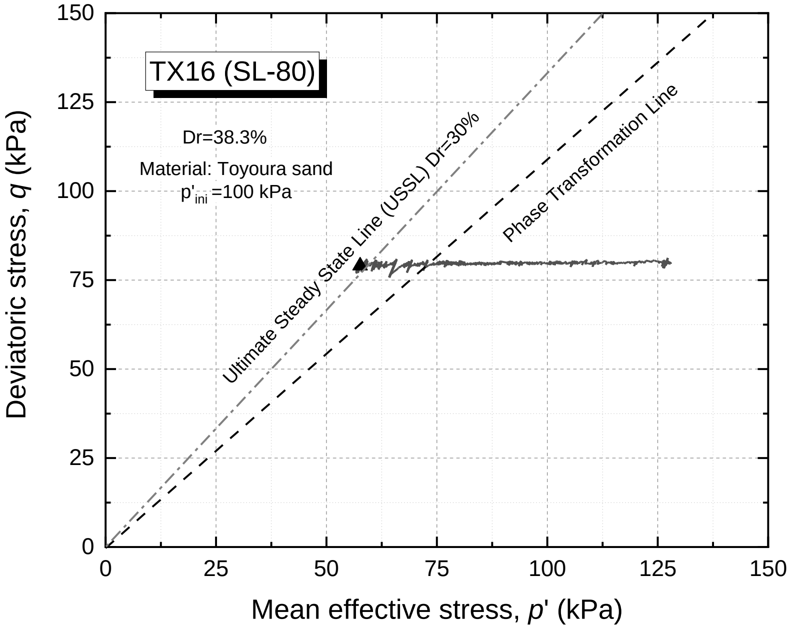

Figure 5-31 The stress path of TX16 (SL-15)

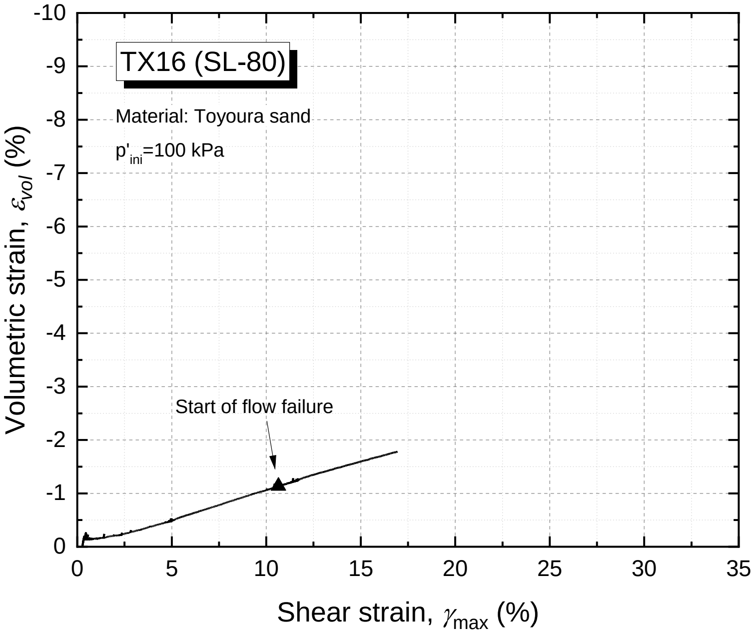

Figure 5-32 Relationship of volumetric strain and shear strain of TX16

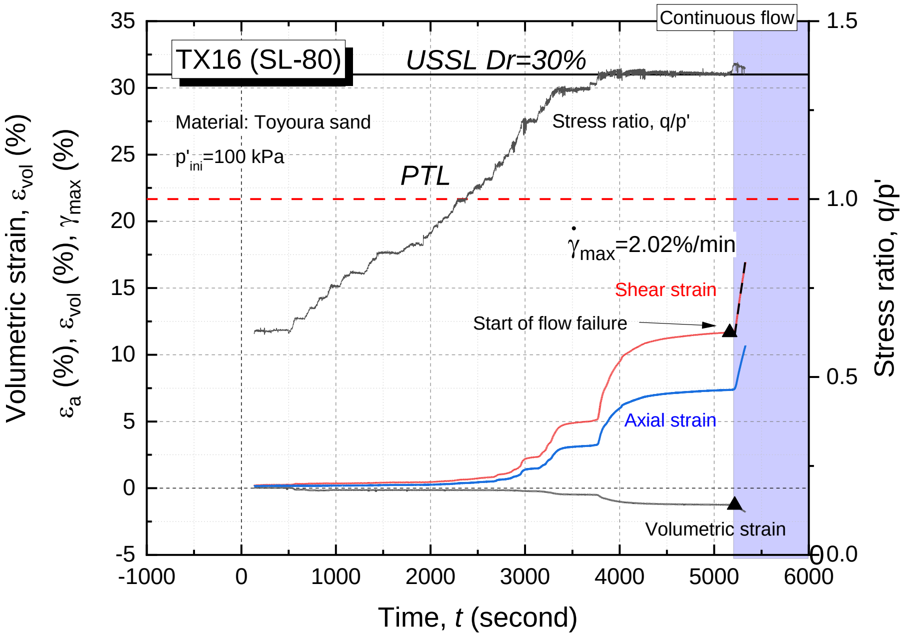

Figure 5-33 Strains development in time series of TX16

The experiments on Toyoura sand having the same initial density (Dr=24.8%-37%) with the different deviatoric stress, ranging from 5 kPa to 80 kPa shows that the higher amount of deviatoric stress acting on the specimen, the faster the rate of the shear strain at failure state.

In the static liquefaction test, as the mean effective stress approach the failure line at the p'-q plane, the dilation behavior under constant stress ratio on the specimen can be investigated, associating the flow failure phenomenon in the element test. This continuity of dilation behavior promotes the loss of inter-particle contact among the soil particles. At this stage, the rate of dilation behavior under constant stress ratio is defined by the amount of shear stress acting on the specimen.

It is important to understand that the rate of shear strain depends on the performance of deviatoric stress in the static liquefaction test. The strain-controlled Triaxial Apparatus uses a motor system to control the test and this might affect the credibility of results because the strain rate measured in this machine might depend on the performance of the motor speed, rather than showing the real behavior of specimen.

In order to address this issue, a static liquefaction test has been conducted in the stress-controlled Triaxial apparatus. The static liquefaction test performance in stress-controlled Triaxial Apparatus (TX27) is shown in Figure 5-34. The reduction of mean effective stress and the deviatoric stress are the same as conducted in strain-controlled Triaxial Apparatus. The development of strains is identical to other tests during the shearing process.

It can be seen that even if the static liquefaction conducted at the stress-controlled apparatus, the stress can be controlled constant during the failure state to measure the shear strain rate. The flow failure starts at the shear strain of around 4.4%. The flow failure rate shows its maximum after reaching shear strain around 15% with the shear strain rate is 5.86%/min.

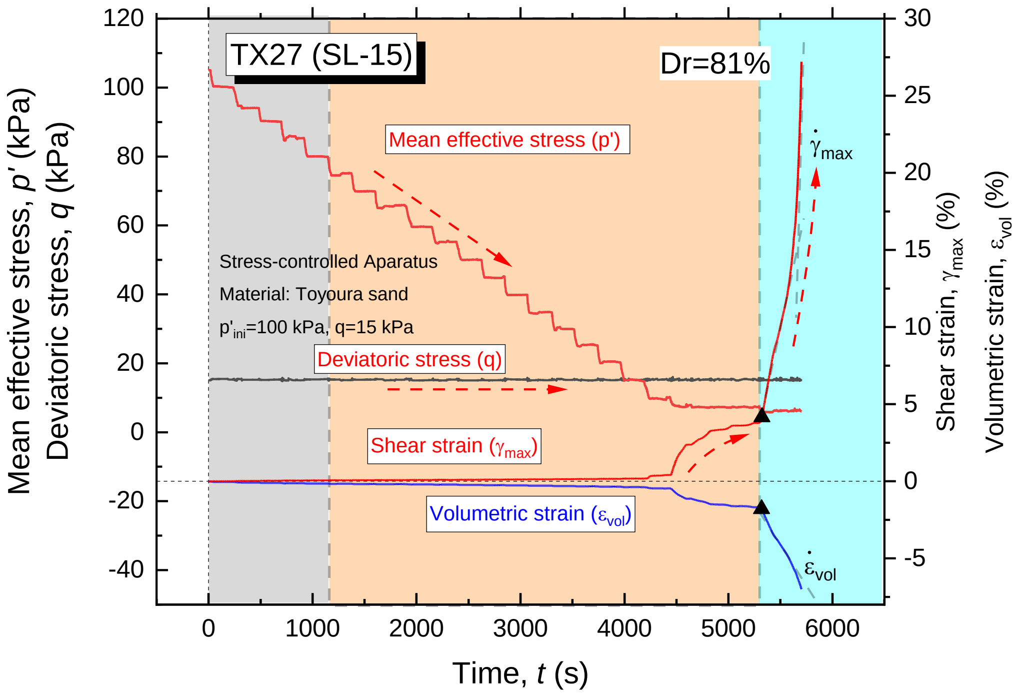

Figure 5-34 The experimental result of TX27 conducted in stress-controlled Triaxial Apparatus

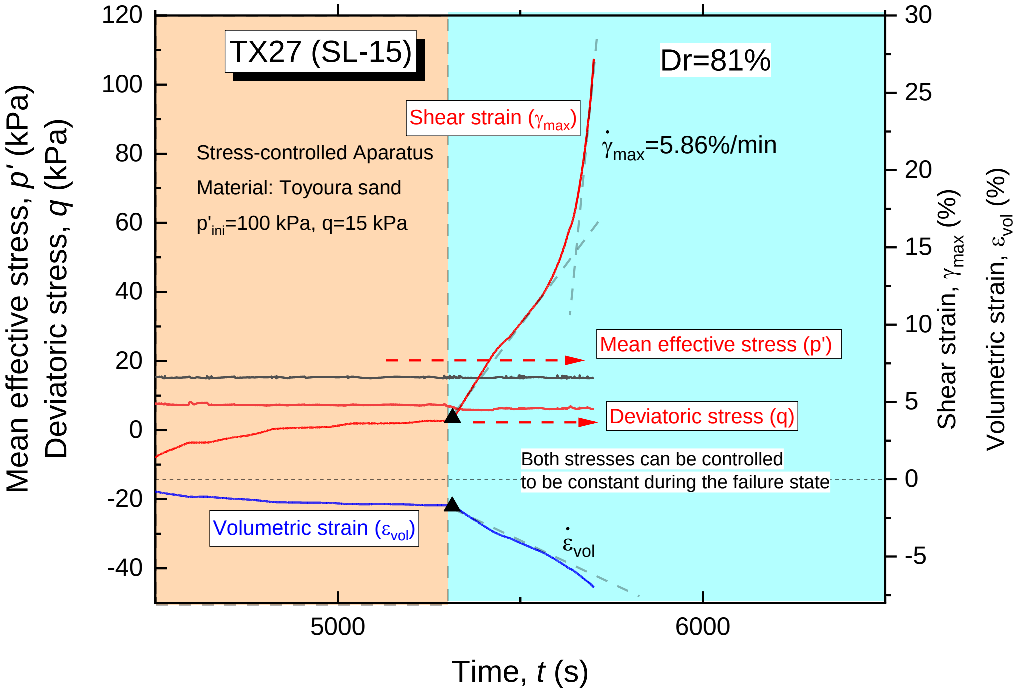

Figure 5-35 The shear strain rate measurement of TX27

5.3.2. Effect of initial density on shear strain rate characteristics of sandy soils

It is evaluated that the effect of the initial density is significant to the dilation behavior of sandy soils. The initial density defines the void distribution of a specimen that has a vital role in the volume expansion which corresponds to the dilation behavior of sandy soil. The results of shear strain rate measurement of Toyoura sand at the constant deviatoric stress and various densities are summarized as follow.

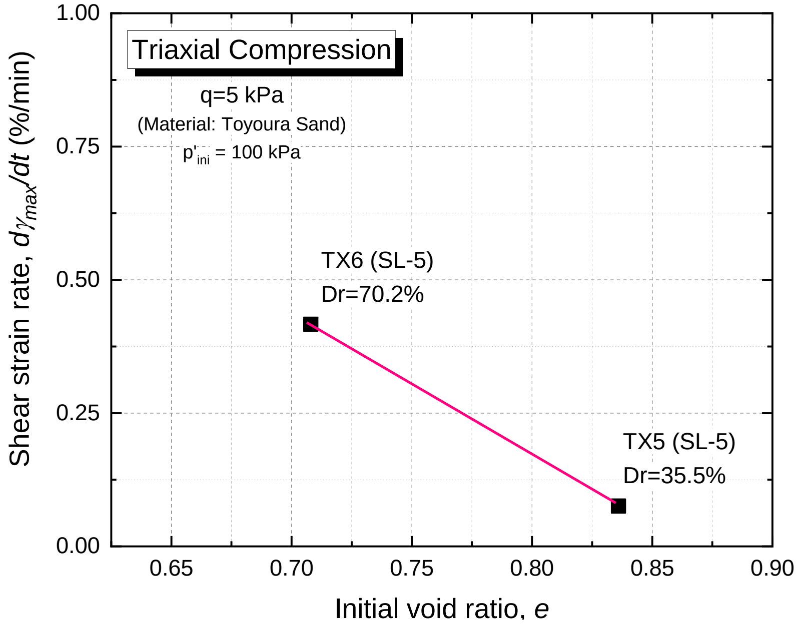

Figure 5-36 The shear strain rate characteristics of Toyoura sand with static shear stress 5 kPa considering the effect of initial void ratio

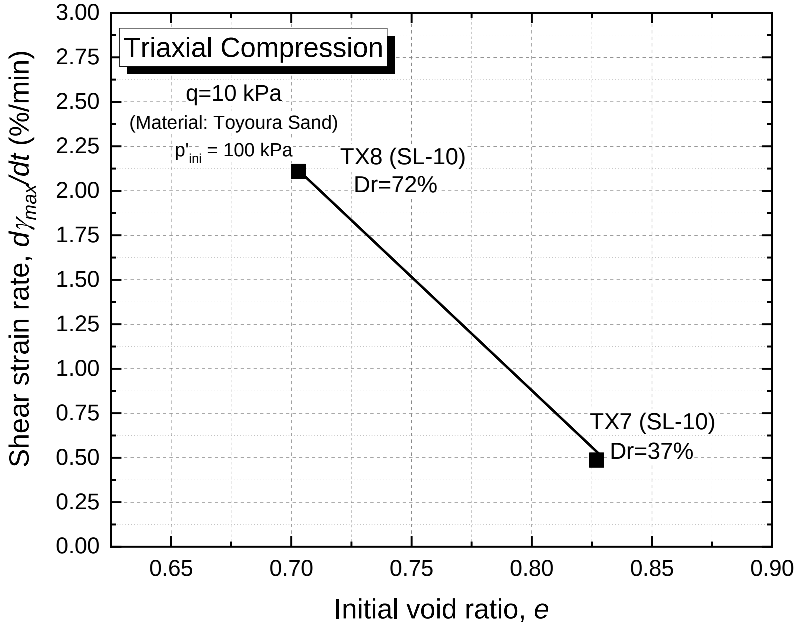

Figure 5-37 The shear strain rate characteristics of Toyoura sand with static shear stress 10 kPa considering the effect of initial void ratio

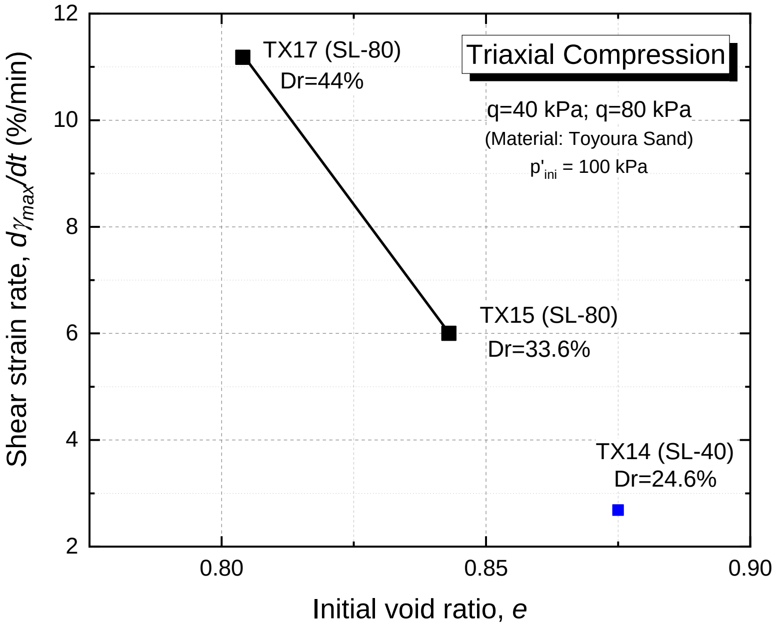

Figure 5-38 The shear strain rate characteristics of Toyoura sand with static shear stress 40 kPa and 80 kPa considering the effect of initial void ratio

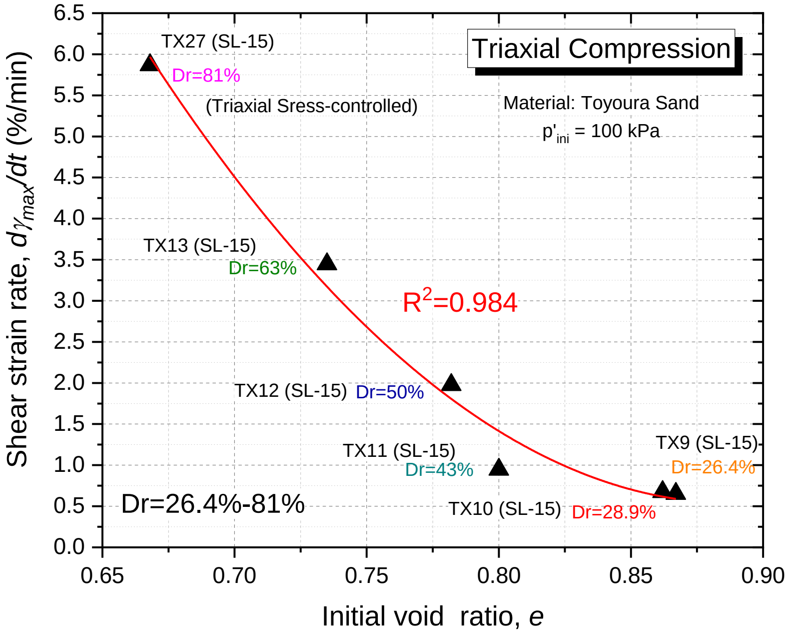

Figure 5-39 The shear strain rate characteristics of Toyoura sand with static shear stress 15 kPa considering the effect of initial void ratio

It is also found that the initial density of a specimen affects the shear strain rate, significantly. Static liquefaction test on Toyoura sand with various densities

(Dr=26.8%-81%), at the same deviatoric stress, q=15 kPa, and initial effective mean stress, p'_{ini}=100 kPa show that the denser the initial density of the specimen, the faster the shear strain rate at failure. In order to explain this finding, the same analogy as the previous explanation could be utilized. In the rapid flow area, the sandy soil undergoes continuous softening behavior.

When the dense specimen reaches the failure line, the amount of volumetric strain developed at this stage is higher than the loose material. This phenomenon can be associated with the theory of shear strength of dense material in which the interlocking of particles defines the shear strength. The denser the specimen, the higher the degree of particle interlocking, which results in higher strength. Thus, in this drained shearing process (static liquefaction test), the amount of volumetric strain necessary to fail the particle interlocking force is higher on dense specimen compared to others.

When the softening behavior started, the volumetric strain development at the dense specimen is already higher than the loose specimen. That higher amount of volumetric strain accumulated affects the rate of softening behavior. When the stress path of a specimen reaches the failure line, the sand particle contact becomes weaker and the softening behavior is continuing. The rate of this softening behavior is promoted by the accumulation of the volumetric strain. The higher the volumetric strain, the faster the softening behavior.

5.3.3. Shear strain rate relationship

In this study, two major variables affecting the flow behavior of clean sand have been employed to understand the characteristics of flow failure, which are static shear stress and the initial density of materials. In order to understand the significance of both variables and their relationship, the relationship graphs has been proposed in Figure 5-40 and Figure 5-41.

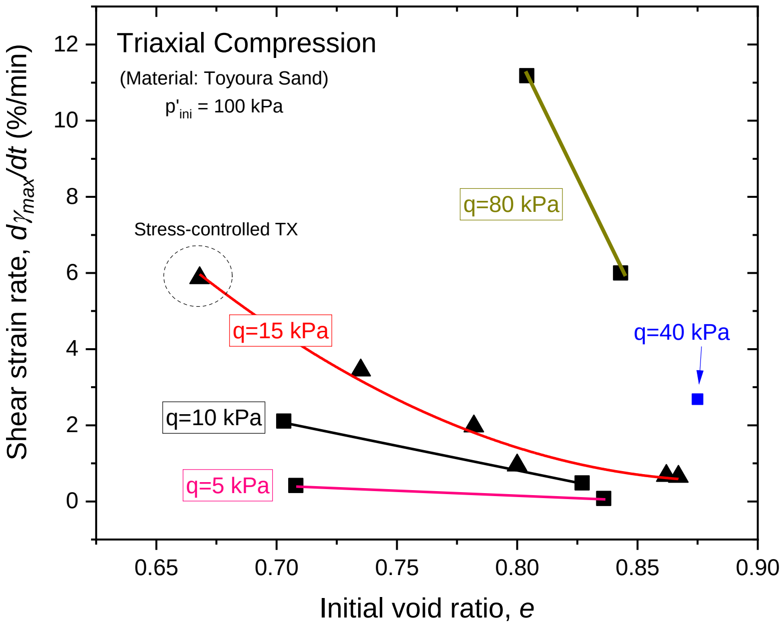

Figure 5-40 Relationship between initial density and shear strain rate by considering the static shear stress condition

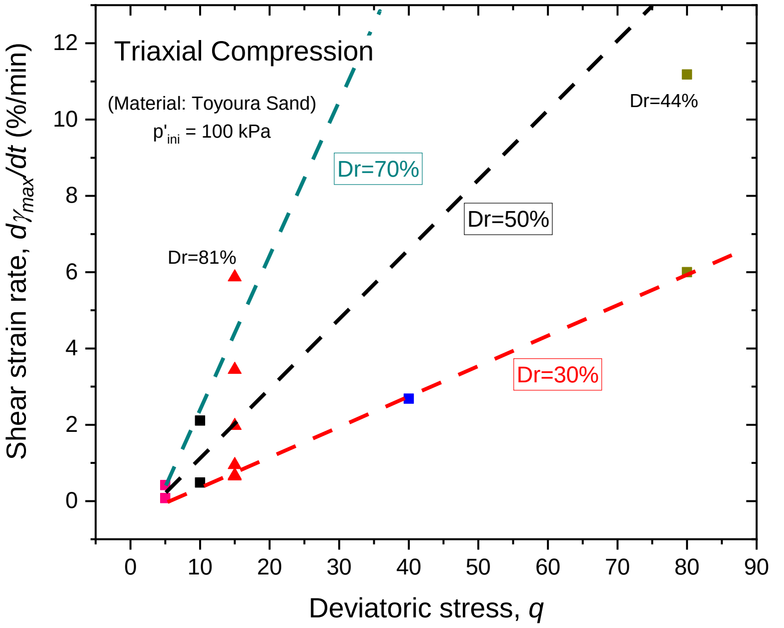

Figure 5-41 Relationship between static shear stress and shear strain rate by considering initial density

According to the graph, it is clear that the effect of static shear stress to the shear strain rate is depended on the initial density of a material. The effect of static shear stress becomes larger at the dense materials (high initial void ratio). Meanwhile, this effect will be decayed as the initial density of material get looser. It could be stated that the flow failure rate of dense sand will be sensitive to the ground inclination, compared to the loose sand.

5.3.4. Shear strain behavior and the dilatancy behavior of sand with fines

In the previous chapter, it is mentioned that the fine content (FC) will reduce the development of the volume expansion of sandy soil. This statement also have been validated using Drained Monotonic Test, stating that the specimen having fine content will most likely show contractive behavior than dilative as the shearing process occurred. The results of shear strain measurement of sand with fines are as follow.

Table 5-2 The test results of shear strain rate measurement conducted on Triaxial Apparatus for sand with fines

Code Test	Global void ratio, *e*	Static shear stress, *q* (kPa)	Mean effective stress, *p'* (kPa)	FC (PI)	Volumetric strain at flow failure point (%)	Shear strain rate (%/min)
TX18 (SL-15)	0.720	15	100	10 (NP)	-1.24	1.09
TX19 (SL-15)	0.683	15	100	10 (NP)	-0.3	0.06
TX20 (SL-15)	0.641	15	100	20 (NP)	-1.35	1.20
TX21 (SL-15)	0.563	15	100	20 (NP)	-2.06	0.17
TX22 (SL-15)	0.659	15	100	20 (IP=11)	0	1.61
TX23 (SL-15)	0.548	15	100	20 (IP=11)	-1.92	0.33

The previous results also showed that the effect of initial density to the shear strain rate of clean sand (FC<0.1) is significant. The denser the initial density, the higher the rate of shear strain development at the rapid flow area. Nevertheless, the contradictive results have resulted from the experiment on mixed sand with fine content. In order to draw the difference of flow behavior on the sand with fines by considering the effect of initial densities, the results of TX20 and TX21 is compared.

Both specimens have FC=20% (Non-plastic) and having the same conditions of testing. The shear strain rate of TX20 is 1.20%/min, while that of TX21 is 0.17%/min. In this case, the initial density of TX20 is higher than the TX21. Thus, it can be inferred that the denser material having fines perform faster than the looser material.

As the dilation behavior of sandy soil is defined by the void redistribution and the volumetric strain development, it could be stated that the volumetric strain rate promotes the shear strain rate development of sand with fines. In the dilation behavior of flow, the rate of migration of fluid to the soil body defines the volume expansion. The fines content, even after the flow continues, hinder the volume expansion of the specimen and thus results in small volumetric strain development. This mechanism can be described by using the volumetric strain rate after the flow failure point. This number represents the rate of water inflow infiltrates to the specimen after the failure condition. From the experiment results of TX20 and TX21, it is clear that the volumetric strain rate of TX20 is 0.051%/min which is faster than that of TX21 with 0.02%/min. Both experiment results are shown in Figure 5-42 and Figure 5-44, respectively for TX20 and TX21.

The summary of the results of other experiments in the sand with fines in Triaxial Apparatus is shown in Figure 5-59 and Figure 5-60. From the summary of experiment results using sand with fines, in contrast to the clean sand’s results, it is clear that the dense material shows a slower shear strain rate compared to the looser sand.

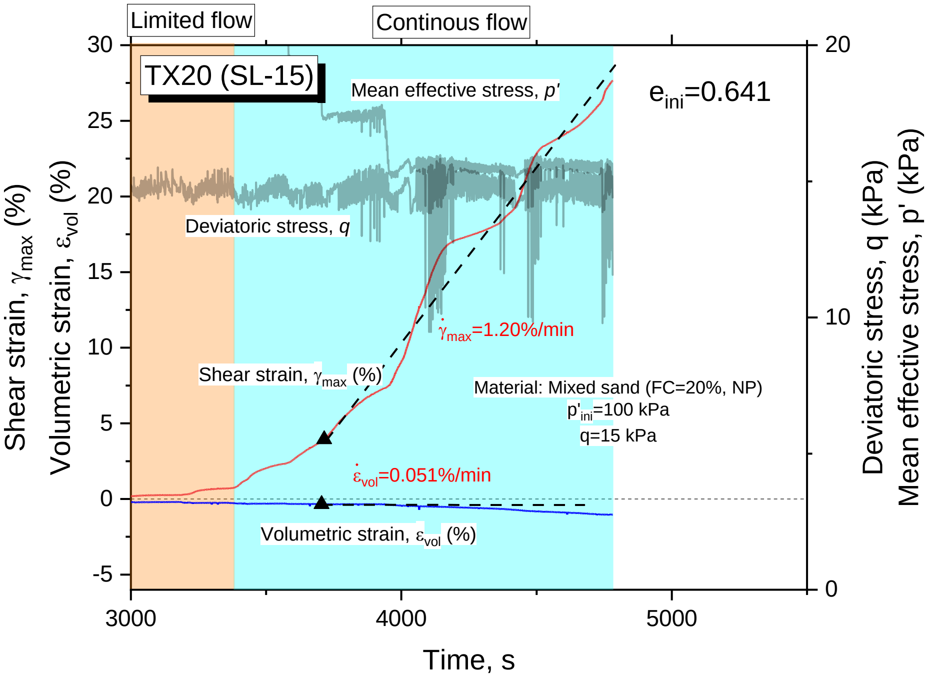

Figure 5-42 The shear strain rate measurement of TX20

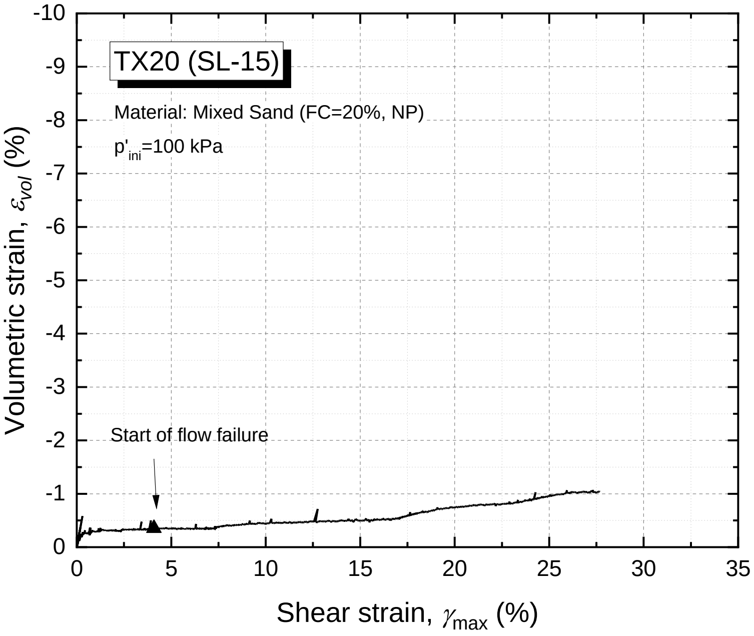

Figure 5-43 Relationship of volumetric strain and shear strain of TX20

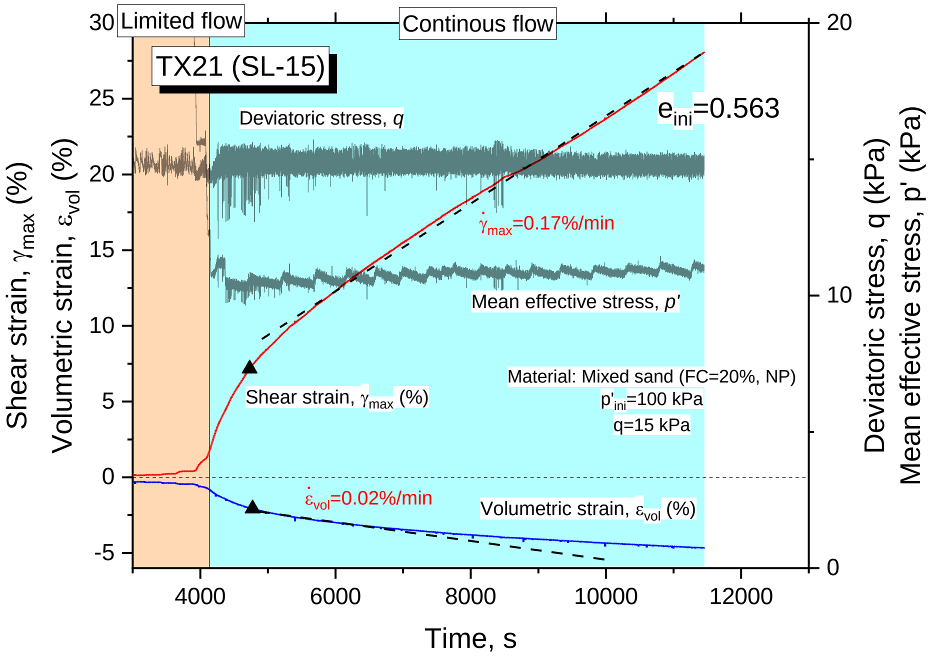

Figure 5-44 The shear strain rate measurement of TX21

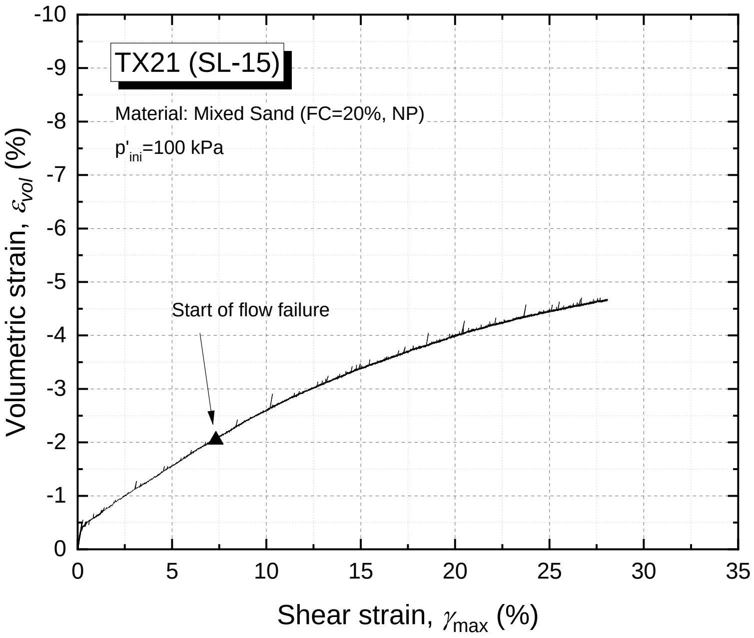

Figure 5-45 Relationship of volumetric strain and shear strain of TX21

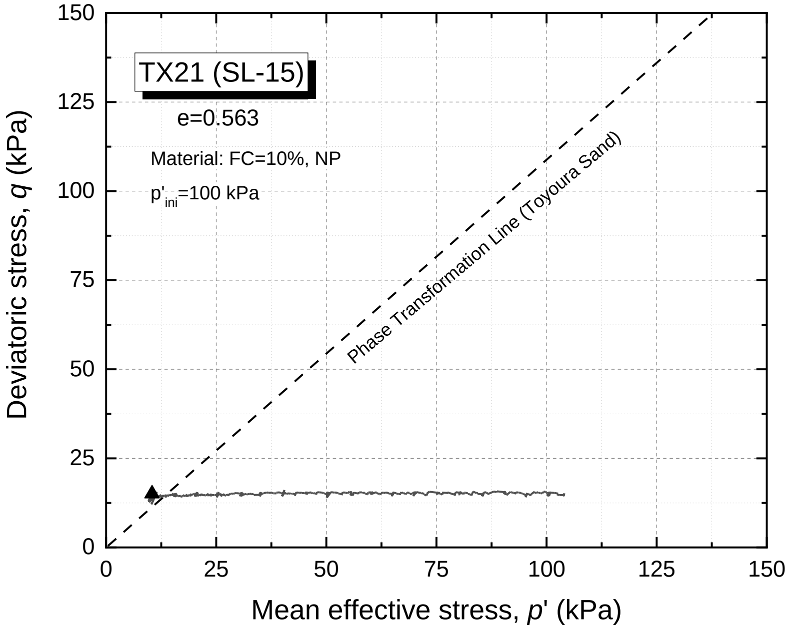

Figure 5-46 The stress-path of TX21

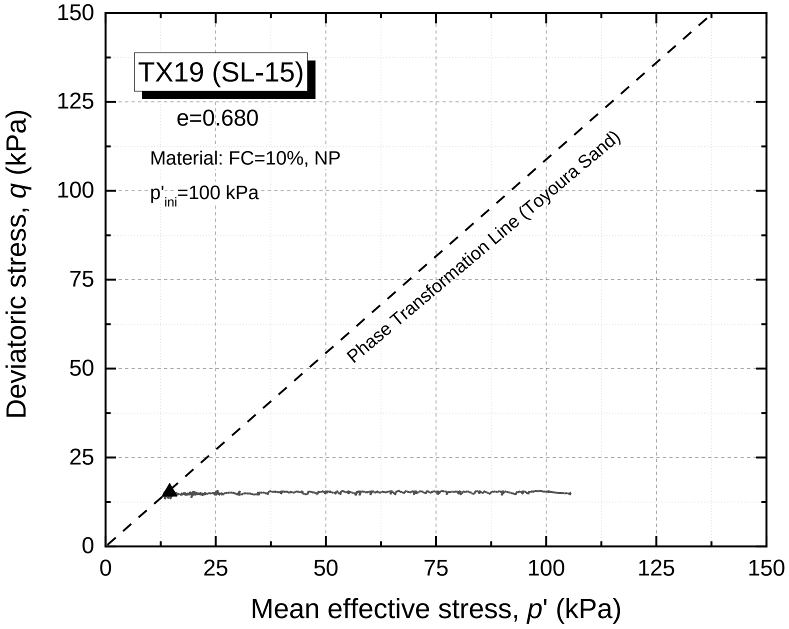

Figure 5-47 The shear strain rate measurement of TX19

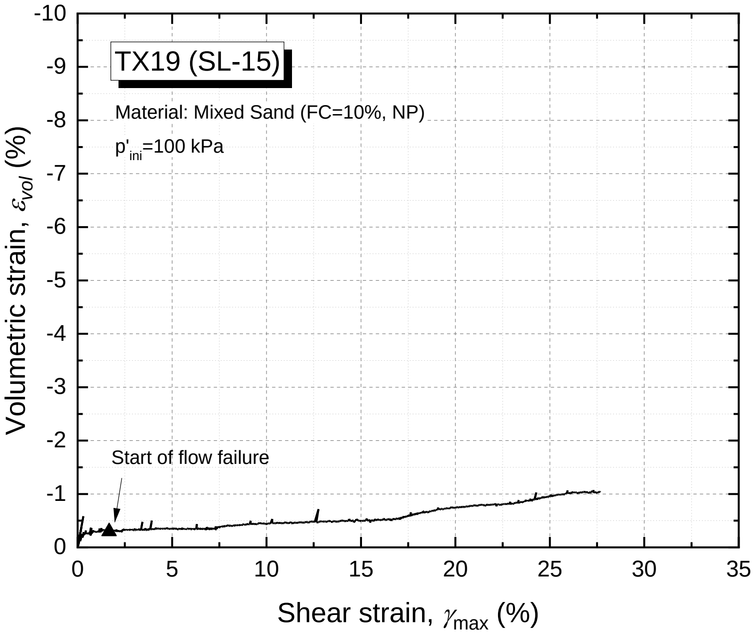

Figure 5-48 The shear strain rate measurement of TX19

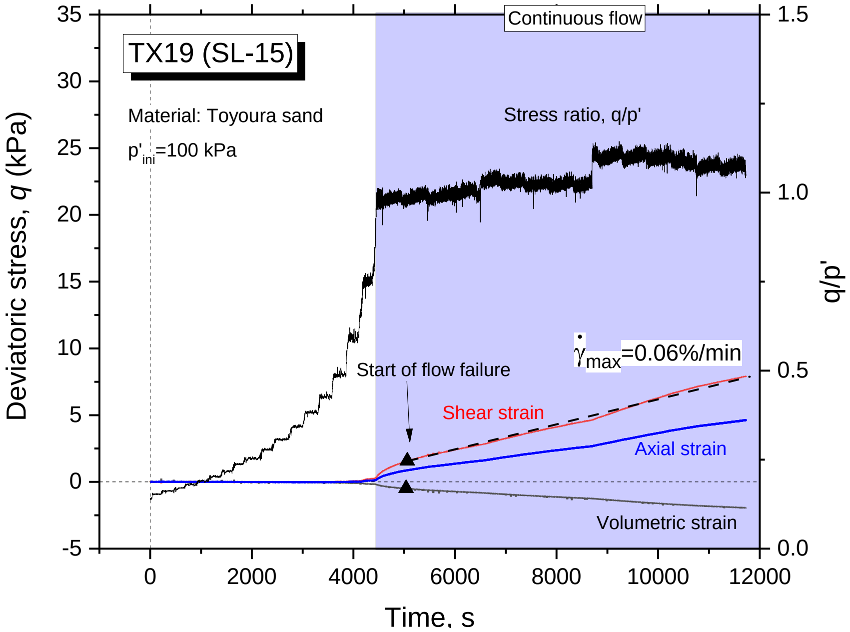

Figure 5-49 The shear strain rate measurement of TX19

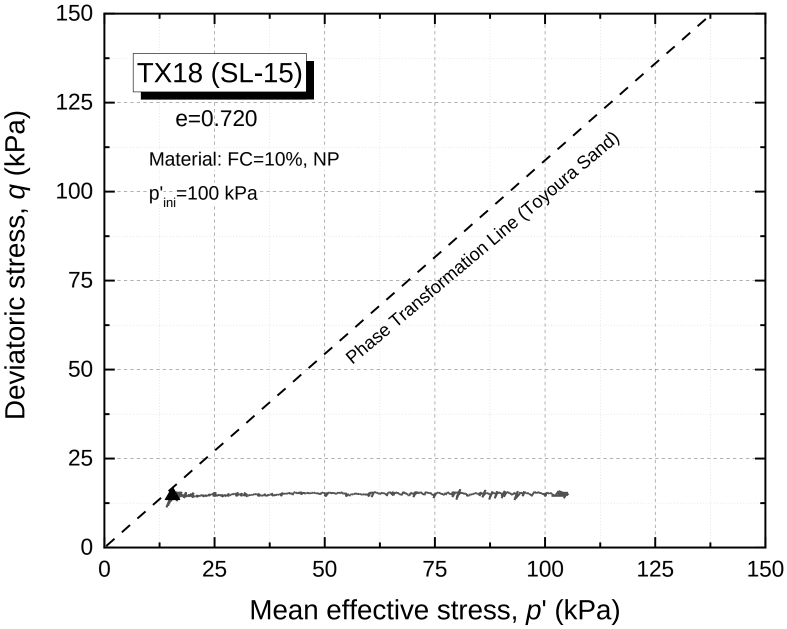

Figure 5-50 The stress-path of TX18

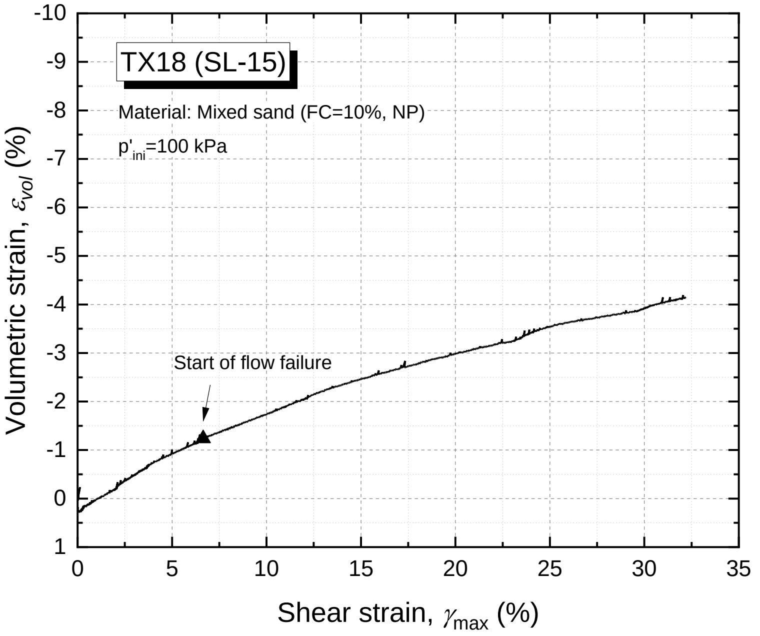

Figure 5-51 Relationship of volumetric strain and shear strain of TX18

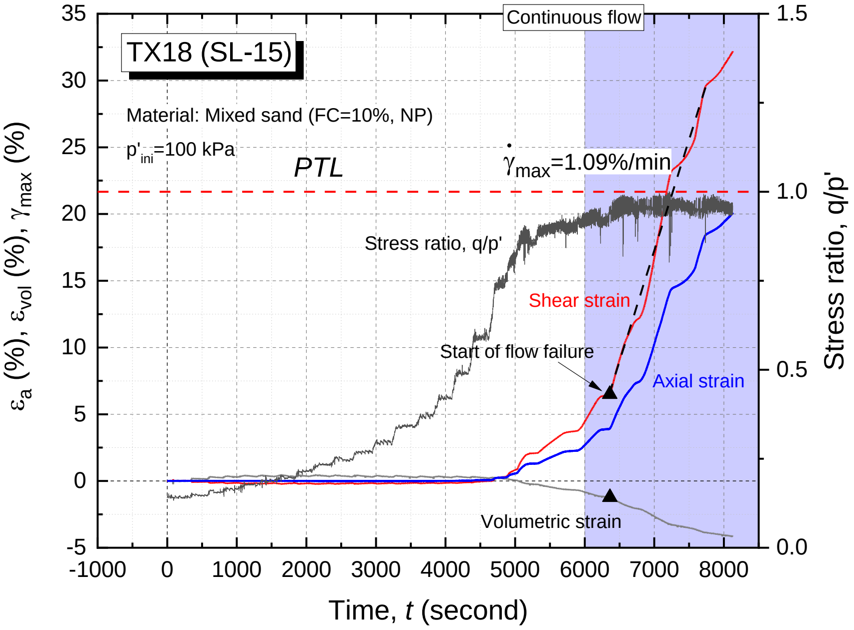

Figure 5-52 The shear strain rate measurement of TX18

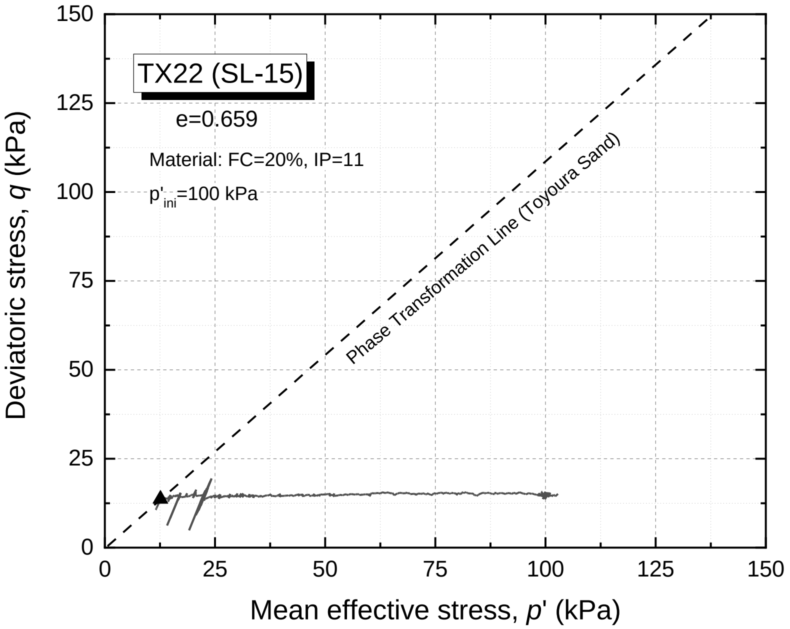

Figure 5-53 The stress-path of TX22

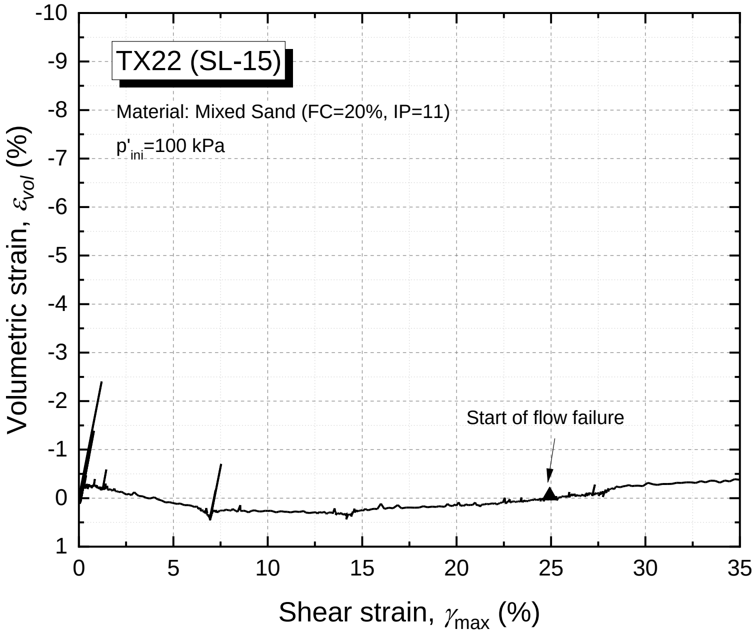

Figure 5-54 Relationship of volumetric strain and shear strain of TX22

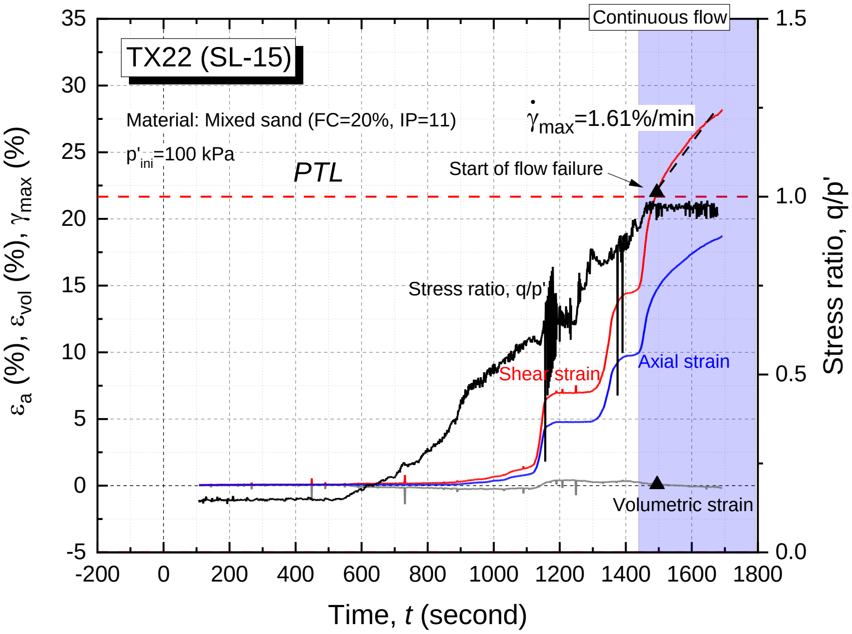

Figure 5-55 The shear strain rate measurement of TX22

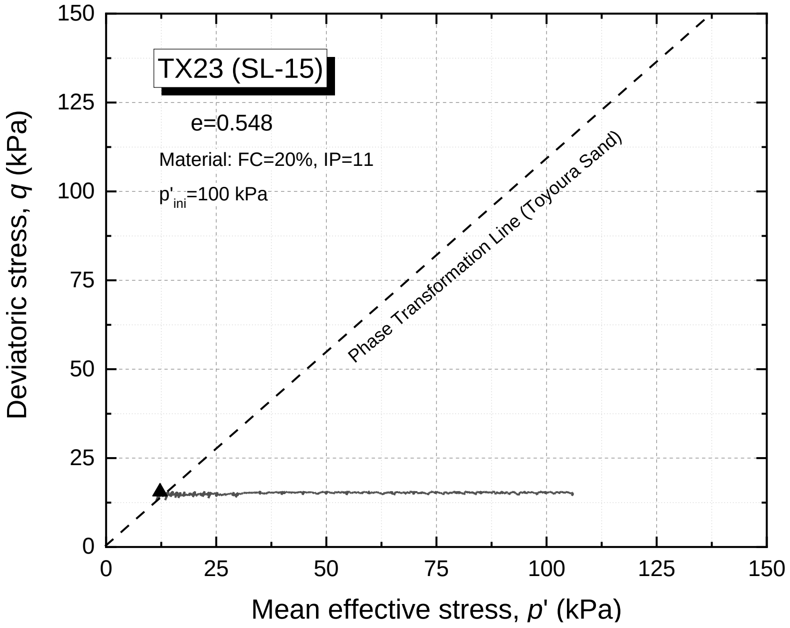

Figure 5-56 The stress-path of TX23

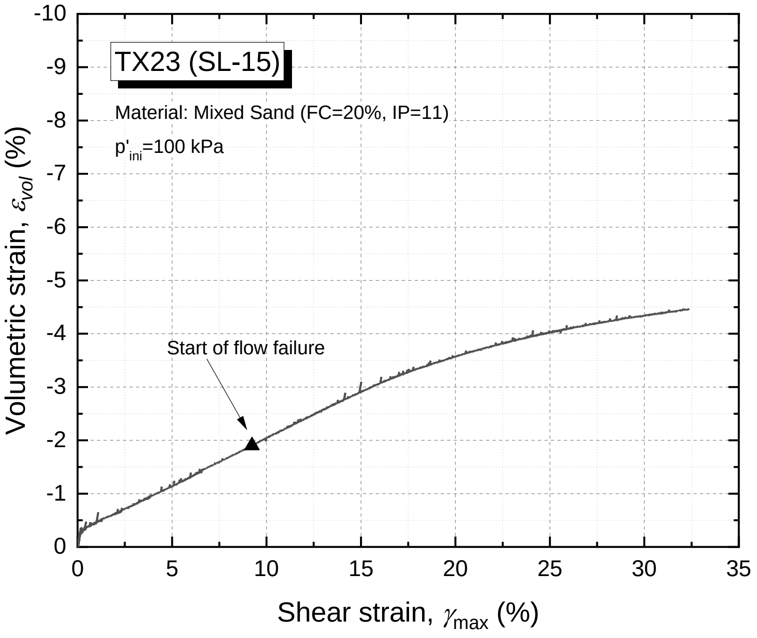

Figure 5-57 Relationship of volumetric strain and shear strain of TX23

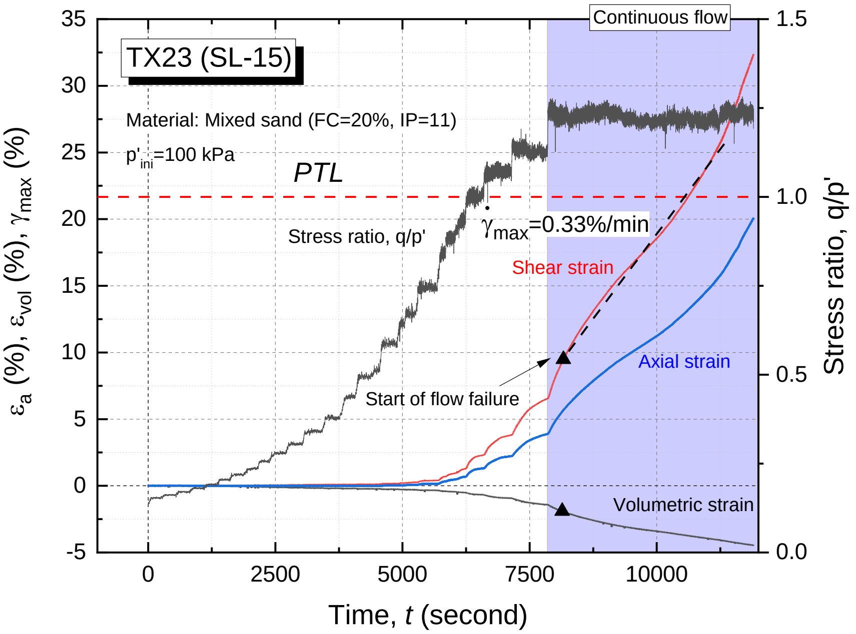

Figure 5-58 The shear strain rate measurement of TX23

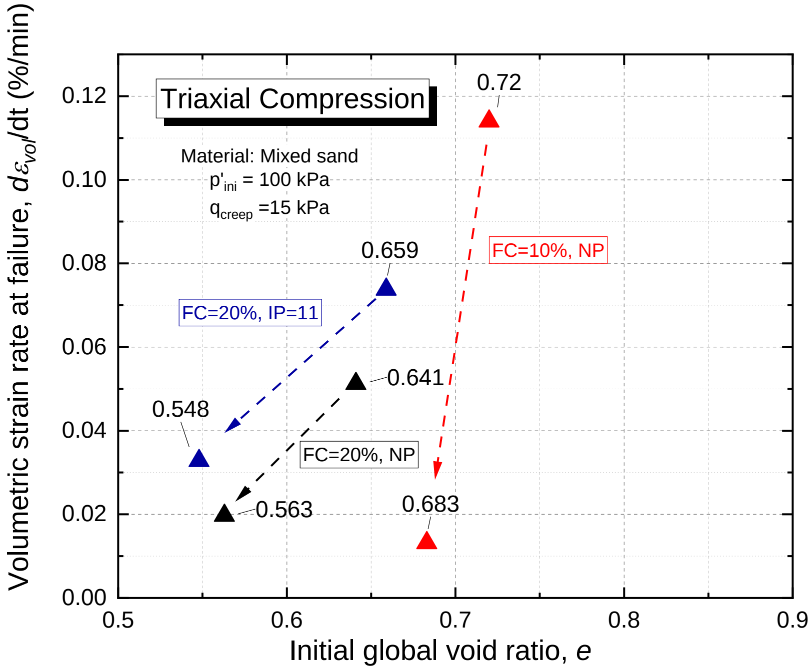

Figure 5-59 The summary of volumetric strain rate measurement of sand with fines in Triaxial Apparatus

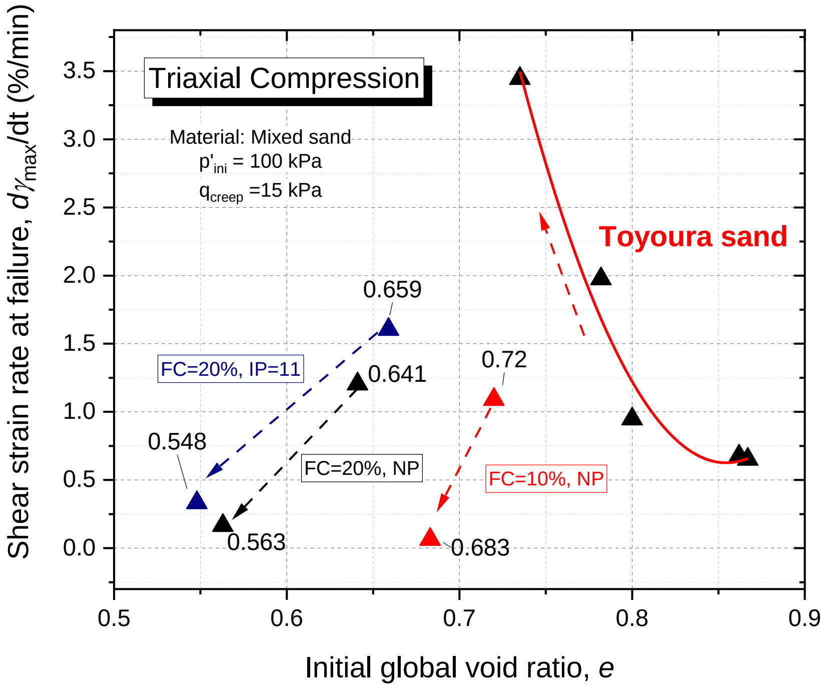

Figure 5-60 The summary of shear strain rate measurement of sand with fines in Triaxial Apparatus

5.4. Summary

The shear strain rate development represents the flow rate characteristics of sandy soils in the element test. This study investigates the effect of static shear stress, initial density, and fine content on the shear strain rate of sandy soil.

1. It is mentioned that the effect of static shear stress on the development of volumetric strain is not significant. However, the effect of static shear stress on the strain rate development is significant. The higher the static shear stress, the faster the rate of shear strain at failure.
2. The experiment results also show that the initial density affects the shear strain rate behavior. The densest the initial density of a material, the faster the shear strain rate at failure.
3. The relationship of both the effect of static shear stress and the effect of initial density on the strain rate characteristics is examined. It is found that the effect of

static shear stress will be significant on the dense specimen and become less significant as the initial density of the specimen is loose.

4. The effect of fine content on the shear strain rate has been observed. In contrary to the clean sand, the dense material of mixed sand with fines show less shear strain rate compared to the loose material. This phenomenon emphasizes the significance of volumetric strain accumulation to the shear strain rate.

5.5. References

Boulanger, R. W., & Truman, S. P. (1996). Void redistribution in sand under post-earthquake loading. *Canadian Geotechnical Journal*, Vol. 33: 829-834.

Casagrande, A., & Rendon, F. (1978). *Gyratory shear apparatus design, testing procedures.* Vicksburg: U.S. Army Corps of Engineers, Waterways Experiment Stations .

Hamada, M., Yasuda, S., & Wakamatsu, K. (1991). Liquefaction induced permanent ground displacement in Niigata city. *International Conferences on Recent Advances in Geotechnical Earthquake Engineering and Soil Dynamics*, *33*. St. Louis.

Japanese Society of Civil Engineers. (1966). *The report of damage investigation in the 1964 Niigata earthquake.* Tokyo: Japanese Society of Civil Engineers.

Kawakami, M., & Asada, A. (1966). Damage to the ground and earth structures by the Niigata earthquake of June 16, 1964. *Soils and Foundations, 6*(1), 14-30.

National Research Council of United States. (1985). *Liquefaction of soils during earthquakes* . Washington, D.C: National Academy Press.

Tokimatsu, K., Taya, Y., & Zhang, J. M. (2001). Effects of pore water redistribution on post-liquefaction deformation of sands. *Proceeding of 15th International Conference on Soil Mechanics and Geotechnical Engineering* (pp. 289-292). Rotterdam : Balkema.

Chapter 6 FLOW DEFORMATION BEHAVIOR OF SANDY SOILS UNDER CONSTANT STATIC SHEAR STRESS AT LARGE STRAIN

6.1. Introduction

In the previous chapters, the flow deformation behavior has been examined using Triaxial Apparatus with the maximum axial strain is 20%. In order to understand comprehensively about this flow behavior, a study on large strain area is conducted by using the Torsional Shear Apparatus with Hollow Cylindrical specimen.

Several researchers have conducted the previous study on the role of initial static shear stress on the undrained cyclic behavior of saturated sand. In previous studies, in the case of simple shear tests (Vaid and Finn, 1979) or torsional shear tests (Tatsuoka et al., 1982), the shear strain level was limited to 10 % due mainly to mechanical limitation of the employed apparatus; as well, in the case of triaxial tests, due to larger extents of non-uniform deformation of the specimen at higher strain levels, the axial strain level could not exceed 20 % (Vaid and Chern, 1983; Hyodo et al., 1991, among others).

In this study, the Torsional Shear Apparatus has been modified to able to achieve shear strain more than 100% at a single amplitude. Thus, the large strain phenomenon could be observed vividly. Moreover, in this Torsional Shear Apparatus, the shear stress is applied directly to the specimen, which is different from the conventional Triaxial Apparatus. This direct shear is more suitable to model the soil element that undergoes the earthquake motion.

To investigate the post liquefaction lateral spreading of sandy ground in undrained shear behavior, Yasuda et al. (1992) studied the post liquefaction shear stress and strain relationship using hollow cylindrical tests under undrained conditions. They concluded that relatively small shear stiffness after cyclic shearing contributes to the post liquefaction lateral spreading. However, it is difficult to explain the large deformation observed in liquefaction areas based only on the shear behavior of undrained sand.

The purpose of this study is to examine the soil condition in the field into the element testing condition, whether the long-distance flow failure could occur at the gently sloping ground or not. Therefore, a very gentle slope condition has been set by assuming the inclination around 3-4% and convert it to the shear static condition. Moreover, it is also assuming that the depth of the flow failure layer is shallow, so in this experiment, the differential stress (τ_d) is controlled to be zero, assuming that there is no additional stress acting on the surface of the soil element.

6.2. Dilation Behavior on Large Strain Level

It is mentioned that the Torsional Apparatus occupied in this study could achieve 100% of shear strain in a single amplitude. As this experiment could model the soil element having earthquake motion (simple shear), the validity of the testing method should be examined first. The stress path of static liquefaction test with constant shear stress loading is illustrated in Figure 6-1. The results of the experiment in time series is presented in Figure 6-2.

In the previous chapter, the dilation behavior of sandy soils has been examined in Triaxial Apparatus until the axial strain reaches 20%. In order to compare the reliability of the test results, a series of static liquefaction experiments using Toyoura Sand with various initial densities have been conducted in Torsional Shear Apparatus. The list of the test are shown in Table 6-1.

Table 6-1 The summary of experiment results conducted in Torsional Shear

Code Test	Relative density, *Dr* (%)	Static Shear Stress, τ (kPa)	Mean effective stress, *p'* (kPa)	Volumetric strain at flow failure (%)	Shear strain rate, $\dot{\gamma}$ (%/min)
TS 1 (23-7.5)	23.4	7.5	100	-1.25	0.28
TS 2 (44-7.5)	44	7.5	100	-1.34	0.79
TS 3 (50-7.5)	50	7.5	100	-0.61	1.37
TS 4 (58-7.5)	58	7.5	100	-0.70	1.98
TS 5 (73-7.5)	73	7.5	100	-2.68	1.02
TS 6 (84-7.5)	84	7.5	100	-4.50	3.52

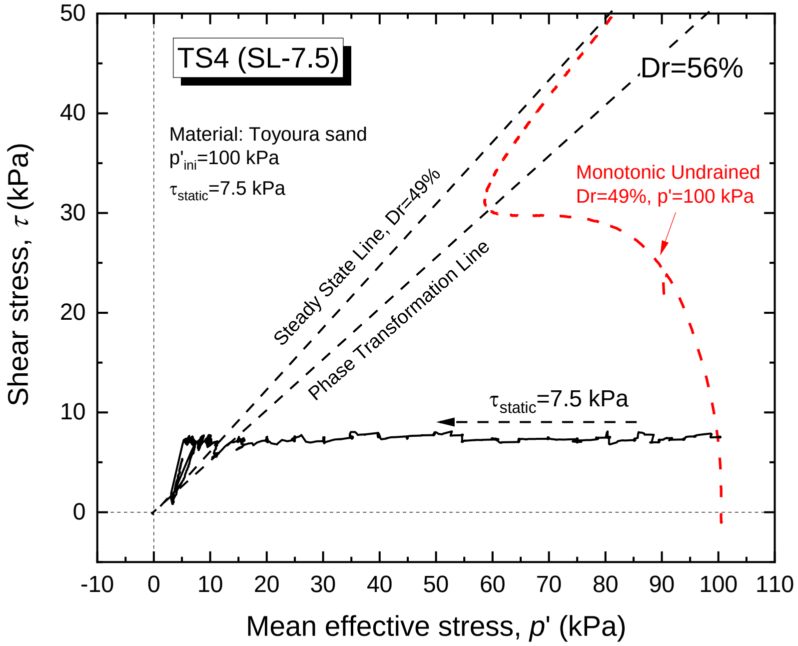

Figure 6-1 Stress path of static liquefaction test conducted in Torsional Shear Apparatus (TS4)

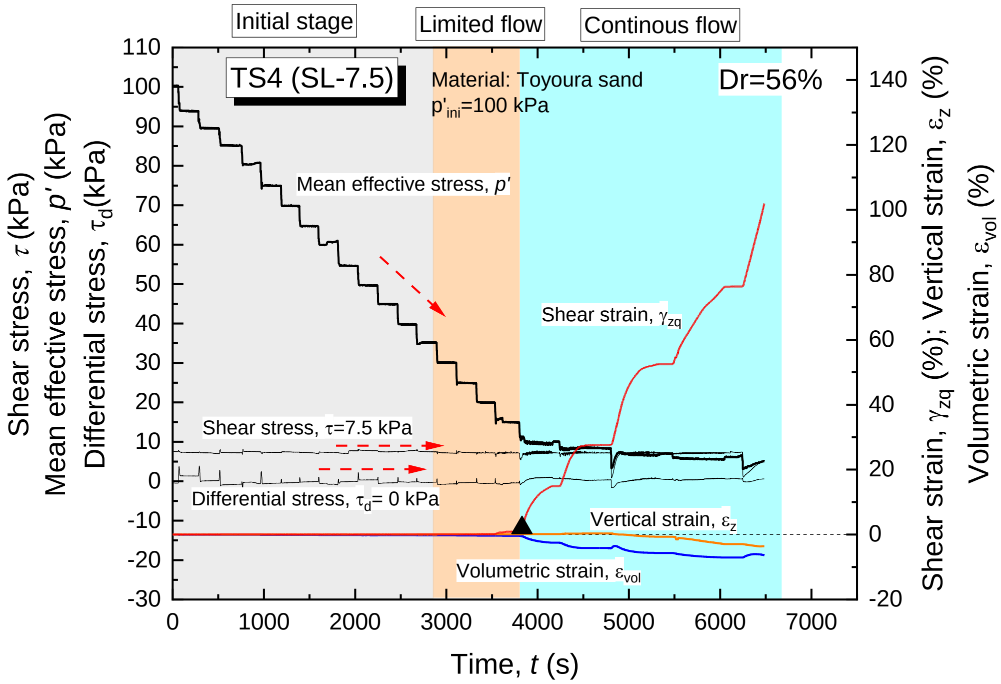

Figure 6-2 The static liquefaction test result in the time series of TS4

In TS-4, the mean effective stress is reduced every 5 kPa within 1 minute and follow by the creep around 3 minutes before reducing the next stage to allow the strains to develop. In this test, shear stress is kept at 7.5 kPa and the differential stress is kept constant at 0 kPa until reaching the failure line. The detail of the measurement of the shear strain rate at failure is shown in Figure 6-3.

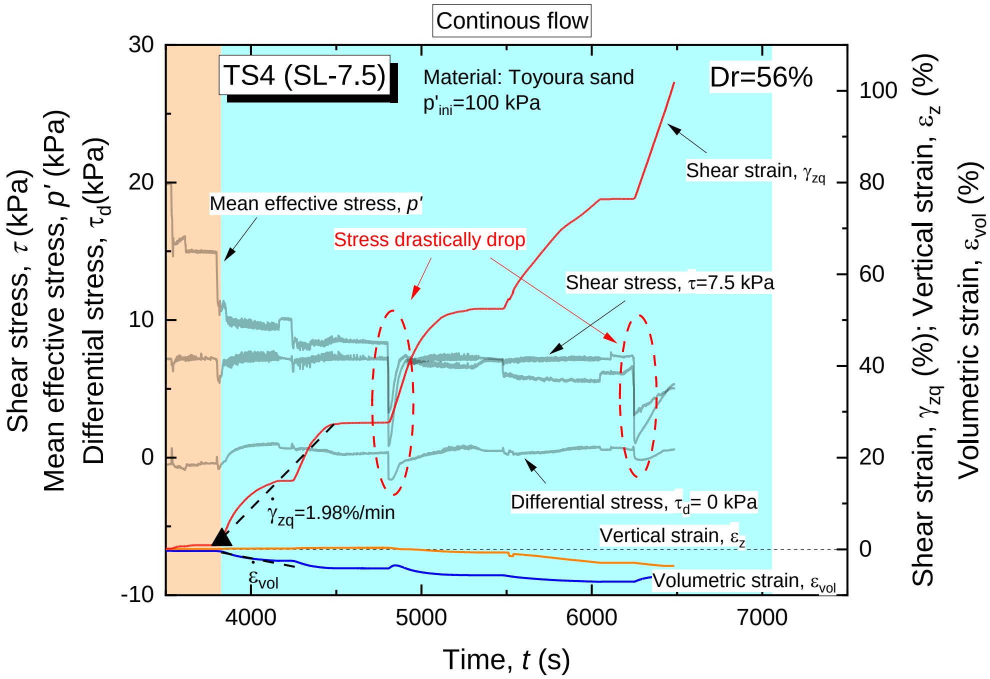

Figure 6-3 The measurement of shear strain rate at failure in Torsional Shear Apparatus (TS4)

It is observed that after the flow failure starts at the shear strain level around 2.88%, the phenomenon of the sudden drop of mean effective stress, shear stress, as well as the differential stress could be observed at the large shear strain level, which around 23%. After the drop, all the stresses are recovered following by the development of shear strain and volumetric strain. The phenomenon of negative vertical strain, showing subsidence is observed after the first stresses drop during the failure. The second stress drop occurs again after the shear strain reaches 80%, following by the longer recovery of stresses.

To examine the shear strain rate, in this study, the measurement of this variable is conducted before the first stress drop, considering the uniformity of the specimen. After the first stress drop, the specimen shape is changed resulting in bias and unreliable calculation results. Therefore, the investigation of this study will be focused on the area before the stress drop.

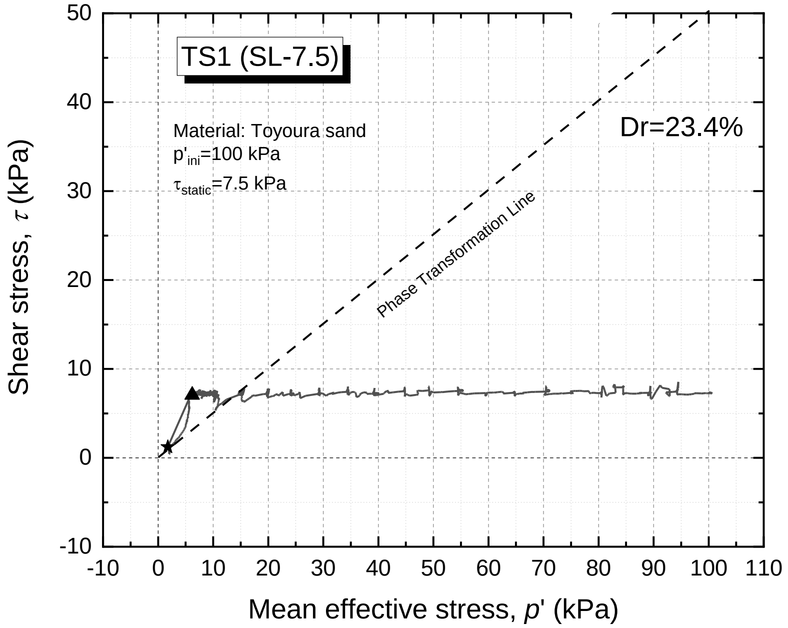

Figure 6-4 Stress path of TS1 (SL-7.5)

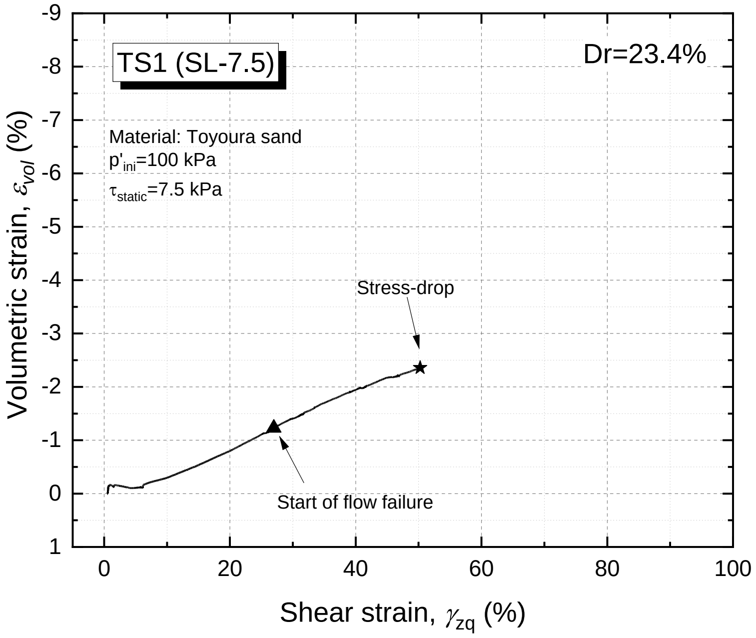

Figure 6-5 Relationship of volumetric strain and shear strain of TS1 (SL-7.5)

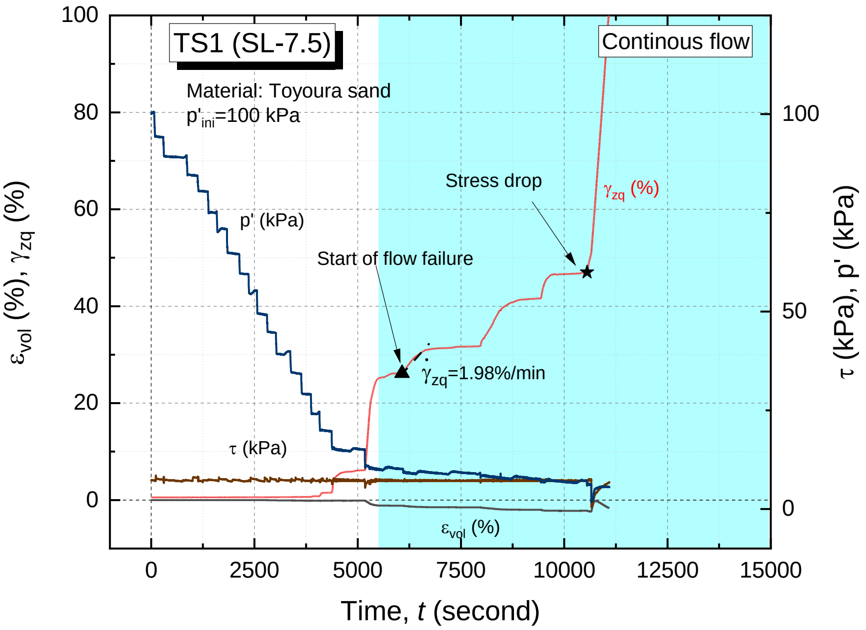

Figure 6-6 Strain development in time series of TS1 (SL-7.5)

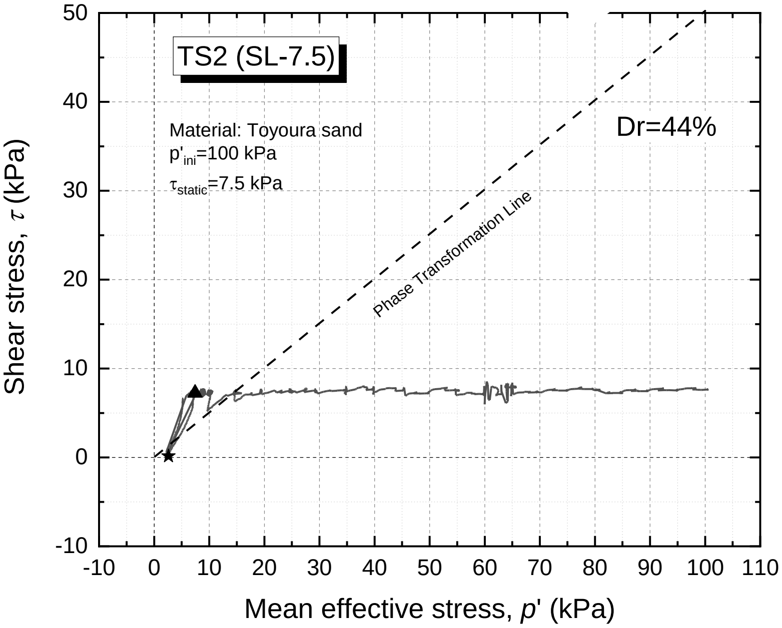

Figure 6-7 Stress path of TS2 (SL-7.5)

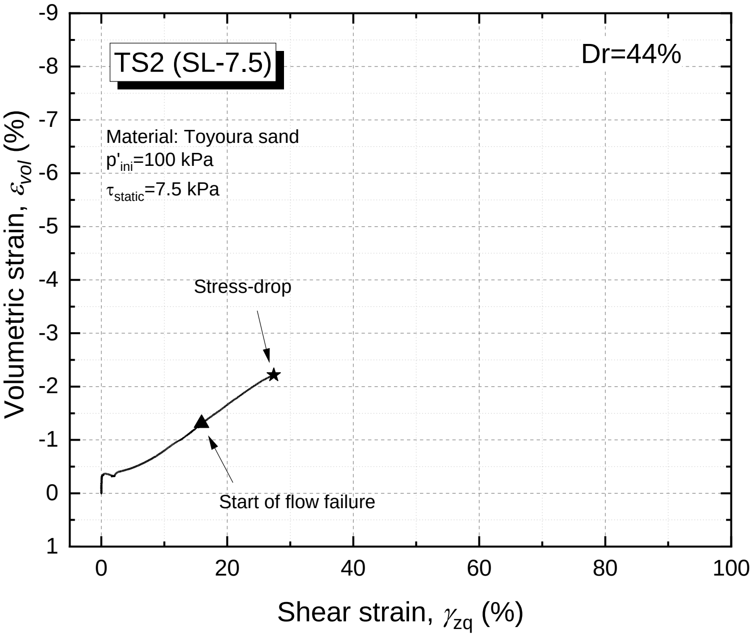

Figure 6-8 Relationship of volumetric strain and shear strain of TS2 (SL-7.5)

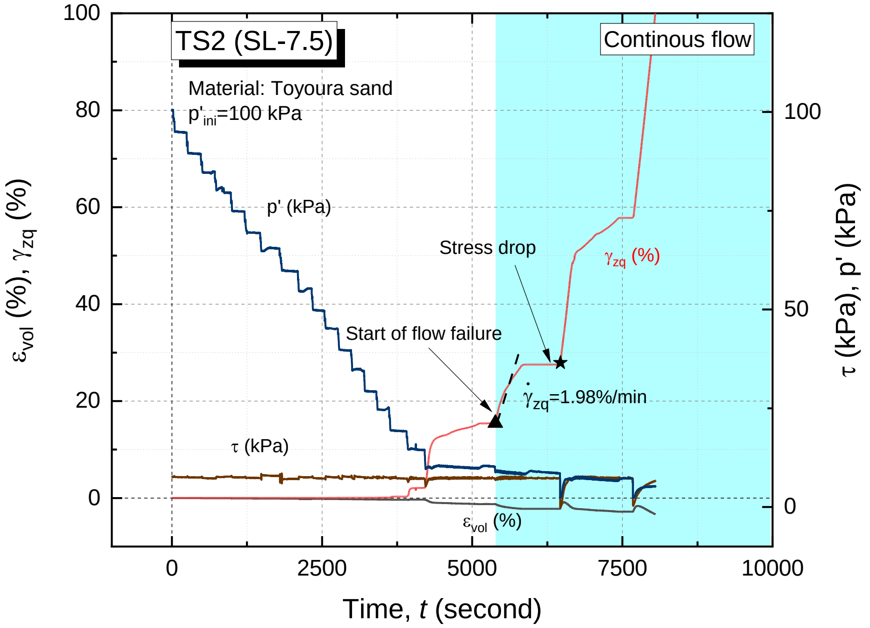

Figure 6-9 Strain development in time series of TS2 (SL-7.5)

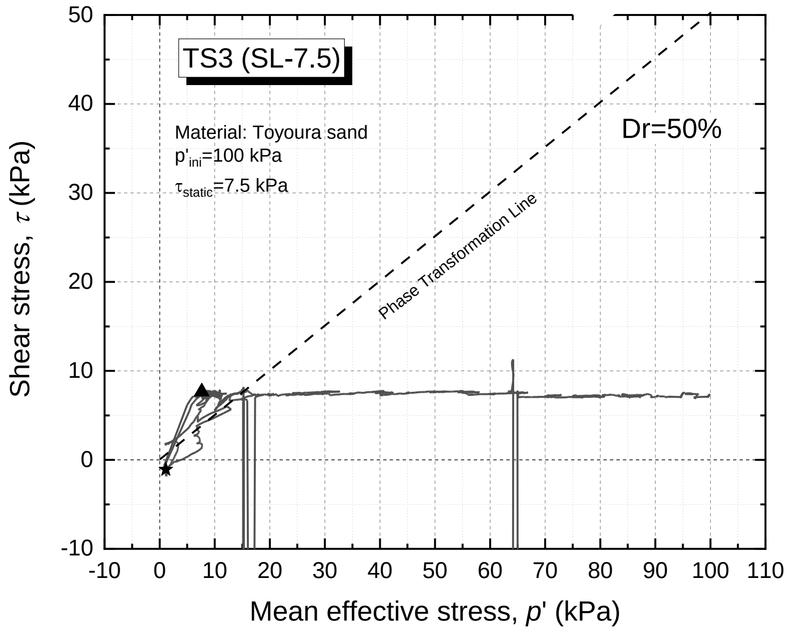

Figure 6-10 Stress path of TS3 (SL-7.5)

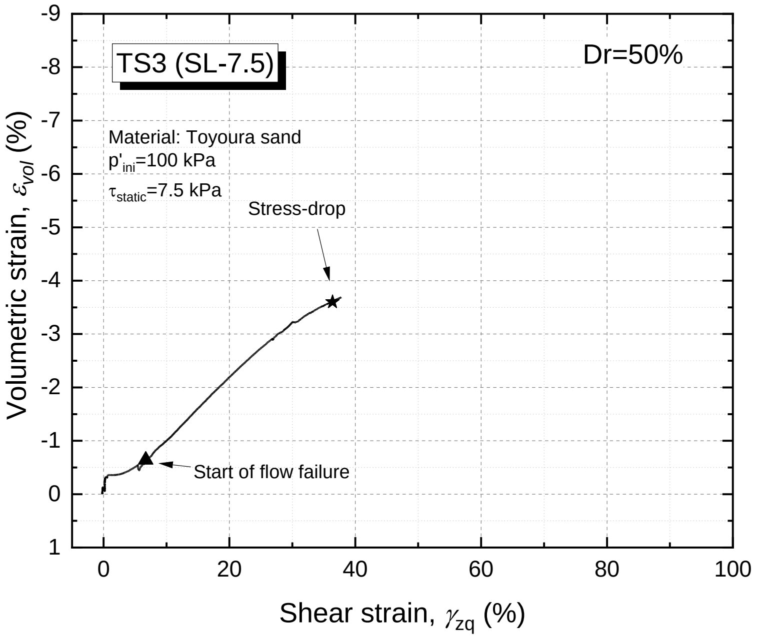

Figure 6-11 Relationship of volumetric strain and shear strain of TS3 (SL-7.5)

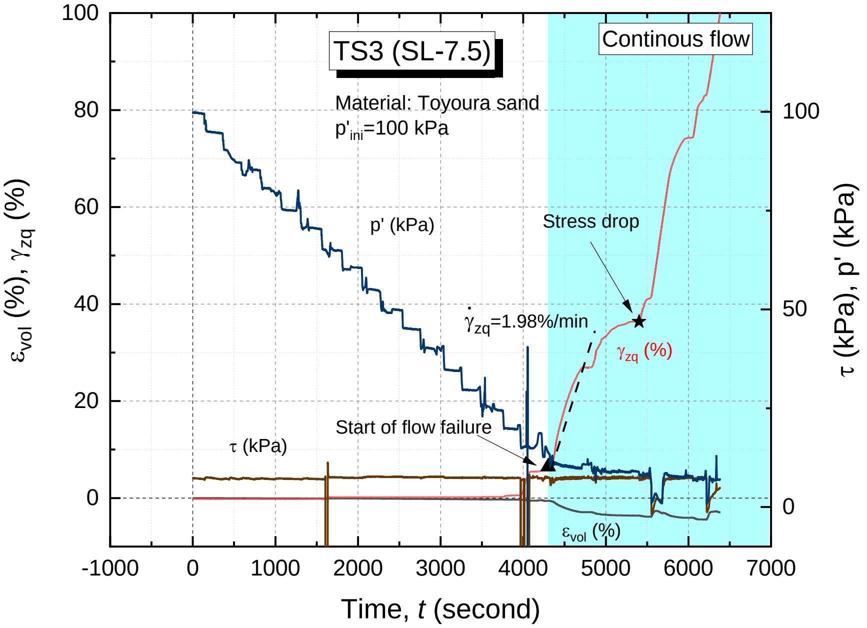

Figure 6-12 Strain development in time series of TS3 (SL-7.5)

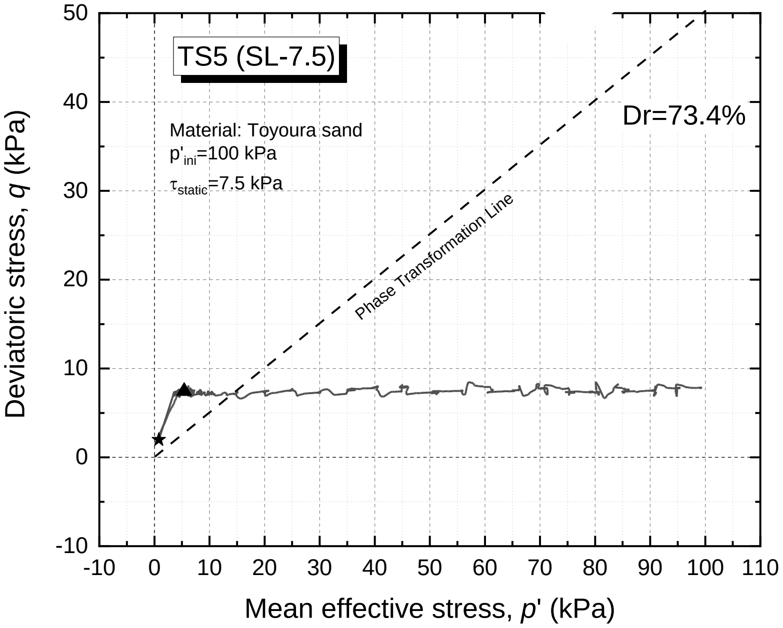

Figure 6-13 Stress path of TS5 (SL-7.5)

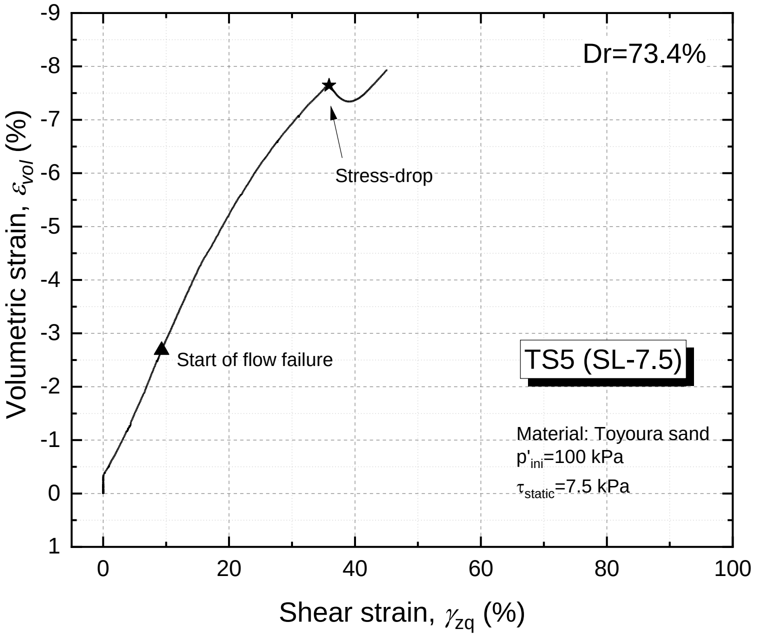

Figure 6-14 Relationship of volumetric strain and shear strain of TS5 (SL-7.5)

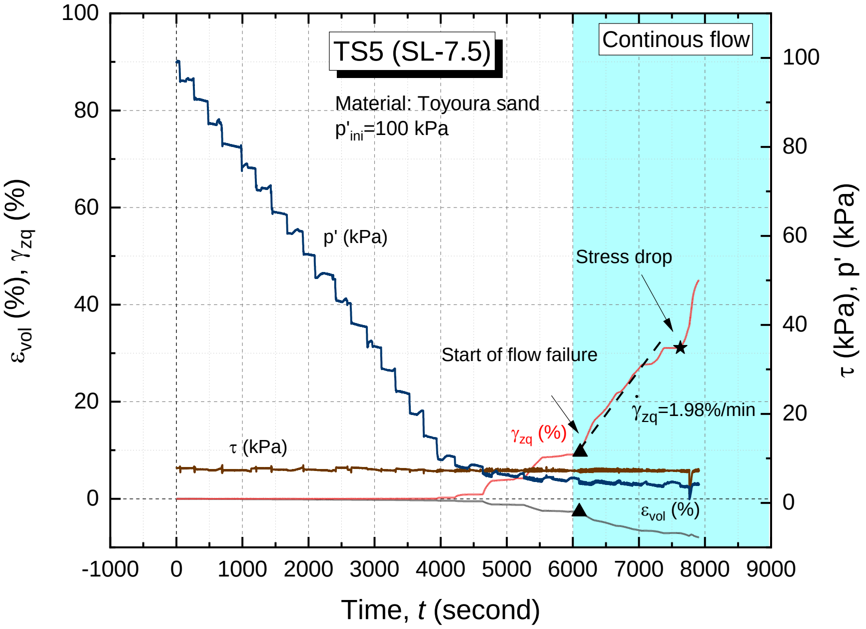

Figure 6-15 Strain development in time series of TS5 (SL-7.5)

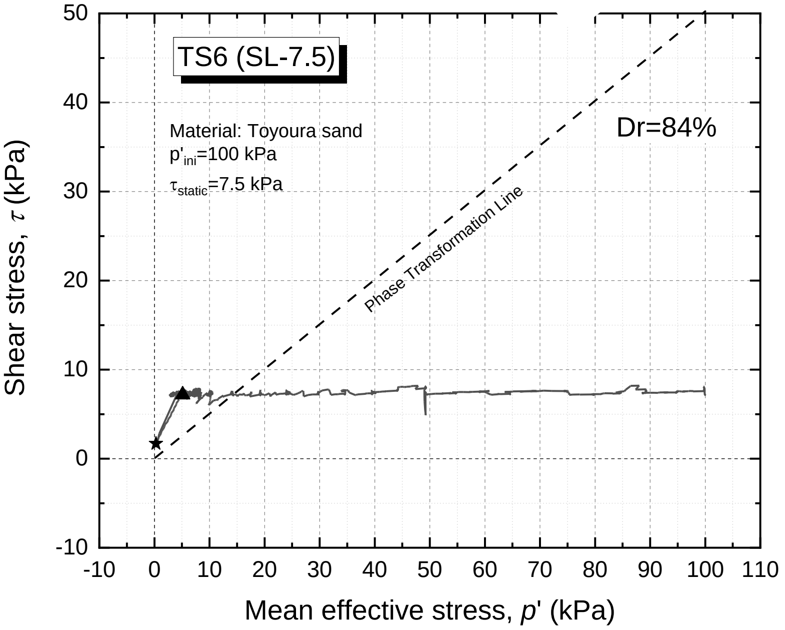

Figure 6-16 Stress path of TS6 (SL-7.5)

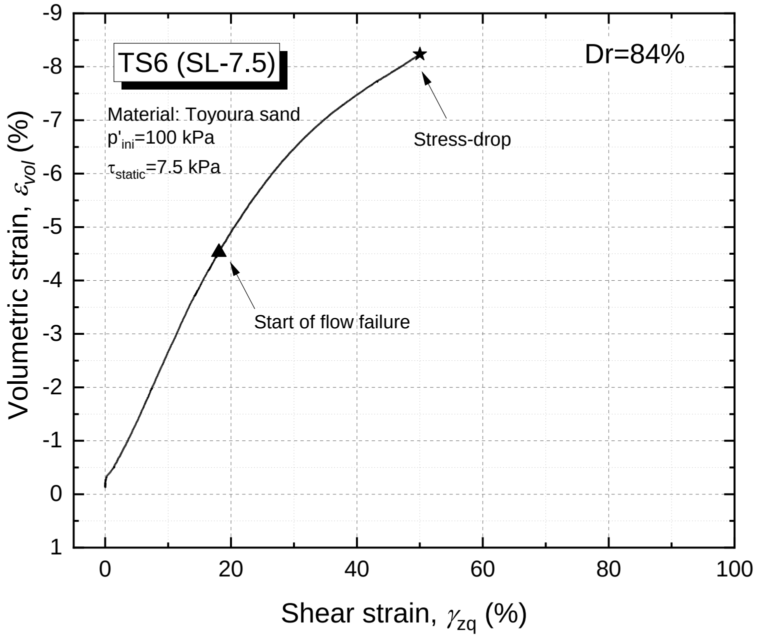

Figure 6-17 Relationship of volumetric strain and shear strain of TS6 (SL-7.5)

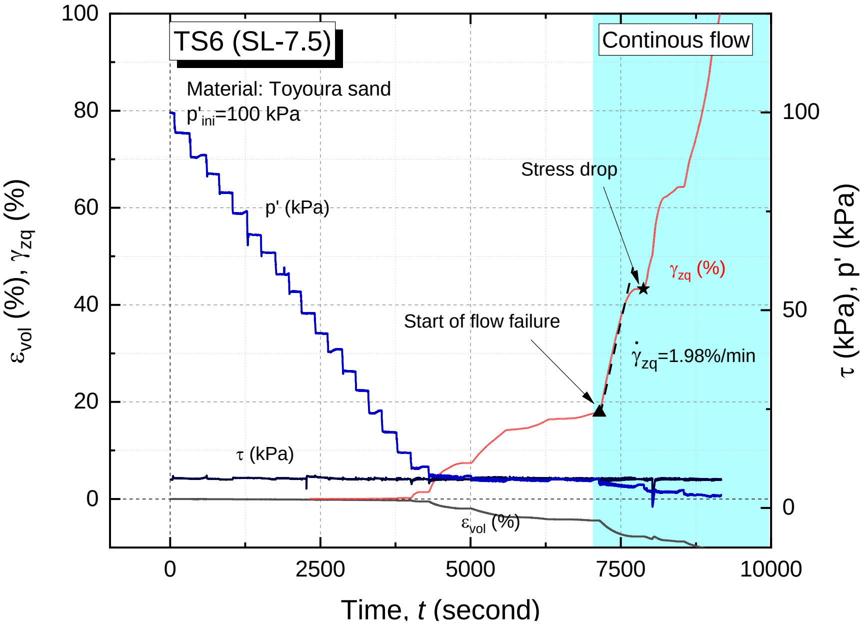

Figure 6-18 Strain development in time series of TS6 (SL-7.5)

6.2.1. Deformation behavior of sandy soil under static liquefaction test in Torsional Shear Apparatus

The deformation behavior of sand under static liquefaction test in Torsional Shear Apparatus is examined using the Digital Image Correlation (DIC) system. This system uses the non-contact measurement methods that acquire images of an object, store images in digital form and perform image analysis to extract the full-field shape, deformation, and motion measurements (Sutton, et al., 2009).

DIC method relies on a contrasting random texture as a speckle pattern on the surface of the specimen (Sutton, et al., 2009). A method has been employed by using spray paint to speckle pattern of the surface of an object (Munoz, Taheri, & Chanda, 2016(a); Munoz, Taheri, & Chanda, 2017(a); Munoz, Taheri, & Chanda, 2016(b); Munoz, Taheri, & Chanda, 2017(b)). In this study, a spackle pattern by using ink adheres to the surface of the membrane which assumed will be deformed together with the surface of the specimen without loss. The speckle pattern is non-repetitive, isotropic, and high contrast with a random pattern.

In this study, a single stereo camera system has been used to capture the image during the test. The camera capture simultaneously the left and right grey-scale images. This camera consists of two high-resolution monochrome stereo cameras (i.e. Fujinon HF75SA-1, 1:1.8/75mm, 3 MP resolution. The images are captured by a snap software using an exposure tie of 37 ms and a frequency of 1 Hz. The total images acquired during the test are computed and calibrated using GOM Correlate 2019 Open software. Figure 6-19 shows the selected points to show pictures captured from DIC analysis. The selected pictures are shown in Figure 6-20.

It can be seen that from A to D point, the uniformity of specimen size can still be observed. Nevertheless, reaching the E point in which te stress drop could be investigated, the uniformity of the specimen becomes less. At point F in which the point after the stress drop, some wrinkels on the specimen membrane can be observed visually. Thus, it can be stated that the specimen behavior before the stress drop are possibly uniform.

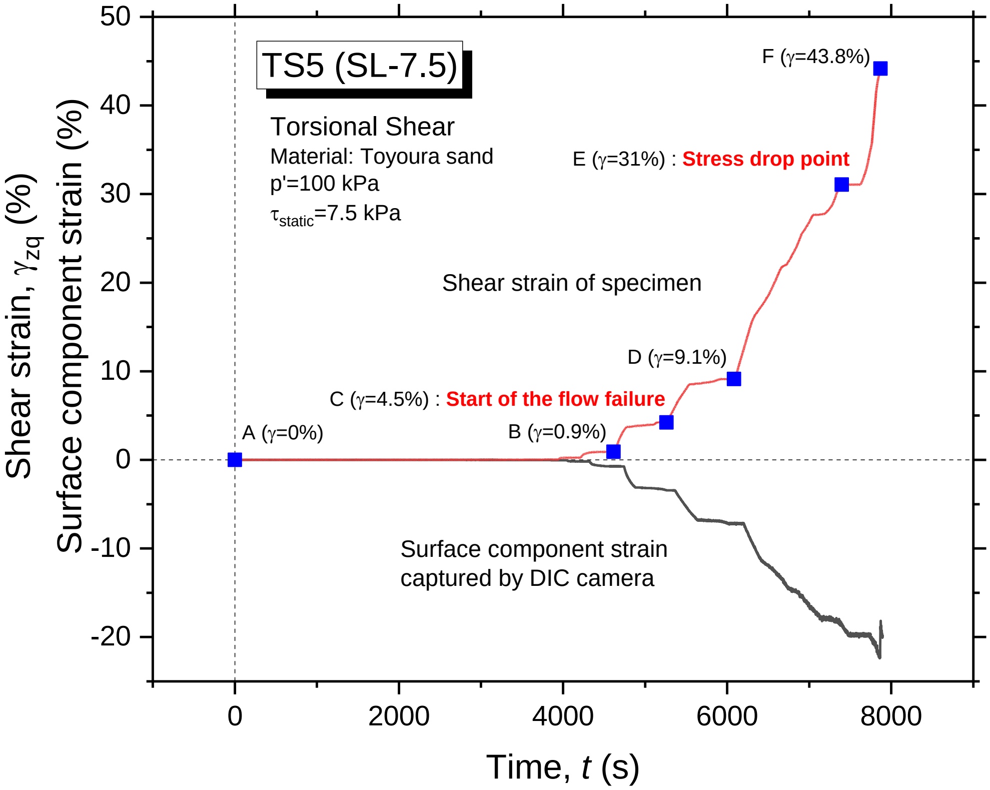

Figure 6-19 The selected points of observation for DIC analysis

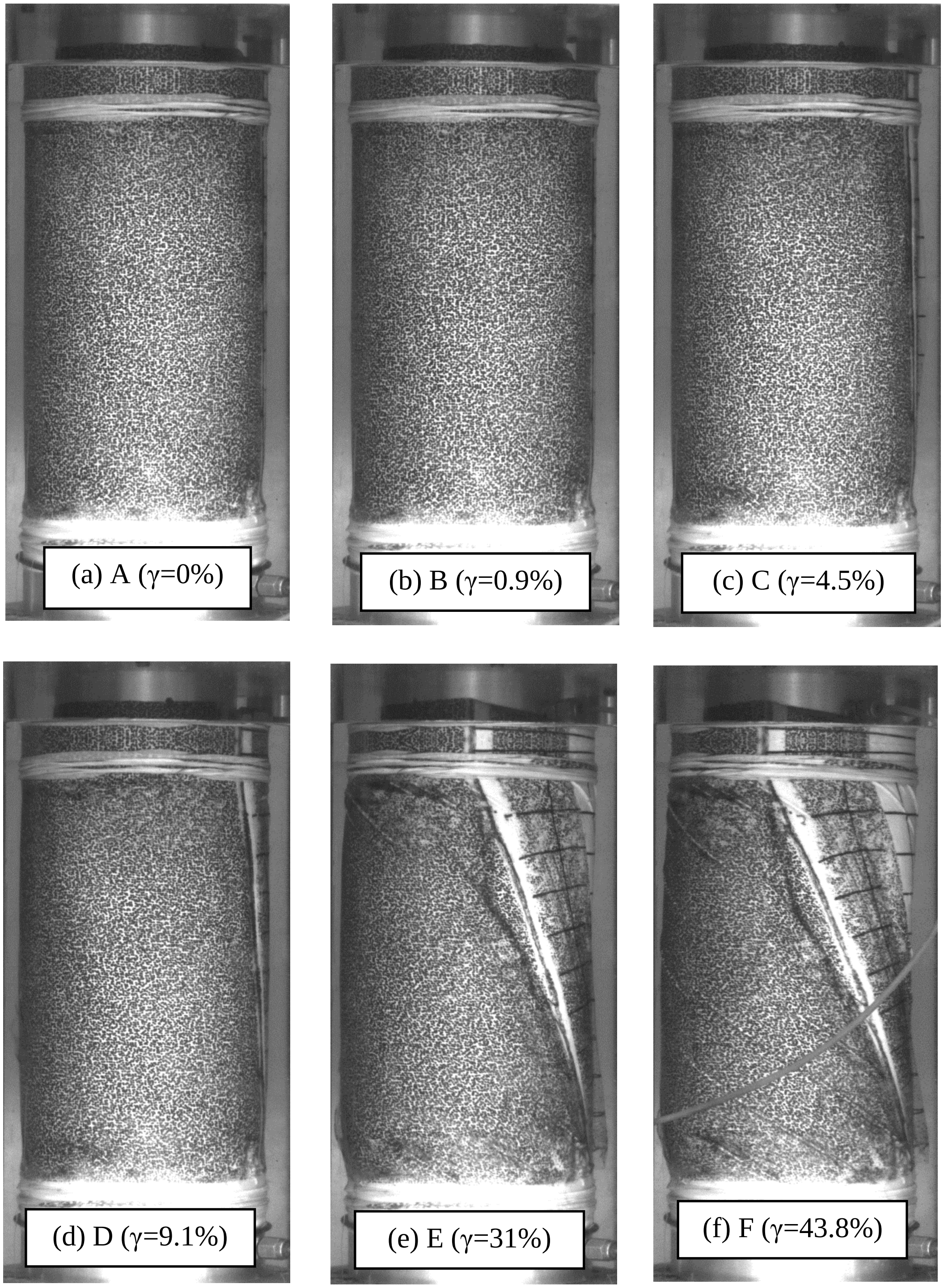
(a) A (γ=0%)
(b) B (γ=0.9%)
(c) C (γ=4.5%)
(d) D (γ=9.1%)
(e) E (γ=31%)
(f) F (γ=43.8%)

Figure 6-20 The results of DIC camera for selected points during test

6.2.2. The effect of drainage mode on the dilation behavior of sandy soil in Torsional Shear Apparatus

In the previous study using Triaxial Apparatus, the drainage mode has been set up from the bottom and up of the pedestal. In this study, it is mentioned as a full drainage condition. The assumption is that in the field, the drainage of water going to the specimen can be from any direction, thus the soil element in the Triaxial Apparatus has been set up for two directions.

The dilation behavior of sandy soil is promoted by the migration of fluid to the soil body. By using this consideration, it is important to understand the effect of drainage mode; half drainage or full drainage to the volume expansion behavior of sandy soil in the fully saturated condition. In order to validate the effect of drainage condition to the result of the test, in Torsional Apparatus, a comparison between one-way drainage (half drainage) and two-way drainage (full drainage) is observed using Toyoura sand. The TS9 is half drainage specimen with Dr=80% while TS5 is full drainage specimen with Dr=84%. The initial test condition of both specimens is set at p'=100 kPa and τ_{static}= 7.5 kPa. The results of the test are shown in Figure 6-21 and Figure 6-22.

It is clear that the result of the experiment with different drainage mode at static liquefaction test in Torsional Shear Apparatus is identical in terms of the development of strains. For both specimens having the same initial density, at the preliminary development before the specimen collapse until the shear strain (γ_{zq}) achieves 30%, the development of volumetric strain is identical, which is around -6% (Figure 6-21). After the specimen collapse due to stress drop, it is observed that the uniformity behavior of the specimen is changed. Nevertheless, at the end of the shearing process (γ_{zq}=100%), the volumetric strain development is not significantly varied, with only -1% difference.

The dilation behavior of both specimens can also be observed in Figure 6-22. The void redistribution is identical during the shearing until γ_{zq}=30%, and even after the specimen collapsed, the final state of the void ratio is the same at γ_{zq}=100%, which is 0.84. Considering these results, it could be stated that the drainage mode of the static liquefaction test does not affect the dilation behavior of the sandy soils.

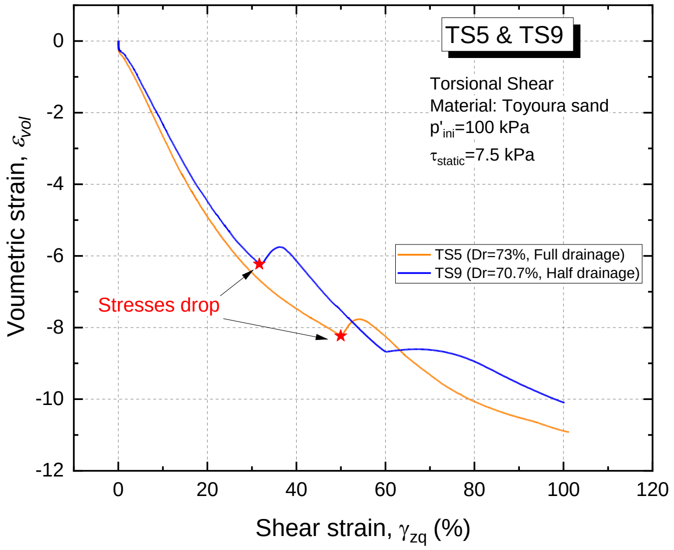

Figure 6-21 Comparison of strain development between Half-Drainage condition and Full-Drainage condition using Toyoura sand at dense state

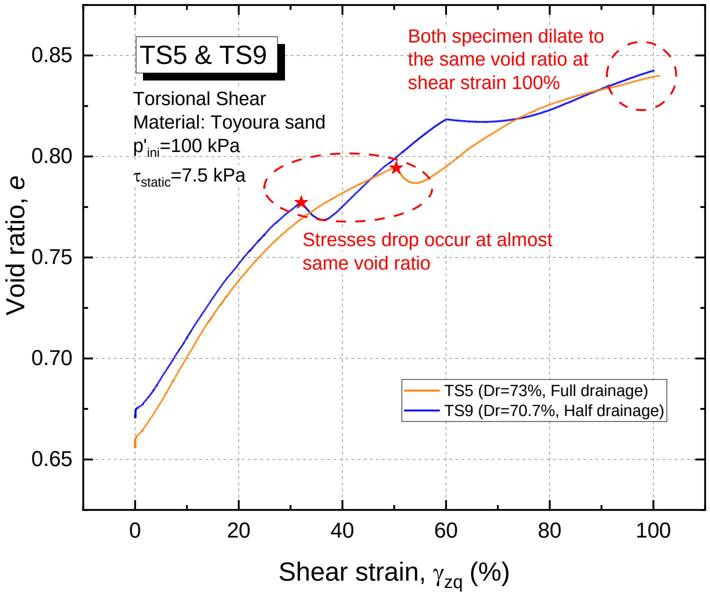

Figure 6-22 Comparison of shear strain development and the initial void ratio between two drainage condition

6.2.3. The effect of confining pressure on the dilation behavior of sandy soil in Torsional Shear Apparatus

In this study, the possibility of flow failure occurred at the gently sloping ground and the shallow depth is examined through static liquefaction test on Torsional Shear Apparatus. In order to understand the effect of the confining pressure on the low-stress ratio (q/p') test, three samples in the dense state (Dr 65%-70%) are prepared with the same stress ratio, but different confining pressure at Table 6-2.

From the experimental results, the specimen with the p'_{ini}=30 kPa, terminate at the shear strain 30%, while the other specimen can reach shear strain up to 100%. At the p'_{ini}=30 kPa, the shear stress is around 2.25 kPa, which is very low and made the accuracy of keeping the shear stress constant at large strain is quite hard.

Nevertheless, from the three data, it is obvious that the volumetric strain development up to 30% shear strain is identical, reaching volumetric strain around -6.2%. TS8 and TS9 perform stress drop at the same strains state. Above the 30% of shear strain, the specimen collapse can be identified, making the specimen deformation non-uniform. However, at the shear strain 100%, the development of volumetric strain could achieve around -10% for both specimens.

Table 6-2 Static liquefaction experiment with different confining pressure at the low-stress ratio

Test name	Dr(%)	p'_{ini} (kPa)	τ (kPa)	Ground inclination, β (%)	Volumetric strain at flow failure (%)	Shear strain rate, $\dot{\gamma}$ (%/min)
TS-7	68.4	30	2.25	1.5-2%	Not measured	Not measured
TS-8	64.1	50	4	1.5-2%	-1.80	0.65
TS-9	70.7	100	7.5	1.5-2%	-2.50	0.93

For all the static liquefaction test conducted in Torsional Shear Apparatus, the differential stress (τ_d) is maintained to be 0 kPa, allowing the vertical strain (ε_z) developed. The vertical strain is developed significantly after the stage of stress drop at the shear strain around 30%. Although the volumetric strain could be developed at the same level for both different confining pressures, at the end of the experiment when the shear strain reachs 100%, TS9 shows the development of vertical strain at -10% while the TS8 shows only -5%. From this results, it is clear that the confining pressure affects the development of vertical strain. The higher the initial confining pressure, the more subsidence will occur.

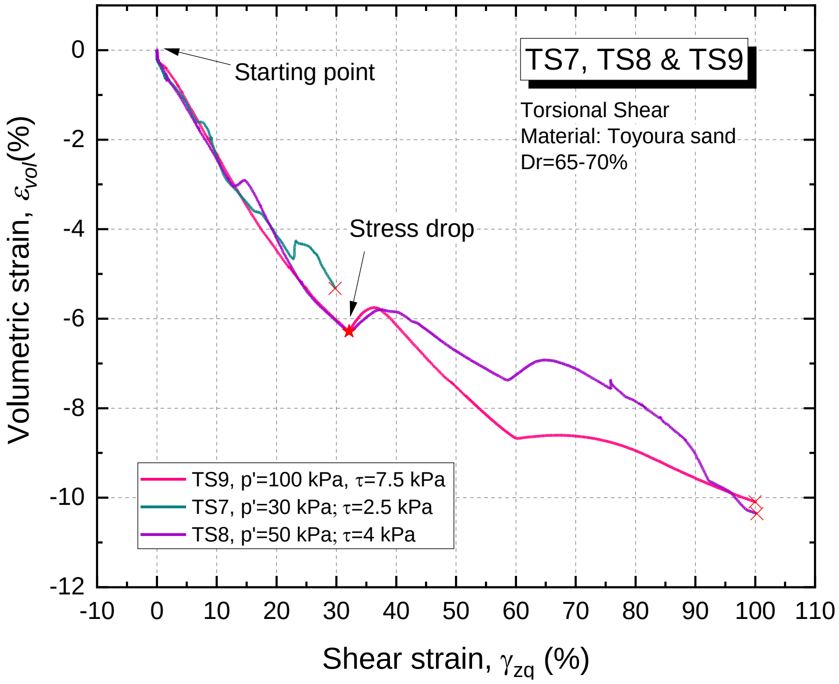

Figure 6-23 Strain relationships of the specimen having different initial confining pressure on static liquefaction test in Torsional Shear Apparatus

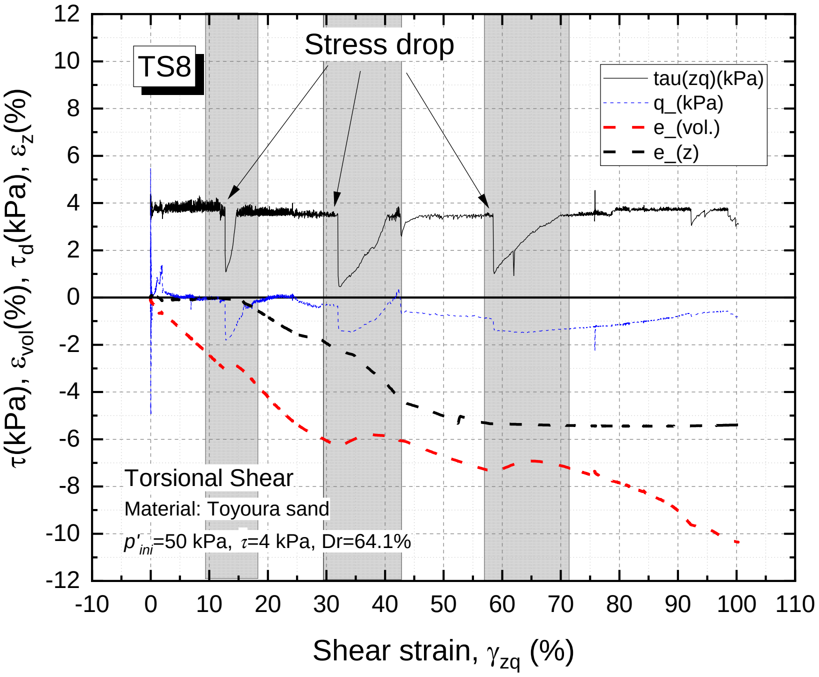

Figure 6-24 Relationship of strains and stresses during the progression of shear strain in TS8

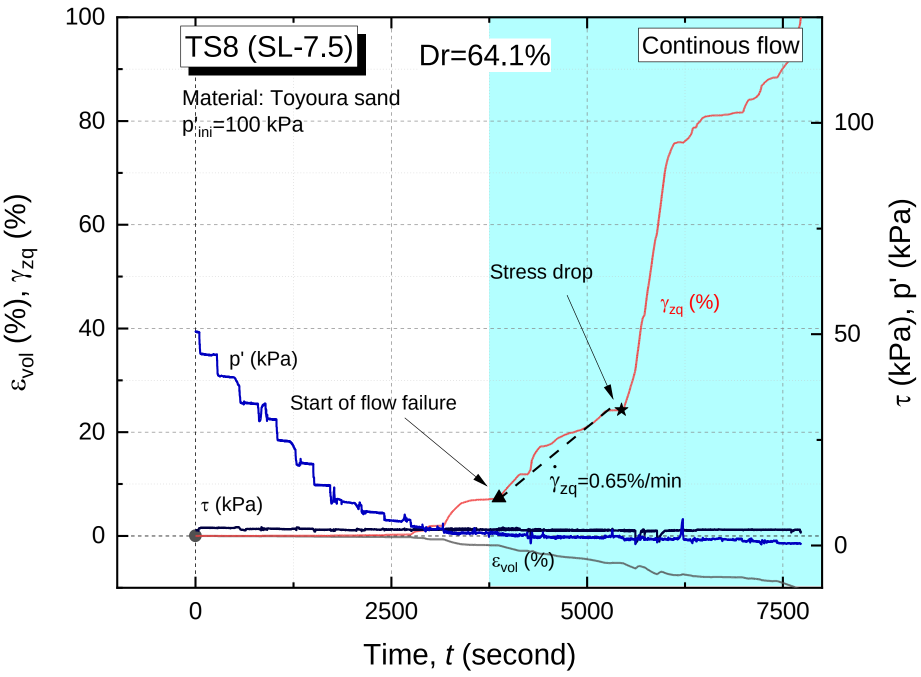

Figure 6-25 Strain development in time series of TS8 (SL-7.5)

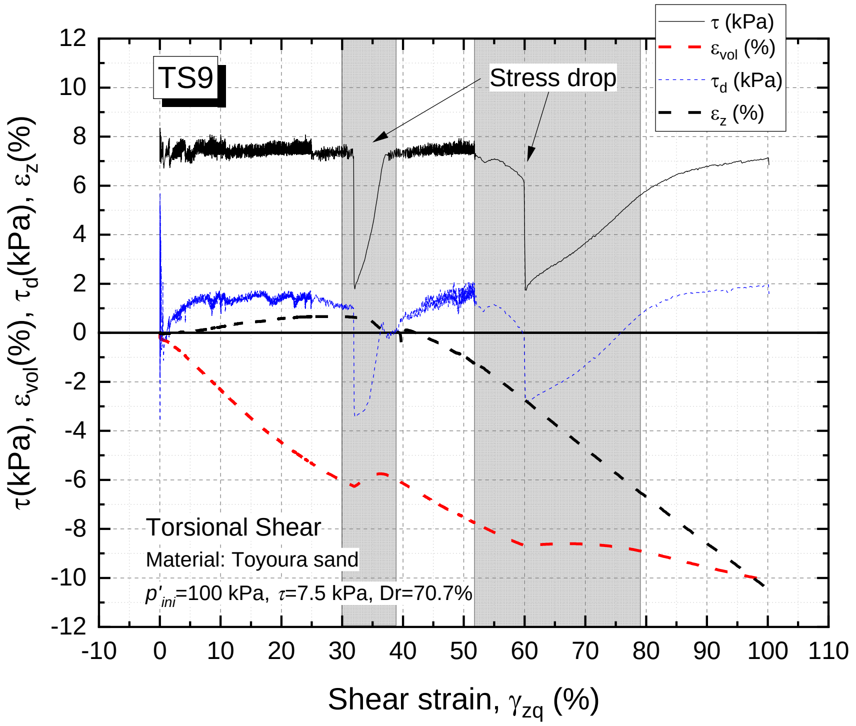

Figure 6-26 Relationship of strains and stresses during the progression of shear strain in TS9

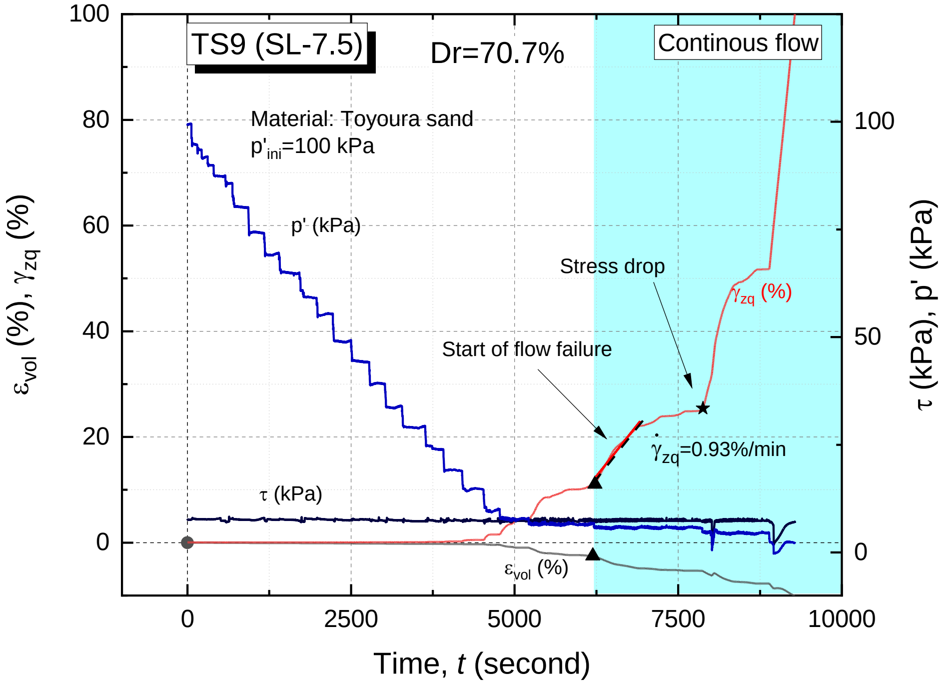

Figure 6-27 Strain development in time series of TS9 (SL-4)

6.2.4. Dilation behavior of sandy soil in Torsional Shear Apparatus

The test results show that the higher the initial density of the specimen, the more the volumetric strain will be developed or the dense material show more dilative behavior than the loose material. These results show a good agreement with one of the Triaxial Apparatus. The amount of the volumetric strain is slightly different between both apparatuses as the mode of shearing is different, including the conversion of stress applied to the specimen. The comparison of the results is shown in Figure 6-28 and Figure 6-29.

6.2.1. Flow rate characteristics of sandy soil in Torsional Shear Apparatus

It mentioned in the previous chapter that the initial density of specimen affects both the volume expansion and shear strain rate, significantly. A comparison is also made to validate the shear strain rate measurement of Triaxial Apparatus in the Torsional Shear Apparatus. It is clear that the tendency of both results shows the same trend, which is higher initial density, the higher shear strain rate, except the specimen having a density of 73% that shows a lower shear strain rate.

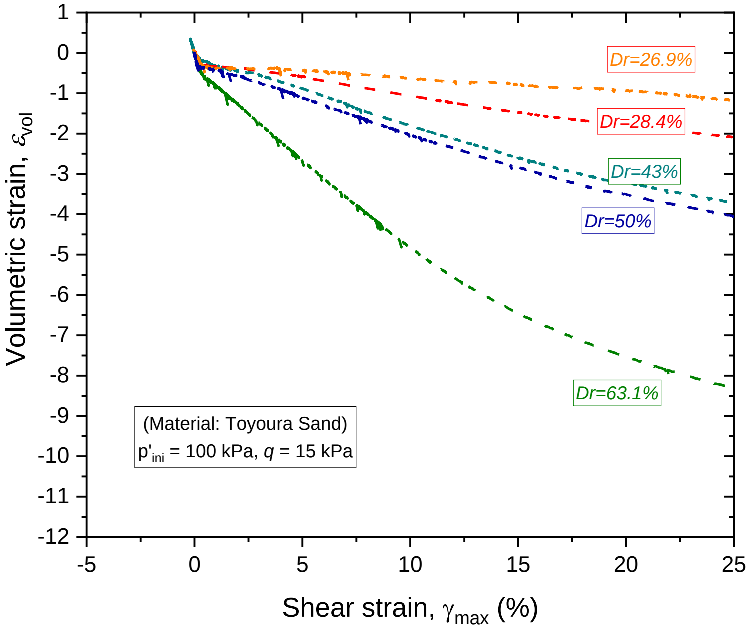

Figure 6-28 Strain relationship of static liquefaction test at Triaxial Apparatus until the maximum shear strain is 25%

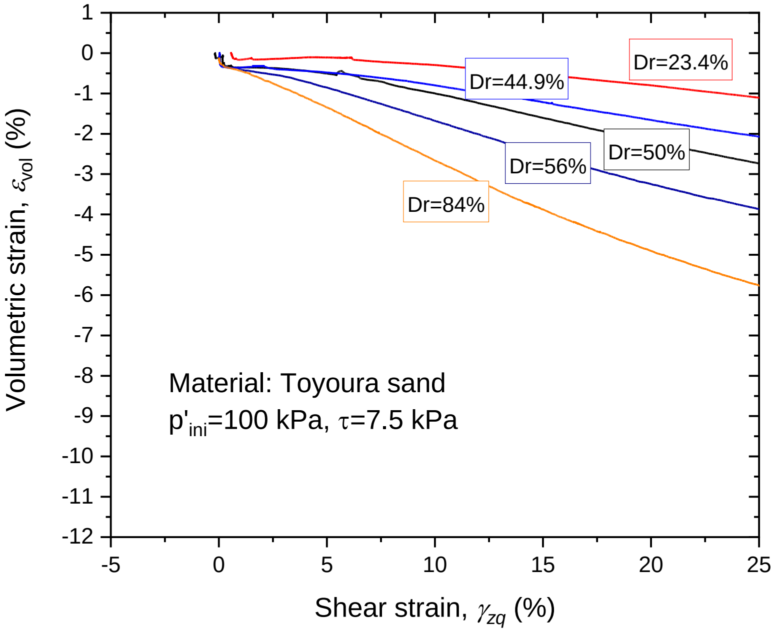

Figure 6-29 Strain relationship of static liquefaction test at Torsional Shear Apparatus until the shear strain is 25%

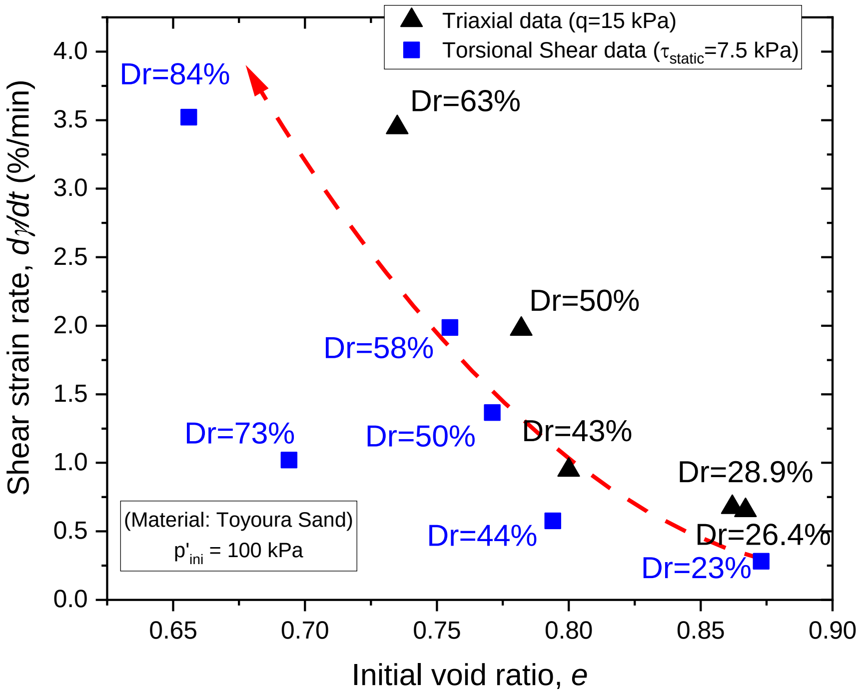

Figure 6-30 A comparison of static liquefaction test on Triaxial Apparatus and Torsional Shear Apparatus for various densities of Toyoura sand

6.3.Loss of Particle Interlocking at Large Strain Level

As the limitation of axial strain measurement on Triaxial Apparatus might affect the validity of testing results, an approachment of investigating the soil behavior under the large strain level has been conducted in the Torsional Shear Apparatus. The modified apparatus using in this study could achieve 100% of shear strain in a single amplitude.

The experiment conducted at the Torsional Shear Apparatus could observe the quick stress drop at large strain (>30% of shear strain level) that could not be observed at the Triaxial Apparatus. This stress drop is promoted by the approach of the stress path of the specimen toward the failure line. The phenomenon of stress drop is illustrated in Figure 6-31.

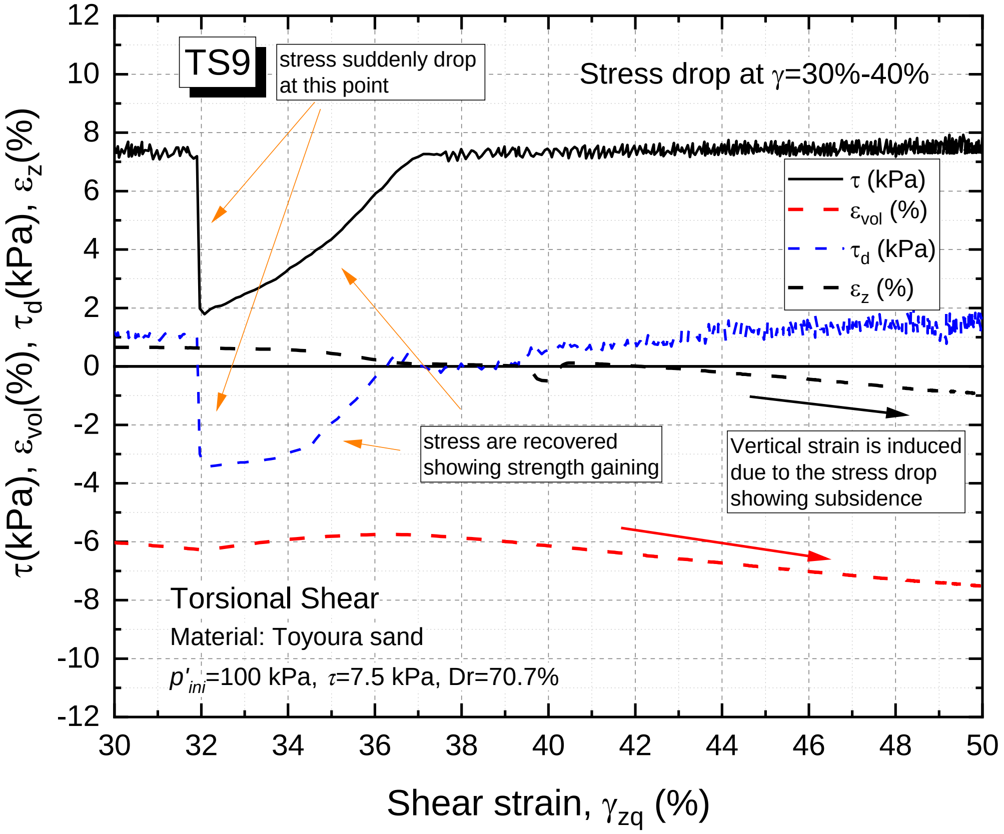

Figure 6-31 The stress drop phenomenon during the static liquefaction test of Toyoura sand with Dr=70.7% at the shear strain level of 30-40%

This stress drop phenomenon could be observed vividly on the medium dense to dense material under static liquefaction test. At first, when the stress path reaches the failure line, the stresses, including shear stress and differential stress are suddenly dropped to 0 kPa. This mechanism showing that the soil particle might lose their contact or interaction or might be due to buckling. After that, as the shear strain keep develops, the void redistribution can take place creating the strength gaining from particle contact (stress recovery). Nevertheless, at this stage, the shape of the specimen is already non-uniform making the sand behavior after the stress drop become unreliable.

The stress drop can happen several times during the strain progression as shown in Figure 6-24 and Figure 6-26, particularly on the dense specimen. The latter stress recovery at the larger strain might take longer than the first stress recovery, showing that the specimen is getting loose. The loose material might not perform the stress drop vividly as the loose material are easy to get deformed during the shearing process but its stress recovery takes longer than the dense specimen.

6.4.Summary

The dilation behavior and flow rate characteristics of clean sand under static liquefaction test at large strain can be observed using Torsional Shear Apparatus. The shearing mode of this apparatus made the result of observed flow failure is more appropriate with the field condition compared to the Triaxial Apparatus, in particular at the large strain level. The summary of the experiment results conducted in Torsional Shear Apparatus is as follows.

1. The flow failure phenomenon that occurred at the gently sloping ground could be observed in the Torsional Shear Apparatus. All the testing conditions represent the field condition of 1.5-2% of inclination.

2. The effect of drainage mode; half-drainage or full-drainage, is not significant to the difference of volumetric strain development. In addition, the softening behavior at $\gamma_{zq} - e$ plane is identical for both specimens having the same densities.

3. The effect of confining pressure on volume expansion behavior is not significant. The difference in confining pressure condition will give a different result on the vertical strain that corresponds to the subsidence after the collapse of the specimen occurred during the shearing process.

4. The experimental results on Triaxial Apparatus and Torsional Shear Apparatus show a good agreement for the volume expansion behavior and flow rate characteristics. The denser the initial density of the specimen, the more dilative the behavior and the faster the shear strain rate at the failure point.

5. The loss of particle interlocking of sand during static liquefaction tests can be observed at large strain levels in Torsional Shear Apparatus. This condition is

represented by the quick stress drop of the specimen during the shearing process when the stress path approaches the failure line.

6.5. References

Hyodo, M., Murata, H., Yasufuku, N. & Fujii, T., 1991. Undrained cyclic shear strength and residual shear strain of saturated sand by cyclic triaxial tests. *Soils and Foundations 31 (3)*, pp. 60-76.

Munoz, H., Taheri, A. & Chanda, E., 2016(a). Fracture energy-based brittleness index development and brittleness quantification by pre-peak strength parameters in rock unaxial compression. *Rock Mechanics and Rock Engineering*, 49(12), pp. 4587-4606.

Munoz, H., Taheri, A. & Chanda, E., 2016(b). Pre-peak and post-peak rock strain characteristics during uniaxial compressiion by 3D digital image correlation. *Rock Mechanics and Rock Engineering*, 49(7), pp. 2541-2554.

Munoz, H., Taheri, A. & Chanda, E., 2017(a). Local damage and proggresive localization in porous stone. *Rock Mechanics and Rock Engineering,* 50(1), pp. 3253-3259.

Munoz, H., Taheri, A. & Chanda, E., 2017(b). Specimen aspect ratio and proggresive field strain development of sandstone under uniaxial compression by three-dimensional digital image correlation. *Journal of Rock Mechanics and Geotechnical Engineering,* 9(1), pp. 599-610.

Sutton, M. A., Orteu, J. J. & Schereier, H., 2009. *Image Correlation for Shape, Motion, and Deformation Measurements.* s.l.:Springer US.

Tatsuoka, F., Muramatsu, M. & Sasaki, T., 1982. Cyclic undrained stress-strain behavior of dense sand by torsional simple shear test. *Soils and Foundations, 22 (2),* pp. 55-69.

Vaid, Y. P. a. C. J., 1983. Effects of static shear on resistance to liquefaction. *Soils and Foundations, 23 (1),* pp. 47-60.

Vaid, Y. P. a. F. W., 1979 . Static shear and liquefaction potential. *Journal of Geotechnical Engineering Division ASCE,* pp. 1233-1246.

Yasuda, S. et al., 1992. The mechanism and simplified procedure for the analysis of permanent ground displacement dur to liquefaction. *Soils and Foundations*, 32(1), pp. 149-160.

Chapter 7 CASE STUDY: FLOW DEFORMATION BEHAVIOR OF SANDY SOILS AT PALU AREA DUE TO 2018 SULAWESI EARTHQUAKE

7.1. Soil Characteristics in the Affected Areas

7.1.1. Dynamic Cone Penetration Test at Petobo

Portable Dynamic Cone Penetration Test (DCPT) has been conducted at four locations around the Petobo area, covering two points at the affected zone and the others in the non-affected zone. Figure 7-1 shows the location of the test sites. The conversion results of the DCPT is presented in Figure 7-2 using the equations provided by Takase et al. (2013). From the test, the N-SPT value at point No. 1, which was several meters from the crown area, was relatively dense than the other spots. No evidence of liquefaction was observed around the spots. The groundwater level is also unidentified in the shallow depth.

In the crown area (upper part), the soil condition is represented by DCPT No. 2 and DCPT No. 3. This location (depth of 5-6 m) is dominated by silty soil with the N-SPT value is less than 5. This indicates that the soil is at the loose state. The groundwater level is found at the shallow depth. The combination of loose soil and shallow groundwater level will possibly lead to the liquefaction due to earthquake shaking. DCPT No. 4 represented the soil condition at the bottom area. As this location is outside the affected area, the N-SPT value is slightly higher than that of the affected location. The groundwater level was found shallow.

In the laboratory, the particle size distribution of the sand ejecta samples found at DCPT location No. 2 and at Jono Oge has been examined according to Japanese Geotechnical Society (JGS) Standard No. 0131, respectively. The result is shown in Figure 7-3. Sand ejecta samples at Petobo show a high percentage of fine contents, achieving about 60%, while sand ejecta collected from Jono Oge show less fine content, about 20%.

Figure 7-1 Location of DCPT test at Petobo, highlighted by the red circle. Points 1 and 4 are outside the affected areas while points 2 and 3 are near the crown area.

After considering the extent of the damaged area, there is a strong hypothesis that there should be external forces or pressure that bring this liquefaction produced flow failure. Moreover, the topography gradient of all the affected areas can be categorized as a very gentle slope ranging from 1-4%.

In Balaroa, a local well-digger who worked for decades in that place informed that before the earthquake happened, supposed that a 6-meter-water pipe inserted to the ground, groundwater could eject to the surface for about 0.5-1 meter high. This information could indicate that in Balaroa, the confined groundwater existed. This information also supports the hypothesis that this type of liquefaction might be forced by the pressure from confined groundwater.

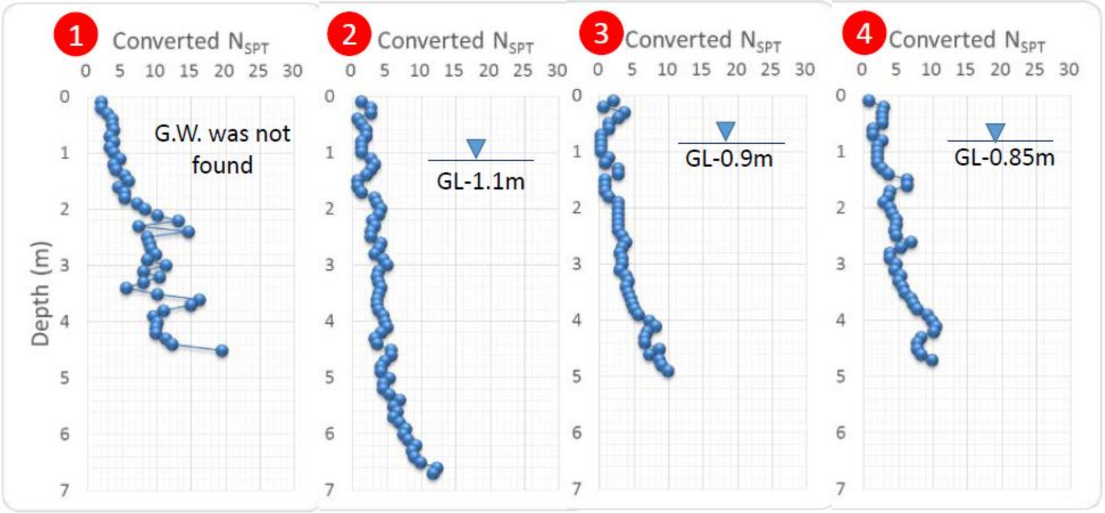

Figure 7-2 Converted N-SPT value from the DCPT test. Groundwater level (GL) at Point 2, 3, and 4 are shallow.

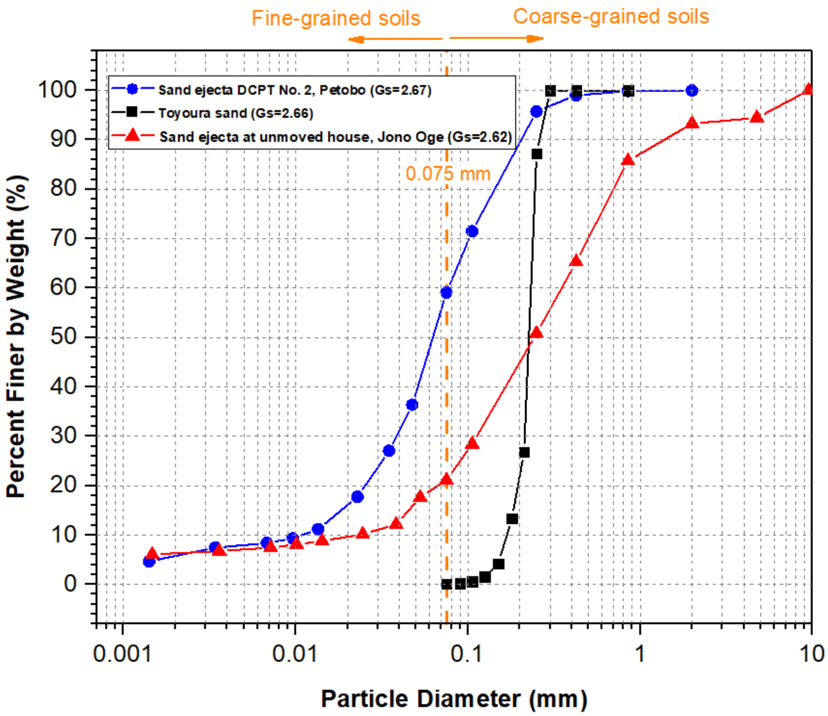

Figure 7-3 Grain size distribution of sand ejecta collected from Petobo and Jono Oge compared to Toyoura Sand. Both samples contain fine-fractions.

7.1.2. Soil layer from trench survey at Sibalaya

From the trench survey conducted in Sibalaya, the characteristics of the soil layer after the flow failure phenomenon can be investigated. The result of Trench No. 3 is shown in Figure 7-4.

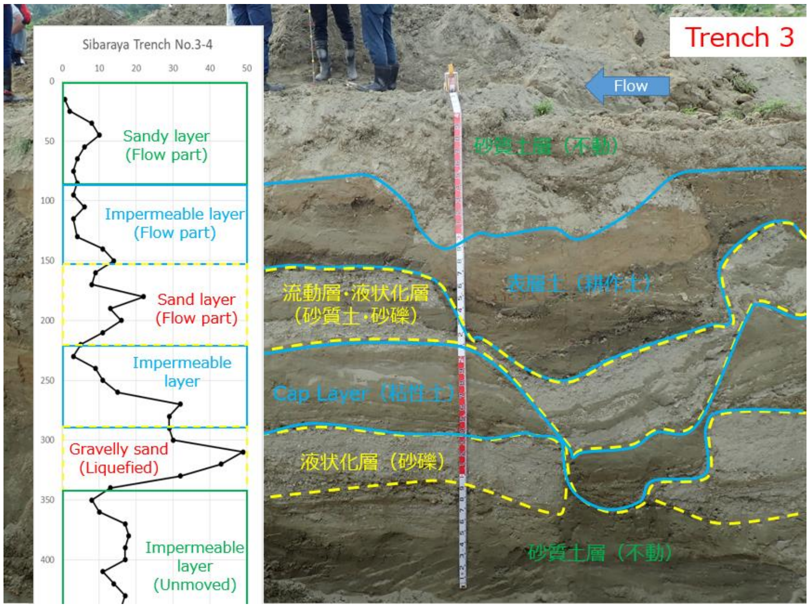

Figure 7-4 Soil layer characteristics at Trench 3 at Sibalaya after the flow failure

It is interpreted that the soil layer consisted of debris layer, impermeable layer, sand layer (flow) part, and gravelly sand layer.

7.1.2.1. Liquefaction resistance of the gravelly sand layer in element test

It is important to investigate the liquefaction resistance of gravelly sand layer on the surrounding areas of Sibalaya. In this study, the liquefaction resistance of this layer is conducted in Triaxial Apparatus with the estimated confining pressure of 70 kPa. The estimation of the density of this layer in the field is 1.6 g/cm^3. In the experiment, the specimen is prepared with the dry tamping method with 5 layers in which the amount of mass in each layers and various numbers of tamping in each layer.

The double-vacuum process is employed to the specimen before the saturation to remove the air inside the specimen. The B value of all specimens is assured more than 0.97. The back-pressure for all the specimens is 200 kPa. After that, the specimen is isotropically consolidated to p'=70 kPa. For the undrained cyclic test, the loading rate is set as 0.2%/minute of axial strain. The list of the experiment is summarized in Table 7-1.

Table 7-1 The experiment result of the undrained cyclic test of gravelly sand from Sibalaya Trench 3

Specimen code	**Density, ρ_{sat} (g/cm^3)**	**Mean effective stress, p' (kPa)**	**CSR**	**Number of cyclic, $Nc_{(DA=5\%)}$**
TX UCL 1	1.579	70	0.3	2
TX UCL 2	1.603	70	0.2	3.5
TX UCL 3	1.579	70	0.1	706
TX UCL 4	1.617	70	0.17	14

The stress path and the stress-strain relationship of TX UCL 4 sample is presented in Figure 7-5 and Figure 7-6.

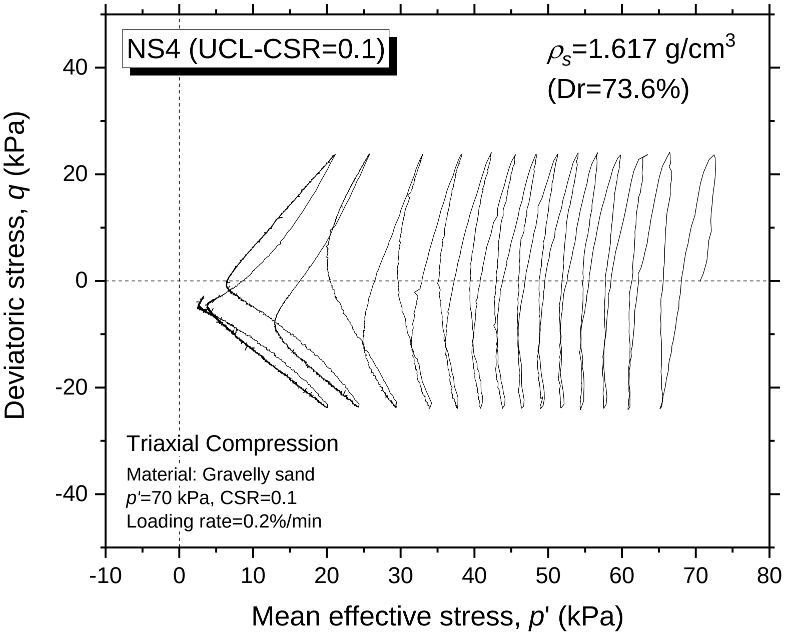

Figure 7-5 Stress path of sample NS4 (UCL-CSR=0.1)

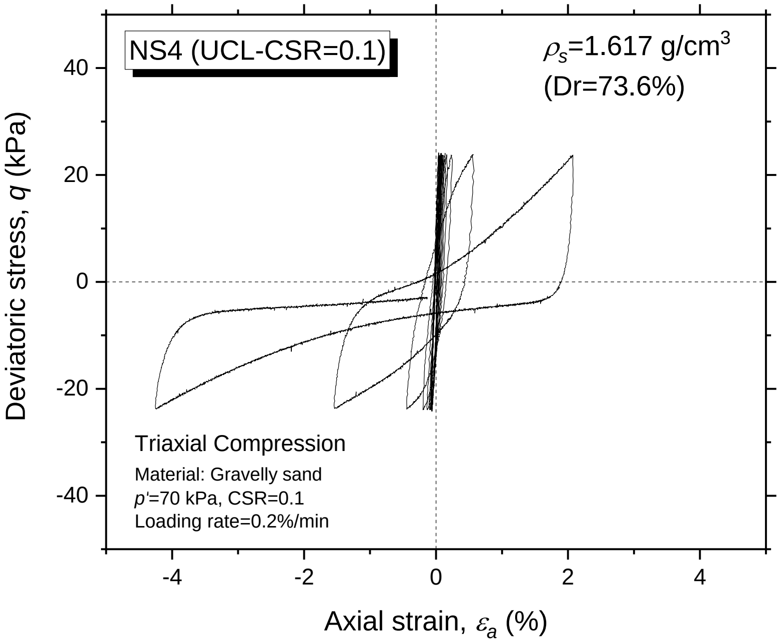

Figure 7-6 Stress-strain relationship of sample NS4 (UCL-CSR=0.1)

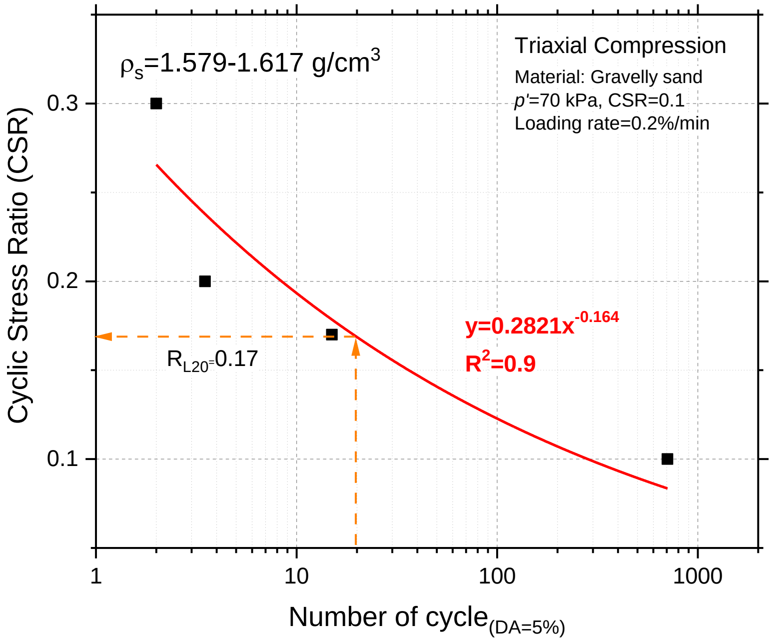

Figure 7-7 The Liquefaction Resistance curve of the gravelly sand sample taken from Trench 3 Sibalaya

From the experimental results, it is found that the liquefaction resistance of gravelly sand (RL_{20}) is 0.17. This number is relatively low compared to the clean sand. Thus this layer is probably liquified during the earthquake shaking due to the 2018 Sulawesi Earthquake.

7.1.2.2. Flow deformation behavior of sandy soil from Trench 3 Sibalaya

By using a static liquefaction test, it is possible to investigate the flow deformation behavior of sandy soil. In this study, the sandy layer specimen taken from the trench No. 3 in the Sibalaya area. The procedure of the static liquefaction is the same as used in the previous chapters using Torsional Shear Apparatus. The mean effective stress (*p'*) is estimated to be 50 kPa. The static shear stress is set as 4 kPa assuming that the ground inclination is around 1.5%. The result of the experiment is shown in Figure 7-9.

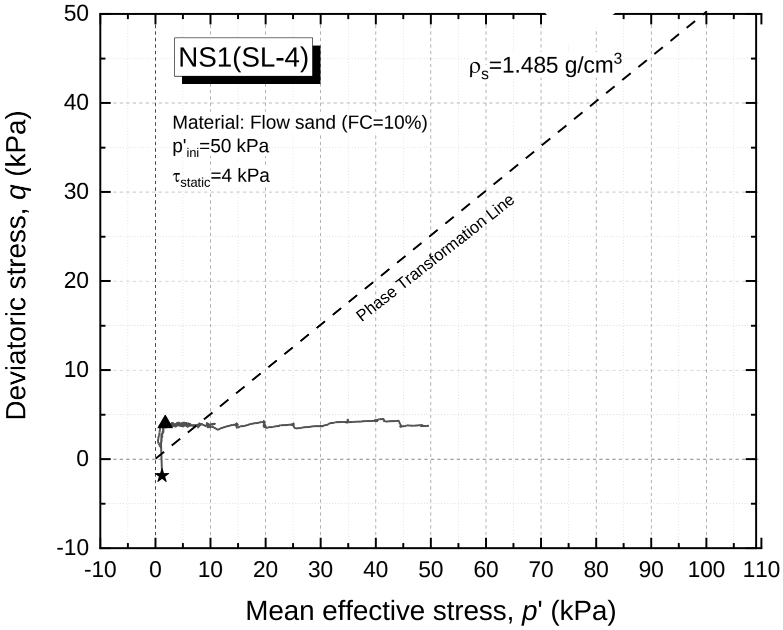

Figure 7-8 The stress path of static liquefaction test using flow sand taken from Trench 3 Sibalaya (NS1)

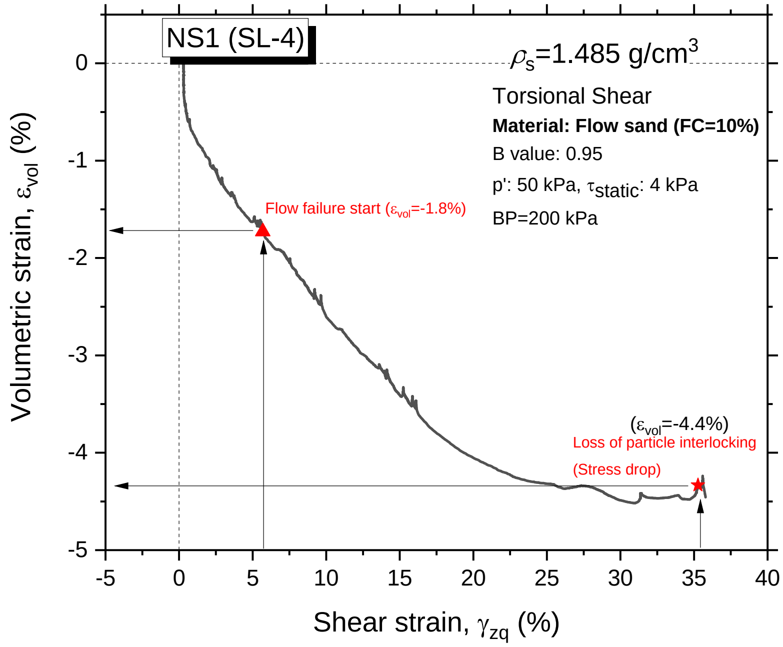

Figure 7-9 The strain relationship of static liquefaction test using flow sand taken from Trench 3 Sibalaya

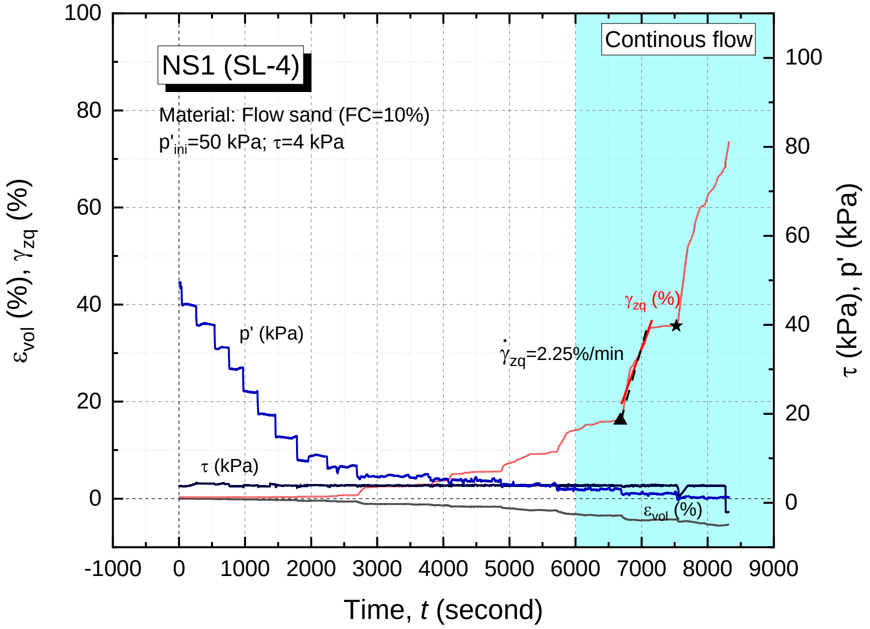

Figure 7-10 The strain development using flow sand taken from Trench 3 Sibalaya (NS1)

From the experimental result, it is found that the sand specimen taken from Trench 3 Sibalaya could behave as a flow material, with the injection of water. In order to make a validation whether the flow failure could not be induced by only due to the soil liquefaction, an experiment of Undrained Cyclic Loading following by the Undrained Monotonic Loading has been done as a comparison to the water injection (static liquefaction) test. In this experiment, the specimen is made to be in a liquefied state by giving a previous shear strain around 10.2% due to cyclic loading. The stress-path of the undrained cyclic test is shown in Figure 7-11. The stress-strain relationship of this undrained cyclic test is presented in Figure 7-12.

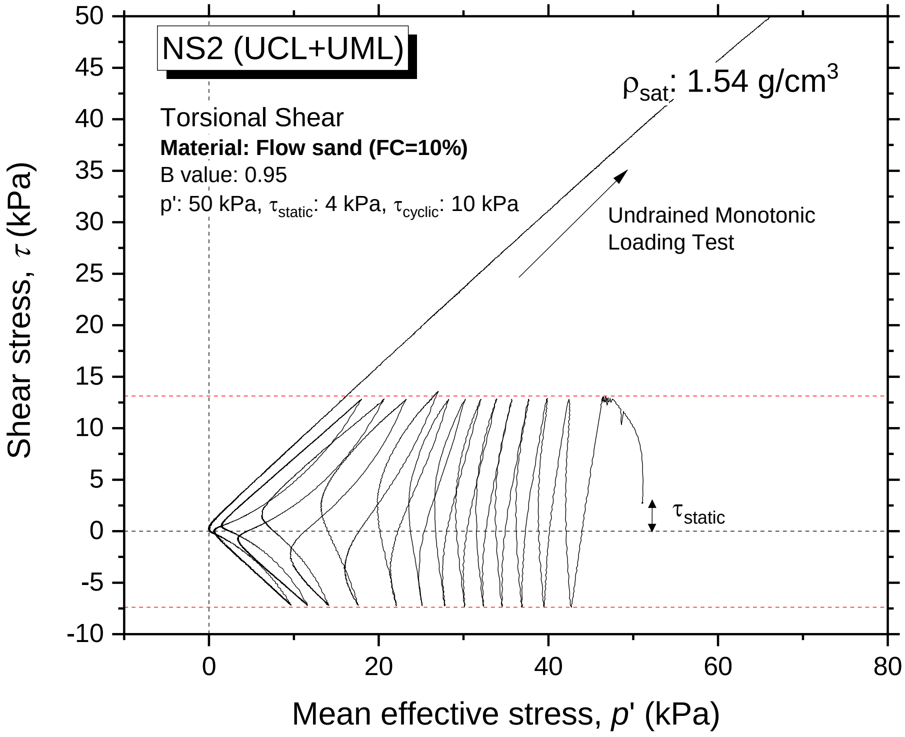

Figure 7-11 Stress-path of the sand specimen under undrained cyclic loading test

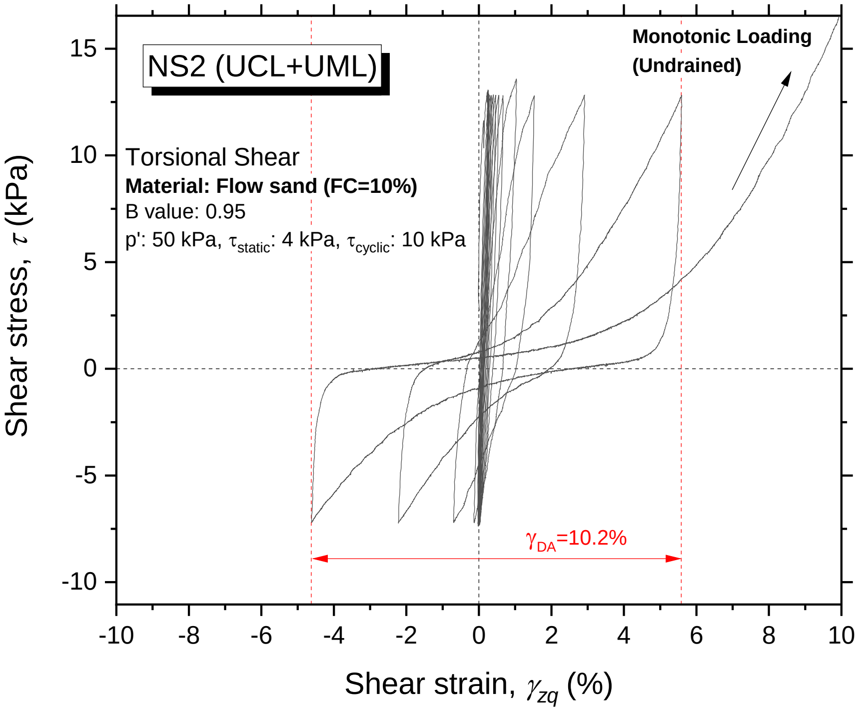

Figure 7-12 The shear strain relationship of the sand specimen under undrained cyclic loading test until shear strain (γ_{zq}) reaches 10.2% (DA) follow by undrained monotonic loading test

After having the shear strain around 10.2%, the specimen undergoes the Undrained Monotonic Loading. The purpose of this experiment is to investigate whether the liquefied specimen can produce flow failure at the gentle ground inclination in undrained conditions. The results of the experiment are presented in Figure 7-13 and Figure 7-14. It is obvious that the strength of the soil can still mobilize the shear stress even after the liquefied state ($\gamma_{zq} > 7.5\%$). The specimen show non flow behavior or strain hardening phenomenon even after liquefied state. This result shows that long-distance flow failure can’t be explained using the undrained concept.

Therefore, one of the hyphothesis to allow the long-distance travel of flow failure is drained condition which allows the water flow to the liquefied specimen. From this assumption, the proposed mechanism of water-inflow for explaining the phenomenon of long-distance flow failure in Palu city is proposed. This consideration is since Palu

City has a unique feature of the confined aquifer profile that allow this assumption might lead to the proposal.

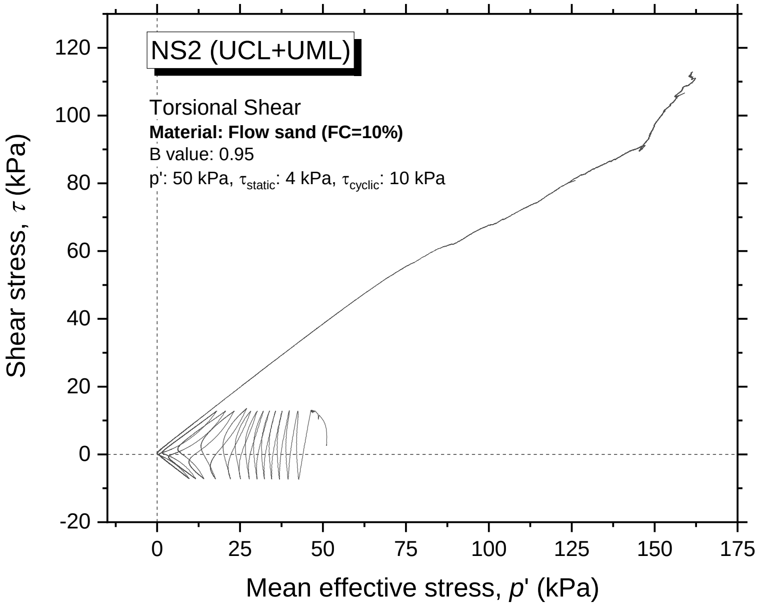

Figure 7-13 The stress-path of undrained cyclic loading test follows by the undrained monotonic loading test

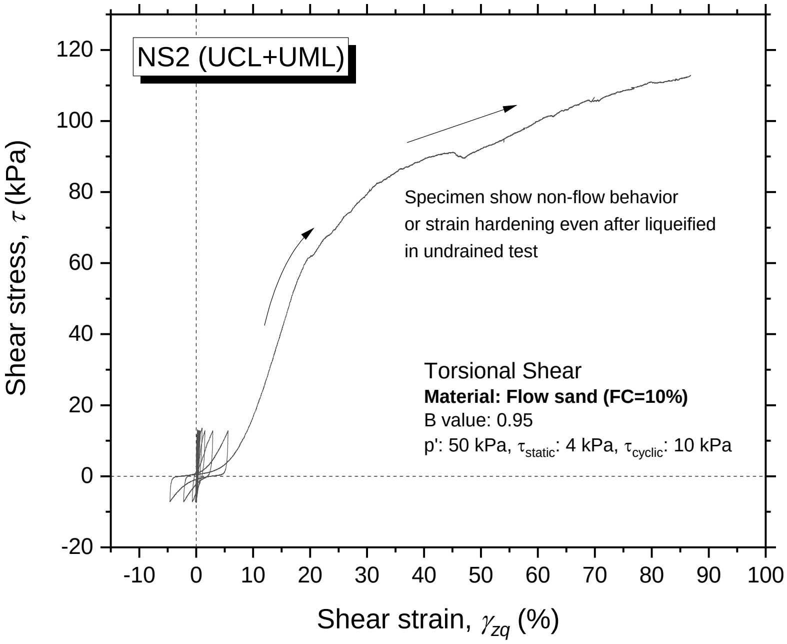

Figure 7-14 The strain relationship of the undrained cyclic test follows by the undrained monotonic loading test

7.2.Proposed Mechanism of Lateral Flow with Confined Aquifer

Bradley et al. (2019) analyzed the possibility of this lateral movement is promoted by the presence of the irrigation channel, particularly at the Petobo and Jono Oge. However, this type of flow movement was also observed at Balaroa in which no irrigation channel was constructed and the ground inclination was also gentle. Considering this fact and the evidences from the field observation (Hidayat, et al., 2020; Kiyota, et al., 2020; Okamura, et al., 2020), a mechanism elaborating the presence of confined aquifer is proposed. Based on this field reconnaissance, some hypothesis, as well as illustrations**,** have been made to understand the mechanism on how this liquefaction-induced-flow failure can occur.

It is estimated that in those three areas, groundwater exists on the sandy soil layer, including the unconfined and confined groundwater. Those type of layers is separated by a low-permeable soil layer, like the fact that there is rice field found at those three locations. This condition is illustrated in Figure 7-15.

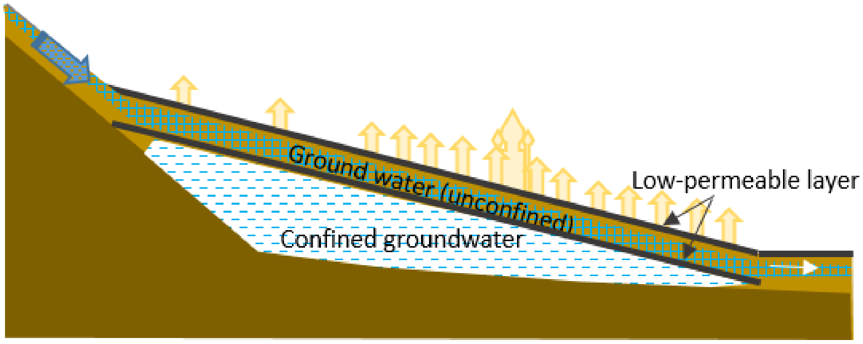

Figure 7-15 Illustration of the initial condition in the affected areas.

When the earthquake occurred, the sandy soil layer was liquefied. This interpretation is in line with the results of Portable DCPT which identifies the loose sandy soil layer in this area. Simultaneously, the earthquake motion also disturbed the low-permeable-layer at the shallow layer (Figure 7-16).

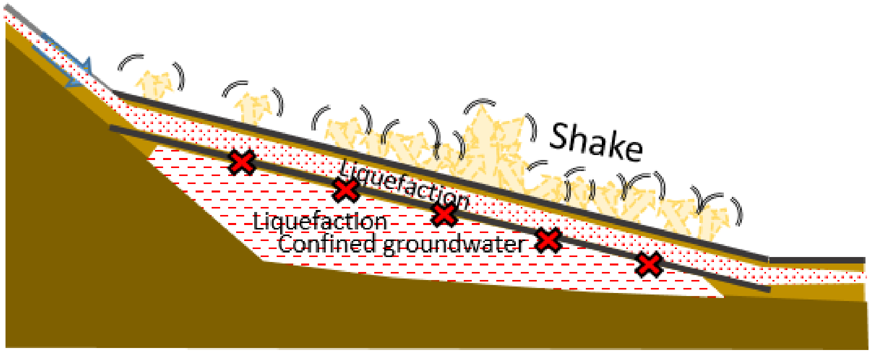

Figure 7-16 The earthquake motion induce liquefaction on the sandy layer and disturb the low permeable layer

As a result, the lateral flow and sand boiling occurred. After the earthquake shaking, the excess pore water pressure is usually dissipated, and the soil layer became stiff again. Nevertheless, in this condition, the dissipation of excess pore water pressure might be restricted by the presence of a low-permeable surface layer (Figure 7-17).

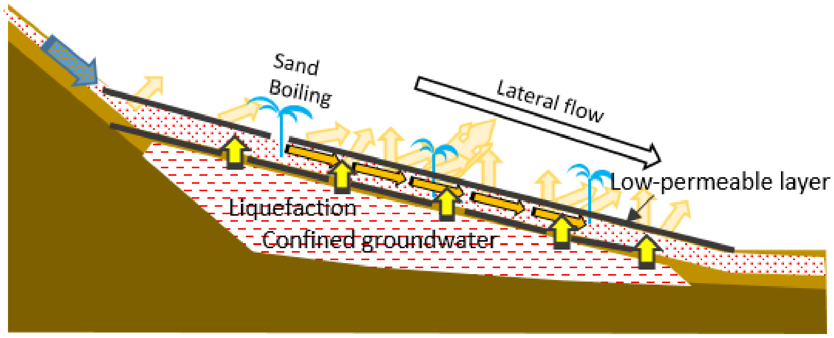

Figure 7-17 Excess pore water pressure is unable to dissipate, so the flow deformation continues to occur

This restriction made the liquefaction state continue, and the flow continues due to the upward osmotic pressure from a liquefied confined aquifer. This flow pushed houses and all the infrastructures to the lower elevation and deposited at the bottom of the slope. In the upper part, tensile cracks start to be developed (Figure 7-18).

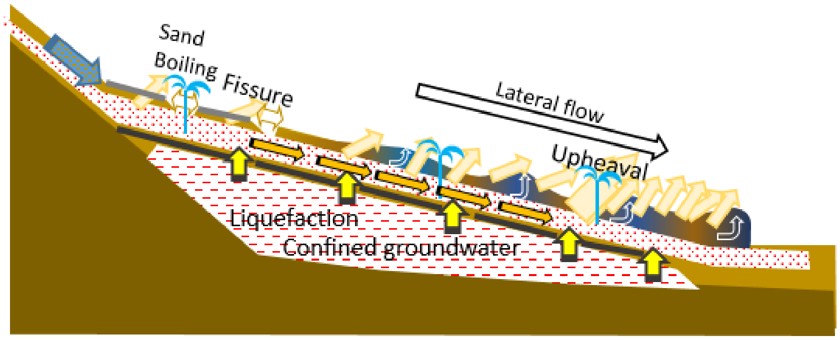

Figure 7-18 The osmotic pressure from the confined aquifer makes the flow continue and push all the buildings

After reaching a large deformation, the liquefaction stopped, and the induced-flow become stable. In some points, the seepage of groundwater from the confined aquifer can still be observed (Figure 7-19).

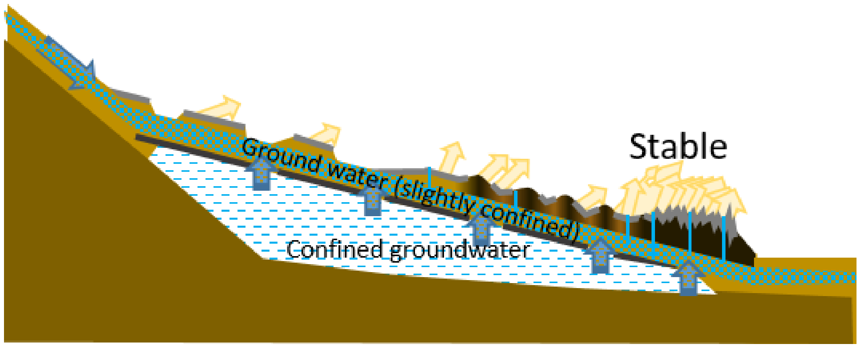

Figure 7-19 The flow stops and all the debris are deposited at the bottom part

7.3.Summary

Long-distance flow failure has occurred at several places in Palu city after the 2018 Sulawesi Earthquake. This flow failure results in a significant financial loss and thousands of casualties, including missing people as this flow mostly hit residential areas. Several points have been pointed out in this chapter, such as:

1. The long-distance flow failure occurred in a gently sloping ground, ranging from 1-4% of soil inclination in all the areas. It is found that there are the shreds of evidence of the soil liquefaction occurred, such as sand boiling, high water table condition, and sandy ground in the loose state. This evidence supports the hypothesis that the soil liquefaction phenomenon promotes this long-distance flow failure. Nevertheless, the classic soil mechanics theory could not explain briefly how this flow failure could travel very far just by considering the factor of soil liquefaction itself.

2. The field observation conducted two weeks after the flow failure occurrence found some inundated pond of freshwater in the affected area. These findings lead to the assumption that the affected area might have a unique feature of a confined aquifer that also affect the soil liquefaction phenomenon around this area.

3. In order to promote a hypothesis of the mechanism of this long-distance flow failure, series of the undrained cyclic test have been conducted to the disturbed sample of gravelly sand layer taken from the Sibalaya Trench 3 in Triaxial Apparatus. The results indicate that this sample has low liquefaction resistance and probably liquefied during the 2018 Sulawesi Earthquake. In addition, a sandy soil layer above the gravelly layer is assummed as the flow layer. In order to investigate whether this sample could flow under a mechanism solely by soil liquefaction, an undrained cyclic loading test follow by the undrained monotonic loading test has been conducted. The result shows that even after the liquefed state (shear strain is developed until 10.2%), the specimen still can mobilize the stress from the monotonic loading, showing no flow behavior. On the other hand, a static liquefaction test also has been conducted to this sand layer, permitting water injected to the specimen during the shearing process. The result show that flow behavior can be observed vividly after shear strain reaches 5.5%, with the volumetric strain around 1.8%. This static liquefaction test result indicates that the phenomenon of long-distance flow failure in Palu City could not be explained solely by conventional soil liquefaction theory.

4. By elaborating on the field observation and the soil element testings conducted in the laboratory, a mechanism of lateral flow with confined aquifer is proposed to

explain how this long-distance flow failure is possibly promoted by an external factor, which is a confined aquifer.

7.4. References

Bradley, K., Mallick, R. & Andikagumi, H., 2019. Earthquake-triggered 2018 Palu Valley Landslides Enabled by Wet Rice Cultivation. *Nat. Geosci.,* pp. 932-939.

Hidayat, R. F. et al., 2020. Reconnaissance on Liquefaction-induced flow failure caused by the 2018 Mw 7.5 Sulawesi Earthquake, Palu, Indonesia. *Journal of Engineering and Technological Sciences*, 52(No. 1).

Kiyota, T. et al., 2020. Overview of long-distance flow-slide caused by the 2018 Sulawesi earthquake, Indonesia. *Soils and Foundations (submitted).*

Okamura, M. et al., 2020. Large-scale flowslide in Sibalaya caused by the 2018 Sulawesi Earthquake. *Soils and Foundations (submitted).*

Chapter 8 CONCLUSIONS AND RECOMMENDATIONS FOR FUTURE STUDY

8.1. Conclusions

Dilation Behavior of Sandy Soil under Constant Shear Test

In order to investigate the dilation behavior sandy soils under constant static shear stress, series of static liquefaction tests have been conducted on Toyoura sand with different static shear stresses, initial densities, and fine content to a single amplitude of axial strain of 20%.

From all the results of the experiment under static liquefaction test, the development of axial and volumetric strain, which corresponds to the dilative behavior of soils, are classified into three areas, which are initial state, limited flow, and rapid flow. The phenomenon of unlimited flow failure can be observed at the rapid flow area, in which even the stress is kept constant, the specimen is kept dilating. All the specimens are dilated toward the steady-state line, regardless of having different static shear stress and initial density. This dilation behavior could be observed in the log p'-e plane.

The effect of the static shear stress to the dilation behavior of the specimen having the same initial density is not significant. Specimen undergo the small static shear stress (q=5 kPa) and the specimen with large static shear stress (q=80 kPa) show only 1% of volumetric strain difference. In addition, the dilative behavior is more pronounced by another factor, which is initial density. The effect of the initial density of the specimen to the dilative behavior is significant. The initial density of the material will define the volume expansion of the specimen. The densest the material, the more volumetric expansion will be developed, implying the more dilative the material.

Fine content affects the volumetric expansion of the material. The more fine content on the sand, the less dilative the specimen will be. As the fine content having smaller particle size compared to the granular material, the fine material will fill the void of the granular material resulting in the change of the void redistribution and the permeability will be reduced. This reduction of and void redistribution change will reduce the development of volume expansion.

Shear Strain Characteristics of Sandy Soils under Constant Shear Stress

The shear strain rate development represents the flow rate characteristics of sandy soils in the element test. This study investigates the effect of static shear stress, initial density, and fine content on the shear strain rate of sandy soil.

It is mentioned that the effect of static shear stress on the development of volumetric strain is not significant. However, the effect of static shear stress on the strain rate development is significant. The higher the static shear stress, the faster the rate of shear strain at failure. The experiment results also show that the initial density affects the shear strain rate behavior. The densest the initial density of a material, the faster the shear strain rate at failure. The relationship of both the effect of static shear stress and the effect of initial density on the strain rate characteristics is examined. It is found that the effect of static shear stress will be significant on the dense specimen and become less significant as the initial density of the specimen is loose.

The effect of fine content on the shear strain rate has been observed. In contrary to the clean sand, the dense material of mixed sand with fines show less shear strain rate compared to the loose material. This phenomenon emphasize the significance of volumetric strain accumulation to the shear strain rate.

Dilation Behavior and Shear Strain Characteristics at Large Strain

The dilation behavior and flow rate characteristics of clean sand under static liquefaction test at large strain can be observed using Torsional Shear Apparatus. The shearing mode of this apparatus made the result of observed flow failure is more appropriate with the field condition compared to the Triaxial Apparatus, in particular at the large strain level.

The flow failure phenomenon that occurred at the gently sloping ground could be observed in the Torsional Shear Apparatus. All the testing conditions represent the field condition of 1.5-2% of inclination.

The effect of drainage mode; half-drainage or full-drainage, is not significant to the difference of volumetric strain development. In addition, the softening behavior at $\gamma_{zq} - e$ plane is identical for both specimens having the same densities. The effect of confining pressure on volume expansion behavior is not significant. The difference in confining pressure condition will give a different result on the vertical strain that corresponds to the subsidence after the collapse of the specimen occurred during the shearing process.

The experimental results on Triaxial Apparatus and Torsional Shear Apparatus show a good agreement for the volume expansion behavior and flow rate characteristics. The denser the initial density of the specimen, the more dilative the behavior and the faster the shear strain rate at the failure point. The loss of particle interlocking of sand during static liquefaction test can be observed at large strain level in Torsional Shear Apparatus. This condition is represented by the quick stress drop of the specimen during the shearing process when the stress path approach the failure line.

Case study: Flow Deformation Behavior of Sandy Soils at Palu Area due to 2018 Sulawesi Earthquake

Long-distance flow failure has occurred at several places in Palu city after the 2018 Sulawesi Earthquake. This flow failure results in a significant financial loss and thousands of casualties, including missing people as this flow mostly hit residential areas. The long-distance flow failure occurred in a gently sloping ground, ranging from 1-4% of soil inclination in all the areas. It is found that there are the shreds of evidence of the soil liquefaction occurred, such as sand boiling, high water table condition, and sandy ground in the loose state. This evidence supports the hypothesis that the soil liquefaction phenomenon promotes this long-distance flow failure. Nevertheless, the classic soil mechanics theory could not explain briefly how this flow failure could travel very far just by considering the factor of soil liquefaction itself.

The field observation conducted two weeks after the flow failure occurrence found some inundated pond of freshwater in the affected area. These findings lead to the assumption that the affected area might have a unique feature of a confined aquifer that also affects the soil liquefaction phenomenon around this area. In order to promote a hypothesis of the mechanism of this long-distance flow failure, series of the undrained cyclic test have been conducted to the disturbed sample of gravelly sand layer taken from the Sibalaya Trench 3 in Triaxial Apparatus. The results indicate that this sample has low liquefaction resistance and probably liquefied during the 2018 Sulawesi Earthquake. In addition, a sandy soil layer above the gravelly layer is assumed as the flow layer. In order to investigate whether this sample could flow under a mechanism solely by soil liquefaction, an undrained cyclic loading test follow by the undrained monotonic loading test has been conducted. The result shows that even after the liquefied state (shear strain is developed until 10.2%), the specimen still can mobilize the stress from the monotonic loading, showing no flow behavior. On the other hand, a static liquefaction test also has been conducted to this sand layer, permitting water injected to the specimen during the shearing process. The result shows that flow behavior can be observed vividly after shear strain reaches 5.5%, with the volumetric strain around 1.8%. This static liquefaction test result indicates that the phenomenon of long-distance flow failure in Palu City could not be explained solely by conventional soil liquefaction theory.

By elaborating on the field observation and the soil element testings conducted in the laboratory, a mechanism of lateral flow with confined aquifer is proposed to explain how this long-distance flow failure is possibly promoted by an external factor, which is a confined aquifer.

8.2. Recommendations for Future Study

For the continuity and the improvement for future study, several recommendations that should be appointed are:

1. Effect of specimen size and drainage valve size

In this study, the experiment mainly uses two types of apparatus, which are Triaxial Apparatus and Torsional Shear Apparatus. However, only one type of specimen size for each testing machine. To improve the results and the accuracy of the future study, the effect of specimen size and the size of the inlet funnel on the pedestal as the source of the water inlet should become the variables of the experiment. This plan will improve the understanding of how the flow of water in the soil body might affect the results of the experiments.

2. Effect of undrained cyclic loading to the dilation behavior

The focus of this study is to investigate the post-failure phenomenon of flow failure. In order to do so, static liquefaction tests using constant deviatoric stress have been chosen to illustrate this phenomenon. However, the static liquefaction test do not count the effect of cyclic loading to strain development. In the future study, it is worth doing to consider the effect of cyclic loading on this post-failure behavior.

3. Effect of soil layering on the dilation behavior of specimen

This study was focused only on investigating the dilation behavior and characteristics of a single element in the soil body. Nevertheless, this phenomenon in the field elaborates on different types of soil layers that might result in the different modes of deformation. Thus, as a future investigation, it is interesting to model these soil layers to the element testing using a big scale of soil elements. This experiment will explain how the dilation behavior might be affected by the soil type and depth.